Novel Methodology for Atomistically Informed Multiscale Modeling of Advanced Composites

by

Ashwin Rai

A Dissertation Presented in Partial Fulfillment
of the Requirements for the Degree
Doctor of Philosophy

Approved February 2018 by the
Graduate Supervisory Committee:

Aditi Chattopadhyay, Chair
Lenore Dai
Hanqing Jiang
John Rajadas
Masoud Yekani Fard

ARIZONA STATE UNIVERSITY

May 2018

ABSTRACT

With the maturity of advanced composites as feasible structural materials for various applications there is a critical need to solve the challenge of designing these material systems for optimal performance. However, determining superior design methods requires a deep understanding of the material-structure properties at various length scales. Due to the length-scale dependent behavior of advanced composites, multiscale modeling techniques may be used to describe the dominant mechanisms of damage and failure in these material systems. With polymer matrix fiber composites and nanocomposites it becomes essential to include even the atomic length scale, where the resin-hardener-nanofiller molecules interact, in the multiscale modeling framework. Additionally, sources of variability are also critical to be included in these models due to the important role of uncertainty in advance composite behavior. Such a methodology should be able to describe length scale dependent mechanisms in a computationally efficient manner for the analysis of practical composite structures.

In the research presented in this dissertation, a comprehensive nano to macro multiscale framework is developed for the mechanical and multifunctional analysis of advanced composite materials and structures. An atomistically informed statistical multiscale model is developed for linear problems, to estimate and scale elastic properties of carbon fiber reinforced polymer composites (CFRPs) and carbon nanotube (CNT) enhanced CFRPs using information from molecular dynamics simulation of the resin-hardener-nanofiller nanoscale system. For modeling inelastic processes, an atomistically informed coupled damage-plasticity model is developed using the framework of continuum damage mechanics, where fundamental nanoscale covalent bond dissociation information is scaled up as a continuum scale damage identifying parameter. This damage model is coupled with a nanocomposite microstructure generation algorithm to study the sub-microscale damage mechanisms in CNT/CFRP microstructures. It is further integrated in a generalized method of cells (GMC) micromechanics model to create a low-fidelity compu-

tationally efficient nonlinear multiscale method with imperfect interfaces between the fiber and matrix, where the interface behavior is adopted from nanoscale MD simulations. This algorithm is used to understand damage mechanisms in adhesively bonded composite joints as a case study for the comprehensive nano to macroscale structural analysis of practical composites structures. At each length scale sources of variability are identified, characterized, and included in the multiscale modeling framework.

This dissertation is dedicated to my parents,

For without them, I am nothing

ACKNOWLEDGMENTS

The completion of this dissertation is a milestone that I would not have reached without the efforts of many people to whom I owe much appreciation. I am forever indebted to my advisor, Regents' Professor Aditi Chattopadhyay, for the guidance, encouragement, and challenge she provided me throughout the doctoral program. I am especially grateful for all her advice and supervision that has helped me mature into someone deserving of the doctoral title.

I would also like to thank the members of my Supervisory Committee, Professor Lenore Dai, Professor Hanqing Jiang, Professor John Rajadas, and Professor Masoud Yekani Fard for all their valuable insight and feedback that helped me improve the quality of the research presented in this work.

Gratitude is also due to my colleagues in Professor Chattopadhyay's research group and the Adaptive Intelligent Materials & Systems center. It was through discussions with Dr. Bonsung Koo, Dr. Joel Johnston, Dr. Luke Borkowski, Dr. Rajesh Neerukati, Dr. Nithya Subramanian, and Mr. Chris Sorini that I was able to develop some of my best ideas, and it was through the help of Mr. Siddhant Datta, Mr. Guoyi Li, Mr. Carlos Lopez, Mr. Akshay Nalla, and Mr. Bhavik Patel that I was able to perform my experiments. I would also like to thank Ms. Megan Crepeau and Mr. Vincent Luu for providing assistance with the day-to-day tasks of the center. Finally, I would like to thank my family and their unending support and love.

I would also like to acknowledge the funding sources, the program manager, and technical liaison that supported this research. The work presented in this dissertation was supported by the Office of Naval Research through grant number N00014-14-1-0068 and grant number N00014-17-1-2029. The program manager was Mr. William Nickerson and the technical monitor was Dr. Anisur Rahman.

TABLE OF CONTENTS

LIST OF TABLES

LIST OF FIGURES

Chapter 1

INTRODUCTION

1.1 Background

Advanced composite materials are increasingly becoming the material of choice for many applications especially in the aerospace, mechanical, and civil industries. Initially developed for niche applications, such as the jet engine fan blades for the Rolls Royce RB-211 aero-engine in the late 1960s (Ramsden 1968), these materials are now being deployed in the manufacturing sector, from heavy industries such as aircraft manufacturing (a premier example of which is the Boeing 787 dreamliner) to mass produced articles, e.g. cell phone cases and bicycle frames. Even industries that use conservative design practices are incorporating advanced composites in their material selection repertoire: building and construction fields are utilizing advanced composites in tall buildings (Taranath 2016) as well as in modern architectural designs, e.g., in the roof of Apple's AC2 Auditorium, one of the largest freestanding composite roofs ever made (Hague 2016).

There are numerous reasons for this gradual shift towards increased advanced composite use over the years. As structural materials, advanced composites exhibit several advantages over traditional metallic materials in high strength-to-weight ratios, high stiffness-to-weight ratios, multifunctional capabilities, buckling resistance, and vibrational damping, to name a few (Daniel, Whitney, and Pipes 1983; Daniel et al. 1994; Jones 1998). Nearly all these advantages originate from the nature of these material systems, primarily because composite materials can be customized for their specific applications. Generally, advanced composites are made up of one or more reinforcing components and a matrix component that binds the reinforcer together to create a single heterogeneous material system. The reinforcing component is usually selected to be high strength, high

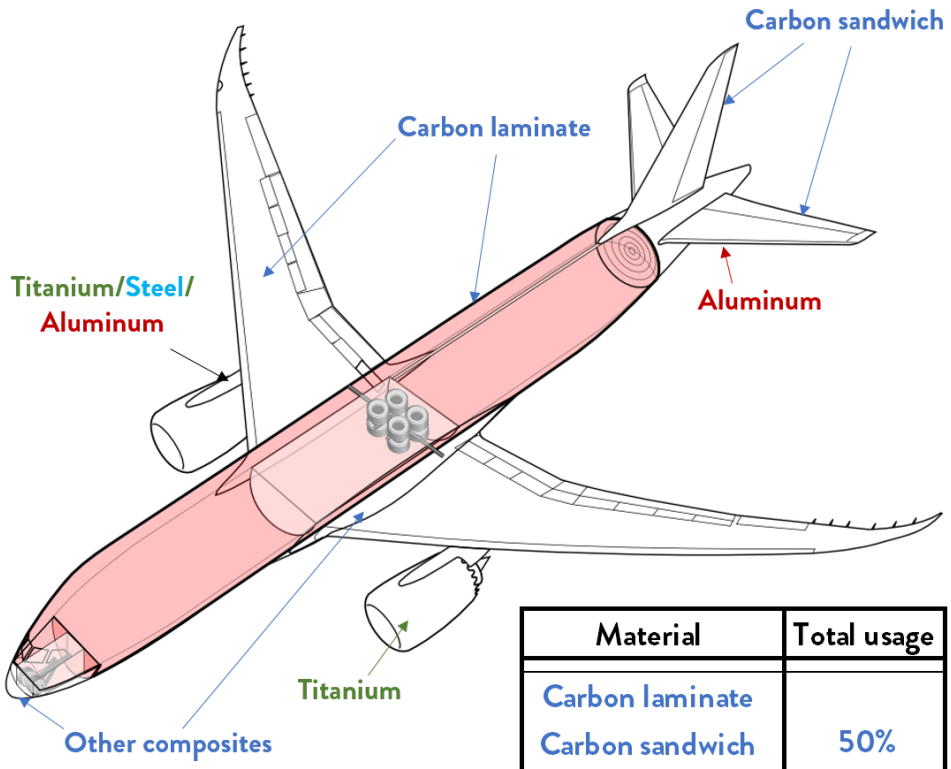

Material	Total usage
Carbon laminate Carbon sandwich Other composites	50%
Aluminum	20%
Titanium	15%
Steel	10%
Other	5%

Figure 1.1. Advanced composite use in the Boeing 787 Dreamliner

Data Source: (Roeseler et al. 2007); *Image Source*: (Wikimedia 2012)

stiffness, and low density fibrous materials, such as glass fiber, carbon fiber, and ceramic fiber. The matrix phase is selected for its binding and manufacturing properties, rather than for its material properties, and includes material such as polymers, ceramics, and metals. A careful combination of the reinforcing and matrix phase can lead to material systems that incorporate specific properties of both the components, including unusually high elastic properties in the direction of the fibers.

The ability to engineer such highly customizable material systems has led to a deviation from traditional design practices and has permitted the introduction of new designs and applications, as well as a reduction in the weight of materials, thereby overcoming some of the compromises of limited material choices (Day 2008). A primary example of these novel material systems is carbon fiber reinforced polymer (CFRP) composites. CFRP composites can be engineered to produce high strength, light weight, fatigue resistant, fire-retardant materials, particularly suited for aerospace, naval, wind, and consumer applications (Gay 2014). Recent advances in nanotechnology have been exploited to further engineer CFRPs to produce carbon fiber nanocomposites, such as carbon nanotube (CNT) enhanced CFRPs, demonstrating additional improvements in mechanical strength, interlaminar fracture resistance, energy absorption, and thermomechanical properties when compared with CFRPs (Green et al. 2009; Inam et al. 2010; Cho, Daniel, and Dikin 2008).

However, with the substantial material design space afforded by new materials, there is a growing need to efficiently engineer novel composite materials, tailoring them for particular applications or optimizing the material structure-property relationship for maximum utility. Although this may be performed through extensive experimental characterization, the large number of physical variables and their complex interactions, especially for nanocomposites, makes this approach infeasible. Hence, an alternative approach must be considered.

1.2 Integrated Computational Materials Engineering

In current engineering practice, assuring short product development cycles is critical for continued global competitiveness. Such operations have been stimulated by the integration of computational tools at various stages of the product development process. At the product design stage, computer aided design (CAD) and computer aided engineering (CAE) tools have supported in-

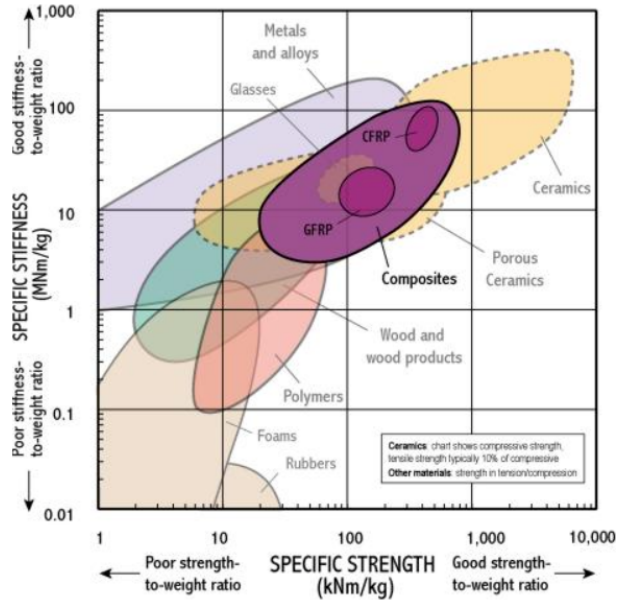

(a) Stiffness versus strength

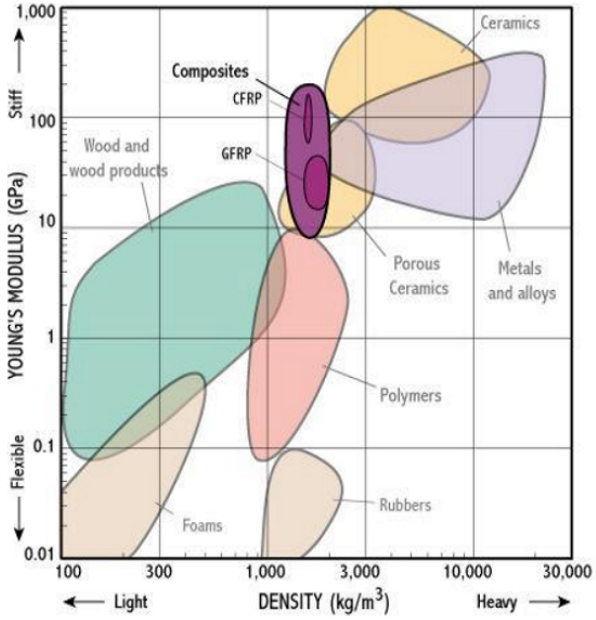

(b) Elastic modulus versus density

Figure 1.2. Material property comparisons

Source: (Lovatt, Shercliff, and Withers 2000) reproduced with permission

novative design solutions (Robertson and Radcliffe 2009), where robotics and automation tools have driven increases in manufacturing productivity (Rigatos 2011). However, materials selection has generally followed an antiquated structure, involving a simple cost-benefit approach for traditional materials from a limited materials list, creating a weak link in integrated product development. The science of predictive simulations for materials engineering can fill this gap by providing computational tools that can automate and optimize the materials selection process, by offering *a-priori* knowledge of the behavior of the most appropriate materials at a fundamental level in the context of the product use. Furthermore, such tools can be utilized to design the material from the ground up, and specifically for its intended purposes. Such an approach of designing the materials for the products by taking advantage of material physics and computational tools is called Integrated Computational Materials Engineering or ICME (National-Research-Council 2008).

An important first step, however, in a successful application of the ICME concept is rigorously establishing the structure-property relationship through a physics based understanding (Olson 2000). Such knowledge can then be consolidated into the development of validated advanced physics based computational tools that can be used to calculate and predict the associated material system behavior using only the basic constituent or process related properties. Such a virtual computational test bed can lead to minimizing experimental investigations, allow for rapid testing and parametric studies of various constituent configurations, provide a fundamental understanding of the mechanics of heterogeneous materials, and permit an ICME approach for designing and optimizing novel materials.

The ICME approach holds special relevance for advanced composites due to the freedom associated with engineering their basic constituents. For example, since fiber reinforced composites and nanocomposites typically consist of a large number of operating variables, validated computational tools can be used to predict their structure-property relationships and can aid in the design, manufacturing, processing, and optimizing the utility of these material systems. Additionally,

such computational predictive approaches may be used to gain insight into some of the most pressing obstacles to advanced composite use in industry, such as the inability to scale nanocomposite properties with size, which has led to large disparities in observed microscale and structural scale properties of nanocomposites (Sochi 2012). Issues also continue to persist in exploiting established CFRP components such as the bonded composite joint, due to the lack of a comprehensive understanding of damage initiation, damage progression, and failure in these materials. In this specific example, a lack of understanding of material properties has led to the use of mechanical fasteners when bonded composite material joints are used in primary load-bearing applications, thus causing 'overdesign' of the advanced composite structures. Hence, comprehensive computational tools may be used to study these types of material behaviors and to determine causes for the inability to scale material properties with size and the generation of 'hot-spot' zones. This capability, in turn, would permit designing materials that can utilize their full potential and developing strategies that help to mitigate and delay failure in advanced composite components.

Although, a strong case exists for developing such computational models, predicting the properties and behavior of advanced composites using only basic constituent properties can be a fundamentally challenging task due to the multiscale nature of these material systems (Kwon, Allen, and Talreja 2008). For a genuine implementation of the ICME approach for advanced composites requires investigation of the constituent behavior at various length scales to produce a network of structure-property relationships. Since the dominant physical mechanisms vary at different observed length scales, each node of this multiscale system must be studied independently to produce a length scale dependent structure-property relationship. However, since implementation of these material systems generally occurs at the macroscale, the understanding at the various scales must also be linked together for this methodology to influence the material and product design process. The scientific approach used for understanding and coupling mechanisms at various length scales and establishing models based on such knowledge is called multiscale modeling (Horstemeyer

2009), and this approach may hold substantial potential for designing and optimizing advanced composite materials and composite structural components.

1.3 Multiscale Modeling of Advanced Composites

It is observed that the dominant material structure in advanced composites is distinctly separate at various length scales due to the inherent heterogeneity of this material system. The advanced composite structure, which can be considered as the macroscale, is manufactured using single or multiple *laminates* that are joined together using various manufacturing processes such as bonding or riveting. The laminates are in turn manufactured by stacking several *laminae* together using a lay-up procedure. The single *lamina* may have a simplistic unidirectional material structure, as is commonly used in *prepregs*, or it may be composed of complex weave geometries.At the length scale of the lamina, small geometrical and material inconsistencies, such as pockets of matrix-rich regions, may play a significant role in material behavior, for example, it may create localized damage 'hot-spot' regions, and hence this scale is separately classified as the mesoscale.

The lamina is made up of fiber bundles, individual reinforcing fibers, additional reinforcements, possibly some forms of fiber coating, and the matrix that binds them. The length scale of the lamina is radically different compared to the length scale of the constituents, which is considered to be the microscale. The microstructure largely involves the interaction of the reinforcement and matrix phase, such as the carbon fiber and the epoxy in CFRPs. The microstructure has been shown to influence bulk composite behavior, and can be practically manipulated to optimize resultant composite properties. Additionally, major sources of stochasticity, such as reinforcement geometry, matrix curing, and fiber volume fraction are introduced at this phase, accounting for the experimentally observed spread in material properties that is characteristic of advanced composites (Shaw et al. 2010; Chiachio, Chiachio, and Rus 2012).

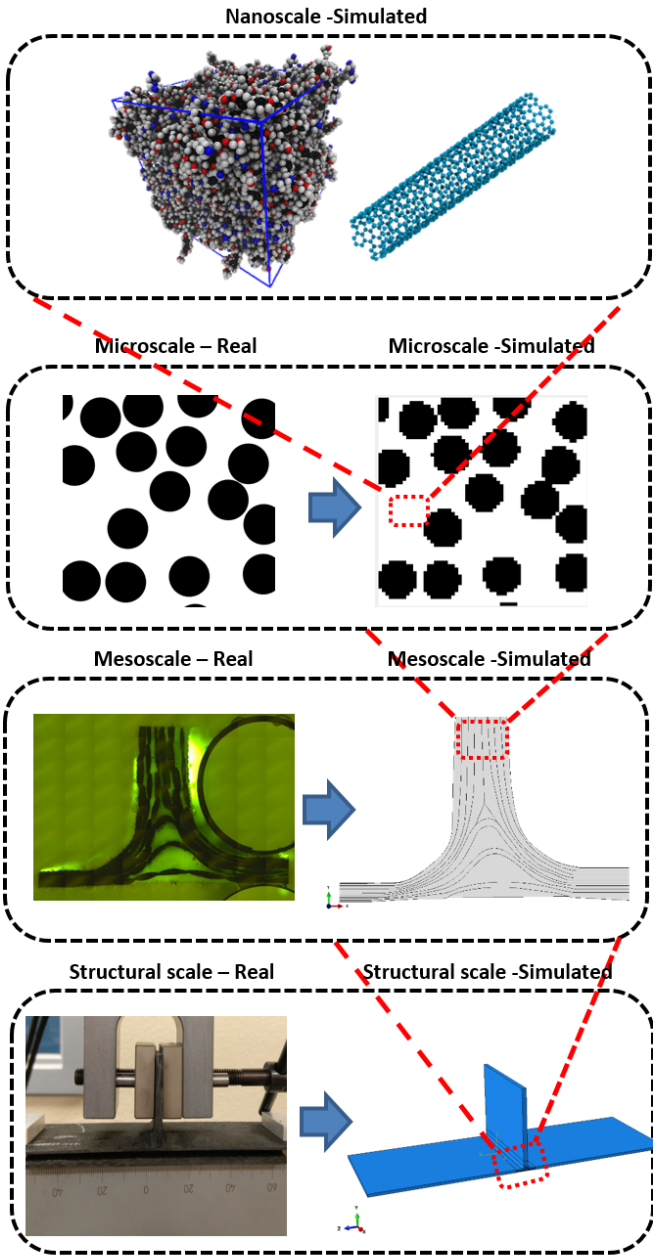

Figure 1.3. Atomistic to structural multiscale modeling scheme

To study the complete spatial domain of the microscale, taking into account the geometry of each microscale constituent that is significant, while also covering the entirety of the mesoscale spatial domain would be an infeasible and intractable undertaking. Instead, a more practical ap-

proach would be to select a periodic portion of the microscale, such that the material response of the small periodic element is representative of the entire geometry. Hence, there is a need to use periodic representative unit cells (RUCs) to study the microscale constituents (Sun and Vaidya 1996). The size of a heterogeneous RUC with volume V can be considered appropriate if the average value of the measured variable from the RUC, $\bar{A}_{RUC}$, is equal to the measure of the variable for the complete geometry $\bar{A}_{geom}$ (Kanit et al. 2003). The average variable measure from the RUC can be calculated by ensemble averaging the local measure of the variable, A, over the spatial domain of the RUC:

$$\bar{A}_{RUC} = \frac{1}{V} \int_V A \, dV \tag{1.1}$$

Finally, the microscale itself can be deconstructed to the most fundamental length scale appropriate for mechanical and structural studies, which would be the atomic scale, where molecules, chains, chemistry, and chemical bonds play a significant role in determining elastic and inelastic properties (Lutsko 1988). The basic causes of stochasticity in properties are also observed to originate at these length scales (Tack and Ford 2008).

Developing a computational framework that incorporates the effects of these relevant length scales is challenging due to the immense spatial domain covered, the significant variations in local fields on change of dominant length scale, and the complex interactions of the various scale dependent phenomenon that need to be physically modeled. Conventional computational methodologies use a top-down approach, employing bulk material analysis or a bottom-up approach using mean field techniques to predict structural scale composite properties. In top-down bulk material analyses, such as the smeared material techniques (Hashin 1980; Tsai and Wu 1971), the structural behavior is evaluated using conventional continuum mechanics approaches, which are then used to resolve lower scale constituent properties. Most of these techniques limit themselves to the lamina level, where laminate stresses are decomposed to calculate lamina stresses using laminated shell theories (Ashton and Whitney 1970) or higher order plate theories (Reddy 1984). The lam-

ina properties are then progressively discounted by comparing lamina stresses with experimentally characterized lamina strengths, to create an iterative highly phenomenological methodology. The microscale may be included by transforming the lamina stresses to microscale constituent stresses using stress amplification factors calculated through finite element (FE) investigations of the micro RUC (Jin et al. 2008). The microscale quantities can then be used to perform microscale damage and failure studies. This is accomplished by extending the previously mentioned iterative phenomenological methodology to account for microscale constituents rather than the lamina properties. Such techniques extend the simple maximum stress/strain criterion or the Tsai-Wu quadratic criterion, to account for fiber failure (Ha, Jin, and Huang 2008) and a plasticity based procedure, such as modifications of the von Mises failure criterion (Christensen 2007) or higher fidelity computational plasticity models (Goldberg, Roberts, and Gilat 2005) for matrix damage and failure. These techniques may also include interface failure and micro-constituent interactions through extensions of the Hashin failure criterion (Camanho and Dávila 2002). The top-down techniques without microscale additions can be computationally efficient and easily implemented into structural design methods, and also allow for the design of straightforward validation experiments. The addition of the microscale aspect, however, can significantly slow down the computational procedure. Furthermore, the phenomenological basis of this technique can lead to large bounds on predictions, lack of insight into the intrinsic material physics, and the requirement of a comprehensive experimental program to supplement the analysis algorithms.

Bottom-up approaches use micromechanics to explicitly incorporate microstructural details into structural analysis using both analytical and semi-analytical techniques (Qu and Cherkaoui 2006). In these methods, the microlevel and macroscale quantities are connected using phase averaged concentration factors, and are developed through an analysis of the microstructural details and some form of homogenization (Buryachenko 2007). For simple microscale geometries, a simplified form of these methods, using a strength of materials approach may be applied to obtain

explicit relatively simple analytical relations between the elastic properties of the microstructure constituents and the macroscale composite. In these cases, through an analysis of ideal loading conditions (e.g., a uniaxial strain field or a uniaxial stress field), the effective properties of the composite can be found as a function of the properties of each individual micro constituent. This is called a rule of mixtures type approach, classified according to the various assumptions , loading direction, and microscale geometry. Some examples of this type of approach are the Hill's method (Hill 1963), Voight approximation, (Voigt 1889), Reuss approximation (Reuss 1929), and composite cylinder assemblage (Hashin and Rosen 1964). The rule of mixtures approach is also greatly expanded in many standard composite texts (Herakovich 1998; Kaw 2005). However, a general approach to micromechanics is to consider ensemble averaged stresses, which are then related to the appropriate global or macroscale quantities (Buryachenko 2001), as shown in equation 1.2.

$$\bar{\underset{\sim}{\boldsymbol{\sigma}}} = \frac{1}{V}\int_V \underset{\sim}{\boldsymbol{\sigma}}\, dV = \frac{1}{V}\left(\int_{V_i} \underset{\sim}{\boldsymbol{\sigma}}^{i}\, dV_i + \int_{V_{ii}} \underset{\sim}{\boldsymbol{\sigma}}^{ii}\, dV_i + \cdots\right) \tag{1.2}$$

where $\underset{\sim}{\boldsymbol{\sigma}}$ is the stress, and quantities $i, ii, \cdots$ represent the various microstructural constituents.

The effective global or macroscale properties are then a function of the individual properties of each microscale constituent and related through a phase averaged concentration factor $\underset{\approx}{\boldsymbol{M}}$ or $\underset{\approx}{\boldsymbol{B}}$, as shown in equation 1.3 and 1.4.

$$\bar{\underset{\approx}{\boldsymbol{C}}} = f(\underset{\approx}{\boldsymbol{C}}_i, \underset{\approx}{\boldsymbol{C}}_{ii}, \underset{\approx}{\boldsymbol{C}}_{iii}, \cdots, v_i, v_{ii}, v_{iii}, \cdots)\, \underset{\approx}{\boldsymbol{M}} \tag{1.3}$$

$$\bar{\underset{\approx}{\boldsymbol{S}}} = f(\underset{\approx}{\boldsymbol{S}}_i, \underset{\approx}{\boldsymbol{S}}_{ii}, \underset{\approx}{\boldsymbol{S}}_{iii}, \cdots, v_i, v_{ii}, v_{iii}, \cdots)\, \underset{\approx}{\boldsymbol{B}} \tag{1.4}$$

where $\underset{\approx}{\boldsymbol{C}}$ is the stiffness tensor, $\underset{\approx}{\boldsymbol{S}}$ is the compliance tensor, and v is the volume fraction. These functions and the relations for the phase averaged concentration factors can then be obtained using various homogenization schemes and approximations. For example, the Voight and Reuss approximations can be utilized to obtain $\underset{\approx}{\boldsymbol{M}}$, or $\underset{\approx}{\boldsymbol{B}}$ as an identity matrix, respectively. Other methods include the Eshelby field that connects the stress and strain fields inside a single inclusion in an infinite matrix, to the far-field or macroscale quantities (Eshelby 1957), which has been applied in

the context of fibrous composites within the self-consistent method (Budiansky 1965; Hill 1965) and generalized self-consistent method (Huang et al. 1994). The special case of the Eshelby field with uniform far field strain boundary conditions has also been used to create the Mori-Tanaka method (Mori and Tanaka 1973) and reformulated for fibrous composites (Benveniste 1987). Another approach to arrive at the micro-macro relations and explicit analytical equations for concentration matrices is the method of cells technique, which approximates local fields in subcells that make up the microscale unit cell, by using continuity equations that are true in an averaged sense (Aboudi 1989) and uses the Taylor's expansion to form a relation for the concentration matrices as a function of macroscale quantities. The two-scale and multi-scale asymptotic expansion with the classical mathematical theory of homogenization has also been used to couple the length scale dependent parameters and to establish relationships between local-global stress/strain fields (Fish, Yu, and Shek 1999). Cosserat homogenization (Forest and Sab 1998; Forest 1998), parametric finite-volume micromechanics (Chen, Urquhart, and Pindera 2005; Pindera et al. 2009), generalized differential expansion (Pasternak and Mühlhaus 2005), and strain-gradient homogenization (Smyshlyaev 2009; Peerlings and Fleck 2004) are further examples of approaches used for the coupling of multiscale spatial domains, which are expanded in various review papers and books (Charalambakis 2010; Kalamkarov, Andrianov, Danishevsâ, et al. 2009; Nemat-Nasser and Hori 2013).

Although, such mean field micromechanics techniques provide an analytical or semi-analytical and mathematically consistent way to couple various scale dependent quantities, they consistently over or underestimate properties due to the assumption of simplistic RUCs, which do not particularly account for the stochasticity in the microscale constituent geometries and properties (Johnston and Chattopadhyay 2013). Furthermore, the study of the nanoscale mechanics becomes critical for materials such as nanocomposites due to the size of the filler materials, which may be around the order of a few molecules. The reinforcing agent may actively interact

with the molecules of the matrix, leading to unique and novel mechanical states that need to be accounted for in computational models. These molecular scale mechanisms become especially important in the investigation of interface effects between constituents, since interface behavior is a known function of the surface morphology at the nanoscale, and can have significant effects on the composite material properties (Drzal, Rich, and Lloyd 1983; Evans, Zok, and Davis 1991; Johnston et al. 2017). Even if current techniques do make use of realistic microscale RUCs, the interaction of the polymer molecules, the effects of nanofillers such as CNTs at the atomic scale, and nanoscale mechanics, in general, are entirely ignored.

Recent interest in investigating nanoscale mechanics in structural materials has led to many studies at the nanoscale using molecular dynamics or MD simulations (Shinoda, Shiga, and Mikami 2004; Yamakov et al. 2004; Wu 2006). Atomistic simulations were recently used to successfully predict epoxy matrix elastic properties (Fan and Yuen 2007) and the stress-strain response of epoxy matrix with CNT nanofillers (Frankland et al. 2003). Similar MD simulation studies that focus on nanoscale mechanics suggest that the unique stress state at the nanoscale in polymer matrix composites and nanocomposites may cause the observed divergence in experimental and predicted response at the higher length scales (Subramanian, Rai, and Chattopadhyay 2015; Subramanian et al. 2015). These studies also show that the stress-strain response at the nano- and the sub-microscale can be significantly different from the average bulk stress-strain response of polymer matrix composites and nanocomposites. These observations suggest that an accurate elastic and damage analysis of these materials cannot ignore the nanoscale atomistic contributions. Therefore, any theoretical framework for modeling these materials must resolve and integrate each scale-dependent constituent, including nanoscale information. Ultimately, the macroscale structural behavior aggregates the mechanics of all the lower length scale elements, which in turn actively influences elastic, damage, and failure properties of the composite structure. Hence, the multiscale nature of these material systems leads to several material-structure relationships at various

length scales, all of which interact and cause the final observed structural response. Thorough inclusion of this multiscale nature, along with the associated scale-dependent causes of uncertainties in the analysis of advanced composites is, therefore, critical for accurate prediction of advanced composite material and component behavior.

1.4 Nanoscale Integration - Challenges

Despite the growing need for multiscale analysis methods for advanced composites incorporating nanoscale effects, a fundamental challenge associated with the integration of these length scales is the incompatibility of the basic framework utilized to model atomic systems, which are considered as discrete systems, and as larger constituents, which can be assumed to be mathematically continuous. Attempts at such an integrated modeling strategy for the analysis of CFRPs with atomistic information have met with serious limitations. Such analysis techniques have been performed using a combination of MD simulations and averaging techniques such as elastic homogenization based micromechanics (Kundalwal and Kumar 2015a), statistical techniques such as Monte Carlo methods (Chui and Boyce 1999) or fully continuum mechanics FE approaches (Fisher, Bradshaw, and Brinson 2002). Homogenization provides reasonably accurate results for elastic analysis; however, it can lead to imprecise results for inelastic and damage analysis due to loss of spatial variability in stress and strain fields (Borkowski, Liu, and Chattopadhyay 2013). Statistical techniques may require an infeasible amount of simulations to accurately characterize the complete spectrum of the nonlinear behavior, and FE methods cannot accurately capture the fidelity at the atomic scale due to the breakdown of the assumptions of continuum mechanics. Recent literature has focused on deriving rigorous mathematical theories for describing the stress state of heterogeneous media, wherein the nanoscale mechanics is implicitly integrated using various forms of homogenization, such as the variational asymptotic homogenized micromechanics

models (Yu and Tang 2007; Oskay and Fish 2004), eigen deformation based reduced order models (Bogdanor and Oskay 2016; Oskay and Fish 2007), mathematical homogenized micromechanics coupled with diffused damage (Murari and Upadhyay 2012), or *ad-hoc* mathematical functions such as the boundary condition free micromechanics theory (Peng and Yu 2015). Since the implicit conditions of the nanoscale mechanics in these methods are bound to certain ideal assumptions, they are not generally applicable and may not provide any special insight into the problem under investigation.

To overcome issues encountered with an implicit nanoscale understanding, some recent studies have used concurrent coupled FE and MD simulations to capture nanoscale mechanics explicitly. In these methodologies, there exists a fine scale and a coarse scale, where these scales directly couple through a handshake or interface region (Miller and Tadmor 2009). The coarse scale may be modeled using continuum FE based approaches and the fine scale is modeled using atomistic approaches. These techniques utilize an energy based governing equation and special forms of coupling boundary conditions, along with various forms of handshake region models (Talebi et al. 2014). Some examples of these techniques are the quasicontinuum model (Shenoy et al. 1998; Tadmor, Ortiz, and Phillips 1996), bridging domain and bridging scale method (Xiao and Belytschko 2004; Wagner and Liu 2003; Qian, Wagner, and Liu 2004), hybrid simulation method (Luan et al. 2006), and the concurrent AtC coupling (Fish et al. 2007; Badia et al. 2008). Most of these techniques differ according to the handshake region model that is employed, and the treatment of the continuum region. It is to be noted, however, that the nanoscale mechanics, when used in these works, utilize empirical force fields that cannot capture fundamental nonlinearities at the nanoscale such as the covalent bond dissociation of polymer chains (Subramanian, Rai, and Chattopadhyay 2015). When reactive bond order force fields are used in these methods, the implementation becomes computationally infeasible. Furthermore, it has been shown that there are certain localized phenomena, such as stress recovery proceeding initial softening and damage

saturation, which can only be captured by explicitly modeling the nanoscale substructures using reactive bond order force fields (Subramanian et al. 2015).

The aforementioned drawbacks motivate the development of a multiscale modeling approach for the elastic and inelastic analysis of advanced composites, such as CFRPs and CNT enhanced CFRP nanocomposites, which utilize nanoscale information obtained using reactive force fields, and bridge this to the higher length scale. Furthermore, this approach should also address uncertainty at the various length scales to permit a realistic analysis of these material systems for novel material development applications or for optimizing material design and performance. As engineering examples and case studies for the application of the developed multiscale approach are presented, critical challenges associated with advanced composites, such as nanocomposite scalability and damage in composite bonded joints, can then be investigated.

1.5 Objectives

This research is focused on accomplishing the following objectives:

- Develop a stochastic multiscale model for CFRPs and CNT/CFRPs that utilize nanoscale derived elastic information and variation in the curing degree to efficiently estimate the composite properties under fundamental uncertainty, and to validate with experimental observations.
- Develop a thermodynamically admissible bridging technique to efficiently transfer inelastic information from discrete nanoscale MD simulations of the polymer matrix to higher length scales, and to model using continuum mechanics.
- Investigate the nonlinear effects of the presence of nanofillers such as CNTs in polymer matrix under mechanical loading, using the developed atomistically informed damage model;

investigate causal effects of damage initiation and propagation in polymer matrix in the presence of CNTs.

- Investigate the variation of piezoresistive properties of the CNTs in the polymer matrix under damage due to mechanical loading.
- Develop an integrated representative unit cell for the high fidelity analysis of CFRPs and CNT enhanced CFRP microstructures; investigate the effect of CNT architecture on damage initiation and propagation.
- Develop low fidelity physics based damage models to capture global microscale response and integrate behavior of the constituent interfaces based on nanoscale information; investigate composite properties under uncertainty.
- Utilize the low fidelity damage models for macroscale integration; investigate mechanical behavior of practical composite structures, such as composite bonded joints, by using the low fidelity atomistically informed damage model.

1.6 Outline

This dissertation is organized as follows:

Chapter 2 introduces a modeling framework for the elastic and limited inelastic analysis of CFRPs and CNT/CFRPs using a novel technique for sampling atomistically derived constituent properties and applying it to a stochastic composite microstructure. This framework enables the generation of distributions of composite properties computationally, accounting of various sources of material uncertainty.

Chapter 3 proposes a thermodynamically admissible constitutive law for thermoset polymers, based on the framework of continuum damage mechanics (CDM), with the damage evolution equation developed from the results of elastoplastic MD simulations. This procedure bridges in-

elastic information from discrete MD simulations to the higher length scale continuum model in a computationally efficient manner. This framework is benchmarked against classical damage and plasticity models, and is validated against experiments.

Chapter 4 establishes an algorithm to generate realistic CNT-polymer microstructures. The concept of embedded meshing is also introduced for effectively modeling CNT-polymer interactions at the sub-microscale. Load transfer and damage mechanisms at the sub-microscale, and effects of CNT kinematics on damage initiation and propagation, are studied using the atomistically informed CDM damage model. This chapter also extends the damage analysis framework to include piezoresistive effects, to study the multifunctional aspect of CNT-polymer matrix under non-pristine conditions. Causal mechanisms for variation in piezoresistive behavior is investigated in this chapter.

Chapter 5 introduces an automated algorithm for the generation of realistic advanced composite microstrutures with or without CNT nanofillers, including material variability. This algorithm permits multiple architectures of the CNTs to be generated in the CFRP microstructure, and allows a holistic high fidelity analysis of the composite at the micro, and sub-microscale. As a case study, two nanocomposite architectures, randomly dispersed CNTs and radially grown CNTs, are investigated. Additionally, an orthotropic low fidelity damage model, based on the Schapery theory (Schapery 1990), is derived for capturing the global RVE response.

Chapter 6 details the generation of a microscale model based on the generalized method of cells (GMC), which integrates nanoscale elastic information, imperfect interfaces where interface behavior is derived from analogous MD simulations, inelastic mechanisms using the atomistically informed CDM damage equations, and realistic composite microstructures. The effect of weak interfaces in the microscale response of CFRP composites is then investigated.

Chapter 7 presents experimental studies on CFRP composite bonded joints in the 'T' configuration. The experimental data is used to generate the mesostructure of the composite joint. This

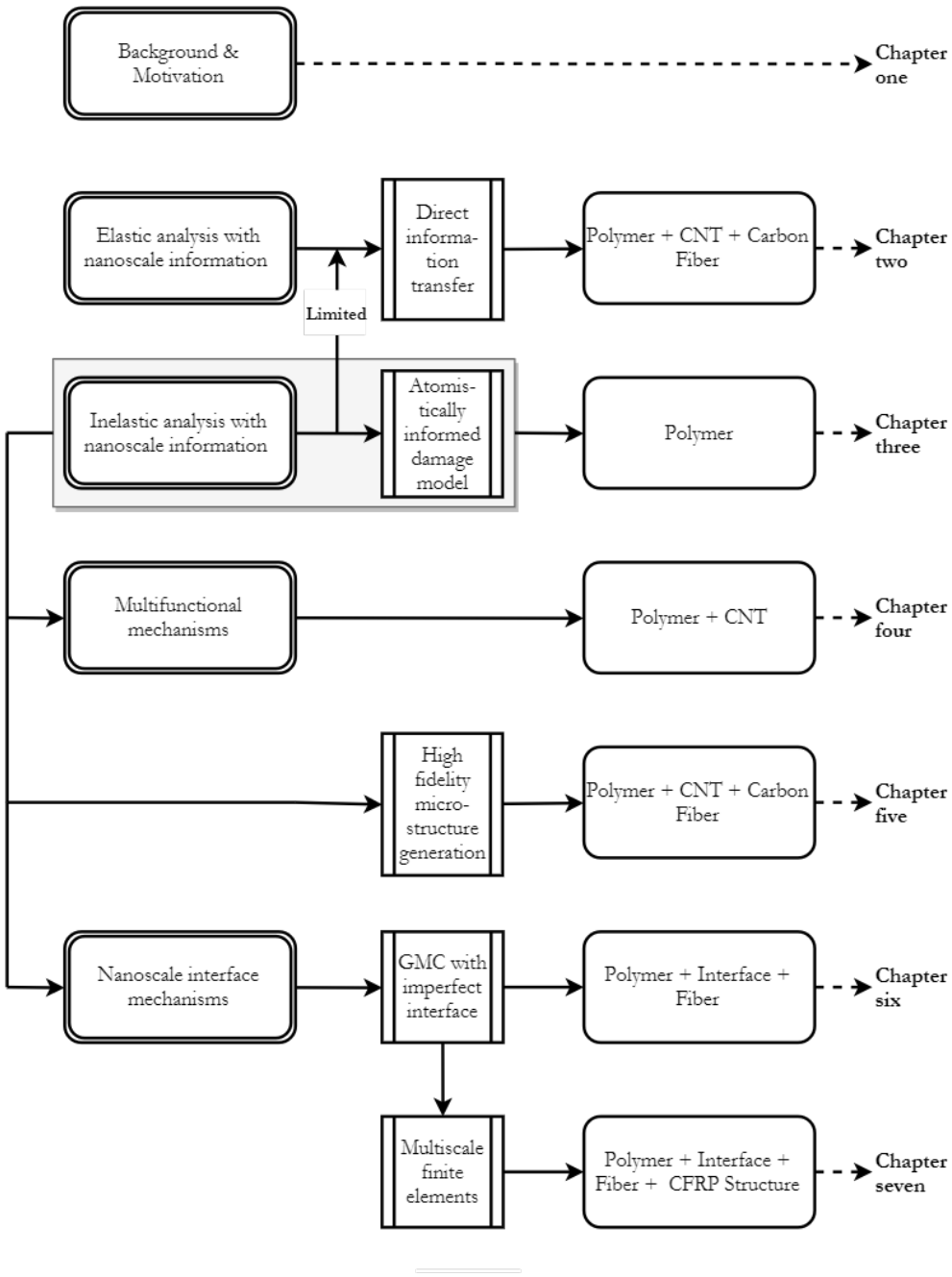

Figure 1.4. Dissertation outline

chapter further elaborates on the development of a multiscale framework that couples the nano-micro-meso-macroscale models for the inelastic analysis of practical composite components. This

multiscale modeling technique is further used to simulate the composite bonded joint response. The simulated data is then compared against the experimental response to ascertain validity of the developed multiscale model.

Finally, important conclusions derived from this research and possible areas for future studies that extend upon this work is presented in chapter 8.

Chapter 2

MULTISCALE ANALYSIS USING DIRECT ATOMISTIC INFORMATION TRANSFER

2.1 Introduction

Mainstream application of carbon fiber reinforced polymer (CFRP) composites and the more recently discovered nanocomposites (Sandler et al. 1999) have seen a surge over the last decade in various industries such as aerospace, automotive, and the consumer application industry. However, use of these materials continues to be associated with caution and conservative design practices due to a host of issues (Cantoni et al. 2014; Czél, Jalalvand, and Wisnom 2016; Sochi 2012) as discussed in Chapter 1. One reason that CFRP composite and carbon nanotube (CNT)/CFRP nanocomposite implementations see limited application is the lack of a complete understanding of the effects that individual constituents can impart to the bulk properties of the macroscale material system (Patel, Rohatgi, and Lee 1993; Fu et al. 1999; Xie, Mai, and Zhou 2005). Additionally, the multiscale nature of these materials in particular, as discussed in Chapter 1, makes a straightforward investigation of this phenomenon challenging (Kanouté et al. 2009). Recent studies have shown that the nanoscale information of CFRP composites is integral to understanding their material-structure property and can lead to successful strategies for scaling material behavior from the nano- and microscale to the macroscale, especially in the case of nanocomposites (Subramanian, Rai, and Chattopadhyay 2015; J. Zhang et al. 2016).

Composite and nanocomposite materials also display a significant amount of scatter, in response to mechanical loading, due to several sources of uncertainty (Vu-Bac et al. 2015; Mesogitis, Skordos, and Long 2014; Sriramula and Chryssanthopoulos 2009). Some of these sources

are related to manufacturing and production, and may be minimized through careful quality assurance (QA) practices. However, a significant amount of stochasticity is introduced into these systems inherently due to the nature of the constituents themselves. The polymer constituent, for example, when used as the matrix displays complex physical and chemical behavior that can result in large local variations in properties. These variations are largely considered a product of atomic scale mechanisms (Subramanian et al. 2015). Additionally, in the case of nanocomposites, nanofillers interact with the polymer molecules creating even larger variations, while introducing uncertainties arising from the dissimilarities in nanofiller geometry (Subramanian, Rai, and Chattopadhyay 2015). The carbon microfiber constituent, on the other hand, is associated with generally stable material properties, but exhibit significant geometric variations at the microscale (Kadla et al. 2002).

In general, manufacturing processes and the practical conditions of production cycles lead to nonsingular randomness in fiber volume percentages at the mesoscale. Although any one of these sources of uncertainty can individually lead to an order N effect on the material properties, at the macroscale all these sources come to interact with each other. As a result, the total uncertainty at the structural scale becomes amplified, leading to an observed N^M effect on material properties. Experimental programs tasked to quantify these uncertainties can be daunting due to the statistically significant amounts of sample testing required, in addition to the associated expenses in composite characterization. To address the above-mentioned challenges, thus, provides the motivation to develop a multiscale model, which incorporates nanoscale information and associated uncertainties, N^1_{nano}, N^2_{nano}, N^3_{micro}, $N^4_{micro} \cdots N^M$ etc. at each length scale, such that the computed composite bulk properties are a function of the atomistic phenomenon as well as the stochasticities at various length scales. Such a framework would significantly reduce validation experiments at the macroscale, and allow optimization of material performance from the ground up.

2.2 Molecular Model

Although novel experimental techniques such as transmission electron microscopy (Wang, Poncharal, and De Heer 2000), atomic force microscopy (Larsen et al. 2002), and spectroscopy (Misra et al. 2006) have been used to gain nanoscale information of composite material systems, they involve cumbersome preparatory work and expensive experimental stages. Recent advances in nanoscale material system modeling have provided the scientific community with a straightforward alternative to such experimental procedures, to characterize atomic systems. However, it is noted that the maturity of these modeling methods are attributed to the above mentioned state-of-the-art experimental techniques, which are used for thorough validation of the models (Hackett, Manias, and Giannelis 1998; Best et al. 2001; Best et al. 2003; Robach et al. 2003). From a materials point of view, the fundamental modeling approach is derived from quantum mechanics (QM)-based methods, which explicitly model the probabilistic quantum behavior of the electrons, and establishes a first-principles technique for characterizing the relationship between atomic structure and its chemical relationships (Atkins and Friedman 2011). However, due to the nature of this approach it is computationally expensive and impractical for systems with more than a few atoms. A 'higher' level of theoretical methods, known as molecular dynamics (MD), utilize the equations of motion (Newton's laws) for individual atoms, and use empirical potentials to model atom interactions (Hoover 1986; Humphrey, Dalke, and Schulten 1996). The kinematics of the system is solved by considering an N-Body problem, with each atom being a single point body; the kinetics are then approximated using empirical constitutive equations that may or may not have been derived from quantum mechanics calculations (Car and Parrinello 1985; Rapaport et al. 1996). Hence, MD simulations provide a platform for modeling large atomic systems containing greater than 10,000 atoms, with reasonable accuracy and computational feasibility.

In this work, MD simulations of the polymer system, Di-Glycidyl Ether of Bisphenol F

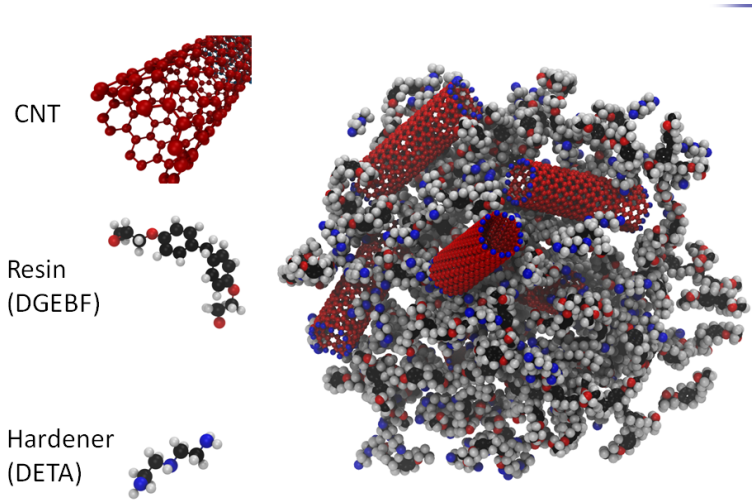

Figure 2.1. The MD unit cell

Source: (Subramanian, Rai, and Chattopadhyay 2015)

(DGEBF) and Di-Ethylene Tri-Amine (DETA), with and without CNTs are performed in the Large-scale Atomic/Molecular Massively Parallel Simulator (LAMMPS). LAMMPS is a classical MD simulation code (Plimpton, Crozier, and Thompson 2007) developed and maintained by Sandia National Laboratories.[1] The tubular single walled CNTs are modeled in the NanoEngineer Toolbox with terminal hydrogen atoms, with diameter ranging between 1 to 2 nm and average length of 60 nm. The periodic matrix unit cell consists of the resin and hardener molecules with randomly dispersed CNTs and a total atom count larger than 100,000. The most appropriate classical force field used to calculate the kinetics of the molecular system for the polymer in the literature was found to be the Merck Molecular Force Field (MMFF) (Halgren 1996), and is applied here. The appropriateness of this force field is based on comparisons of a few experimental parameters, as found through equivalent MD simulations of this resin system with the MMFF (Koo et al. 2014). To correctly account for bond, angle, dihedral deformations among bonded interac-

[1] It is to be noted that the atomistic model presented in this section was developed by Ms. Nithya Subramanian. All MD simulations are credited to her.

tions, and improper out-of-plane distortions of the CNTs, a combination of the Optimized Potential for Liquid Simulations (OPLS-AA) parameter set (Jorgensen, Maxwell, and Tirado-Rives 1996) and the Consistent Valence Force Field (CVFF) parameter set (Zang et al. 2009) is used to describe the kinetics of the nanotubes. Additionally, the non-bonded Van der Waals forces are simulated using the classical Lennard-Jones potential, and Coulombic forces are modeled using the Coulumb potential (Verlet 1967).

Table 2.1. Chemical details of the resin and hardener

Type	Name	Constituent Weight ($g\,mol^{-1}$)	Chemical Formula
Epoxy resin	DGEBF	313	$C_{19}H_{20}O_4$
Hardener	DETA	103	$C_4H_{13}O_6$

An important aspect of the epoxy system for practical use in composites is the curing process, wherein, the resin and hardener form crosslinking covalent bonds under excitation through temperature and pressure (Tillet, Boutevin, and Ameduri 2011). It is well known that the phenomenon of epoxy curing and properties of the polymer, and consequentially the composites, are strongly related (Loos and Springer 1983). At the atomic scale, this process of curing is largely affected by kinematics and molecule location, which can be efficiently calculated using MD simulations. The 'crosslinking degree' or the 'conversion degree', which is a measure of the epoxy cure, can then be defined in the atomic unit cell as the ratio of fully formed crosslinked bonds to the theoretical maximum crosslinked bonds between the resin molecules and the hardener molecules. In this work, mechanical investigations of the polymer and nanopolymer unit cells are preluded by curing simulations, where the unit cells are randomly generated and crosslinking degree of the unit cell is then calculated. Since this technique requires a mechanism for simulating bond formation, a cut-off based bond formation technique is used. The covalent bond between appropriate resin and hardener molecules is assigned when these molecules reach a cut-off distance equivalent to the Van der Waals radius, a value calibrated to experimental curing degrees (Koo et al. 2014).

Additionally, temperature and pressure are controlled using the Nose-Hoover thermostat and a Berendsen barostat. Following the computational curing process, the MD polymer and nanopolymer unit cell is used as a virtual testbed to calculate mechanical properties. Elastic Young's modulus is calculated through uniaxial simulations, and by measuring the gradients of the stress-strain response, uniform hydrostatic pressure is applied to characterize bulk modulus. Shear modulus is then calculated as a function of the other elastic constants through an isotropic assumption.

Although the above-mentioned simulation process models the elastic behavior, inclusion of inelastic phenomenon would require calculating the response of covalent bonds that are much farther from their equilibrium bond length. These types of calculations cannot be performed using the quadratic form of the classical force fields, and would require dissociation or saturation of the bond response after reaching a critical bond length (Brenner et al. 2002). Such behavior can be simulated using bond order force fields for which the ReaxFF reactive bond order force field for hydrocarbons (Van Duin et al. 2001) with appropriate bond order based potential parameter sets (Li and Strachan 2011; Singh et al. 2013) is used in this work to simulate the inelastic bond response of the epoxy-resin and CNT atomic system.

2.3 Elastic Information Bridging

The schematic for the methodology for transferring material property information, consolidated from MD simulations of the polymer and nanopolymer systems is shown in Figure 2.2. As described in section 2.2, MD simulations can be used to model the fundamental curing process of the hardener and the epoxy resin, which is stochastic by nature; the cured atomic unit cell can then be used to run virtual mechanical tests. Through these computational exercises, the probability of crosslinking for a spectrum of conversion degrees can be calculated, which can further be used to find a probability distribution of mechanical properties. Since the atomistic simulations provide

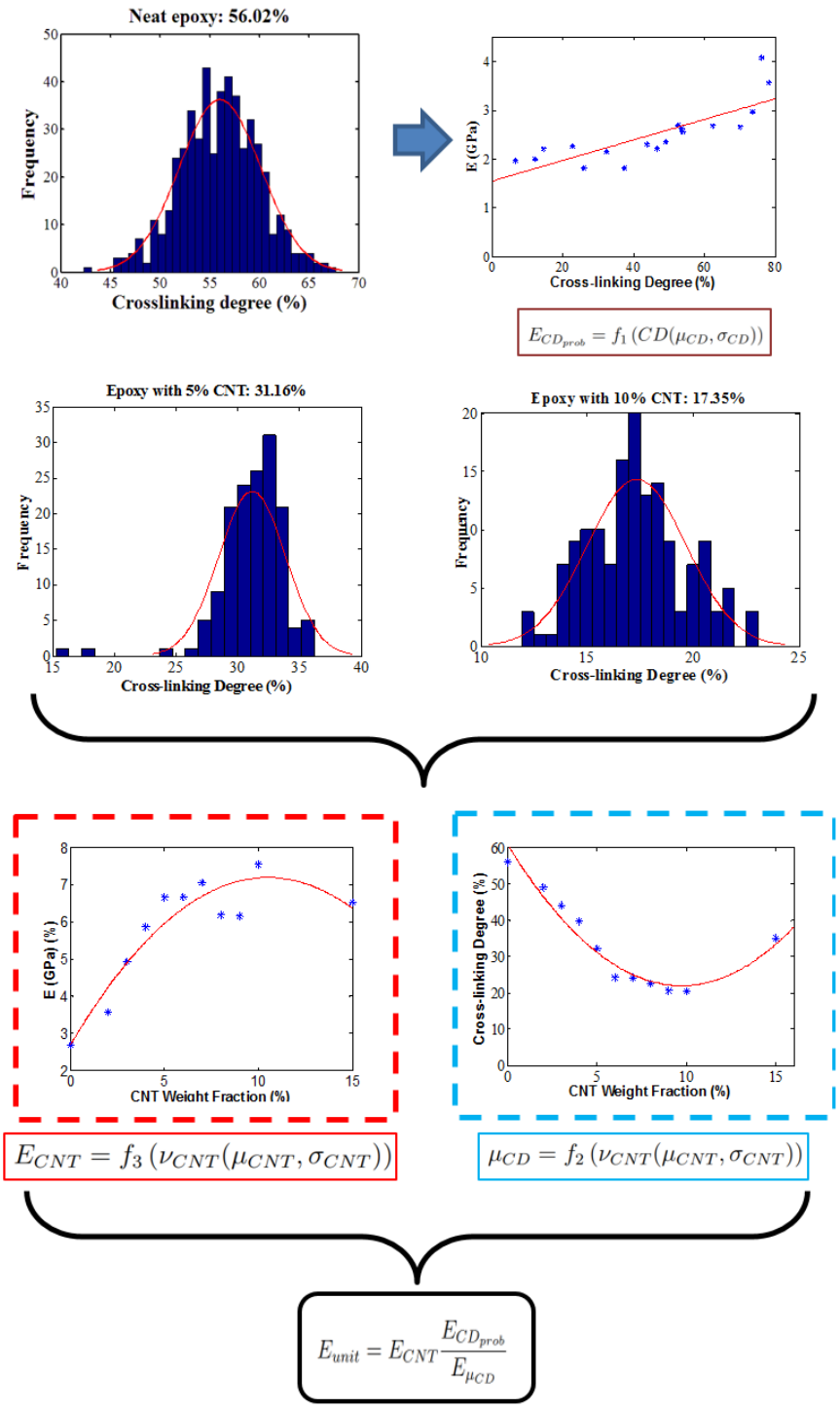

Figure 2.2. Atomistic information sampling framework for continuum modeling

a distribution of most likely material properties, this information serves as an input to the continuum matrix model. The mechanical properties obtained from the MD simulation of DGEBF (Di-Glycidyl Ether of Bisphenol F) epoxy resin and DETA (Di-Ethylene Tri-Amine) hardener is shown in Figure 2.3, as computed by Subramanian et al (Subramanian, Rai, and Chattopadhyay 2015). Due to the linear nature of this relationship within the domain of realistic crosslinking degrees, a linear model is chosen to represent the elastic property variation with crosslinking and is shown in equation 2.1.

$$E_{CD} = 0.0159(CD) + 1.566 \tag{2.1}$$

where CD is the crosslinking degree and E is the Young's modulus in gigapascals. Since the crosslinking degree is inherently a probabilistic term, the distributional version of these models, as opposed to the deterministic version need to be introduced. Let μ_{CD} be the mean of the crosslinking degree and σ_{CD} be the standard deviation. Then the deterministic equation 2.1 can be rewritten with stochastic terminologies as:

$$E_{\mu_{CD}} = 0.0159(\mu_{CD}) + 1.566 \tag{2.2}$$

And a probabilistic version of equation 2.2 would require the introduction of appropriate semantics for the input variable as displayed in equation 2.3.

$$E_{CD_{prob}} = 0.0159(CD(\mu_{CD}, \sigma_{CD})) + 1.566 \tag{2.3}$$

For a similar crosslinking degree versus mechanical properties relationship, in the case of nanocomposites, the CNT weight fractions have to be accounted for in the sampling scheme. The frequency spectrum of the crosslinking degree, and the Young's modulus variation with CNT weight fraction, as observed from MD simulations of the resin-hardener-CNT system is shown in Figure 2.4. As expected, inclusion of the CNTs changes the material properties; however, it is also found that the inclusion of the CNTs causes a shift in crosslinking degree distribution (Subramanian, Rai, and Chattopadhyay 2015). This shift, along with the change in CNT weight fraction,

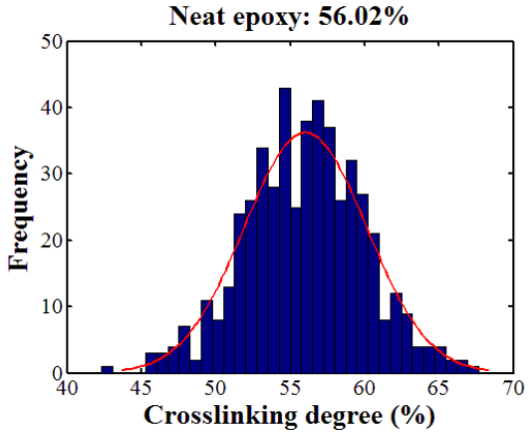

(a) Distribution of crosslinking degree

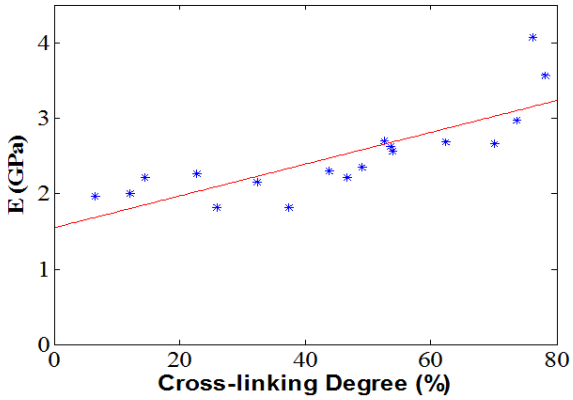

(b) Variation of Young's Modulus with crosslinking

Figure 2.3. Atomistically derived material properties of polymer matrix

Source: (Subramanian, Rai, and Chattopadhyay 2015)

has to be accounted for in a single equation, which can then be used for sampling properties at the microscale. For this reason, a probabilistic second order polynomial model for material property variation with CNT weight fraction is constructed as displayed in equation 2.4.

$$E_{CNT} = -0.03837(\nu_{CNT}(\mu_{CNT}, \sigma_{CNT})^2) + 0.95096(\nu_{CNT}(\mu_{CNT}, \sigma_{CNT}) + 2.4459 \quad (2.4)$$

where E_{CNT} is the Young's modulus of the nanopolymer in gigapascals, ν_{CNT} is the weight fraction of the CNT, μ_{CNT} is the mean of the CNT weight fraction, and σ_{CNT} is the standard deviation of the weight fraction. The weight fraction is considered a stochastic term, with a fixed

standard deviation of 0.25% since electron microscopy images from reported literature on CNT-enhanced nanocomposites indicate large variations in weight fraction of CNTs within polymer matrix (Bose et al. 2009; Menzer et al. 2011). The mathematical relationship between the CNT weight fraction and its effect on the crosslinking degree was seen to be best modeled using a quadratic relationship, described by the following equation:

$$\mu_{CD} = 0.50056(\nu_{CNT}(\mu_{CNT}, \sigma_{CNT})^2) - 9.5905((\nu_{CNT}(\mu_{CNT}, \sigma_{CNT})) + 66.324 \quad (2.5)$$

A change in the Young's modulus of the nanopolymer caused by variations in the crosslinking degree, as well as the CNT weight fraction, would require the Young's modulus calculated from equation 2.4 to be adjusted by the variation in crosslinking degree. This can be done by multiplying E_{CNT} to the normalized neat epoxy variations due to crosslinking degree. The Young's modulus of a nanopolymer unit cell can hence be found using the following consolidated equation:

$$E_{unit} = E_{CNT}\frac{E_{CD_{prob}}}{E_{\mu_{CD}}} \quad (2.6)$$

A similar procedure can be used to estimate the remaining material properties, such as the bulk moduli and shear moduli. Figure 2.5 shows the variation of these properties for the polymer system, as calculated from the MD simulations. Since the atomic simulations for the polymer shows that the material is isotropic for a multi-thousand molecule system, the Poisson's ratio and the shear modulus can be calculated from the elastic relations for isotropic materials, which is mentioned in equation 2.7 for reference.

$$E = 2G(1 + \nu_p) = 3K(1 - 2\nu_p) = \frac{9KG}{3K + G} \quad (2.7)$$

where ν_p is the Poisson's ratio, G is the shear modulus, and K is the bulk modulus.

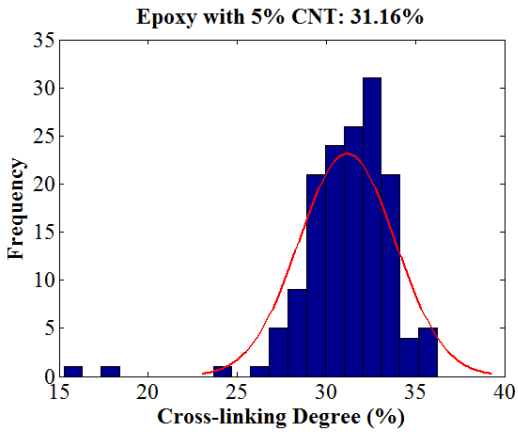

(a) Distribution of crosslinking degree

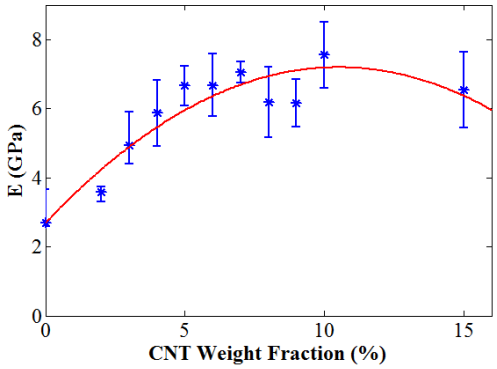

(b) Variation of Young's Modulus with CNT weight fraction

Figure 2.4. Atomistically derived material properties of polymer matrix with CNTs

Source: (Subramanian, Rai, and Chattopadhyay 2015)

2.4 Microscale Continuum Modeling

To bridge the properties obtained from atomistic simulations consolidated in equation 2.6 to the higher length scale, a 3D stochastic microscale continuum model is developed within the finite element (FE) framework using the commercial FE package ABAQUS. Figure 2.6 displays the discretized FE model of an advanced composite microstructure, suitable for elastic investigations. Variants of this model are generated in ABAQUS using scripting procedures and an algorithm that

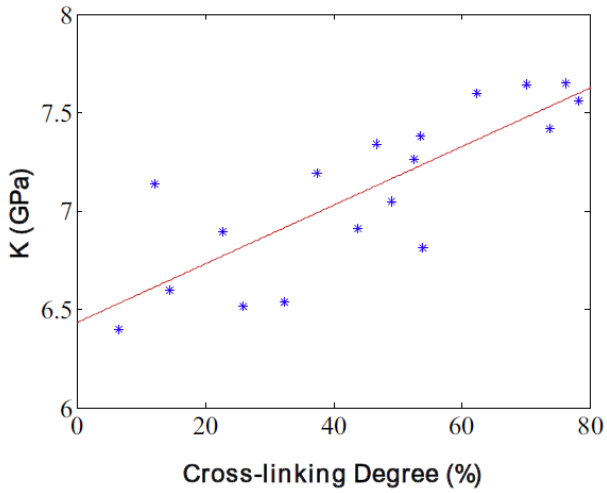

(a) Variation of bulk modulus of polymer from MD simulations

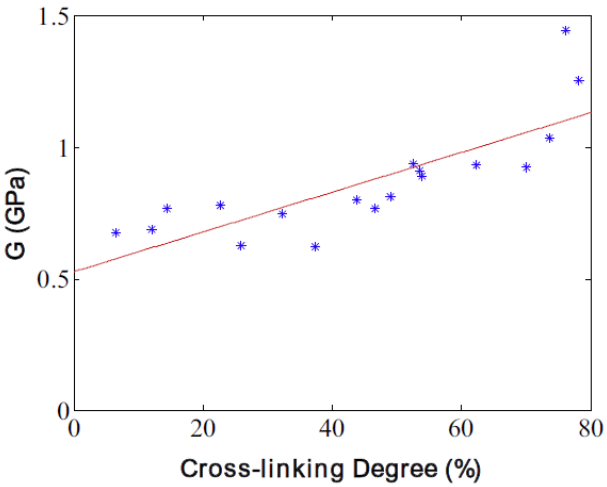

(b) Variation of shear modulus of polymer from MD simulations

Figure 2.5. Variation of additional elastic properties from MD simulations

Source: (Subramanian, Rai, and Chattopadhyay 2015)

perturbs the values of the stochastic variables. The sampling of variations from the probability distribution functions (PDFs) of the input variables enables each model execution to contain unique values pertaining to matrix material property and fiber geometry. In the current investigation,

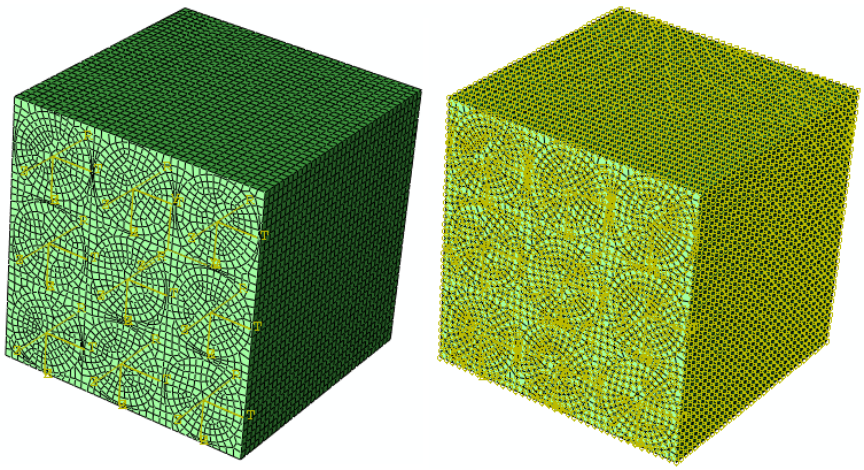

Figure 2.6. FE microscale discretization of the microscale RUC

large number of models are generated and executed to accurately characterize the distribution of responses.

The microscale model presented in this chapter accounts for stochasticity in fiber placement, geometry, and volume fraction by varying the fiber center position within a range of a single fiber/matrix unit cell and the dimensions of the single fiber/matrix unit cell. Hence, the assembled multi-fiber microstructure essentially resembles multiple eccentric single fiber/matrix unit cells, as seen in Figure 2.8. Though stochasticity in fiber placement is present, the fiber centers are bound within its unit cell, which leads to a reduced representation when compared to realistic microstructures. Since it has been shown that reduced representations are sufficient for the stochastic analysis of elastic properties of composites (Borkowski, Liu, and Chattopadhyay 2013), realistic microstructures, in terms of fiber placement, was not modeled in this investigation for computational simplicity. To provide realistic properties for the fiber volume fraction and fiber geometry, the uncertainty in these variables are characterized based on results from confocal microscopy investigations performed on an IM7/EPON 862 laminate microstructure using the Zeiss LSM confocal microscope. The IM7/EPON 862 sample was manufactured through a wet-layup process, and cured in a vertical axis heated press under a common cure cycle. The microstructure samples

were placed in an epoxy puck, and polished using varying abrasive materials. The distributions of the stochastic parameters are found to be near-Gaussian in nature, and a Kolmogorov–Smirnov (KS) test is performed to confirm and justify the normality of the distributions. The characteristic parameters related to the uncertainty in fiber volume fraction and fiber diameter, calculated from the microstructural study, are reported in Table 2.2. The material properties of the fiber is assumed to be linear-elastic orthotropic, and the variation in properties is assumed to follow a normal distribution based on standard tests and data presented in manufacturer data sheets for the IM7 fiber system (Hexcel 2016).

Table 2.2. Parameters of the Gaussian distributions for the fiber stochastic variables

Property	Mean	σ_{dev}
Fiber Volume Fraction	71.75%	4.67%
Fiber Diameter	6.99 μm	0.3209 μm

The variation in material properties of the polymer matrix and the nanopolymer with dispersed CNTs is included by sampling material properties using equation 2.3 or 2.6, respectively. The matrix properties are sampled and can then be applied stochastically to achieve spatial variation in properties of the matrix. This methodology simulates uneven curing of the polymer and sub-microscale variations in crosslink between the resin and the hardener. The microscale model assumes perfect adhesion between the fiber and the matrix at the interface. Although, this technique can model the uneven curing of the epoxy, the random nature of the material property generation may lead to unphysical variation in values in neighboring matrix cells. To avoid unrealistic gradients in the material properties between neighboring matrix cells, some degree of correlation in these properties must be observed. Hence, the Pearson's correlation coefficient (PCC) is used to constrain the neighboring material properties. The PCC is a statistical measure of correlation between any two variables and may have a value between ± 1. This technique is applied by numbering all the matrix cells and generating the material properties such that the PCC after every

N cells alternate between 0.5 and -0.5. A PCC of ± 0.5 provides a compromise between fundamental randomness of material properties and correlation between neighboring subcells. The formula used for the PCC in this case is:

$$r = \frac{\sum_{i=1}^{N}(x_i - \bar{x})(E_{unit,i} - \bar{E}_{unit})}{\sqrt{\sum_{i=1}^{N}(x_i - \bar{x})^2}\sqrt{\sum_{i=1}^{N}(E_{unit,i} - \bar{E}_{unit})^2}} \tag{2.8}$$

where r is the PCC which can take the value ± 0.5, x is the number of matrix sections, $\bar{x}$ is the mean of the total number of matrix sections. The comparison between the variation in material property for 1000 epoxy sections generated using the completely random technique and the correlated technique with $N = 50$ can be seen in Figure 2.7.

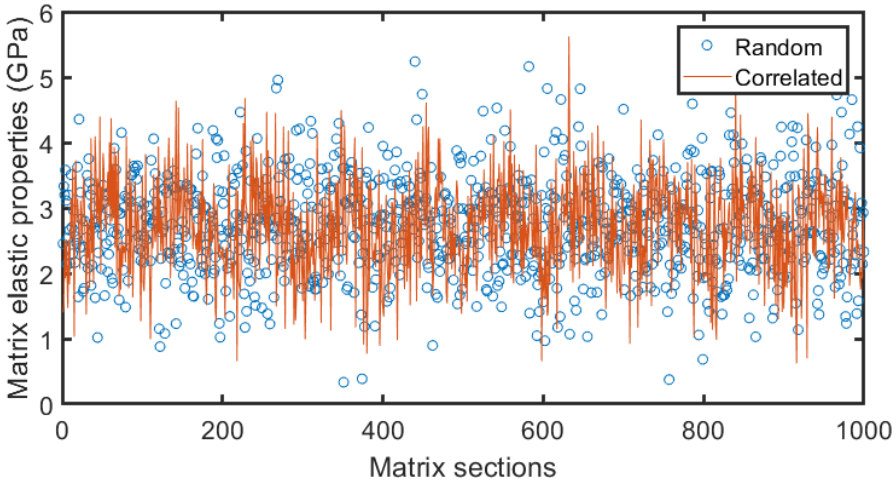

Figure 2.7. Variation in material property in 1000 epoxy sections

For investigating the uniaxial response of the composite microstructure, it is important to replicate the periodicity of the unit cell geometry. The microstructure model exhibited in Figure 2.6 represents a small unit of the composite structure, and its edges are considered to be infinitely replicable. This periodicity can be simulated using periodic boundary conditions (PBCs) at the continuum level to mitigate size effects arising from the arrangement of multiple fiber-matrix unit cells, and to significantly reduce the computational expense of simulating larger representative unit

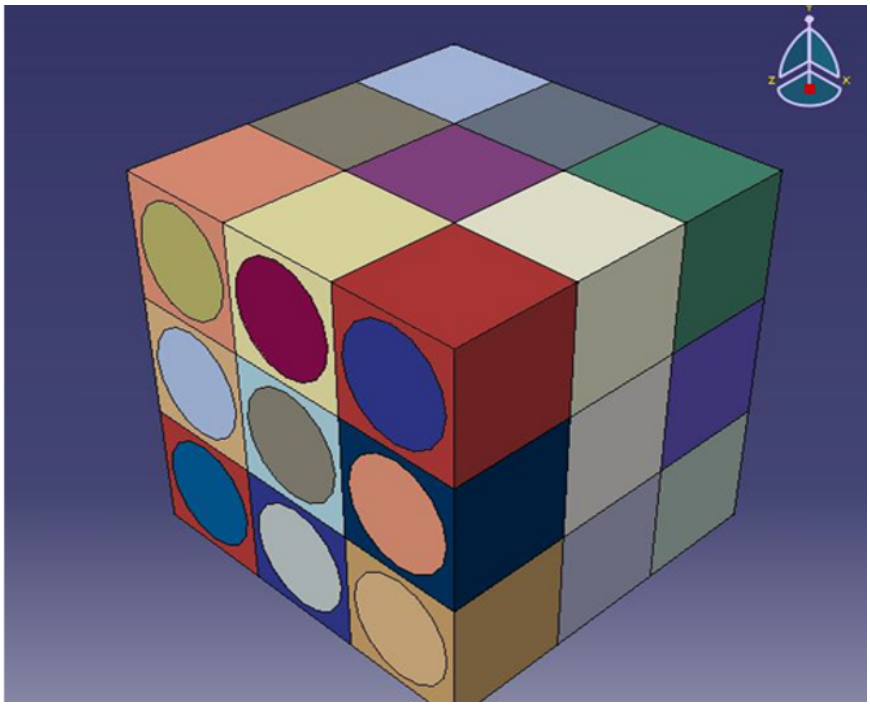

Figure 2.8. Microstructure geometry

cells (RUCs). The PBCs are derived by considering the applied strain increment as an additive form of the averaged strain increment and a periodic strain increment (Pellegrino, Galvanetto, and Schrefler 1999). Hence, the PBCs for a volume ∂V can be implemented using equation 2.9, which is periodic on ∂V where u_i are the displacements at the boundary of the cell that lead to changes in microstructure behavior, and u_i^p are the periodic displacements that do not play a part in global deformations. Equation 2.9 can be rewritten in a discretized form suitable for implementation in the FE framework (Segurado and Llorca 2002), and is displayed as equation 2.10, where the elements D_{ij} correspond to the global strains, and P_1 and P_2 represent a set of symmetrically opposite points on the RUC. It is to be noted that the indices in these equations correspond to the indicial notation used in continuum mechanics (Heinbockel 2001). In ABAQUS, equation 2.10 is applied as equation constraints on every nodal pair along all three degrees of freedom, using fictitious reference points for each face (Barbero 2013). To facilitate the application of the PBCs,

the geometry is meshed using a swept mesh control system, which generates nodes on collinear symmetrically opposite points of the RUC.

$$u_i = D_{ij} y_j + u_i^p u_i^p \tag{2.9}$$

$$u_i(P_2) - u_i(P_1) = D_{ij} \left(y_j(P_2) - y_j(P_1) \right) \tag{2.10}$$

Additionally, this methodology also simplifies the application of a uniaxial displacement field, since the PBC equation constraints can be modified for the loading direction to include a positive net global displacement, along with the period components. The global response of the unit cell is then calculated by ensemble averaging over the unit cell spatial domain. The microscale model hence determines the effective material property of the microscale RUC by measuring the gradient of the stress-strain response, which is obtained by calculating the effective resistance force to a small applied displacement. The mesh for the microstructural FE analysis consists of hexahedral elements, and its complexity depends on the fiber placement in each unit cell. Figure 2.9 shows the results of the mesh convergence studies for determining the optimum number of elements required. The edge seed length refers to the distance between two nodes (ABAQUS 2013). The extensive mesh convergence study leads to an optimum seeding size of 0.6 along the fiber direction (85,000 elements) and a seeding size of 0.95 transverse to the fiber direction (30,000 elements).

Figure 2.9 shows a comparison of stress contours of an RUC with $4 \times 4 \times 4$ unit cell with perfectly ordered geometry and an RUC of similar size with microstructure variability. The comparison is a clear indication that geometric perturbations lead to local variations in stress. The changes in fiber geometry and location produce a redistribution of stresses, and regions with very low polymer cross-linking degree may serve as stress concentration hot spots.

To estimate the deterministic accuracy of the developed microscale continuum model, the computed material properties from a single run with only mean values of the included sources of uncertainty applied are compared with material property data from available literature for a system

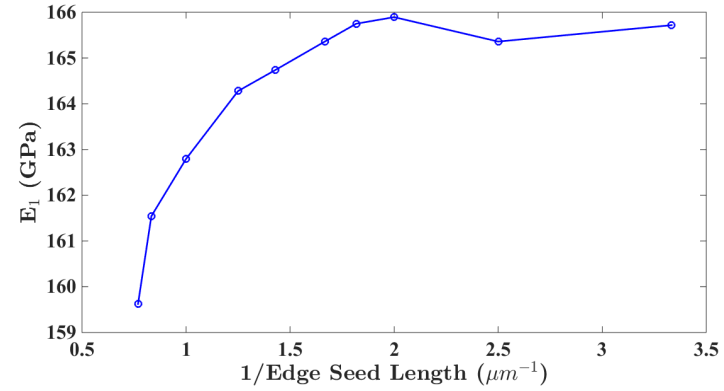

(a) Mesh convergence for E_1

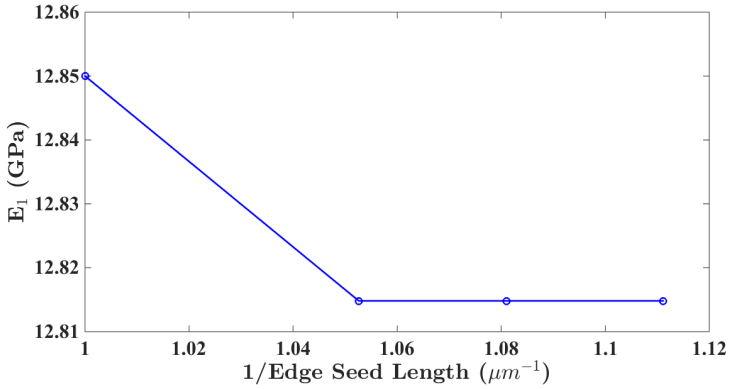

(b) Mesh convergence for E_2

Figure 2.9. Mesh convergence study

containing IM7 fiber and the 8552 epoxy system. For validation, only neat epoxy models are used, and a deterministic mean volume fraction of 0.6 is applied. The models show good comparison with experimentally observed properties for both E_1 and E_2 obtained from the literature and is reported in Table 2.3.

Table 2.3. Comparison of predicted elastic moduli of the composite system with literature data

Tensile Modulus	Literature (GPa)	Model Prediction (GPa)	Error (%)
E_1 (Fiber Dir)	164 (σ_{dev}=11.85)	165.3595	0.83
E_2 (Transverse Dir)	12 (σ_{dev}=1.7)	12.81481	6.79

The stochastic microscale model is then used to determine material properties under all major

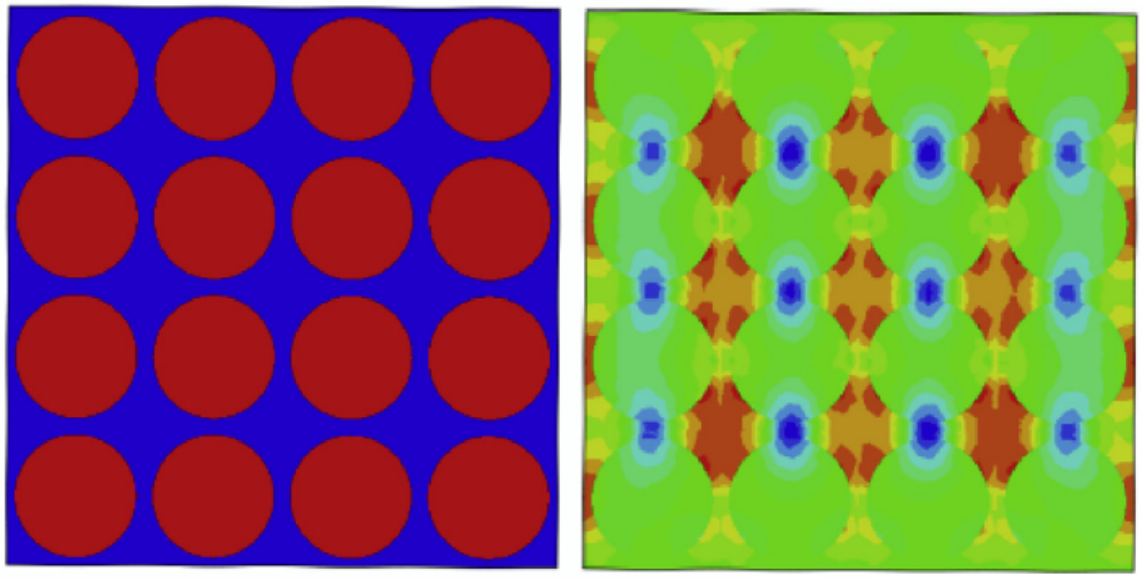

(a) Perfectly ordered microstructure

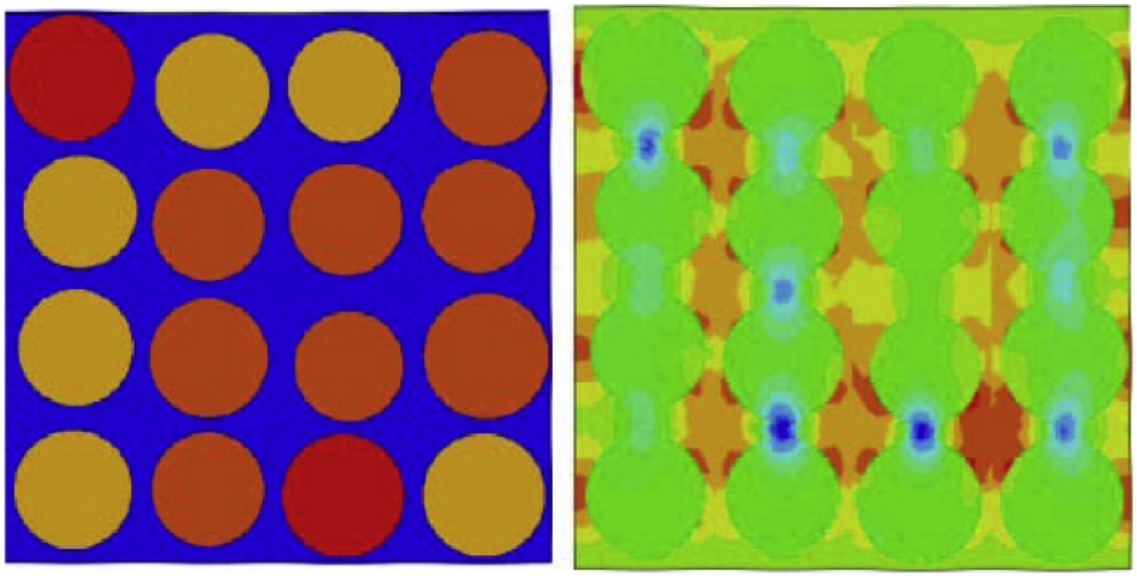

(b) Disordered microstructure

Figure 2.10. Comparison of stress contours

sources of aleatory uncertainties by collecting the responses over various model executions. These multiple responses are consolidated to obtain a distribution of material properties. The homogenized properties, obtained from over 600 independently perturbed FE simulations, are compiled to generate variational histograms, as shown in Figures 2.11, 2.12, and 2.13. It is to be noted that

the RUCs containing fibers embedded in CNT-enhanced polymer are modeled with the weight fraction of the CNT in each section of the matrix phase sampled around a specific mean value (1% or 3%). Statistical parameters derived from the histogram data sets are outlined in Table 2.4 and compared with experimentally observed uncertainties for the neat-epoxy sample.

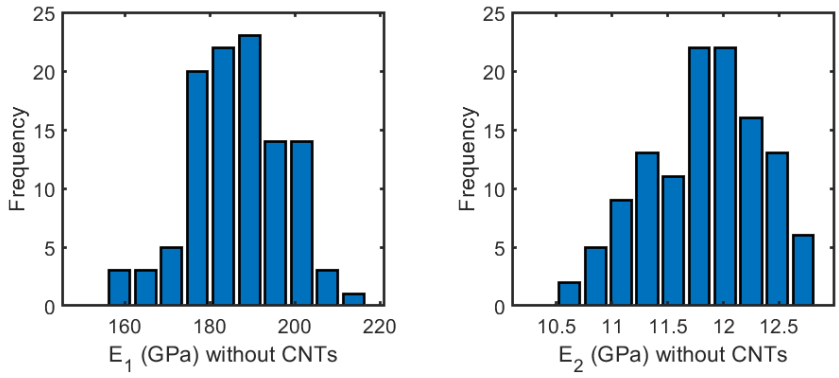

Figure 2.11. Histograms of neat epoxy/fiber material properties

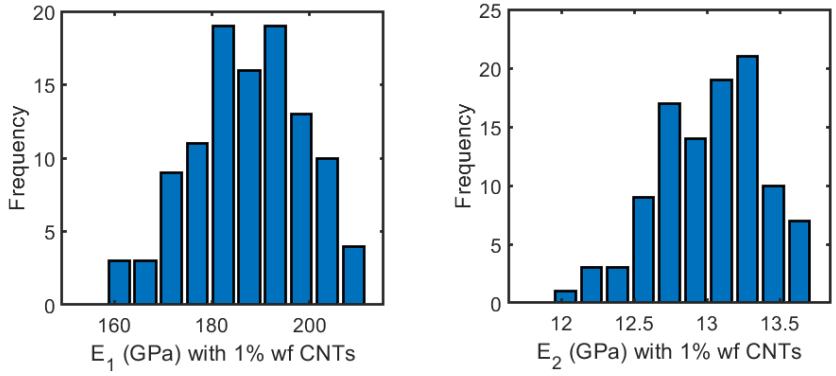

Figure 2.12. Histograms of 1% weight fraction CNT-epoxy/fiber material properties

In Table 2.4 it can be seen that the elastic properties in the direction of the fiber (E_1) does not show much variability with addition of CNTs. Load in the direction of the fibers is largely carried by the fibers and is only slightly reinforced by the CNTs. Additionally, since the CNTs are assumed to be randomly dispersed, the overall reinforcement effect compared to the elastic

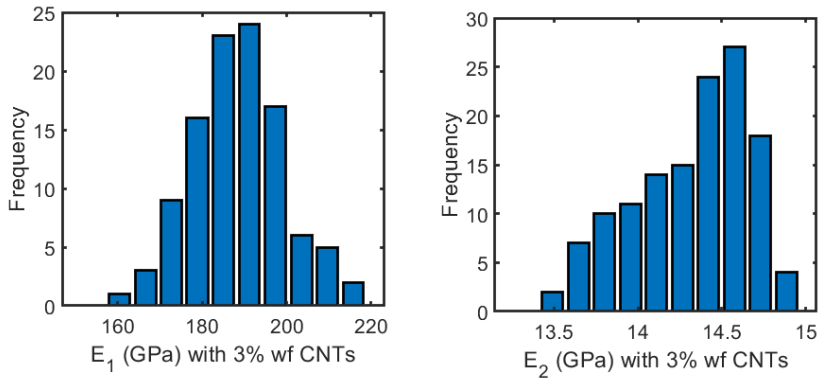

Figure 2.13. Histograms of 3% weight fraction CNT-epoxy/fiber material properties

properties of fiber in the E_1 direction is minimal. In the transverse axis, however, an increase of 10.4% in the average transverse modulus (E_2) of the RUC with an addition of 1% CNT by weight is observed. Furthermore, an increase of 22% in transverse modulus of the RUC is observed when the weight fraction of CNT in the matrix is increased to 3%. Since the matrix is the major load carrying constituent in the transverse axis, the reinforcing effect of the CNTs is significant. The elastic property contrast between the CNTs and the matrix, which is generally in the order of terapascals, leads to increased stiffness in the overall nanomatrix when compared to the neat-epoxy matrix. However, this analysis assumes perfect bonding between the CNTs and the matrix, which may be appropriate for small deformation elastic analyses. This hypothesis will be tested thoroughly in Chapter 6 which studies the role of imperfection in interfaces.

An interesting effect of the stochastic analysis is the probability of decrease in elastic properties with the addition of CNTs as compared to the maximum transverse elastic modulus of the neat epoxy. Intuitively, it seems appropriate to assume that any addition of CNTs to the neat-epoxy matrix will always be associated with increased elastic properties compared to the neat-epoxy matrix. This would be expected in a deterministic analysis where the new properties of the nanomatrix is seen as proportional to the amount of added fillers. A stochastic analysis, on the other hand, allows for the study of non-intuitive cases, e.g., matrix consisting of poorly cured epoxy with low

Table 2.4. Results from stochastic microscale continuum model

Wf CNT in matrix (%)	Mean E_1 (GPa)	Mean E_1 Literature (GPa)	Error (%)
0	163.4	164	0.367
1	164.8	-	-
3	165.3	-	-
Wf CNT in matrix (%)	σ_{dev} in E_1 (GPa)	σ_{dev} in E_1 Literature (GPa)	Error (%)
0	11.483	11.85	-3.196
1	11.511	-	-
3	10.783	-	-
Wf CNT in matrix (%)	Mean E_2 (GPa)	Mean E_2 Literature (GPa)	Error (%)
0	11.73	12	2.301
1	12.95	-	-
3	14.31	-	-
Wf CNT in matrix (%)	σ_{dev} in E_2 (GPa)	σ_{dev} in E_2 Literature (GPa)	Error (%)
0	1.5358	1.7	-10.691
1	1.7845	-	-
3	1.7341	-	-

weight fraction of CNTs compared with well cured neat-epoxy matrix. In this case, the nanomatrix mixture will display lower elastic properties when compared to the neat-epoxy sample. The histograms and datasets in Figures 2.11, 2.12, and 2.13 demonstrate the probability of obtaining lower properties in the nanomatrix when compared to the neat-epoxy matrix. A ratio of sets calculation from this data, shown in equation 2.11 and 2.12, indicates the probability of achieving a lower transverse tensile modulus, even with the addition of higher weight percentage of CNT to the epoxy matrix. It is observed thus that when the elastic properties of the matrix and probable conversion degrees are calculated using MD simulations in a random sample, there is a 24.51% probability of encountering lower material properties in a 1% weight fraction CNT-epoxy mixture when compared to the neat epoxy. This probability decreases to 5.26% when 3% weight fraction CNT nanopolymer is compared with 1% CNT weight fraction mixture.

$$P_1(\text{Lower}E_2) = \frac{E_2(\text{Mean 1\% Weight Fraction CNT})}{\text{Max}(E_2(\text{No CNT}))} = 0.2451 \tag{2.11}$$

$$P_2(\text{Lower}E_2) = \frac{E_2(\text{Mean 3\% Weight Fraction CNT})}{\text{Max}(E_2(\text{1\% Weight Fraction CNT}))} = 0.0526 \tag{2.12}$$

In summary, the elastic microscale RUC model with stochastic matrix material properties obtained from MD simulations, and with varying fiber volume fractions and random fiber geometries, results in predictions of the composite material properties that are in close agreement with the experimental data, which takes into consideration both mean values and standard deviations. Furthermore, these results also demonstrate that the stochastic simulations are in closer alignment with experimental data when compared with the deterministic simulations. Modeling the inherent uncertainty naturally present in experiments is, therefore, critical for accurate predictions of the elastic response of advanced composites.

2.5 Limited Inelastic Simulations

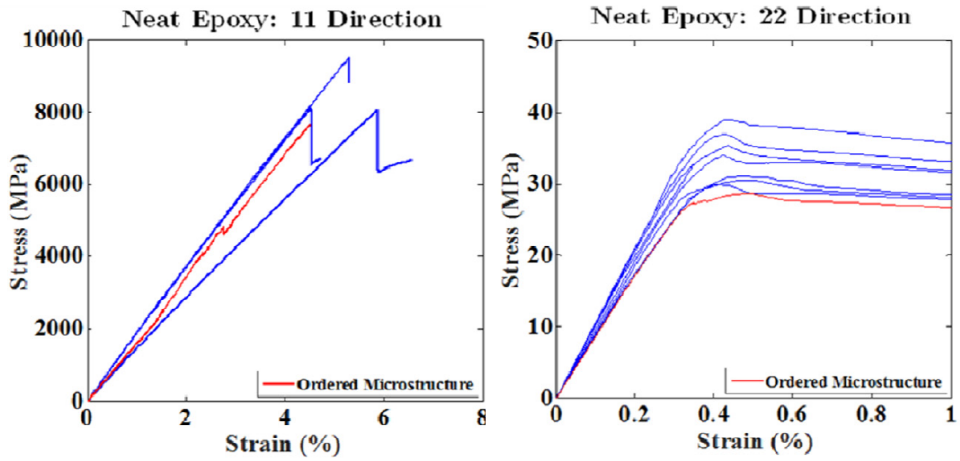

Figure 2.14. Nonlinear stress-strain response with direct inelastic atomistic information for neat epoxy

To characterize the plastic behavior of the composite and nanocomposite, the inelastic information from MD simulations is directly applied to the FE model using the strain hardening phase

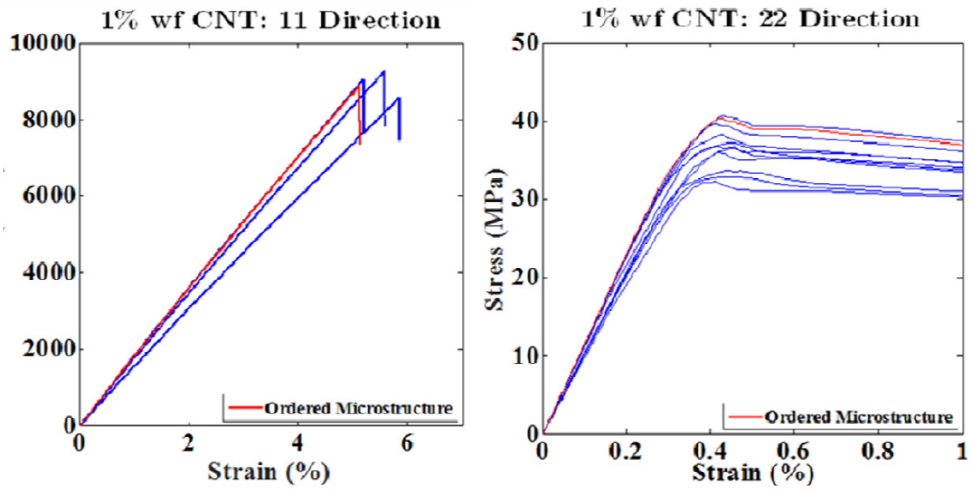

Figure 2.15. Nonlinear stress-strain response with direct inelastic atomistic information for epoxy with 1% weight fraction CNT

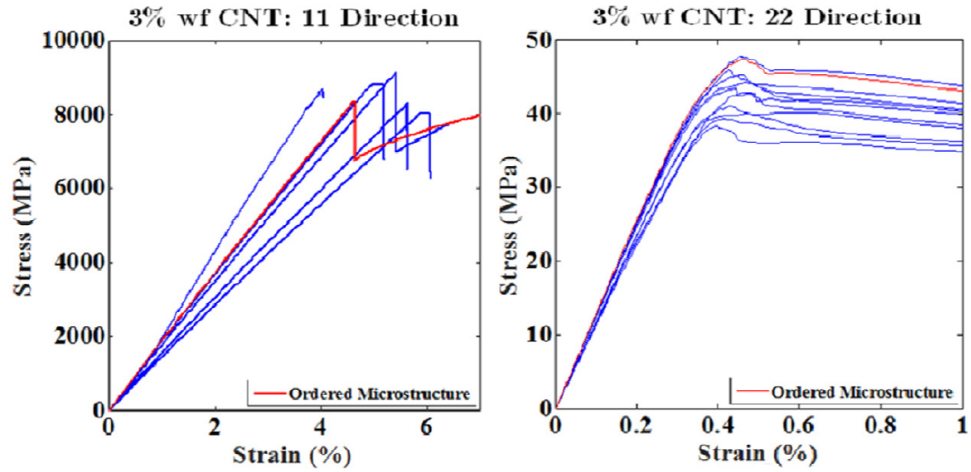

Figure 2.16. Nonlinear stress-strain response with direct inelastic atomistic information for epoxy with 3% weight fraction CNT

beyond the yield point of the polymer and nanopolymer. The yield point is computed using MD simulations with bond order based reactive force field, as detailed in Section 2.2. The stress-strain curve from this calculation is then used to define the material properties of the microscale model wherein plasticity is defined explicitly based on the physics arising at the atomistic length scale. The stress-strain curve from MD simulations is normalized and applied as a hardening tabular

input to a generic ABAQUS elasto-plastic material model. The MD stress-strain response was explicitly calculated for 0%, 1%, 2%, 3%, 4%, and 5% CNTs by weight fractions. Since the stochastic microstructure and model generation algorithm for the nanocomposite assigns a distribution of CNT weight fractions, the continuum stress-strain response for the particular weight fraction was obtained from the appropriate MD stress-strain response using linear interpolation, with the assumption that all the interpolation points on different loading paths are characterized by the same number of steps on the same plastic surface (Pellegrino, Galvanetto, and Schrefler 1999). The generation of the geometry and elastic properties for the inelastic models, including the effect of stochasticity in the various uncertain variables, remains the same as discussed in the previous sections.

The stress-strain response obtained from the non-linear microscale model for the neat composite, 1% weight fraction nanocomposite, and 3% weight fraction nanocomposite, can be seen in Figures 2.14, 2.15, and 2.16, respectively. It is observed that significant inconsistencies and variations are present in the failure of the E_1 simulations. The loss of mesh objectivity due to the application of a kinetic hardening model with softening tabular inputs leads to an ill-defined material state, which causes uncertain failure in the E_1 direction. Moreover, the response in the E_2 direction also seems unrealistic, compared to experimental observations, since the post-peak softening was not captured. Hence, this model cannot be used to extract any meaningful predictions or insight into the non-linear processes in advanced composites under mechanical loading at the continuum length scale. An alternate methodology will have to be developed using parameters, observed at the atomic scale, that may be scaled to identify damage at the higher length scales in a consistent manner.

2.6 Summary

The direct transfer of information, from atomistic to the continuum scale, can have substantial benefits in increasing accuracy of predictions in elastic property predictions of advanced composites. In this chapter, a statistical methodology was developed to transfer linear elastic information from atomic scale MD simulations of the resin-hardener-nanofiller system into microscale finite element models of the CFRP and CNT/CFRP system. Sources of variabilities were also included in the modeling framework to obtain distribution of properties, which allowed a probabilistic analysis of possible material properties. The analysis prediction of both mean the standard deviations of the composite properties was observed to be in close agreement with experimental values. Using this modeling technique, possible distribution of elastic properties of the CNT/CFRP system were obtained.

Although this methodology proved accurate for predictions of linear elastic properties, it was observed that the inelastic information could not be directly transferred due to fundamental differences in the time-scale and length-scale of the MD simulations and the FE simulations. Additionally, in the inelastic domain, the definition of stress from MD simulations does not remain consistent with nodal stresses calculated using FE (Subramaniyan and Sun 2008). Since MD simulations are based on energy formulations, utilizing energetically driven information transfer techniques may lead to a more consistent theoretical basis for information bridging and address the challenge of inconsistent definitions of parameters that are transfered. Hence, this motivates the development of an energy driven, thermodynamically admissible framework for transferring inelastic information from MD simulations to the continuum model for damage and non-linear analysis of advanced composites.

Chapter 3

CDM BASED ATOMISTICALLY INFORMED DAMAGE FORMULATION

3.1 Introduction

The coupling of inelastic molecular dynamics (MD) information with continuum scale modeling is a challenging problem due to fundamental differences between the two techniques. Computational limitations add a second layer of complexity to a straightforward implementation of coupled MD-continuum methodologies. MD simulation methods involve modeling of molecules as point objects, which then form the discrete basis for creating a numerical model. Continuum approaches, by definition, assume the continuous functions of the governing variables. This assumption leads to a limiting of the maximum size of the finite element (FE) models that may be considered, wherein the integration points would have to be represented by a minimum of a few thousand molecules to be valid. As a result, large computations are needed for direct coupling between MD simulations and FE models. Section 1.1 shows recent studies that have considered concurrent and semi-concurrent coupled FE and MD simulations to explicitly capture nonlinear nanoscale mechanics (Talebi et al. 2014). However, the nanoscale mechanics when used in these works utilize empirical force fields that cannot capture fundamental nonlinearities, such as bond breakage of polymer chains at the nanoscale (Subramanian et al. 2015). When reactive bond order force fields are used in these methodologies, the implementation becomes computationally infeasible. Furthermore, it has been shown that there are certain localized phenomena, such as stress recovery that follows initial softening and damage saturation in nanopolymers (see Figure 3.1) and that can only be captured through explicit modeling of the nanoscale substructures using reactive bond order force fields (Subramanian, Rai, and Chattopadhyay 2015).

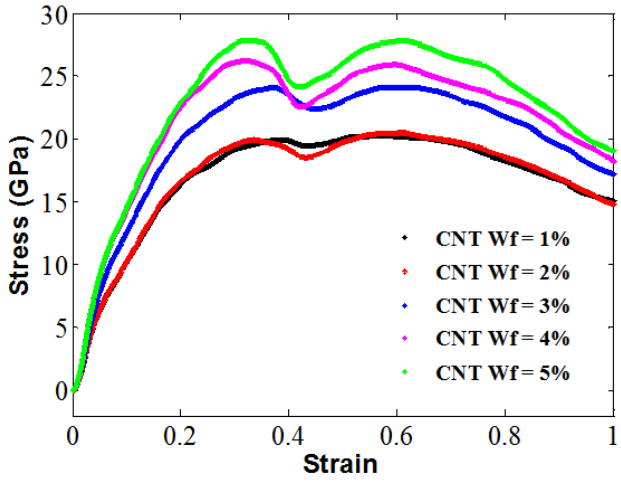

Figure 3.1. Stress-strain response of CNT nanopolymers from MD simulations with reactive force fields

Source: (Subramanian, Rai, and Chattopadhyay 2015)

The continuum damage mechanics (CDM) approach has shown promise in modeling inelastic and damage response in materials. CDM has its roots in metal plasticity, but has been developed for many other applications, such as ceramic matrix composites in a multiscale framework (Shojaei et al. 2014) and to describe micro-crack distributions in the form of a fourth order damage-included fabric tensor (Voyiadjis and Kattan 2006). Similarly, the Internal State Variables (ISV) concept, used to describe the present state of the material, is seen as compatible with the CDM framework (Horstemeyer and Revelli 1997). Recent work on modeling polymer plasticity using ISVs, defined from fundamental molecular phenomena without utilizing approximate *ad-hoc* mathematical functions, was shown to be highly successful in modeling large-deformation compressive behavior in thermoplastics (Bouvard et al. 2010). Thus, an arrangement involving CDM and ISVs offers the scope and potential to implement continuum-based inelastic functions influenced by MD simulations and polymer mechanics as a way to express the damage state of both matrix and nanopolymer and to arrive at an inelastic analysis of advanced composites.

Motivated by the above requirements for damage modeling in polymers and nanopolymers,

this chapter proposes a constitutive law for thermoset polymers based on the CDM framework and in conjunction with a damage evolution equation that is developed from elastoplastic MD simulations results using the reactive force fields. The proposed method allows a physical description of damage mechanisms based on the fundamental nanoscale damage simulations of a polymer matrix. A set of constitutive equations are then derived using a thermodynamic framework, as proposed by Coleman and Gurtin (Coleman and Gurtin 1967), as well as a classical CDM methodology, as described by Lemaitre (Lemaitre 1985). Additionally, hardening equations are based on polymer physics, wherein special consideration for volumetric damage and stress triaxialities are applied.

3.2 Thermodynamics and Damage Mechanics

To fully understand the methods discussed herein outlining the derivation of the atomistically informed damage model for thermoset polymers, a number of related concepts will need to be reviewed. This section discusses the thermodynamics of inelastic processes, the concept of ISVs, and introduces continuum damage mechanics. For any given body of volume V and surface ∂V, considered to be a closed system and existing in an equilibrium state, the internal energy E can be characterized as:

$$E = \int_V e_V \, dV \tag{3.1}$$

where e_V is the internal energy per unit volume. For such a body the first law of thermodynamics, using the principle of energy conservation as the basis, states that any change in internal energy of the body has to equal the added heat Q and work W done on the body. The differential form of this law can be presented as:

$$dE = dQ + dW \tag{3.2}$$

The second law of thermodynamics states that for such an enclosed system as the body under

investigation, the total entropy may never decrease; it can remain equal in the case of reversible systems, and it will increase for irreversible processes. This law can be reformulated for continuum mechanics applications as the Clausius-Duhem inequality (Gurtin and Williams 1966), the differential form of which is shown below:

$$\rho\dot{\eta} \geqslant -\nabla \cdot \left(\frac{q}{T}\right) + \frac{\rho s}{T} \tag{3.3}$$

where ρ is the mass density of the body, η is the entropy per unit mass, q is the heat flux vector, T is the absolute temperature, and s is any energy source per unit mass. In this notation, the time derivative of a variable A is presented as $\dot{A}$. To use the Clausius-Duhem inequality for the purpose of constructing material constitutive equations, equation 3.3 needs to be expressed in terms of internal energy and the Cauchy stress σ. Using the product rule for the divergence operator, equation 3.3 can be rewritten as:

$$\rho\dot{\eta} \geqslant -\frac{1}{T}\nabla \cdot q - q \cdot \nabla\left(\frac{1}{T}\right) + \frac{\rho s}{T} \tag{3.4}$$

Simple manipulation of the divergence operator on $\frac{1}{T}$ yields:

$$\rho\dot{\eta} \geqslant -\frac{1}{T}\nabla \cdot q + \frac{1}{T^2} q \cdot \nabla T + \frac{\rho s}{T} = -\frac{1}{T}\left(\nabla \cdot q - \rho s\right) + \frac{1}{T^2} q \cdot \nabla T \tag{3.5}$$

Equation 3.2, which shows the balance of energy, can be written for continuum mechanics applications as:

$$\rho\dot{e} - \sigma : \nabla v = -(\nabla \cdot q - \rho s) \tag{3.6}$$

where e is the internal energy per unit mass (specific internal energy) and v is the velocity gradient. Substituting equation 3.6 in 3.5 and after rearranging some terms, the following expression can be easily arrived at:

$$\rho(\dot{e} - T\dot{\eta}) - \sigma : \nabla v \leqslant -\frac{q \cdot \nabla T}{T} \Rightarrow \sigma : \dot{\epsilon} - \rho(\dot{e} - T\dot{\eta}) - q \cdot \frac{\nabla T}{T} \geqslant 0 \tag{3.7}$$

where the velocity gradient has been substituted with the time derivative of strain $\dot{\epsilon}$ for small displacements. Equation 3.7 represents the standard Clausius-Duhem inequality used in continuum mechanics applications.

Usable material constitutive models are formulated through set(s) of nonlinear time derivative differential equations with primary variables being the strain rate (leading to flow equations with the inelastic strain rate as the variable) and some ISVs. Within this framework, ISVs homogenize certain lower length scale phenomena that cause changes in the internal energy of the system and essentially represents these effects at the length scale being explicitly investigated. An example of an ISV is an all-encompassing damage variable D, which may reflect the effects of microscale damage, such as void growth and microcracks at the macroscale. Material models may have various such ISVs to characterize different phenomenon, e.g., hardening, back stress, grain slip, and polymer crazing, all of which depend on the inelastic behavior that needs to be reproduced. However, the critical step required for successful integration of the ISVs into the governing equations is the derivation of ISV evolution, obtained from particular scalar potentials (Stamm 1993). These thermodynamic potentials can be defined for equilibrium states, which are determined by the values of the ISVs and the observable variables. One such potential is the Helmholtz free energy that provides a measure of useful work obtained from an enclosed system in equilibrium and isothermal isobaric conditions. For such systems, the Helmholtz free energy can be defined as:

$$\bar{\psi} \equiv E - TS \tag{3.8}$$

Using the definition of internal energy and its relation with e_v (shown in equation 3.1) and e, the time derivative of the Helmholtz specific free energy ψ can be shown to be equal to the rate of change of the specific internal energy:

$$\dot{\psi} = \dot{e} \tag{3.9}$$

Hence, the rate of change of the Helmholtz specific free energy can be used interchangeably with the rate of change of the specific internal energy for a body under all conditions described above.

These potentials can now be used to characterize inelastic processes of a material system in a thermodynamically consistent form by substitution into the Clausius-Duhem inequality equation 3.7 for complete applicability with material response formulations.

$$\sigma : \dot{\epsilon} - \rho(\dot{\psi} - T\dot{\eta}) - q \cdot \frac{\nabla T}{T} \geqslant 0 \tag{3.10}$$

Additionally, the inelastic processes are defined as caused by the thermodynamic forces associated with each of the ISVs, thereby creating a change in the potential due to a variation in the ISV. The thermodynamic force applicable to each ISV can then be calculated as the gradient of the change in potential due to a change in the ISV.

$$A = \frac{\partial \psi}{\partial B} \tag{3.11}$$

Equation 3.11 shows an example of the thermodynamic affinity calculation or the thermodynamic force A associated with an ISV B, which creates an inelastic phenomenon characterized by change in the potential ψ. The evolution laws for the ISV $\dot{B}$ will then have to be formulated such that these phenomena may agree with experimental observations. Thus, equations 3.10 and 3.11 provides the basic thermodynamic framework for the construction of viable nonlinear material models.

One of the main causes of nonlinear processes in any material under standard static loading conditions is intrinsic damage that occurs over various length scales under the application of energy (Ju 1990). A pristine continuum macroscale body may see the introduction and growth of nano- and microscale discontinuities such as voids and microcracks under mechanical loading. Such discontinuities may be studied using the framework of fracture mechanics; however, due to the random by which these damages are generated, the number of 'cracks' that will need to be studied simultaneously and the complex damage paths involved, make the fracture mechanics framework difficult to employ. As an alternative, the theoretical background of continuum damage mechanics (CDM) may be applied to such problems in a far more effective manner. CDM studies the homogenized effects of such nano- and microscale damages at the macroscale using

a state variable defined as damage. Additionally, an understanding of this damage variable can be developed from the previously discussed thermodynamics of irreversible processes, which provides a firm practical basis for the CDM theory. An explanation of this damage variable as well as theoretical principles of CDM are presented next in this section.

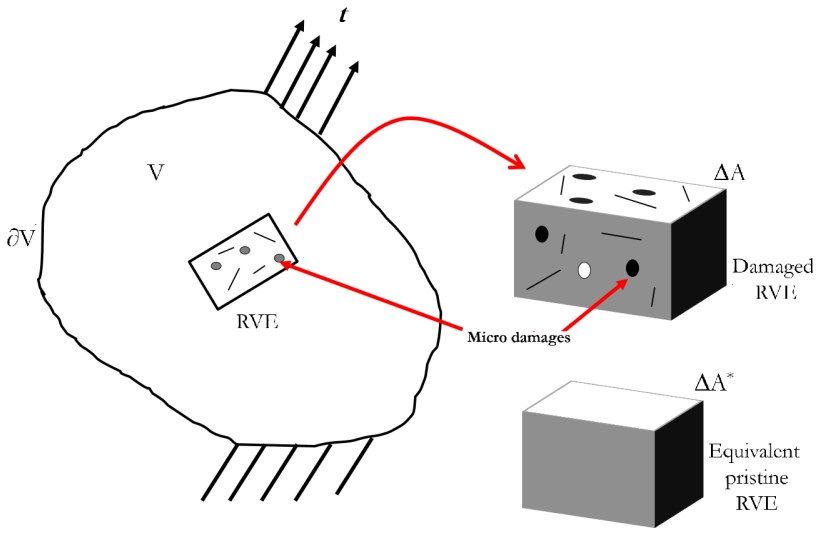

Figure 3.2. Damaged RUC and an equivalent pristine RUC

For the purposes of understanding the CDM concept, consider a representative unit cell (RUC) with a volume at least an order of magnitude larger than the largest 'damage' or discontinuity, as shown in Figure 3.2. Since the body that the RUC represents is under traction loading, the RUC will also experience mechanical stress. For simplicity, a uniaxial stress state in the RUC can be considered, which can be calculated by the component of the force normal to the surface of the RUC, $F_n = F\hat{n}$. The uniaxial stress can then be measured by:

$$\sigma = \frac{F_n}{\Delta A} \tag{3.12}$$

where ΔA is the area of the RUC under consideration, and $\hat{n}$ is the normal vector to ΔA. However, due to the discontinuities presented by the voids, microcracks, and other microscale damages, the effective area ΔA^* that resists the applied force F_n will undoubtedly be less than the RUC area

ΔA. Let ΔA_D be the aggregate total area consumed by the discontinuities that do not play a role in resisting the applied load. The ratio of the damaged area to the total area then represents the level of 'pristiness' of the RUC. Under the assumption that the discontinuities are isotropic and scattered in a random fashion, this ratio can be defined as a scalar damage variable D, which can be written as:

$$D = \lim_{\Delta A \to 0} \frac{\Delta A_D}{\Delta A} \tag{3.13}$$

It can easily be seen that the scalar variable D is bounded between 0 and 1, with $D = 0$ representing a completely pristine material and $D = 1$ representing complete deterioration of the RUC. However, in realistic cases there exists a value of damage less than unity that will cause large scale coalescence of damage leading to macroscale failure. This critical damage factor is represented by D_c.

With the introduction of damage, it is observed that the stress on the RUC cannot be measured using equation 3.12, which does not account for the reduction in area due to the discontinuities. The mechanical resistance in the damaged RUC can instead be measured using the effective uniaxial stress σ^* that accounts of the reduction in area.

$$\sigma^* = \frac{F_n}{\Delta A - \Delta A_D} = \frac{F_n}{\Delta A \left(1 - \frac{\Delta A_D}{\Delta A}\right)} \tag{3.14}$$

Substituting equation 3.13 and 3.12 in 3.14, the following expression is obtained:

$$\sigma^* = \frac{\sigma}{1 - D} \tag{3.15}$$

Equation 3.15 is the primary equation relation of the effective stress concept, which relates the stresses in a damaged body to the stresses in a pristine body, along with the measure of the damage variable. This concept permits the calculation of stresses in a damaged body by studying the pristine body, as long as an independent physical relationship to calculate the damage variable can be found.

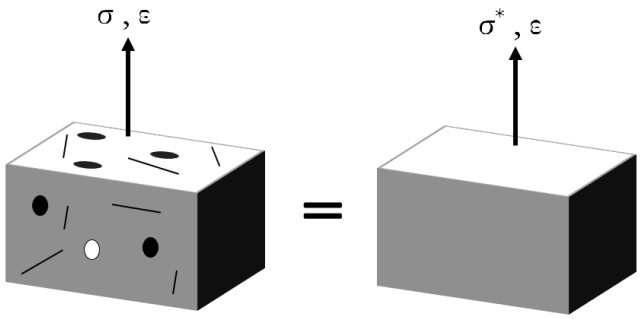

Figure 3.3. The strain equivalence principle

An additional concept that is used in CDM applications to facilitate the derivation of governing equations is the principle of strain equivalence. This principle along with the equivalent stress concept allows the constitutive equations of the pristine material to be used for studying the damaged material, as long as the effective stress is used. The principle of strain equivalence states that the strain in a damaged material is equal to the strain in a pristine material, as long as the damage and effective stress is taken into consideration in the constitutive equations.

$$\epsilon_e = \frac{\sigma^*}{E} = \frac{\sigma}{E(1-D)} = \frac{\sigma}{E^*} \tag{3.16}$$

where ϵ_e is the elastic strain, E is the elastic modulus of the pristine material, and E^* can be considered to be the effective elasticity modulus of the damaged material such that $E^* < E$. The effective elastic modulus homogenizes the reduction in area $\Delta A - \Delta A_D$ due to the presence of discontinuities, and allows the use of traditional constitutive models with reduced stiffness that may be characterized through physical models or they may be phenomenologically measured through experiments. Figure 3.3 illustrates the concept of strain equivalence. The various concepts discussed in this section provides the necessary background material required for deriving the atomistically informed damaged model, which has firm rooting in the thermodynamics of irreversible processes and CDM. The next section presents the formulations of the proposed damage model.

3.3 Continuum Formulations

3.3.1 Coupled Damage-Plasticity Theory

The continuum description for damage analysis uses the CDM concept, the formulations for which have been classically derived by Lemaitre (Lemaitre 2012) and Chaboche (Chaboche, Boudifa, and Saanouni 2006). Since these formulations are based on a thermodynamic framework as defined by Coleman and Gurtin (Coleman and Gurtin 1967) the free energy has to be specified. The Helmholtz specific free energy is assumed to be a function of the following state variables: the elastic strain $\underset{\sim}{\boldsymbol{\epsilon}}^e$, the isotropic damage variable D, and the internal strain like variable associated with chain movement and hardening/softening ξ. [2] The hardening variable is explained further in the following sections. The expression for the Helmholtz free energy is:

$$\psi = \frac{1}{\rho_0}\bar{\psi}(\underset{\sim}{\boldsymbol{\epsilon}}^e, D, \xi) \tag{3.17}$$

where ρ_0 is the original density. The total strain can be decomposed into the elastic and plastic strains through an additive decomposition such that:

$$\underset{\sim}{\boldsymbol{\epsilon}} = \underset{\sim}{\boldsymbol{\epsilon}}^e + \underset{\sim}{\boldsymbol{\epsilon}}^p \tag{3.18}$$

It is to be noted that this work uses the small strain assumption; however, the additive decomposition can still be used in a finite strain framework using updated Lagrangian formulations. In this case the elastic strain tensor becomes equivalent to a hypoelastic formulation in agreement with the Green-Naghidi stress rate (Jeridi, Laiarinandrasana, and Sai 2015).

By recalling equation 3.10, the Clausius-Duhem inequality can be reduced for isothermal iso-

[2] The notation for second order tensors and fourth order tensors used in this chapter are $\underset{\sim}{\boldsymbol{A}}$ and $\underset{\approx}{\boldsymbol{A}}$ respectively. All other variables can be considered to be scalar.

baric conditions, such that $\dot{T} = 0$ and $\nabla T = 0$, which leads to the following relation:

$$\underset{\sim}{\boldsymbol{\sigma}} : \dot{\underset{\sim}{\boldsymbol{\epsilon}}} - \rho\dot{\psi} \geqslant 0 \tag{3.19}$$

The classical arguments made by Coleman (Coleman and Gurtin 1967) allows the derivation of the Cauchy stress from the Helmholtz potential, since the Cauchy stress happens to be the thermodynamic force or thermodynamic affinity associated with the state variable ϵ^e as mentioned in equation 3.11. With this knowledge and with equation 3.17, the Cauchy stress can be defined from the thermodynamic potentials as:

$$\underset{\sim}{\boldsymbol{\sigma}} = \rho\frac{\partial\psi}{\partial\underset{\sim}{\boldsymbol{\epsilon}}^e} = \frac{\rho}{\rho_0}\frac{\partial\bar{\psi}}{\partial\underset{\sim}{\boldsymbol{\epsilon}}^e} \tag{3.20}$$

Substituting equation 3.17, 3.18, and 3.20 in equation 3.19, the following inequality can be arrived at:

$$\frac{\rho_0}{\rho}\underset{\sim}{\boldsymbol{\sigma}} : \dot{\underset{\sim}{\boldsymbol{\epsilon}}}^p - \frac{\partial\bar{\psi}}{\partial D}\dot{D} - \frac{\partial\dot{\psi}}{\partial\xi}\dot{\xi} \geqslant 0 \tag{3.21}$$

The gradients can be substituted with conjugate thermodynamic force variables such that equation 3.21 can be simply written as:

$$\frac{\rho_0}{\rho}\underset{\sim}{\boldsymbol{\sigma}} : \dot{\underset{\sim}{\boldsymbol{\epsilon}}}^p + Y\dot{D} - k\dot{\xi} \geqslant 0 \tag{3.22}$$

which is the intrinsic dissipation inequality. Y and k are the thermodynamic affinities associated with damage D and the internal strain due to chain entanglement in the polymer ξ respectively. The associated thermodynamic affinities are then defined as:

$$Y = -\frac{\partial\bar{\psi}}{\partial D} \qquad \text{and} \qquad k = \frac{\partial\bar{\psi}}{\partial\xi} \tag{3.23}$$

The negative sign associated with Y is present to ensure that the dissipation inequality is always satisfied.

The free energy term can be additively decomposed to a term that is defined by the elastic energy and a term defined by the hardening variable, since both damage and elastic strain operate

on the elastic energy term.

$$\bar{\psi} = \bar{\psi}^e + \bar{\psi}^k \tag{3.24}$$

The elastic term of the free energy can be further expanded as:

$$\bar{\psi}^e = \frac{1}{2}\, \underset{\sim}{\boldsymbol{\epsilon}}^e : \underset{\sim}{\boldsymbol{\sigma}} \tag{3.25}$$

where σ will have to be replaced by the effective stresses as mentioned in equation 3.15. Substituting the effective stresses, and utilizing the strain equivalence principle as formulated in equation 3.16, the following relation for the elastic energy term can be obtained:

$$\bar{\psi}^e = \frac{1}{2}(1-D)\, \underset{\sim}{\boldsymbol{\epsilon}}^e : \underset{\approx}{\boldsymbol{L}} : \underset{\sim}{\boldsymbol{\epsilon}}^e \tag{3.26}$$

where $\underset{\approx}{\boldsymbol{L}}$ is the stiffness matrix. To expand the hardening variable, a quadratic hardening free energy term is assumed as:

$$\bar{\psi}^k = \frac{1}{2}\, C_k \xi^2 \tag{3.27}$$

where C_k is a material parameter that represents the internal stresses developed by chain movement and entanglement. The complete expression for the specific free energy can now be written as:

$$\psi = \frac{1}{\rho_0}(\bar{\psi}^e + \bar{\psi}^k) - TS = \frac{1}{2\rho_0}(1-D)\, \underset{\sim}{\boldsymbol{\epsilon}}^e : \underset{\approx}{\boldsymbol{L}} : \underset{\sim}{\boldsymbol{\epsilon}}^e + \frac{1}{2\rho_0} C_k \xi^2 - TS \tag{3.28}$$

where the specific absolute temperature T and specific entropy S is also present due to the definition of the Helmholtz free energy as mentioned in equation 3.8. However, these variables do not play a large part in the governing equations as can be seen in the final expressions.

A straightforward methodology to deal with density differences due to various phenomenon, such as void nucleation and growth is to associate it with damage due to volume changes using a dependent variable D_v (Chaboche, Boudifa, and Saanouni 2006):

$$\frac{\rho}{\rho_0} = 1 - D_v \tag{3.29}$$

Substituting equation 3.28 and 3.29 in equation 3.20 provides a relation for Hooke's law for the non-pristine material and is expressed as:

$$\underset{\sim}{\boldsymbol{\sigma}} = \rho\frac{\partial\psi}{\partial\underset{\sim}{\boldsymbol{\epsilon}}^e} = (1-D_v)(1-D)\underset{\approx}{\boldsymbol{L}} : \underset{\sim}{\boldsymbol{\epsilon}}^e \tag{3.30}$$

The thermodynamic affinities defined in equation 3.23 can also be further expanded using equation 3.28 as:

$$Y = -\frac{\partial\bar{\psi}}{\partial D} = \frac{1}{2}\underset{\sim}{\boldsymbol{\epsilon}}^e : \underset{\approx}{\boldsymbol{L}} : \underset{\sim}{\boldsymbol{\epsilon}}^e \tag{3.31}$$

$$k = \frac{\partial\bar{\psi}}{\partial\xi} = C_k\xi \tag{3.32}$$

The total plastic potential ϕ governing material behavior assumes plastic, damage, and hardening potentials $\phi_{p,D}$ and ϕ_ξ. The plastic potential is chosen such that the effects of damage and volumetric change are also considered:

$$\phi = \phi_{p,D}(\frac{\rho_0}{\rho}\underset{\sim}{\boldsymbol{\sigma}}, k, D, D_v) + \phi_\xi \tag{3.33}$$

The plastic potential ϕ also known as the yield function, is chosen as a modification of the classical Lemaitre yield function (Lemaitre 1985):

$$\phi = \frac{\rho_0}{\rho}\frac{\sigma^*_{eq}}{1-D} - k - \sigma_y \leqslant 0 \tag{3.34}$$

where σ_y represents the yield stress. The scalar equivalent stress σ^*_{eq} is formulated such that hydrostatic stresses can be considered. Hence, a combination of the first and second invariants is taken using a variable elliptic form as used in works of Green and Besson (Green 1972; Besson and Guillemer-Neel 2003) and Chaboche (Chaboche, Boudifa, and Saanouni 2006):

$$\sigma^*_{eq} = \sqrt{J(\underset{\sim}{\boldsymbol{\sigma}})^2 + \alpha f(D, D_v) I(\underset{\sim}{\boldsymbol{\sigma}})^2} \tag{3.35}$$

where α is the degree of ellipticity and is taken to be 0.5 in this work. $f(D, D_v)$ is a function of the damage parameters used to couple the yield function with the associated damage. In this work,

this function is assumed to be varying only with volumetric damage and specified as $f(D, Dv) = D_0 + D_v$, where D_0 is a small phenomenological constant used to couple hydrostatic stresses with the deviatoric components even when D_v is 0. When α is 0, the yield function reduces to the classical Lemaitre form.

3.3.2 Evolution of State Variables

The plastic strain evolution equation can be obtained using the classical plasticity normality conditions. We can denote the plastic strain rate as:

$$\dot{\underset{\sim}{\boldsymbol{\epsilon}}}^p = \dot{\lambda}\frac{\partial\phi}{\partial(\frac{\rho_0}{\rho}\underset{\sim}{\boldsymbol{\sigma}})} = \frac{\dot{\lambda}}{1-D}\frac{\partial\sigma^*_{eq}}{\partial\underset{\sim}{\boldsymbol{\sigma}}} \tag{3.36}$$

where the viscoplastic multiplier is obtained using the Peric formulations (Peric 1993) and is shown below:

$$\dot{\lambda} = \frac{1}{K}\left[\left(\frac{\phi+\sigma_y}{\sigma_y}\right)^{\frac{1}{n}} - 1\right] \tag{3.37}$$

where K and n are the viscoplastic constants.

To evaluate the internal strain evolution due to chain entanglement requires an inclusion of polymer chain mechanics. In general, it is understood that the physics of polymer hardening are vastly different from that of metals due to the nature of polymeric materials; as such, the physics of polymer chain motion and entanglement is simulated with an internal strain like quantity. The evolution of the internal strain due to chain entanglement, ξ, is described by evolution equations formulated by Anand and Gurtin (Anand and Gurtin 2003). The equation, as simplified by Bouvard et al. (Bouvard et al. 2010), is described as follows:

$$\dot{\xi} = h_0\left(1 - \frac{\xi}{\xi^*}\right)\dot{\lambda} \qquad\qquad \dot{\xi}^* = g_0\left(1 - \frac{\xi^*}{\xi_{sat}}\right)\dot{\lambda} \tag{3.38}$$

The evolution equation for the internal strains describes obstacles to chain movements such as chain entanglement points. The internal strain produced due to these obstacles and the resultant

entanglement can be represented by the term ξ. The energy barrier that opposes chain movement is described by the term ξ^*. As more chains escape the entanglement points, there is a lowering of the energetic barrier resulting from the increased cooperative motion of chains. Hence, ξ^* decreases as ξ increases until the saturation point ξ_{sat} is reached. h_0 and g_0 are the associated hardening moduli. The internal stresses due to chain entanglement in the polymer network can then be evaluated using:

$$k = \frac{\partial \bar{\psi}}{\partial \xi} = C_k \xi \tag{3.39}$$

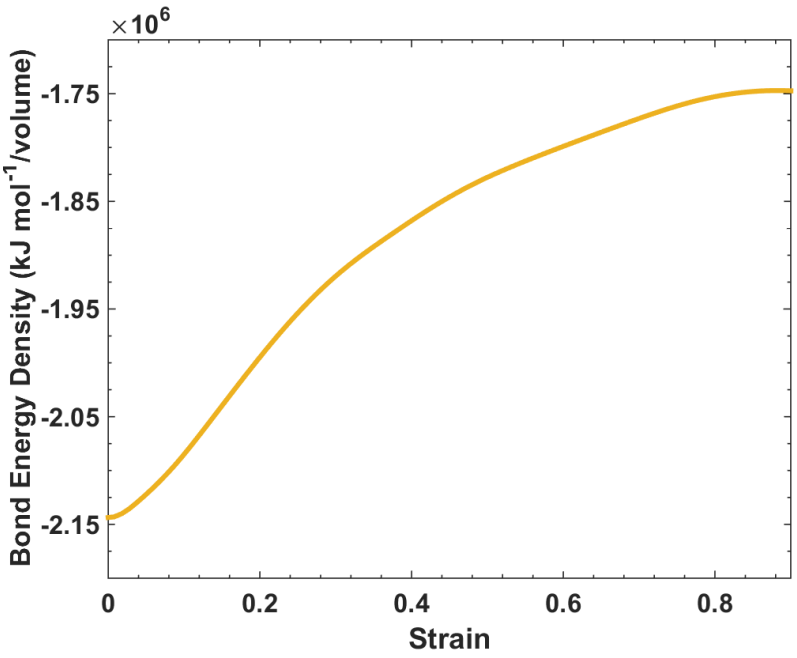

Figure 3.4. Representative BDE density progression with applied strain

The damage evolution for metals is generally adopted to be a simple nonlinear power law function of Y due to the simplicity and effectiveness of this functional form for metallic materials. However, damage physics in polymers is vastly different from damage mechanisms in metals and requires a separate evolution equation that considers the kinetics of polymer damage. To account for the physics of polymer damage, damage evolution is instead chosen to surrogate the MD simulations of fundamental damage occurring in the polymer. For thermoset polymers, under isother-

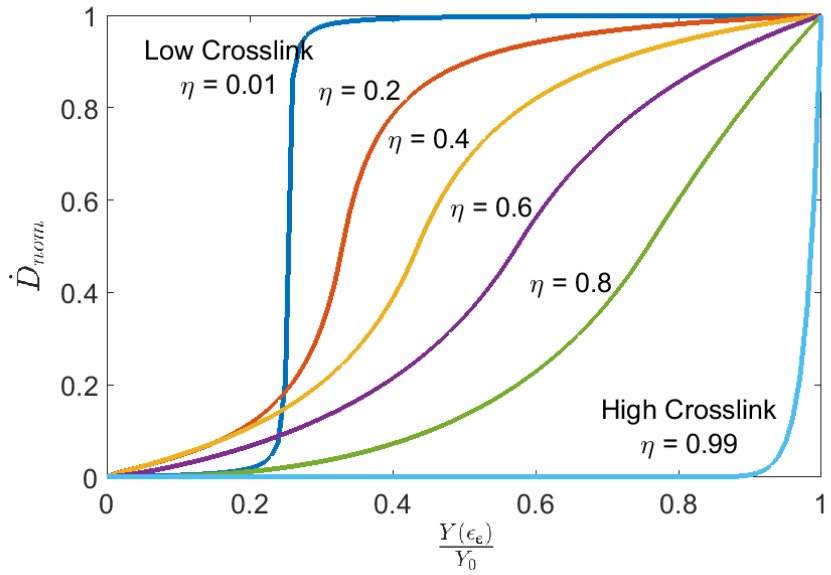

Figure 3.5. Damage evolution for a spectrum of crosslinking degrees

mal conditions, and at operating temperatures below the glass transition temperature, the energy variations due to successive bond breakages at the atomistic scale have shown to be related to damage at the continuum level (Subramanian, Rai, and Chattopadhyay 2015).

Figure 3.4 shows the progression of bond disassociation energy (BDE) density under mechanical loading calculated using MD simulations as described in section 2.2. The BDE density is an approximation of fundamental damage occurring at the atomic scale due to successive covalent bond breakage. To account for the observed damage kinetics, a sigmoidal damage evolution law, with parameters varying according to crosslinking degree, is used following the BDE trend observed in MD simulations. It is shown in Chapter 2 that the polymer stiffness is a function of the crosslinking degree (Subramanian et al. 2015). Additionally, at low crosslinking degree, i.e., low curing, the polymer exists in a viscous state where damaging the material requires application of minimal energy. At a high crosslinking degree, i.e., high curing, the polymer is stiff requiring higher application of energy to damage. Hence, the damage evolution equation is chosen such that it reflects the change of the nature of damage with change in crosslinking degree, and expressed

as:

$$\dot{D} = \frac{\dot{\lambda}}{2} \cdot \left[\operatorname{sgn}(\chi) \cdot \frac{-(1-\eta)|\chi| - |\chi|}{-2(1-\eta)|\chi| + (1-\eta) - 1} + 1 \right] \tag{3.40}$$

where $\operatorname{sgn}()$ is the signum function and χ is defined as:

$$\chi = 2 \left(\frac{Y}{Y_0} \right)^{\frac{1}{2(1-\eta)}} - 1 \tag{3.41}$$

η is the crosslinking degree and Y_0 is a material parameter associated with the maximum energy required to begin damaging the material. Figure 3.5 shows the variation of nominal rate of damage $\dot{D}(\dot{\lambda} = 1)$ versus normalized elastic energy $\frac{Y}{Y_0}$.

Finally, the evolution of the dependent volumetric damage parameter is simply obtained through the equations of mass conservation of volume changes induced due to plasticity. It can be expressed as:

$$\dot{D}_v = (1 - D_v)\, tr(\dot{\underset{\sim}{\boldsymbol{\epsilon}}}^p) \tag{3.42}$$

where the trace of the plastic strain rate is considered.

3.3.3 Yield Stress Variation with Crosslinking

Since, the analysis presented in the previous section considers variation of material behavior with the polymer crosslinking degree, a relationship between yield stress σ_y and crosslinking degree η needs to be determined. In this work, the relationship is found through experimental characterization. The experimental procedure for testing the polymer dog-bone samples as detailed by Fard et al. (Fard, Liu, and Chattopadhyay 2011) was followed. Uniaxial quasi-static test of flat dog-bone specimen made from Epon E863 Resin and Epi-Cure 3290 hardener (100/27 weight ratio) was performed. To find the relationship between crosslinking degree and yield stress, specimens with varying total cure times were tested under uniaxial tension until failure. The curing times for the tested specimens are shown in Table 3.1. Since the specimen are cured for varying

amounts of time, the hypothesis is that each specimen will also have varied crosslinking degrees, since the crosslinking degree is a function of the curing time and temperature. The temperature during the cure process was maintained to be constant and all the samples were cured at the same temperature to control one of the variables; hence, the temperature is not considered to be a curing variable.

Table 3.1. Specimen Cure Times

Specimen Number	Curing Time (Hours)
Specimen 1	6.5
Specimen 2	7
Specimen 3	7.5
Specimen 4	8

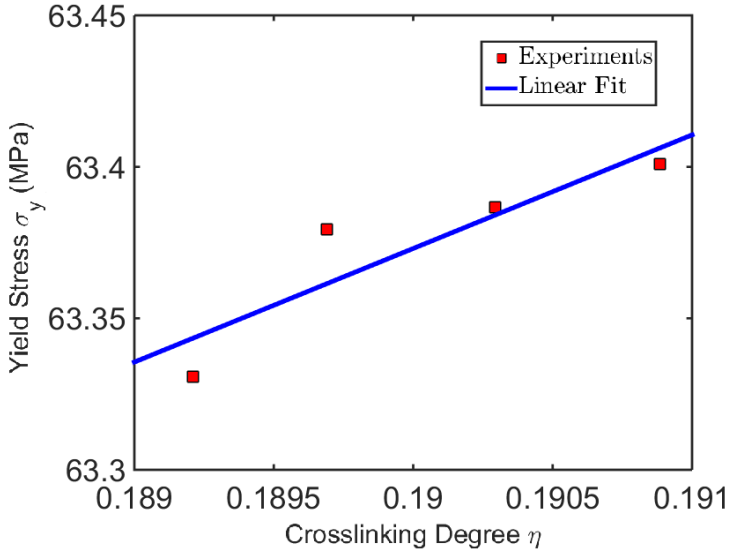

Figure 3.6. Yield stress vs. crosslinking degree

The yield stress of each specimen was measured using the 0.2% method, where the yield stress is considered to be the point where a line, originating at 0.2% strain and parallel to the elastic response, bisects the experimentally observed stress-strain response. Additionally, the elastic modulus was calculated using standard procedures for uniaxial tests, by measuring the gradient of a

linear model that fits the elastic response. Using equation 2.1 and the curing times reported in Table 3.1, the crosslinking degree for each specimen was back-calculated. The relationship between crosslinking degree and the corresponding yield stress was observed to be linearly dependent and can be seen in Figure 3.6. The following linear model was found to be the closest fit to the observed response:

$$\sigma_y = 37.495\eta + 56.249$$

This model replaces the yield stress σ_y in equation 3.34, which makes the crosslinking degree the primary variable that drives tunable parameters. However, the crosslinking degree cannot be arbitrarily applied to fit experimental data, since the crosslinking degree is an experimentally characterizable material parameter.

3.4 Verification and Validation

Table 3.2. Damage Model Parameters

η	.19	h_0	2
$\dot{\epsilon}$	.005 per sec	g_0	1
K	15	ξ_{sat}	0.08
n	2.5	ξ_0	0.12
σ_y	63.375 MPa	C_k	2.8 GPa
Y_0	.12 MPa		

For verification of the proposed damage model, it is benchmarked against a widely used classical porous plasticity model and a classical CDM model available in literature, namely, the Gurson model as modified by Tvergaard and Needleman (Tvergaard and Needleman 1984), and the classical Lemaitre CDM model (Lemaitre 1985, 2012). Realistic material parameters for an aerospace grade polymer are applied to the Gurson-Tvergaard-Needleman(GTN) model. Subsequently, the Lemaitre CDM model is fitted to match the GTN model by changing the values of parameters

associated with Lemaitre's damage evolution law. Following this, the proposed model is provided with the same parameters as applied to the Lemaitre CDM model. To ensure a similar basis for comparison, all three models use the same hardening definition as explained in section 3.3, and additional parameters are detailed in Table 3.2. The specific parameters used in the GTN and Lemaitre CDM model are detailed in Table 3.3. The classical Lemaitre damage evolution equation used in this section is expressed as:

$$\dot{D} = \left(\frac{Y}{S}\right)^{s}(1-D)^{-\beta+1}\dot{\lambda} \tag{3.43}$$

Table 3.3. Model Parameters

	GTN		Lemaitre
η	0.19	η	0.19
σ_y	63.75 MPa	σ_y	63.75 MPa
q1	1.5	S	$1 \times 10^7 J/m^3$
q2	1.0	s	1.0
q3	1.0	Y	.12 MPa
f_c	0.1	β	1.0
f_F	0.4		
f_N	0.08		
μ_N	0.05		
s_N	0.01		

The comparison of the three models can be seen in Figure 3.7. It is observed that the GTN model underestimates initial damage until the critical porosity volume fraction is reached. The critical porosity volume fraction can be a phenomenological parameter and is hard to define, especially for polymers. The classical CDM model overestimates damage due to the exponential damage evolution function, which generally estimates metal physics accurately; however, the model does not successfully capture polymer damage kinetics. The atomistically informed damage model developed in section 3.3 shows the same trend as the classical models until substantial nonlinearity is observed, followed by stable damage evolution. This trend seems to correlate with physical

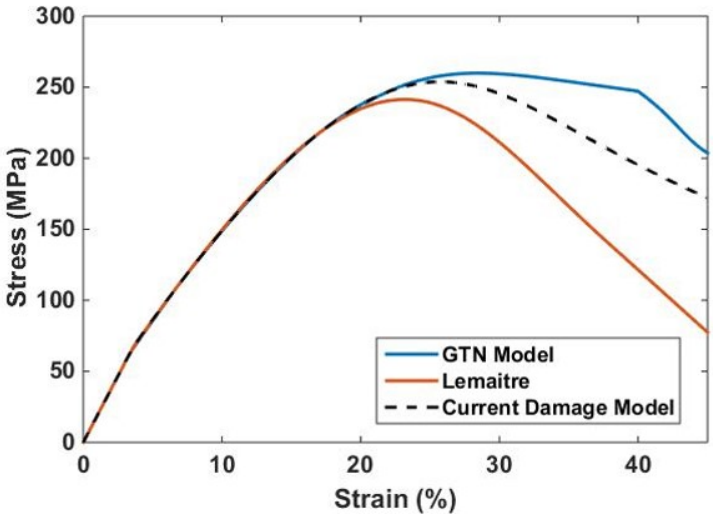

Figure 3.7. Model benchmarking

evidence of slow initial damage evolution, followed by a faster rate as cracks coalesce, and subsequently followed by a slower rate as the damaged state saturates. The comparisons with classical models provide a verification of the atomistically informed damage model, which can now be tested for validity by comparison with actual experimental observations.

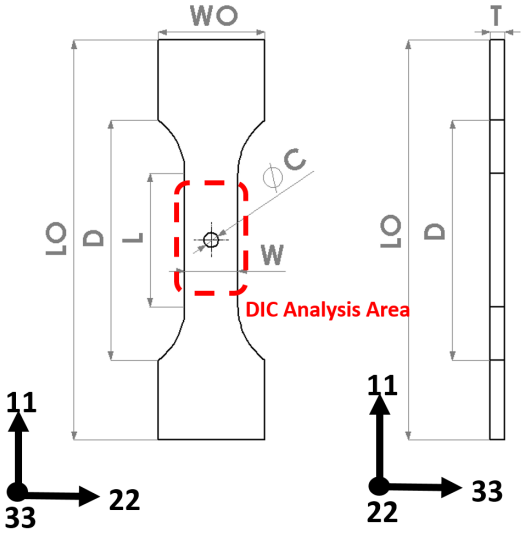

Figure 3.8. Open-hole specimen details

Validation of the atomistically informed damage model is performed by comparing the pre-

Table 3.4. Open-hole specimen dimensions

Dimensions	C	D	L	LO	T	W	WO
Values (mm)	3.5	58.5	32.5	97.5	3.5	13	26

dictions from numerical simulations with the derived damage model to the observed local and global strain response of a polymer open-hole tension experiment. To perform the experiment, appropriate specimens were manufactured using Epon E863 Resin and Epi-Cure 3290 hardener (100/27 weight ratio). The design and manufacturing of the specimen, as well as experimental procedure is based on ASTM standard D638 (ASTM-D638-14 2014), as modified by Yekani Fard et al. (Fard, Liu, and Chattopadhyay 2011) for the testing of open-hole polymer specimens under uniaxial tension. Specimen details are presented in Table 3.4 and Figure 3.8.

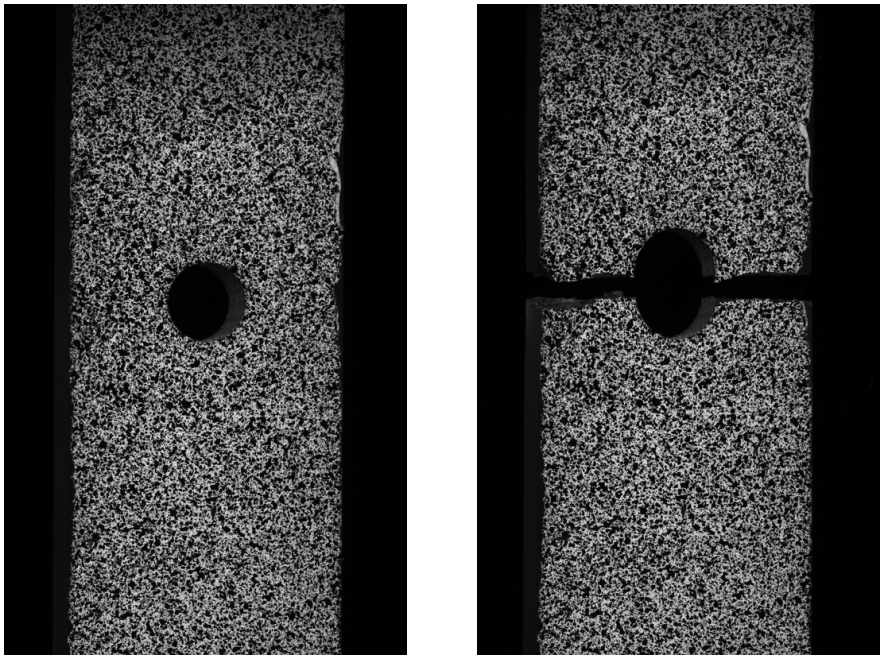

(a) Unloaded configuration (b) Failed specimen

Figure 3.9. Open-hole test specimen displaying speckle pattern

To begin the testing process, the specimen is gripped at the ends using hydraulic grips in an MTS mechanical testing machine. 3-D Digital Image Correlation (DIC) was used to measure

the displacement and strain field contours on the surface of the open-hole test specimen. The DIC system takes digital images during the experiment and then tracks a random speckle pattern shown in Figure 3.9, which is painted on the surface of the specimen to calculate relative and rigid body displacements. The displacement field is then post-processed to obtain corresponding strain fields. The stereo-vision capabilities of DIC ensures a highly accurate in-plane and out-of-plane displacement and strain measure of a surface.

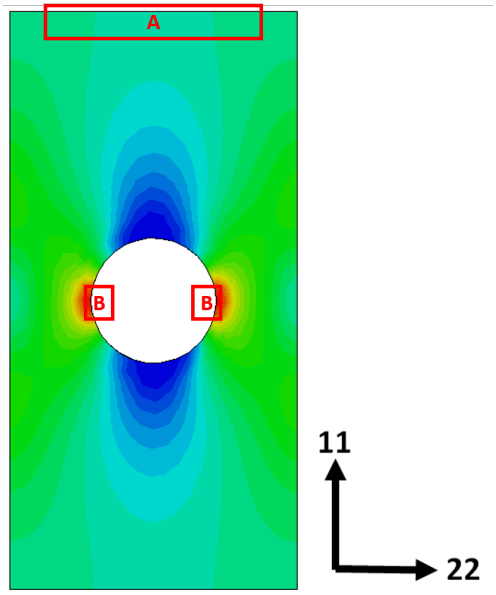

Figure 3.10. FE model stress contours in the 11 direction

The specimen was tested in displacement control at a rate of 1mm per minute to ensure quasi-static conditions. The displacement and strain field calculations were performed only for the stem portion of the test coupon, as shown in Figure 3.8. Rigid body displacement of the specimen from the DIC results was used to calculate and ensure minimal grip slip. A numerical model of the specimen is generated in ABAQUS, a commercial FE package, and then virtually tested under the same conditions as the experiment. The formulations presented in section 3.3 are implemented in ABAQUS using a user sub-routine with damage model parameters detailed in Table 3.2 and then applied to the polymer material. The numerical model is meshed with 1550 3-D C3D8R solid

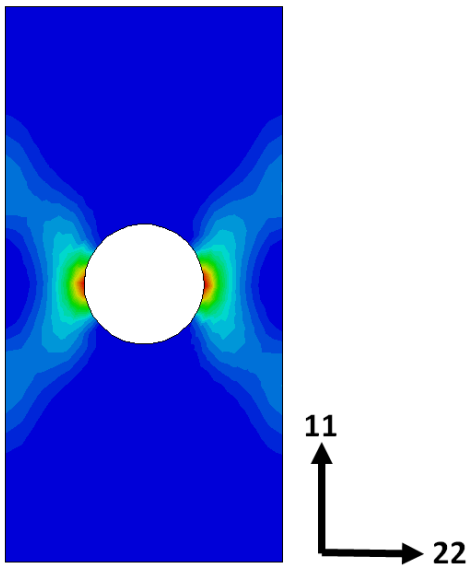

Figure 3.11. FE model damage contours

brick elements with reduced integration. A finer mesh is generated near the hole to capture the stress concentration effects. Only the stem portion of the experimental specimen is modeled. The boundary conditions emulate the experiment with the bottom surface constrained in 11 direction (for orientation see Figure 3.8) and a displacement applied at the upper surface in the positive 11 direction under quasi-static conditions.

The stress contours in the loading direction (σ_{11}) obtained from the FE simulation are shown in Figure 3.10, where the classical stress concentration contours around the open-hole can be observed. The damage contours in Figure 3.11 show a clear cross localization pattern at the onset of nonlinear behavior around the region. Figure 3.12 shows the comparison of the far field strain between the experimental results and the FE model versus the applied displacement. The reported strain is an average value measured at a few points far away from the hole and in the loading direction (ϵ_{11}) which is shown as section A in Figure 3.10. To maintain a fair comparison, the strains were measured at the same points in the FE model as the DIC images of the experiment. It can

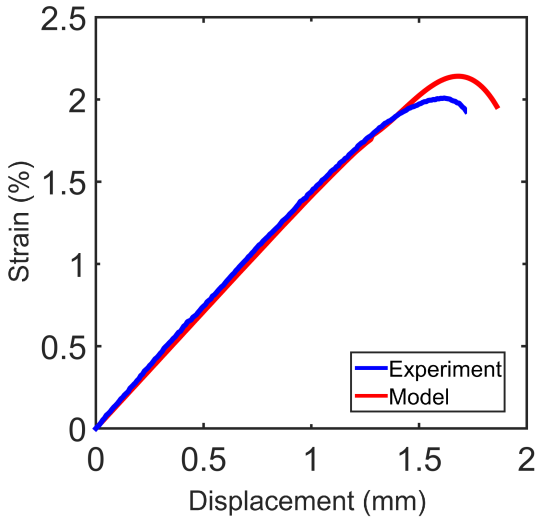

Figure 3.12. Far-field strain comparison of experiment and model

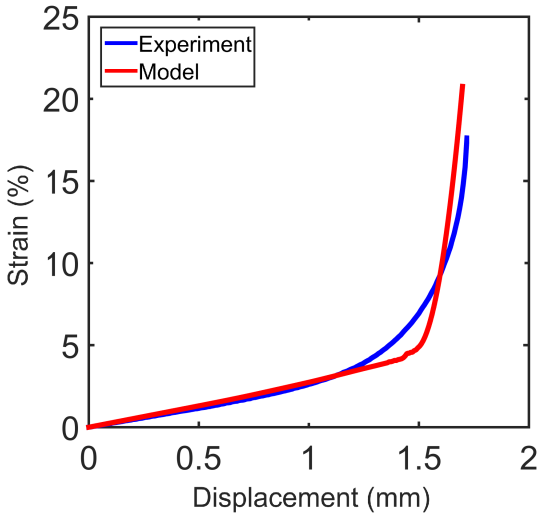

Figure 3.13. Near-field strain comparison of experiment and model near hole

be seen that nonlinearity in far field strains and complete fracture of the specimen were captured reasonably well by the model.

Figure 3.13 shows the strain evolution (ϵ_{11}) around the field of the hole. These strains were measured as an average value taken from section B in Figure 3.10. The local area around the hole

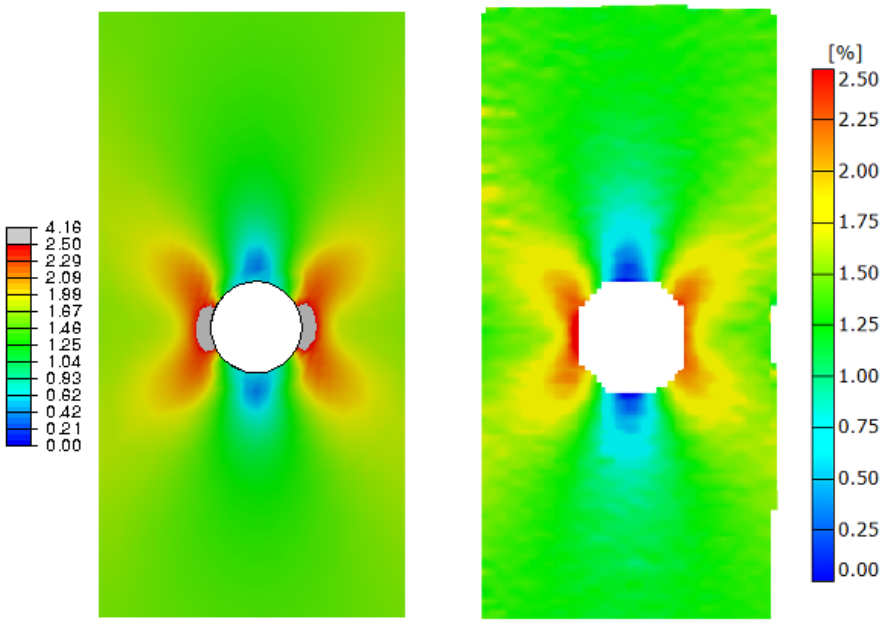

Figure 3.14. Comparison of model (left) and experimental (right) strain contours at 50% final load

experiences increased stresses due to the concentration effects and, at larger crosshead displacements, this leads to concentrated plasticity and damage in the polymeric material relative to the far field regions. This phenomenon is exhibited as nonlinearly increasing strains in Figure 3.13. The slight mismatch around 5% strain is attributed to the plasticity algorithm, which depends on the plastic potential activating the damage formulations. This mismatch can be corrected by taking better measures of the yield point for the damage formulation and, in future work, will be evaluated based on MD simulations of the polymer. The strain contours in the loading direction (ϵ_{11}) from the experiment, as captured by the DIC software, is then compared against the strain contours from the FE model in Figure 3.14 and Figure 3.15. It can be seen that the model closely follows the experimental results in the far field regions as well as at the local region around the hole. The model successfully captures the nonlinear increase in strains and the resulting fracture due to local plasticity and damage, which are the essential characteristics of the open-hole test.

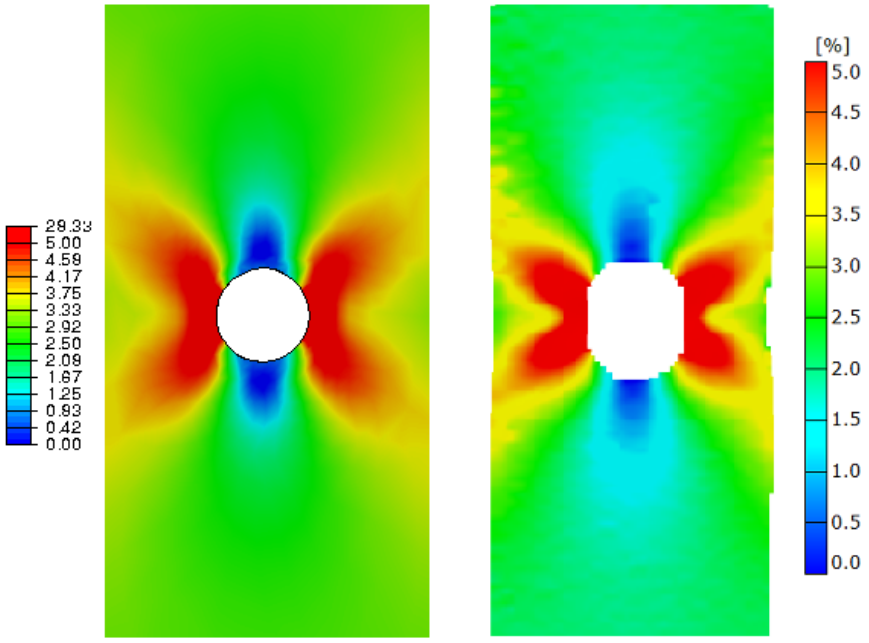

Figure 3.15. Comparison of model (left) and experimental (right) strain contours at 95% final load

3.5 Damage Model Predictions for Neat Polymer

This section presents results and predictions from the proposed damage model for neat polymer. Figure 3.16 shows the comparison of the damage model to a uniaxial tension experiment. From the experimental values, it is possible to calculate the crosslinking degree by performing an inverse calculation for the modulus using equation 2.1. The crosslinking degree was calculated to be $\eta = .19$ in the performed experiments. This value was used as input to the damage model, and the rupture criteria D_c, which is defined as the percentage of damage at which global material failure occurs, was set to be 2.5%. Figure 3.18 shows the predictions of the model with D_c set to 30%. Similar parameters as in the simulations performed in the previous section are used for the damage model and are detailed in Table 3.2.

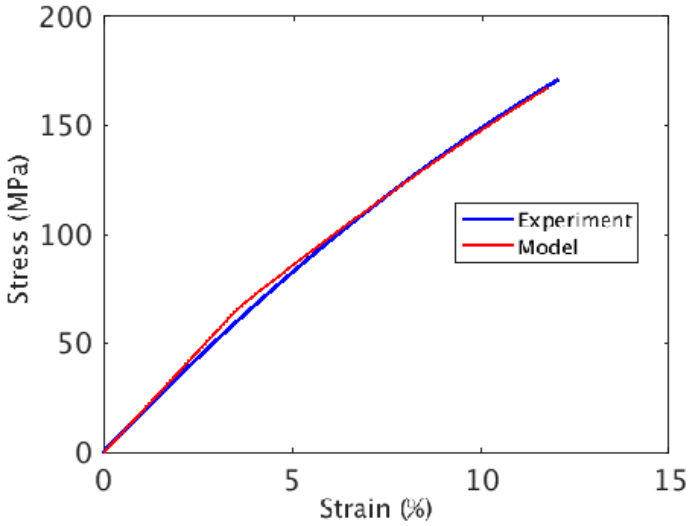

Figure 3.16. Model and experiment comparison with $D_c = 2.5\%$

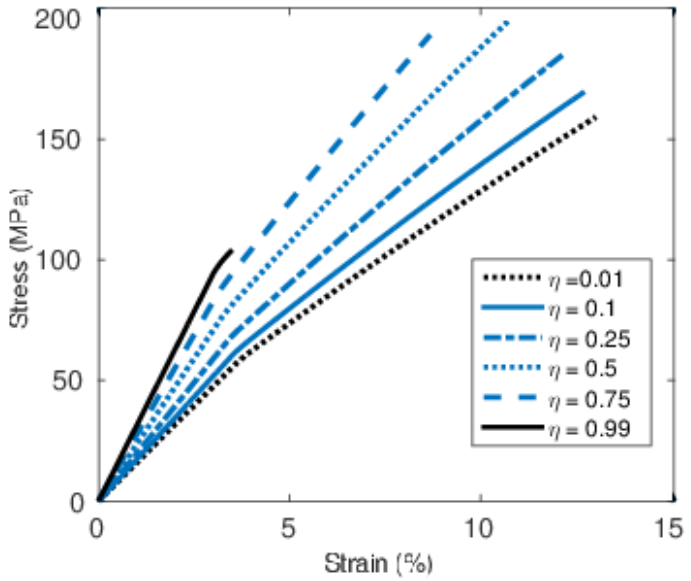

Figure 3.17. Simulated stress-strain response for varying crosslinking degree

3.5.1 Variation with Crosslinking Degree

The variation of stress-strain response with crosslinking degree is shown in Figure 3.17. At low crosslinking degrees the model predicts greater post yield behavior as compared to higher

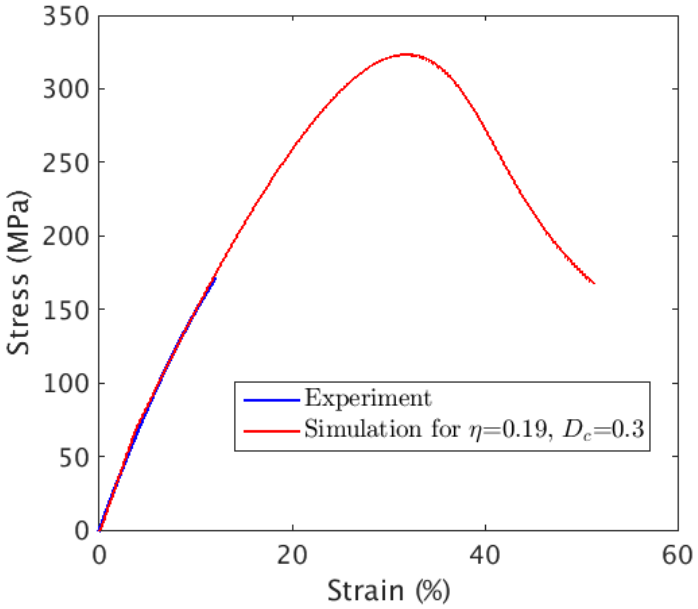

Figure 3.18. Stress-strain response with $D_c = 30\%$

crosslinking degrees, where the post yield region decreases considerably. The maximum ultimate strength is reached at about 60% crosslinking, subsequent to which, there is a rapid decrease in ultimate strength. At extremely high crosslinking degrees, the model predicts a behavior wherein the material fails with almost no post yield response similar to a brittle material response.

3.5.2 Evolution of Internal State Variables

The evolution of the damage variable D and the damage evolution $\dot{D}$ is shown in Figure 3.19a for two extreme values of the crosslinking degree at $D_c = 2.5\%$. It is observed that at lower crosslinking degree, the damage evolution is slower, whereas at higher crosslinking degree, damage evolution is rapid. This trend implies that at lower crosslinking degree, a larger post yield response can be expected while smaller post yield region can be expected for higher crosslinking degree as seen in Figure 3.17. Figure 3.19b shows the damage variables D and $\dot{D}$ for crosslinking degree $\eta =$

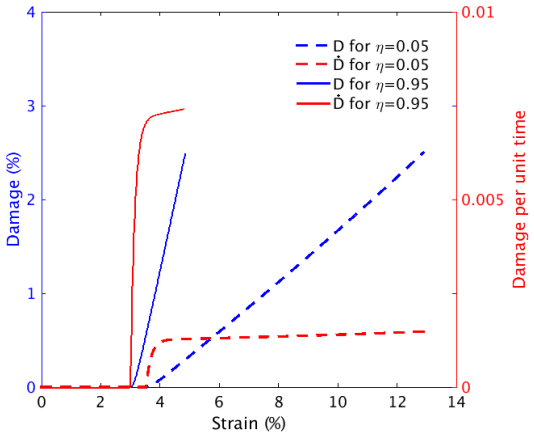

(a) Damage parameters at $\eta = .05$ and $\eta = .95$ with $D_c = 2.5\%$

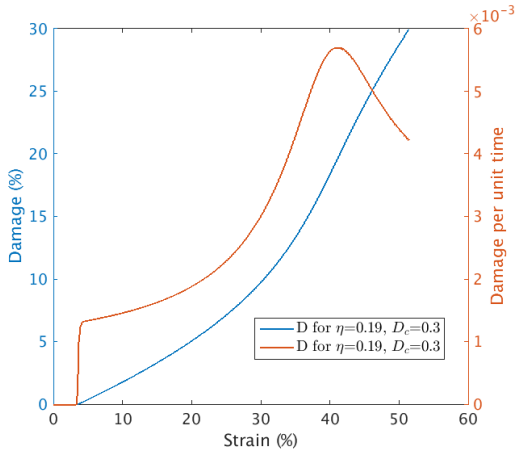

(b) Damage parameters at $\eta = .19$ with $D_c = 30\%$

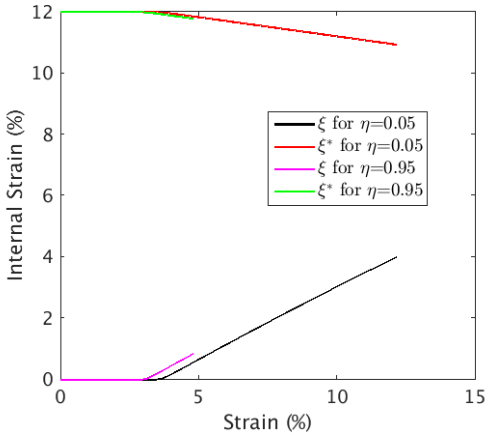

(c) Hardening parameters at $\eta = .05$ and $\eta = .95$ with $D_c = 2.5\%$

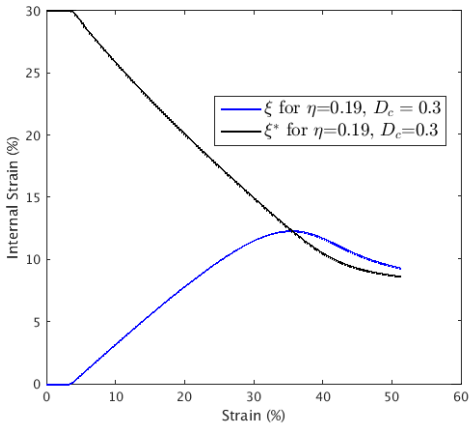

(d) Hardening parameters at $\eta = .19$ with $D_c = 30\%$

Figure 3.19. State variable evolutions

.19 and $D_c = 30\%$. The effects of the sigmoidal damage evolution on the damage variable can be seen in these figures. The initial increase in damage evolution is caused by initiation of damage and is followed by a nonlinearly increasing damage profile, which can be attributed to progressive damage. This state leads to a peak in damage evolution causing a saturated state of damage in the material. Following the peak, there is a decrease in the rate of damage which consequently decreases damage accumulation.

3.5.3 Evolution of Hardening Parameters

The evolution of the hardening parameters are shown in Figure 3.19c. It can be seen that ξ^* decreases as ξ increases until eventually the saturation values are reached. ξ displays the internal strain due to chain entanglements and obstacles to chain movement. As chain movement increases and the associated energy increases; the barrier to this movement, displayed by ξ^* decreases, leading to more chain movement and continued decrease of chain entanglement. At lower strains this phenomenon is a major cause of hardening and softening in polymers (Anand and Gurtin 2003; Bouvard et al. 2010). Figure 3.19d shows the hardening parameter evolution for $\eta = .19$ and $D_c = 30\%$. This figure clearly illustrates the state at which saturation has been attained, and hence there is an equalization of ξ and ξ^*.

3.6 Summary

This chapter introduced the development of, and formulations for a constitutive law for thermoset polymers based on the CDM framework and in conjunction with a damage evolution equation that is developed from elastoplastic MD simulations results using reactive force fields. This thermodynamically admissible framework uses various ISVs to define material damage, hardening, and volumetric damage, based on MD simulations of covalent bond breakage under mechanical loading, polymer physics, and stress triaxialities respectively. The developed damage formulations were rigorously benchmarked with classical plasticity algorithms and validated by predicting the inelastic mechanisms observed in open-hole tests.

Since these formulations utilize the energy form of the inelastic information obtained from MD simulations, it does not display the drawbacks observed in section 2.5. In this form, successful inelastic information transfer between the nanoscale and continuum scale has been shown to be

possible in a computationally efficient manner. Additionally, the atomistically informed damage model was also used to provide insight into the manner of damage accumulation in neat polymer. In the subsequent chapter, the CDM based atomistically informed damage model is applied for the study of the inelastic behavior in carbon nanotube enhanced nanopolymers, nanocomposites, and carbon fiber reinforced polymer composites.

Chapter 4

DAMAGE AND MULTIFUNCTIONAL MECHANISMS IN CNT NANOPOLYMERS

4.1 Introduction

The use of carbon nanotubes (CNTs) for structural and multifunctional nanotechnology applications is an area of growing scientific interest (Thostenson, Ren, and Chou 2001; Yu and Kwon 2009). In particular, nanocomposites that use CNTs as reinforcing nanofillers in the polymer matrix have been shown to exhibit superior multifunctional properties under controlled environments (Balazs, Emrick, and Russell 2006), such as improved stiffness (Dean et al. 2006), *in-situ* damage sensing (Datta et al. 2015), precise thermal management (Biercuk et al. 2002) and increased toughness (Coleman et al. 2006), thus presenting potential for unique applications. However, a critical obstacle preventing the integration of nanostructures into practical applications is the inability to scale the performance gains and multifunctional capabilities of nanocomposites for commercialization purposes (Sochi 2012). In other words, a deep divide remains between the theoretical predictions and the experimental observations of the mechanical, strength, and damage properties of CNT-nanocomposites at the macroscale. These differences translate into limitations, e.g., minimal increase in fracture characteristics (Gojny et al. 2004; Qiu et al. 2007) and low strength and fatigue life compared to predicted values (Y. Ren et al. 2004). Such discrepancies have been attributed to geometrical inconsistencies in the CNT composition at the submicroscale, such as lack of alignment, agglomerations and poor dispersion of the CNTs (Wicks, Villoria, and Wardle 2010) that are not accounted for in most macroscale theoretical formulations. Limited efforts have been devoted to a comprehensive analysis of the cause of these discrepancies. Recent studies have also shown that the local nanoscale and sub-microscale stress-strain response

of nanocomposites can significantly differ from the average bulk response, with the local stress-strain response around the filler material indicating stress concentration sites (Subramanian et al. 2015). Such localized sub-microscale response may lead to accelerated damage initiation which may account for the difference in theoretical and predicted macroscale response in these materials.

Additionally, there remains a lack of literature focusing on the change in multifunctional abilities of nanocomposites in the damaged state. It has been shown that material degradation in CNT-nanocomposites can lead to substantial nonlinear effects in the multifunctional properties (Thostenson and Chou 2008). A thorough understanding of the relationship between damage state of nanocomposites and its mechanical and electrical properties is necessary to improve the capabilities of these material for applications such as *in-situ* sensing of damage initiation, propagation, and onset of failure in composite structures. Most computational studies limit their domain to elastic regimes to study the piezoresistive behavior of the CNTs in nanopolymers using finite element based techniques (X. Ren et al. 2015) or global electrical resistance change under strain using simulated electrical circuits based on a percolation networks (Shimamura, Yasuoka, and Todoroki 2007). Representative unit cell (RUC) approaches have also been used as 3D resistor network models to predict the electrical properties of CNT nanocomposites at and after percolation (Hu, Masuda, et al. 2008) as well as purely macroscale continuum and fracture mechanics techniques to study measurement sensitivities (Gallo and Thostenson 2015). However, there remains a lack of literature focusing on the post-yield and damage behavior of CNT infused nanocomposites, and change in multifunctional abilities in the damaged state. Since the multifunctional phenomenon in nanocomposites have sub-microscale origins, understanding variations of these properties with change in material state requires comprehensive multiscale models that include physics based formulations of coupled electro-mechanical constitutive relations, as well as damage initiation and progression.

The previous chapter detailed the development of an atomistically informed continuum dam-

age mechanics (CDM) based formulation that captures polymer damage under isothermal conditions and within operating temperatures lower than the glass transition temperature. This chapter details the application of the atomistically informed damage model to a CNT/polymer system to achieve a sophisticated understanding of the load transfer, damage initiation, and propagation in CNT nanocomposites at the length scale of the filler material and its effects at the microscale. The developed damage law is applied to an RUC consisting of bulk polymer, and a sizable number of CNTs, which are explicitly modeled and randomly oriented. Additionally, a coupled electro-mechanical formulation is developed, coupling the induced and mechanical strain as a function of the applied global and local strain due to damage, to accurately model piezoresistivity of the nanocomposite. Such a methodology can provide new insights into damage trends, crack initiation, and propagation at the sub-microscale of CNT nanocomposites, as well as, explain the phenomenon of piezoresitivity variations under material degradation at the sub-micro and microscale.

4.2 Microscale Nanocomposite Modeling

The damage theory detailed and validated in Chapter 3 is incorporated into a microscale model to investigate the microscale and sub-microscale, load transfer and damage effects of CNTs, in a polymer matrix. A microscale RUC of the polymer is generated in the finite element (FE) framework and CNTs are inserted into the polymer model by explicitly modeling them using a vertex generation algorithm, in the FE global coordinate system. Two arrangements of CNTs: (i) randomly dispersed and (ii) entangled agglomerates, which are shown in Figure 4.2, are generated and studied in detail. The randomly dispersed CNT arrangement is indicative of a nanocomposite system wherein the CNTs are thoroughly mixed in the matrix. A realistic composition of CNTs in a randomly dispersed arrangement involves CNTs that may or may not be uniformly spaced

apart from each other, but will not form entangled agglomerates. However it may be possible for local bunching of a few CNTs ($< 10\,\mathrm{CNT}$) to take place. Entangled agglomerates are modeled as dense spheres of CNTs ($> 100\,\mathrm{CNT}$) as they are generally observed under transmission electron microscopy images (J. Li et al. 2007). The CNTs are randomly generated, by assigning a coordinate $(x_i, y_i, z_i)^j$, to each vertex, where i denotes the vertex number and j denotes the CNT. The vertices of the CNTs are calculated using the transformation formula:

$$\begin{aligned} x_1^j &= L_{\mathrm{CNT}}\sqrt{1-\phi^2}\cos(\theta) \\ y_1^j &= L_{\mathrm{CNT}}\sqrt{1-\phi^2}\sin(\theta) \\ z_1^j &= L_{\mathrm{CNT}}\phi \end{aligned} \tag{4.1}$$

where $(x_i, y_i, z_i)^j$ are the coordinates of the vertices of the CNT in the global coordinate system of the FE model, $\theta = 2\pi\alpha$, $\phi = 2\alpha - 1$ and α is randomly generated with a value between 0 and 1. L_{CNT} is the length of a CNT segment. The agglomerated CNT arrangement is generated by constraining the first vertex of the CNT such that it remains inside a sphere with the radius equal to the agglomerate radius, r_{agg}. The agglomerate radius is chosen to be one fourth of the RUC dimensions in this work, to include as much of a far field effect as possible, while maintaining computational economy. The first vertex of the CNT in the entangled agglomerate arrangement can then be calculated using:

$$\begin{aligned} x_1^j &= r_{\mathrm{agg}}\cos(\theta)\sin(\cos^{-1}(\phi)) \\ y_1^j &= r_{\mathrm{agg}}\sin(\theta)\sin(\cos^{-1}(\phi)) \\ z_1^j &= r_{\mathrm{agg}}\cos(\cos^{-1}(\phi)) \end{aligned} \tag{4.2}$$

The remaining vertices of the CNT are calculated using the random vertex generation formula described by equation 4.1. Unlike the agglomeration case, all the vertices in the randomly dispersed arrangement are generated using equation 4.1.

Figure 4.1 shows a schematic of the CNT generation algorithm. The schematic contains 3 segments and four vertices for illustrative purposes, however, the generated CNT geometries contain

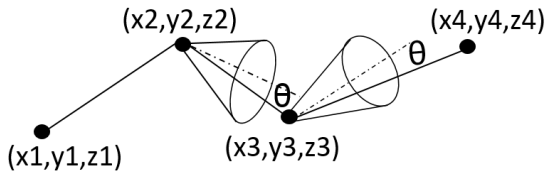

Figure 4.1. Schematic of the CNT generation algorithm

Table 4.1. Table of CNT Properties

CNT Length	0.5 μm
CNT Dia	9 nm
Type	Single Walled
Elastic Modulus	475 GPa
Poisson's ratio	.35

7 segments with 8 vertices per CNT, along with 3D waviness. This vertex generation algorithm is used to calculate the vertices for 2000 CNTs leading to a total of 16000 vertex points per FE model of the micro RUC. The randomized transformation formula imparts waviness to the CNTs, thus creating realistic CNT geometries rather than perfectly straight idealized CNT geometries. In fact the waviness, radius, length and material properties of the CNTs can be controlled to model either fully stochastic CNT systems or ordered ideal CNT arrangements. The number of CNTs in a model remains constant at 2000. The unit cell dimensions are varied in order to alter the weight fraction of the CNTs in the micro RUC. The material properties and dimensions of the CNTs are obtained from Romanov et al. (V. S. Romanov et al. 2015) and are reported in Table 4.1. The generated models for the randomly dispersed CNT arrangement and the agglomerated CNT arrangement, can be seen in Figures 4.2a and 4.2b respectively. Three dimensional truss elements are used to model the CNTs with 8 nodes per CNT, since the nanotubes only provide structural reinforcement in the matrix, and also since investigating the stress variation through the CNTs is not of interest in this study.

The nanocomposite model, generated using the algorithm described above, is irregular and difficult to mesh using conventional techniques. Hence, the approach of embedded elements is

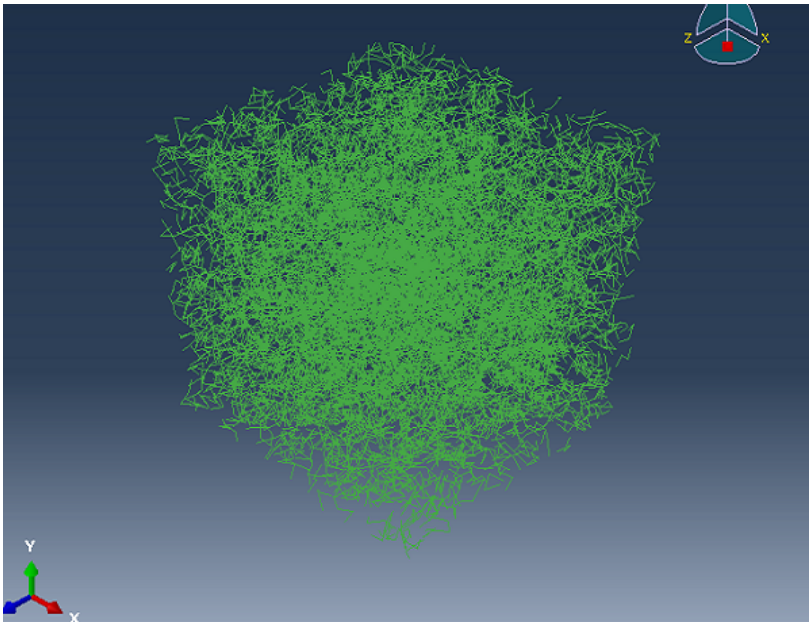

(a) Randomly dispersed CNT arrangement

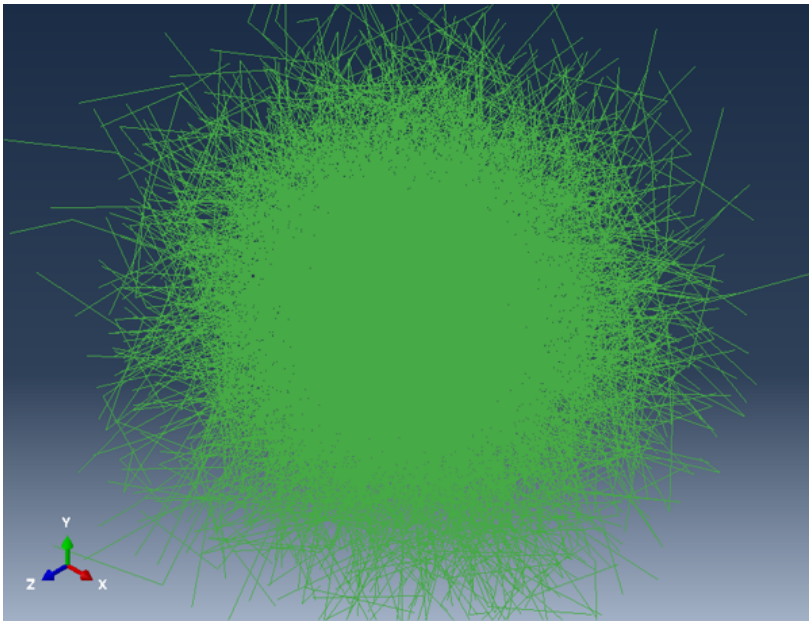

(b) Entangled agglomerate CNT arrangement

Figure 4.2. CNT Mesh

used to achieve the meshing required in this case (Dolbow and Harari 2009). The embedded element technique allows the constraining of the nodal translational degrees of freedom of a group

of elements that lie embedded in a group of host elements. In this technique, the embedded nodal degrees of freedom are appropriately interpolated from the values of the nodal degrees of freedom of the host elements (ABAQUS 2013).

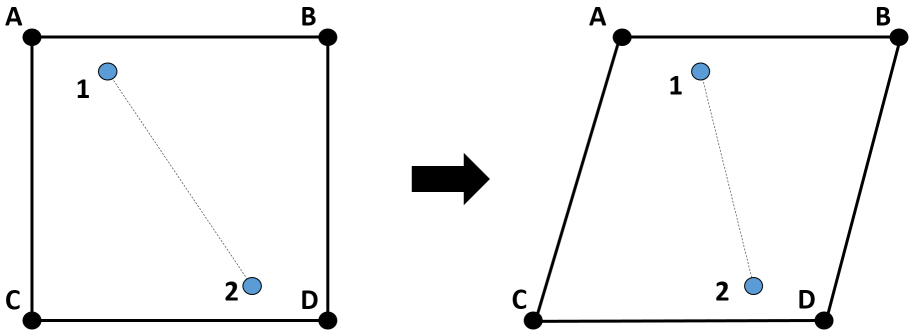

Figure 4.3. Schematic of the embedded element technique

A schematic of the embedded technique is displayed in Figure 4.3. In this schematic, the host element is made of nodes A-B-C-D and nodes 1-2 belong to the embedded element. The displacement of node 1 is calculated by appropriate weight factors determined based on the geometric location of node 1 in the host element and hence, is mainly influenced by the displacements of nodes A-B. Similarly, node 2 displacement is mainly influenced by the displacements of nodes C-D. Consequentially, the displacement field of the host element is influenced by the presence of the embedded element and its stiffness properties. The embedded element displacements are therefore obtained without the need for intermediate nodes, as would be the case in a conventionally meshed model. In the general case, assuming two bodies B^1 and B^2 subjected to finite deformation, such that B^1 is entirely embedded within B^2, their movements will be coincidental at their interface. This automatically assumes displacement and traction continuity through the shared boundary. Then the embedded technique is used to find a kinematic coupling operator R such that:

$$R \cdot u_{\partial B^1} = u_{\partial B^2} \tag{4.3}$$

$$R = F(\rho_{B^1}, C_{B^1}, \rho_{B^2}, C_{B^2}) \tag{4.4}$$

where C_{B^*} is the elastic tensor of the materials B^*, ρ_{B^*} is the density of the material B^*, and $u_{\partial B^*}$ is the boundary displacements of the material B^*.

The method of embedded elements has been utilized and thoroughly benchmarked for the simulation of CNTs in polymer by Romanov et al. (V. Romanov et al. 2013; V. S. Romanov et al. 2015). A simple demonstration of the method can be performed for a single CNT in an infinite polymer matrix modeled using the embedded element method. The stresses from this model can be compared with the analytical solution for a slender cylindrical reinforcement in infinite matrix as formulated by the Cox equation (Lacroix et al. 1992). According to this equation the axial stress along the cylindrical reinforcement is given by:

$$\sigma_r = E_r \epsilon \left[1 - \frac{cosh\left(\frac{2nx}{d}\right)}{cosh(ns)} \right] \tag{4.5}$$

where σ_r is the axial stresses in the reinforcement, E_r is the Young's modulus in the axial direction of the reinforcement, and d is the diameter of the reinforcement. The comparison of the stress measures obtained from the analytical solution of the Cox's equation, and the embedded mesh numerical solution is shown in Figure 4.4. Good comparison with the analytical solution indicates applicability of the embedded mesh method for the analysis of nanocomposites with randomized CNTs in a polymer matrix.

The polymer model is generated using 5000 elements of 8-noded 3-D solid C3D8 brick element, and used as the host mesh within which, the CNT elements are embedded. The translational degrees of freedom of the embedded elements are constrained to the response of the polymer mesh. This technique provides a computationally efficient means of generating a complicated nanocomposite model while minimizing the total degrees of freedom. Furthermore, periodic boundary conditions are applied to the edges of the nanocomposite model to simulate the periodic behavior of the RUC according to equation 2.10

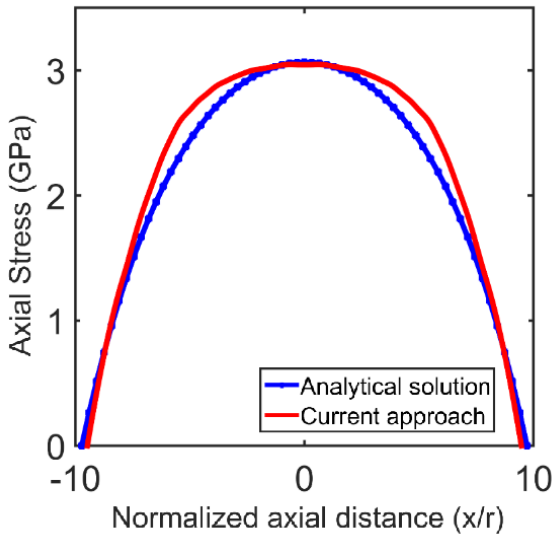

Figure 4.4. Comparison of analytical and embedded mesh solutions of axial stresses in CNT within infinite matrix

4.3 Modeling of Piezoresistivity

Recently, there has been an increased interest in developing computational techniques for the mechanical and multifunctional analysis of CNT nanocomposites. This interest as been mainly driven by recent successes in demonstrating nanocomposites as embedded strain sensors for *in-situ* real time strain and damage sensing (Hu et al. 2010; Kang et al. 2006; Datta et al. 2015). Such a sensing system can lead to the development of self-sensing smart structures that can be inspected remotely in real time for structural integrity in methodologies such as Structural Health Monitoring (Neerukatti et al. 2014). However, to develop such a system it is of foremost importance to understand the mechanism of piezoresistivity in CNT nanocomposites. Much experimental work has been conducted to study the electro-mechanical properties of CNT nanocomposites. It has been experimentally proven that a minimum amount of volume fraction of CNTs, known as percolation, is required to form conductive paths leading to significant electrical effects (Meincke et al. 2004). Furthermore, it has also been shown that the piezoresistivity is nonlinear at higher ap-

plied strains (Hu et al. 2010) and under damage (Datta et al. 2015) and in these works one of the major contributors to the nonlinearity was hypothesized to be the tunneling effect. Ultrasonic tests of failed CNT nanocomposites have shown CNT pullouts leading to the hypothesis that the inherent piezoresistivity of the CNTs should not be a major piezoresistive mechanism due to low load transfer to the CNTs after pullout (Hu et al. 2011). However, a methodical scrutiny of these mechanisms can only be practically performed through studying multiscale models that can recreate the electro-mechanical coupling under damage.

The piezoresistivity of CNT nanocomposites is mainly driven by two primary mechanisms: (i) inherent CNT piezoresistivity (Kang et al. 2006; Dharap et al. 2004; Zhang, Suhr, and Koratkar 2006), and (ii) the electron tunneling effect (Park, Kim, and Youngblood 2008; Hu, Karube, Yan, et al. 2008; Wichmann et al. 2009; Hu et al. 2010). Electron tunneling is a quantum mechanical effect which leads to the creation of a tunneling current path between a barrier that violates classical mechanics. This occurs due to the probabilistic wavelike properties of electrons that allows non-zero probabilities of an electron moving through an obstructing energy barrier. CNTs have been known to demonstrate electron tunneling effects (Gau, Kuo, and Ko 2009) especially when present as reinforcing filler materials within nanocomposites. The electron tunneling effect, which is a function of the distance between the CNTs, can be modeled using the Simmon's equation for tunneling resistance (Simmons 1963). This closed-form relation between neighboring CNT distance and the resistance between the nanotubes is based of the theory of electric tunnel effects for asymmetric junctions and provides a relationship for the electron flow between electrodes that are separated by a sufficiently thin insulating film. Using the Sommerfield model and the Wentzel–Kramers–Brillouin approximation, the approximate expression for the tunneling current density between an electrode-interface-electrode system is found to be:

$$J = J_0 \left\{ \lambda \, exp\left(-A_1\sqrt{\lambda}\right) - (\lambda + eV) \, exp\left(-A_1\sqrt{\lambda + eV}\right) \right\} \tag{4.6}$$

where J is the current density in the electrodes, h is the Planck's constant, e is the electron charge,

V is the voltage between the electrodes, d is the distance between the electrodes, m is the mass of the electron, λ is the height of the electrical tunneling barrier which is around 0.5 eV to 2.5 eV for epoxy (Hu et al. 2011) and where

$$J_0 = \frac{e}{2\pi h} \cdot \frac{1}{(\beta d)^2} \tag{4.7}$$

$$A_1 = \frac{4\pi\beta d}{h}\sqrt{2m} \tag{4.8}$$

$$\beta = 1 - \frac{1}{8\lambda^2 d}\int_{-\frac{d}{2}}^{\frac{d}{2}} \left[\lambda\left(x\right) - \lambda\right]^2 \, dx \tag{4.9}$$

In this case, it is assumed that the barrier is almost equal and the thickness of the interface is constant. The general equation 4.6 can be reduced for low voltages $V \approx 0$ such that:

$$J = \frac{e^2}{h^2 d}\left(\sqrt{2m\lambda}\right) V \exp\left(-\frac{4\pi d}{h}\sqrt{2m\lambda}\right) \tag{4.10}$$

Making use of the basic relations between current density, voltage, and resistance $J = \frac{I}{A}$ and $V = I \times R^{\text{tunnel}}$, the tunneling resistance is then found to be:

$$R^{\text{tunnel}} = \frac{h^2 d}{Ae^2\sqrt{2m\lambda}} exp\left(\frac{4\pi d}{h}\sqrt{2m\lambda}\right) \tag{4.11}$$

where R^{tunnel} is the tunneling resistance and A is the cross-sectional area of the tunnel. This equation can be modified for resistivity as:

$$\frac{\rho_1^{\text{tunnel}}}{\rho_0^{\text{tunnel}}} \approx exp\left\{\frac{4\pi\sqrt{2m\lambda}}{h} d_0 \left(\frac{d_1}{d_0} - 1\right)\right\} \tag{4.12}$$

where ρ^{tunnel} is the local electrical tunneling resistivity, d_0 is the distance between CNTs before straining, and d_1 is the distance between CNTs after straining. Since the local strain field can be used to calculate d_1 (Yasuoka, Shimamura, and Todoroki 2010), the damaged induced local strain field can hence, be used to measure the changes in tunneling resistivity. From this relationship, it can easily be seen that a nonlinear coupling between damage and strain will lead to nonlinearity in the evolution of tunneling resistivity under damage as well.

The second mechanism involved in piezoresistivity of CNT nanopolymers is the inherent piezoresistivity shown by individual CNTs. A single CNT is inherently piezoresistive, wherein an applied strain causes the carbon-carbon bond lengths to change, which in turn causes electrical property variations in the CNT. This mechanism can be modeled by coupling the CNT strain to the piezoresistivity of the CNTs (Ren and Seidel 2013) as:

$$\Delta \underset{\sim}{\boldsymbol{\rho}}^{CNT} = \underset{\approx}{\boldsymbol{G}} : \underset{\sim}{\boldsymbol{\epsilon}}^{CNT} \tag{4.13}$$

where $\underset{\approx}{\boldsymbol{G}}$ is a tensor of the piezoresistive strain coefficients. Approximate values for these coefficients were numerically calculated by Ren and Seidel (X. Ren et al. 2015). The effective piezoresistivity of the RUC is then obtained using ensemble averaging of the individual piezoresistivities from the two mechanisms.

4.4 Mechanical and Piezoresistive Response Under Damage

Microscale RUCs of the polymer matrix with periodic boundary conditions and embedded CNTs, generated using the CNT generation algorithm, are modeled and inserted into a bulk polymer model using the embedded mesh technique. The results of the microscale model with the nanopolymer RUC under quasi-static uniaxial tensile loading, are presented here. The model is simulated in the commercial FE Package ABAQUS with the damage equations implemented as a user material subroutine. The simulations are conducted under a constant strain rate of 0.005 strain per second to ensure quasi-static conditions.Unless otherwise mentioned, the measured stress is in the loading direction (σ_{11}). The local stress-strain response is obtained by measuring the local stress (σ^l_{11}) versus the local strain (ϵ^l_{11}). The global stress-strain response is obtained by ensemble averaging the stress (σ_{11}) and strain (ϵ_{11}) values for the whole model.

Figure 4.5 shows the comparison of damage contours between a model that contains neat epoxy and a model containing CNTs in an epoxy polymer. The neat polymer model shows con-

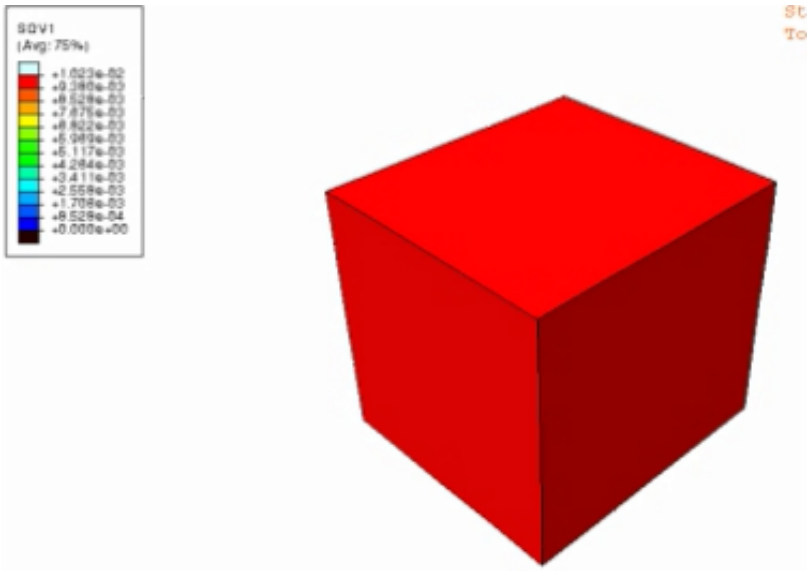

(a) Isotropic damage contour with no CNTs

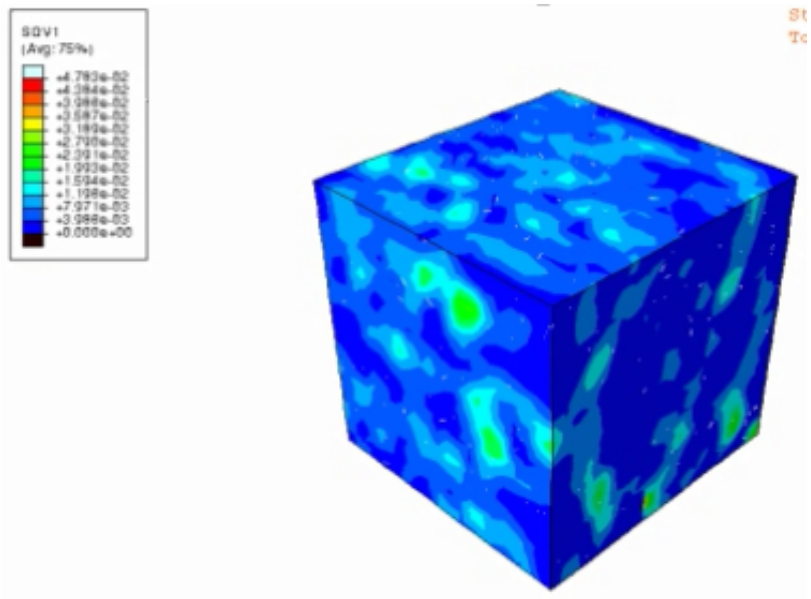

(b) Local damage contours due to presence of CNTs

Figure 4.5. Anisotropy in damage due to heterogeneity

stant damage signifying a homogeneous isotropic damage profile, while the nanopolymer model shows localized damage. The sub-microscale damage concentration is caused due to the presence of CNTs which cause local damage, and which may lead to stochastic damage initiation sites, and

accelerated damage progression. The significance of the CNTs as damage initiators are studied further.

4.4.1 Localized Response and Averaged RUC Behavior

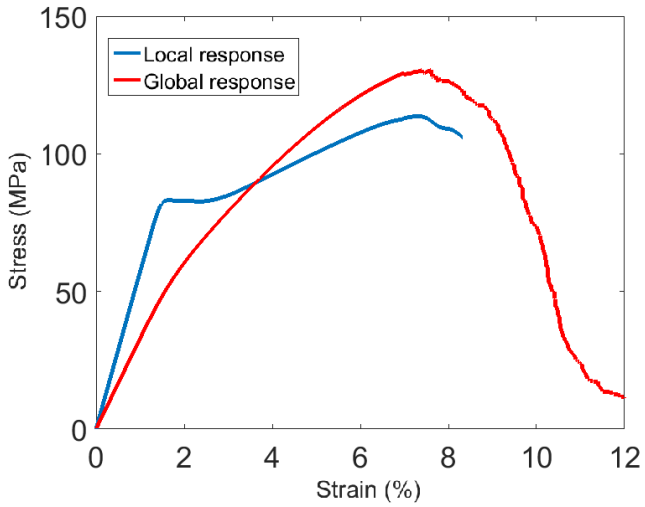

Figure 4.6. Global stress-strain response of the RUC compared with stress-strain response of local regions around the CNT

Figure 4.6 exhibits the global stress-strain response of a 1% weight fraction CNT-polymer RUC compared to the stress-strain response of a local region around a single CNT. As seen from Figure 4.6, the local stress-strain response in the vicinity of the CNTs exhibit an initial drop in stress followed by a recovery phase. The local response around the CNTs displays a similar trend as seen in molecular dynamics (MD) simulations of the CNT-polymer RUC as shown in Figure 3.1. However, it is observed that the global response of the RUC does not show the recovery phenomenon observed in the MD results. The inelastic response predicted by the continuum model in the vicinity of the CNT, and the response from the MD model, exhibit a highly localized behavior, while the global response displays a more spatially averaged response. This implies that

there is high spatial variation in the stress-strain response within the RUC and that, although the average response demonstrates isotropic behavior, locally the RUC displays highly anisotropic behavior.

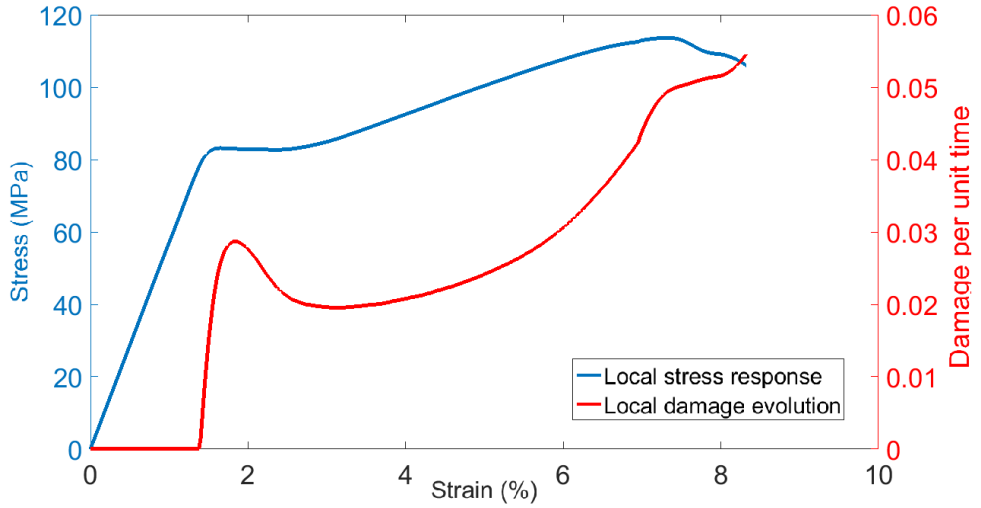

Figure 4.7. Damage evolution in the continuum model at local regions around the CNT compared with local stress-strain response

The characteristic stress-strain trend at local CNT-rich regions, labeled 'Local response' in Figure 4.6, can be explained from parallel discrete and continuum viewpoints. From a nanoscale perspective, the initial elastic region of the stress-strain curve indicates the stretching of bonds in the CNTs and the polymer chains due to mechanical deformation. The yield point followed by softening which leads to the first dip in the stress-strain curve as seen in Figure 3.1 corresponds to bond scission of the weaker covalent bonds. Subsequently, the polymer chains become taut and molecular chain sliding initiates, resulting in the hardening observed in the stress-strain curve previously referred to as the recovery phase. The final stress drop indicates successive bond dissociation in the molecular system resulting in failure. From the continuum perspective, the stress-strain response can be explained by the local damage evolution trend shown in Figure 4.7. The damage curve shows a peak that corresponds to the first drop in stress seen in the local stress-strain curve of Figure 4.6. After the initial peak, the damage rate decreases and then evolves at a controlled

rate. This explains the drop in stress at higher strains past the recovery phase seen in the local stress-strain curve. The high stiffness provided by the CNTs allow a large amount of the load to be carried locally by the CNTs until a point is reached where there is a separation between the CNT group and the polymer around it. This corresponds to the first peak in the damage evolution curve in Figure 4.7 and the corresponding dip in the local stress-strain curve seen in Figure 4.6. After the separation occurs, a more meaningful and natural load division occurs between the CNTs and the polymer, and further damage occurs as a normal progression of cracks in the flawed material. The post-load redistribution stage can be observed after the peak in the damage evolution curve. This similarity in the inelastic MD response and the local continuum response provides further indirect evidence that successful sub-microscale inelastic information transfer, between MD and FE simulation, for nanopolymers is possible using the atomistically informed damage methodology.

4.4.2 CNT Configuration Effects

The randomly dispersed CNT arrangement shown in Figure 4.2a can be scanned at the sub-microscale to make certain local patterns of CNTs apparent using virtual voxels. The voxels isolate a sub-volume of the nanocomposite material so that local CNT patterns can be discerned and studied apart from the larger mass that is shown in Figure 4.2a. Each voxel contains around 5-15 CNTs. Due to the random nature of the arrangement in Figure 4.2a, some of these voxels are denser than others. This simulates highly dispersed CNTs within an epoxy volume. The pattern of CNTs observed within these sub-volumes can then be reduced to three configurations.

A schematic of the three configurations is shown in Figure 4.8. Configuration 1 represents a sub-volume containing approximately uniformly dispersed CNTs, arranged symmetrically within the sub-volume. The CNTs do not bunch together and are approximately equally spaced apart. Configuration 2 represents a sub-volume that contains a relatively large amount of CNTs. These

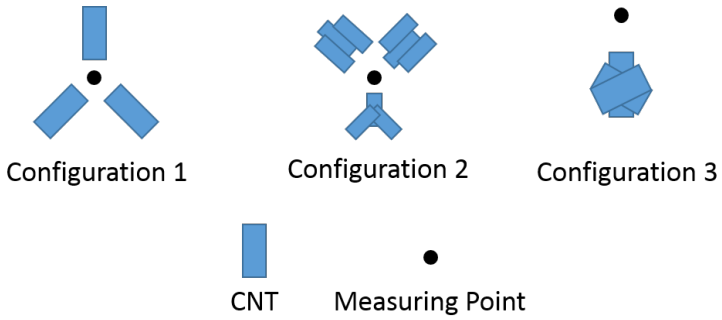

Figure 4.8. Schematic of the CNT configurations in the randomly dispersed CNT model

CNTs lie very close to each other forming local bunches. However, the CNTs are nearly symmetric with respect to each other within the sub-volume such that there is an even spatial variation in stiffness. Configuration 3 represents sub-volumes that are surrounded by a single bunch of CNTs asymmetrically present within the cubic sub-volume. This configuration exhibits a relatively large matrix rich area and an uneven spatial variation in stiffness within the sub-volume. It is important to note that the bunched CNTs referenced in this section do not represent agglomeration. In this case a bunch of CNTs contains a small number (< 10) while agglomerations contain a relatively larger number of CNTs (> 100). Additionally, a few other patterns were observed such as sub-volumes with zero CNTs, however, such sub-volumes were rare and not studied independently. Figure 4.9 exhibits representative images for each configuration from the model. The beam rendering option in ABAQUS was utilized to show the cylindrical geometry in these images.

Figure 4.10 shows the difference between the global loading direction stress-strain response of the microscale nanocomposite RUC and the local stress-strain response at the sub-microscale around the CNT nanofillers within the nanocomposite. The local response of the sub-volumes is the averaged response for similar configurations surveyed within the larger mass. It was observed that local configurations of the CNTs at the sub-microscale significantly affected the local stress-strain behavior and the damage characteristics. Configuration 1 exhibits the most delayed damage initiation and damage progression relative to the other configurations. The stress-strain response

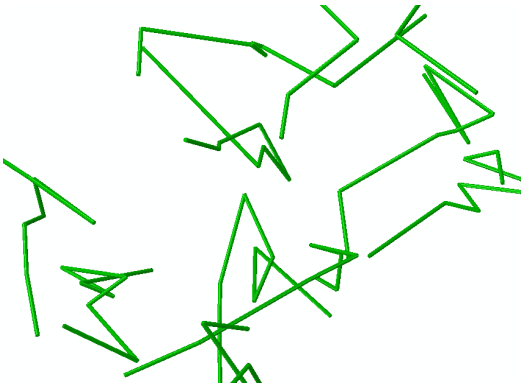

(a) Configuration 1

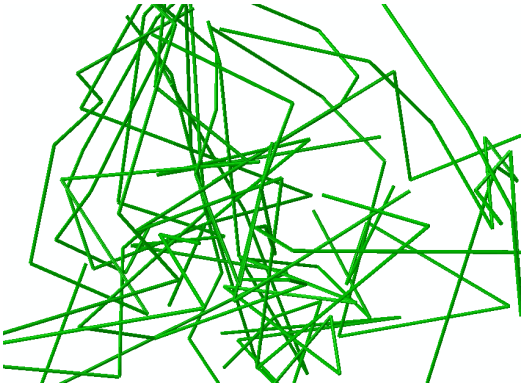

(b) Configuration 2

(c) Configuration 3

Figure 4.9. Representative CNT configurations images from the CNT model

of configuration 1 is similar to the response observed locally near a single CNT in a nanocomposite where the CNTs are ideally structured and spaced apart. This response also complements the previous assertion that the stress-strain response of a single CNT in a polymer network exhibits a

unique trend of an initial peak followed by softening, a recovery phase, and secondary softening up to failure. The unique stress-strain response displayed by configuration 1 is only possible due to the spacing and symmetric structure of this configuration. Furthermore, this also suggests that the MD simulation of a CNT polymer unit cell represents an ideally spaced CNT structure due to the periodic conditions applied at the edges of the MD unit cell.

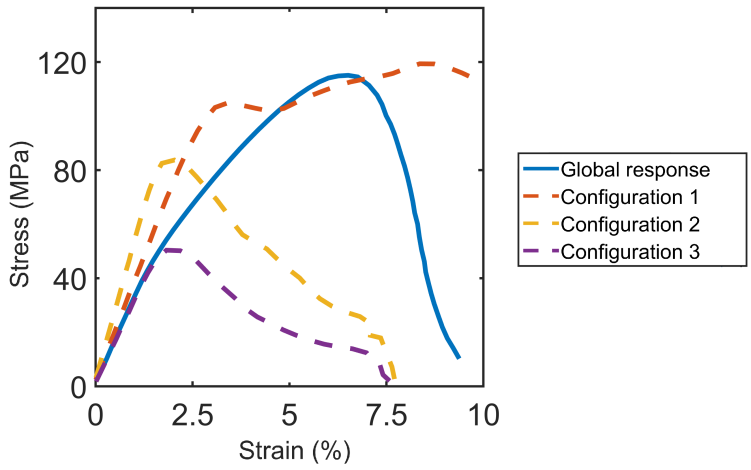

Figure 4.10. Stress-strain response for different configurations of CNTs

Configuration 2 shows early damage relative to configuration 1 and also displays faster damage evolution leading to accelerated local failure. This occurs due to the large stiffness differential between the CNT bunches and the surrounding matrix. However, configuration 2 shows relatively better load transfer compared to configuration 3, due to the proximity of neighboring CNTs and display better damage characteristics than configuration 3. Configuration 3 shows earliest damage initiation relative to the other configurations and rapid damage evolution due to the large stiffness differential between CNT-rich and CNT-free area. Configuration 3 contains a large matrix rich zone which causes the significant spatial stiffness differential and poor load transfer characteristics, since this configuration also lacks neighboring CNTs, leading to rapid damage escalation and local failure. The global microscale response can also be seen in Figure 4.10 which is the aggregate response of all the local configurations, including the representative ones presented in this

section. It is observed that the global response is markedly different compared to the various local responses due to the complex sub-microscale mechanics and interactions that influence the local response.

4.4.3 Agglomeration Effects

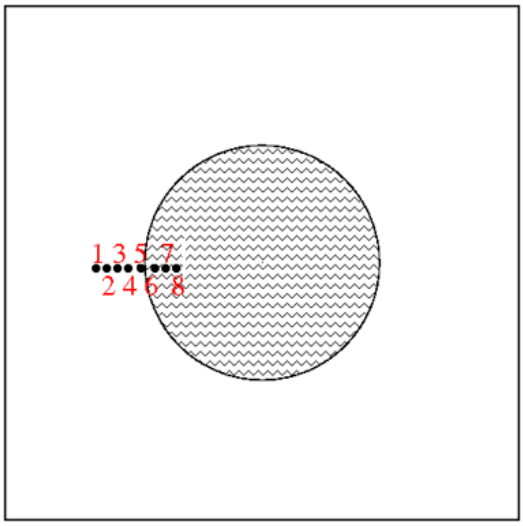

Figure 4.11. Chosen points about the agglomerate

The microscale nanocomposite model with entangled CNT agglomerate arrangement is tested in ABAQUS under the same conditions as the randomly dispersed CNT model. The stress variations in the matrix of the agglomerate nanocomposite model is studied. It is observed that the matrix within the agglomerate displays a stress free condition while the matrix surrounding the agglomerate is under high tensile stress. Since, the matrix is present throughout the agglomerate in this model, this would physically represent a state of high degree of wetting leading to high permeability of the polymer within the entangled CNT agglomerate.

In order to better understand the stress variation and damage progression in the matrix constituent around the agglomerate, a set of 8 points were chosen such that points 1-3 appear at the

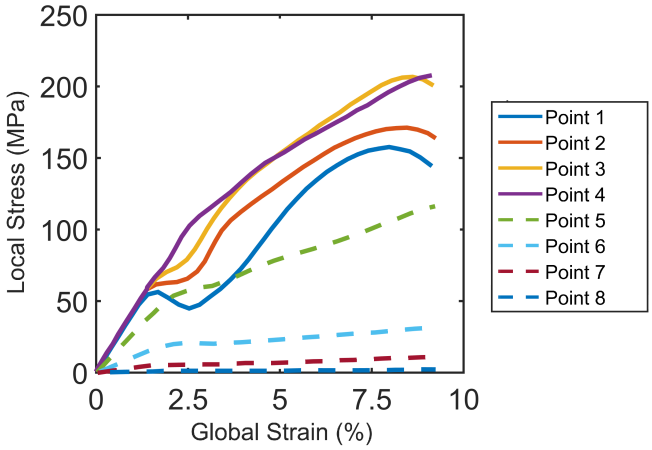

Figure 4.12. Stress at chosen points

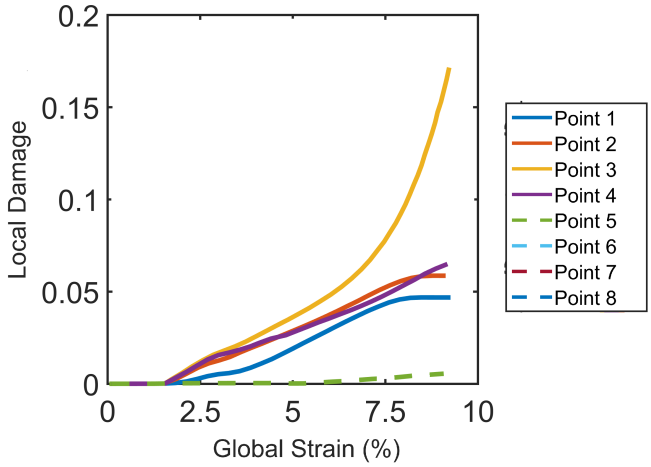

Figure 4.13. Damage at chosen points

immediate exterior of the agglomerate, points 4-5 appear at the interphase of the agglomerate and the matrix, and points 6-8 appear in the interior of the agglomerate. The chosen measuring points permits the study of the spatial transition of stress fields in the matrix from the exterior of the interphase to the interior. A schematic of the chosen points relative to the agglomerate is shown in Figure 4.11. The local stress response compared to the globally applied strain at each of the chosen measuring points is also recorded and exhibited in Figure 4.12. The stress is measured in the direction of loading and is local to the measuring point.

A transition in the stress field in the matrix is apparent with the zones exterior to the agglomerate exhibiting the unique stress-strain response discussed previously. The zone exterior to the agglomerate boundary contains loose strands of CNTs. These are the ends of the CNTs entangled within the agglomerate. At the sub-microscale these strands can represents equally spaced CNTs. The interphase zone (the agglomerate boundary) is relatively more CNT-dense than the agglomerate exterior and the stress field transitions in the matrix to a brittle-like nature in this zone. The stress field in the matrix inside the agglomerate is minimal or nonexistent due to the high concentration of CNTs in this region. The CNTs dominate the load transfer mechanism within the agglomerate and produces a stress free condition in the matrix. Figure 4.13 displays the damage in the matrix at each of the chosen measuring points and can be used to visualize the transition in damage evolution between the matrix at the agglomerate exterior and the interior. It is observed that maximum damage occurs at the interphase region between the matrix and the agglomerate. This damage profile indicates a separation of the polymer and the agglomerate surfaces leading to crack formation, concentrated around the interphase region. These microcracks lead to rapid damage propagation leading to global failure. Experimental work on CNT-epoxy systems have shown similar results, with CNT agglomerates acting as stress concentration and damage initiation sites (Zhou et al. 2008). Thus, entangled agglomerates in close contact could lead to interaction of the microcracks forming at this region and the consequent rapid failure of the overall system.

4.4.4 Variation with Weight Fraction of CNTs

The global failure stresses and strains with respect to change in weight fraction of CNTs is presented in Figure 4.14. The increase in weight fraction of CNTs causes increased brittle response with higher failure stress but lower failure strain. An increase in weight fraction of CNTs leads to

an increase in the amount of various sub-optimal sub-micro configuration of CNTs. Though the larger number of CNTs leads to higher global elastic properties, the randomness of orientation and larger sub-optimal sub-micro CNT configurations lead to an increase in 'hotspot' areas compared to lower CNT weight fraction material. These hotspot areas combine with larger differentials in internal stresses in the polymer to cause faster damage initiation and propagation in the material leading to lower failure strains for higher weight fraction of CNTs.

4.4.5 Variation of Piezoresistivity with Damage

As can be seen from Figure 4.15, considerable nonlinearity in piezoresistivity is observed once damage initiates in the nanocomposite. This is explained by the mechanics of the damage state, and their impact on the inherent and tunneling mechanisms of piezoresistivity. Since the first peak in damage evolution occurs due to the large difference in load distribution between the CNTs and the surrounding polymer, the separation of the polymer from the CNT surfaces leads to only slight local displacement between the CNTs. Locally the CNTs are not displaced at this stage and since the electron tunneling effect, as modeled by equation 4.12, depends on the distance between the CNTs, a large change in piezoresistivity is not observed. Further loading leads to a sustained evolution of damage which suggests damage propagation within the epoxy matrix leading to large local displacements around the CNTs. The considerable displacement introduced between CNTs contributes to a large increase in piezoresistivity. Similar responses have been observed in experimental studies of nanopolymer as strain sensors. Figure 4.17 shows the results of the resistance variation with respect to applied strain in a GFRP composite with embedded CNT nanopolymer (Datta et al. 2015). The resistance variation of the nanopolymer was studied explicitly using contact electrodes *in-situ*. The highly non-linear post-damage resistance change was clearly observed, as predicted by the coupled piezoresistive-damage model. Thus, the nonlinearities in piezoresis-

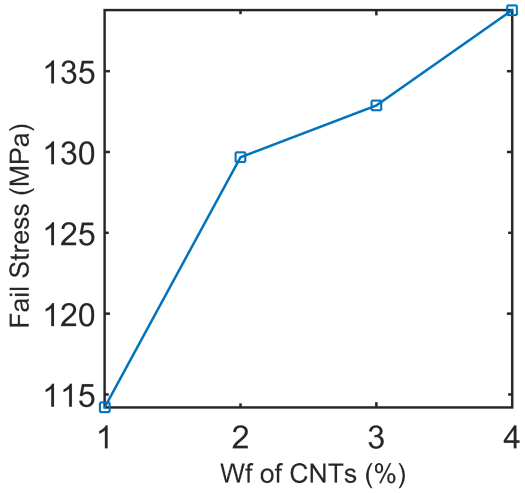

(a) Failure stress variation with weight fraction of CNTs

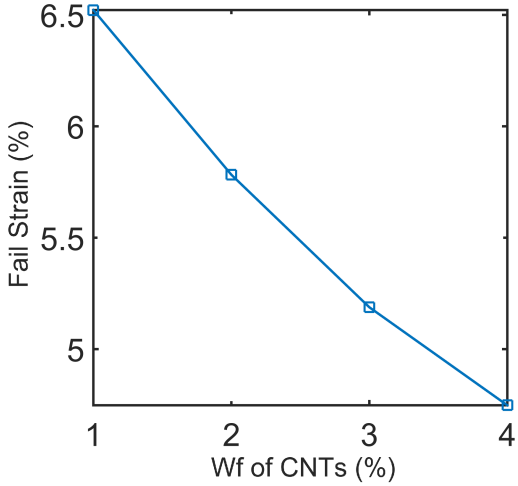

(b) Failure strain variation with weight fraction of CNTs

Figure 4.14. Variation of failure properties with weight fraction

tivity seen in these experimental studies can be attributed to the complex mechanism of damage initiation and propagation in nanocomposites.

To gain further insight into the phenomenon of piezoresistivity variations with damage, each of the two modeled piezoresistivity mechanisms, the inherent and tunneling resistivity, are studied separately as visualized in Figure 4.17. The low tunneling resistivity at low strains is attributed

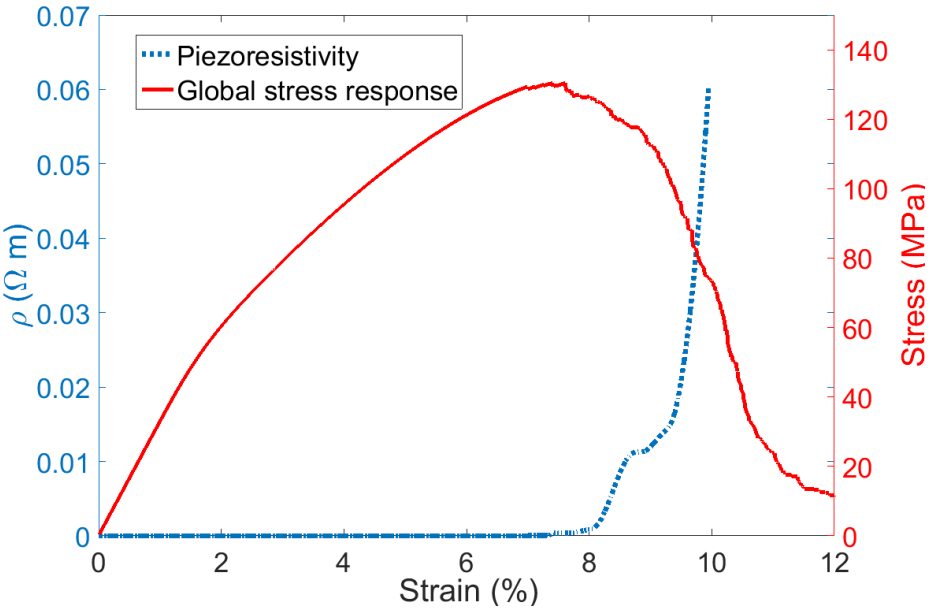

Figure 4.15. Variation of piezoresistivity under strain

to the saturated conductive paths formed by the randomly oriented CNTs and the low amount of displacement between the CNTs at low global strains. Hence, before substantial damage occurs in the nanocomposite, the change in piezoresistivity is driven by inherent piezoresistivity of the CNTs. Similar trends were also reported by Ren and Seidel for randomly oriented CNTs (X. Ren et al. 2015). However, after substantial damage occurs, the stresses on the CNTs decrease due to load redistribution which lowers the effects of the inherent piezoresistivity. Hence, material damage can cause a critical change in piezoresistive mechanisms within the nanocomposite. Moreover, the local displacements between the CNTs lead to loss of conductive paths which further increases the resistivity of the nanocomposite. Due to this reason, the inherent piezoresistivity mechanism becomes largely redundant at large global strains, while the tunneling effect dominates.

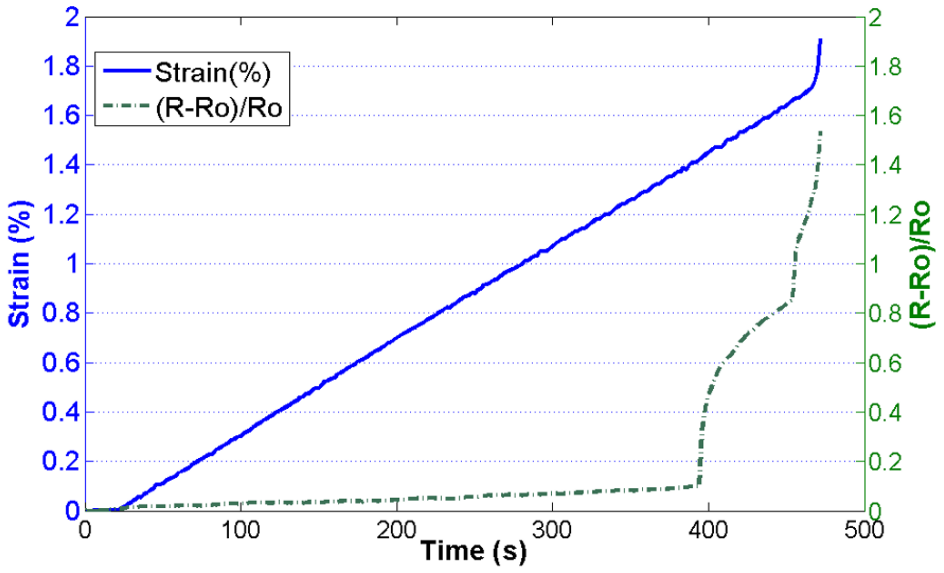

Figure 4.16. Resistance variation with strain in embedded nanopolymer sensor

Source: (Datta et al. 2015) reproduced with permission

4.5 Summary

This chapter demonstrated a framework for explicitly modeling CNT-epoxy nanocomposites containing atomistic information at the continuum scale. It was shown that using this framework, inelastic information transfer from MD to FE simulations can be performed in a relatively efficient manner for nanocomposites. Furthermore, use of this technique exhibited the complex local damage phenomenon that occurs at the sub-microscale in nanocomposites which may have critical consequences at the higher length scales. In particular, it was observed that the most desirable material response is obtained when the CNTs are spaced evenly apart from each other, however this is difficult to achieve in practice. The least desirable response occurs when small bunches of CNTs form asymmetrically in a matrix rich region. This phenomenon emphasizes the need to include local information in the study of CNT nanocomposites. This also highlights the need for effective CNT dispersion during the manufacturing of CNT nanocomposites. Furthermore,

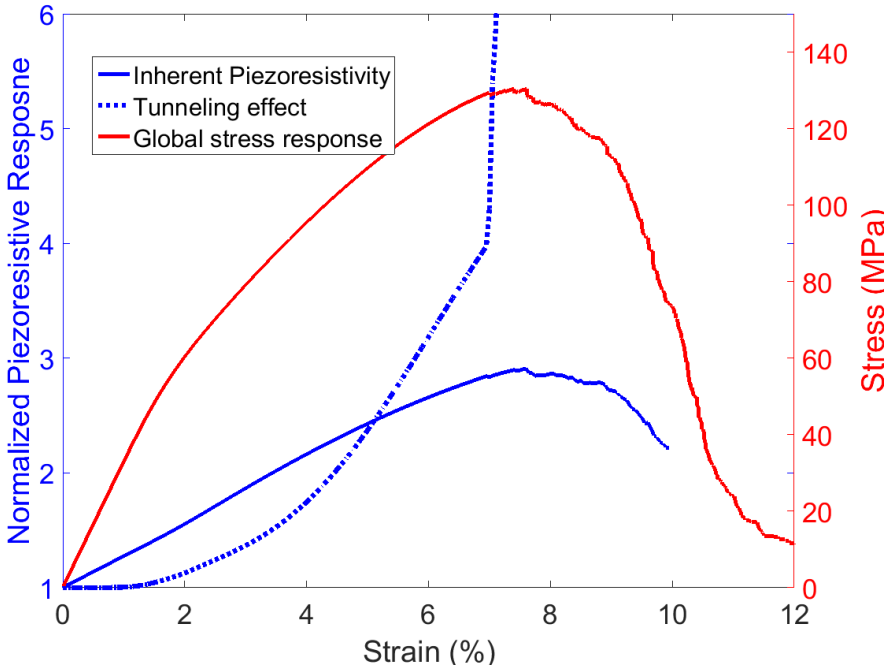

Figure 4.17. Piezoresistivity due to inherent and tunneling mechanisms

CNT agglomerates were seen to produce a stress-free region in the interior and cause a radial separation between the polymer and the agglomerate surfaces due to the large spatial variation in stiffness between the agglomerate and the polymer.

Additionally, damage was also linked to multifunctional effects of the nanopolymer and the intimate coupling of these two phenomenon was explicitly studied. A considerable change in piezoresistivity in nanocomposites was seen to be introduced due to damage; this is attributed to the local displacements introduced between the CNTs which hinders the electron tunneling phenomena. The driving mechanism for piezoresistivity in the CNT nanocomposites before damage appears to be the inherent piezoresistivity. After substantial damage occurs, the electron tunneling piezoresistivity increases and the inherent piezoresistivity decreases causing a switch in piezoresistive mechanisms. Such a simulation of local-global coupled multifunctional analysis at the submicroscale and microscale respectively, was previously not possible without a concurrent MD-FE

simulation which are highly resource intensive and possess limited potential. The next chapter introduces an additional micro fiber component to model and study non-linear effects in carbon fiber reinforced polymer (CFRP) composites and CNT enhanced CFRP composites.

Chapter 5

MULTIFIDELITY MODELING OF ADVANCED COMPOSITE MICROSTRUCTURES

5.1 Introduction

Carbon fiber composites reinforced with a polymer matrix containing carbon nanotubes (CNTs), have shown improvements in mechanical strength, interlaminar fracture resistance, energy absorption, and thermomechanical properties (Green et al. 2009; Inam et al. 2010; Cho, Daniel, and Dikin 2008) compared to traditional carbon fiber reinforced polymer (CFRP) composites. However, it has been observed that the nanocomposite properties do not scale linearly with size, with large disparities in microscale and structural scale properties, such as stiffness and failure strengths, that have been shown to exist (Sochi 2012). As discussed in Chapter 4, such discrepancies have sub-microscale origins, relating to carbon nanotube geometry, nanotube concentrations, and the mechanics of the polymer and nanofiller. To mitigate the foregoing drawbacks, advances in nanotechnology have been exploited to engineer novel CNT architectures such as nanoforests (Y. Zhang et al. 2006), which utilize appropriate substrates to grow highly aligned dense mats of CNTs, fuzzy fibers (Garcia, Hart, and Wardle 2008) that contain CNTs radially grown on the microfibers, and CNT ropes (Chou et al. 2010), which utilize ultra-long strands of CNTs as a replacement for microfibers. Particularly, the fuzzy fiber architecture has shown increased in-plane strength, interlaminar shear strength, and fracture properties (R. Li et al. 2015). However, the observed improvement in properties due to the addition of the CNTs is generally lower than the predicted theoretical values (Kundalwal and Kumar 2015a).

Possible causes for the discrepancies between experimental results and theoretical predictions

are the modeling approaches utilized for predicting material properties or behavior, which may not be appropriate for a complex heterogeneous material system such as the CNT/CFRP. As mentioned in Chapter 1, bulk analysis techniques and mean field micromechanical techniques do not consider the sub-microscale mechanics, leading to unreliable predictions. Additionally, conventional CFRP analyses with atomistic integration, which are performed by a combination of molecular dynamics (MD) simulations and averaging techniques such as elastic homogenization based micromechanics (Kundalwal and Kumar 2015b), statistical techniques such as Monte Carlo methods (Chui and Boyce 1999) or a fully continuum mechanics finite element (FE) approach (Fisher, Bradshaw, and Brinson 2002), cannot be applied for inelastic analyses, or are computationally inefficient for large systems. Hence, this chapter describes a novel multiscale framework wherein each constituent of the CNT/CFRP material system is explicitly modeled and assembled into a realistic microscale RUC using the FE method. The matrix constituent is modeled using a physical damage evolution law developed in Chapter 3. Since the CNTs are modeled explicitly, a thorough post-linear investigation of the interaction between the CNTs, matrix, and the microfiber constituent can be performed. Such a study can provide insight into the load transfer mechanism, and damage initiation and propagation phenomenon in randomly dispersed CNT nanocomposites and radially grown fuzzy fiber nanocomposites at the sub-micro and micro length scales. Additionally, a surrogate orthotropic material model, based on the Schapery potential theory (Schapery 1990), that reproduces the nanopolymer behavior, is also formulated. This material model can be calibrated with the response obtained from the high fidelity nanocomposite model and applied along with various microscale frameworks to replicate the global behavior of the high fidelity RUC, hence achieving a robust and computationally efficient method for performing multiscale studies that can be easily adopted for structural analysis.

5.2 Microscale High Fidelity Model

5.2.1 Constituent Models

To perform an accurate high fidelity analysis of the CNT embedded CFRP system, all three constituents of the CNT/CFRP nanocomposite, (i) microfiber (ii) polymer (iii) CNTs, need to be generated individually, and combined in a single RUC. Additionally, such a methodology would also require the inclusion of deterministic or stochastic geometric and material properties. Since, MD simulations of polymer curing yields a distribution of most likely crosslinking degree, and the associated relationship between the crosslinking degree and material properties, the FE polymer matrix model can be designed to incorporate this information. The FE model of the polymer constituent is divided spatially into multiple sections, with a stochastically assigned crosslinking degree in each section, sampled from the distributions obtained through MD simulations. This algorithm ensures stochastic spatial variation of material properties in polymer unit cells to represent non-uniform curing as discussed in section 2.3. The polymer matrix model, including the various subsections, is displayed in Figure 5.1a.

The microfibers are generated using the hard-core model to recreate experimentally observed carbon fiber composite microstructures (Borkowski, Liu, and Chattopadhyay 2013). The hard-core algorithm randomly perturbs perfectly ordered square packed circular fibers within the boundaries of the square RUC region until a microstructure resembling a random fiber pattern is achieved. The random perturbations are performed repeatedly in a brute force step-by-step manner and avoids fiber overlap by rejecting any step perturbation that causes interference. Hence, each fiber has an equal likelihood of residing at any location of the RUC as long as that location is devoid of other fibers. Periodicity of the RUC is maintained using continuity conditions enforced when the fiber passes over the RUC boundary. To ensure adequate resemblance with experimen-

tally obtained microstructures, statistical measures such as the Ripley's K-function and pair distribution function are utilized. The perturbation of the ordered microstructures are carried out until the statistical measure of randomness obtained from the simulated microstructure is equal to the measure obtained from microstructures of CFRP samples generated through microscopy studies. Figure 5.2 compares an experimental microstructure and the hard-core simulated microstructure.

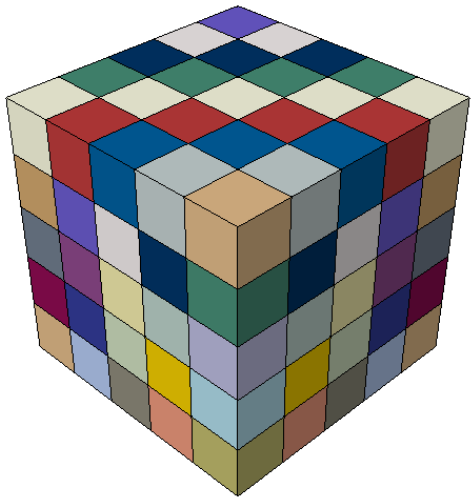

(a) Polymer model with spatial variation in material properties

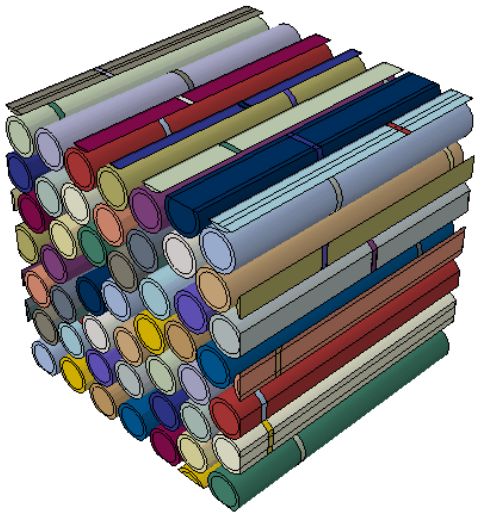

(b) Simulated fiber microstructure

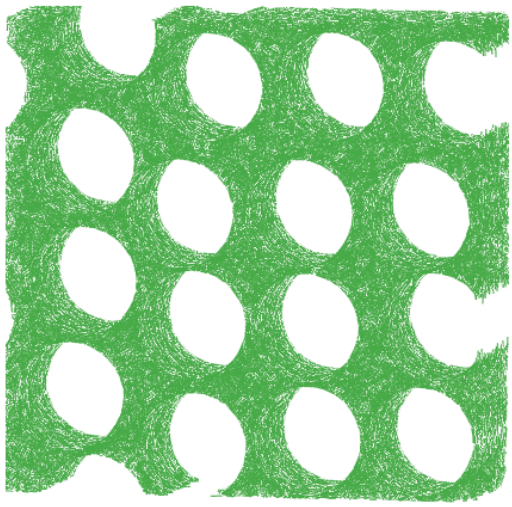

(c) Simulated randomly dispersed CNT architecture

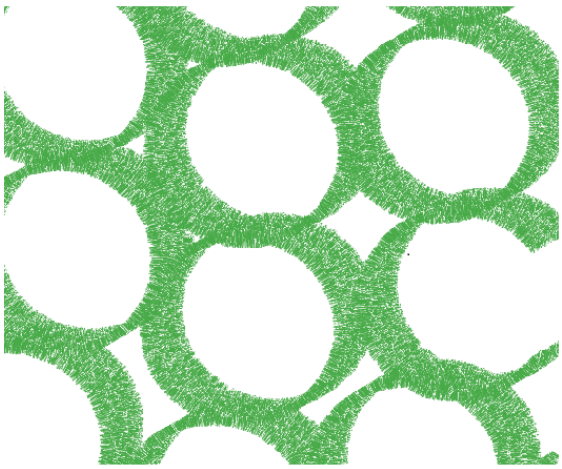

(d) Simulated radially grown CNT architecture

Figure 5.1. Microstructure constituents

Additionally, the material properties that are assigned to each fiber, are sampled from a Gaussian distribution to represent variation in fiber material. An example of the simulated FE microstructure used in the analysis can be seen in Figure 5.1b.

The CNTs can be generated using the transformation algorithm, as described in section 4.2. However, to generate consistent CNT architectures, the CNT vertices must be examined for vi-

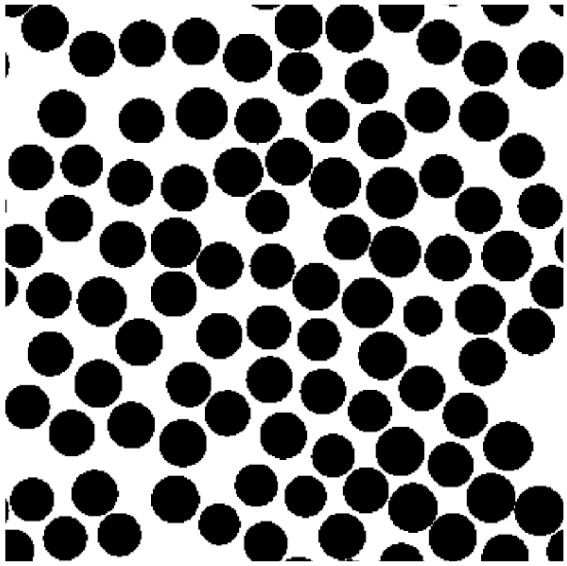

(a) Experimental microstructure

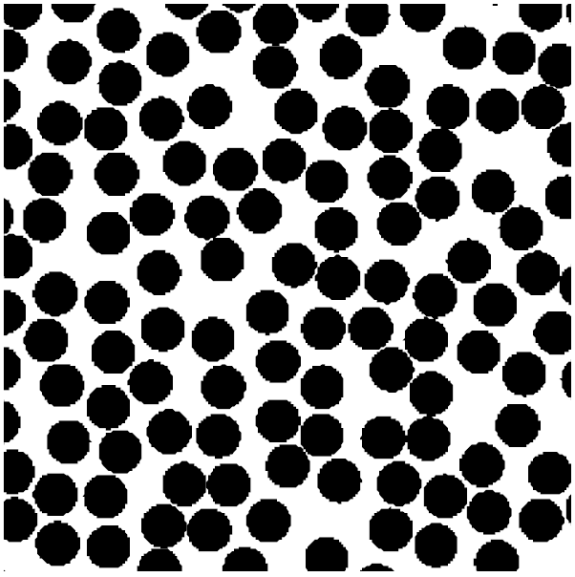

(b) Hard-core simulated microstructure

Figure 5.2. Comparison of experimental and computational microstructure

ability. Such as in the case of the randomly dispersed architecture, vertex coordinates x_i, y_i, z_i is rejected if it is occupied by a microfiber, or if it is outside the bounds of the RUC. In the case of the radially grown architecture, vertex x_1, y_1, z_1 for each CNT is constrained to remain on the circumference of the microfiber while the other vertices are restricted according to the same

constraints as the randomly dispersed architecture. Figures 5.1c and 5.1d show an example of the simulated randomly dispersed CNT architecture, and the fuzzy fiber CNT architecture. The material properties and dimensions of the CNTs are reported in Table 4.1. Three-dimensional truss elements with 8 nodes per CNT are chosen to model the nanotubes since the CNTs provide structural reinforcement in the matrix only and the stress variation through the CNTs is not of interest in this study.

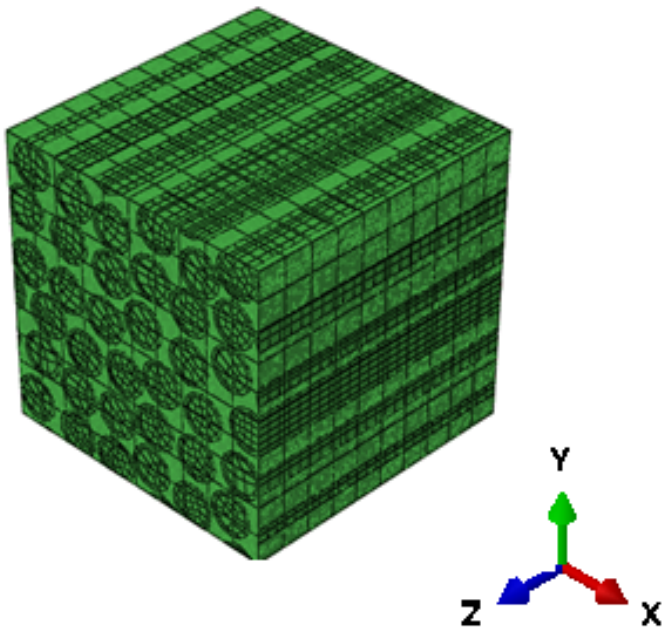

Figure 5.3. Final assembled model

To automate the task of creating and analyzing the nanocomposite model, a stand-alone module called the COmputational Nanocomposite ANalyzer (CONAN) is developed as a MATLAB graphical user interface. This module generates RUCs of nanocomposites or traditional composites using only the material properties and basic geometric properties of the constituents, which can be input as mean values for deterministic analyses, or as a distribution, for stochastic analyses.

Furthermore, the module provides the user with the options for generating realistic microstructures, or generating ordered ideal microstructures. The inputs required for CONAN are detailed here. For the generation of the microfiber, the mean radius of the fiber is required. Optionally, the standard deviation of the fiber radius can also be provided for generating microfibers with stochastic radii. Such information can be gathered from microstructures of the target fibers obtained using microscopy or from the manufacturer datasheets. Additionally, elastic properties of the fiber are required as an input and may be entered as a mean value or as a Gaussian distribution. Elastic properties of the fiber can be obtained from material datasheets or from single fiber tension tests. The fiber failure stress may be entered for simulating fiber breakage. The size of the representative unit cell (RUC) is controlled by entering the volume fraction of the fiber, and the required number of fibers that need to be generated, with a minimum of one and recommended maximum of one hundred. The CNT submodule requires the elastic properties, the weight fraction in percentage and certain geometric properties. The length, waviness and diameter of the CNTs may be controlled appropriately to simulate long tubes, short tubes, wavy tubes and straight tubes. Additionally, the user may choose the configuration of the CNTs, which are randomly dispersed or radially grown around the microfibers. CNTs as fiber coating may be simulated by using a combination of a radially grown arrangement with high waviness (V. S. Romanov et al. 2015). The module generates Python scripts, using the input data, which is further used to create the corresponding FE models in the commercial FE software ABAQUS. Several loading conditions such as tension in the fiber direction, tension in the transverse direction, in-plane shear and transverse shear may be simulated. The module also applies periodic boundary conditions, iteratively meshes the system to ensure minimum degree of freedom, applies the embedded mesh conditions as detailed in section 4.2, and runs the FE jobs automatically. The user may also change solver parameters such as the time increments, total step time, and size of output files. Figure 5.3 shows the final assembled model. The module can also be used to post-process the FE model internally which au-

tomatically reports the overall stress-strain data, maximum stress, modulus of the unit cell for the corresponding loading direction, and damage contours at certain loading points, along with plots for data visualization. Additionally, the module is self-contained and only requires the ABAQUS solver and MATLAB libraries.

5.2.2 Microstructure Analysis

As a case study for microstructure analysis, the microscale RUCs with random and radially grown CNT architectures and 0.1% weight fraction of CNTs are generated using the high fidelity model generation algorithm detailed above. These RUCs are loaded transverse to the fiber, corresponding to the positive x-axis in Figure 5.3, under quasi-static conditions up to complete failure or untill the end of the simulation.

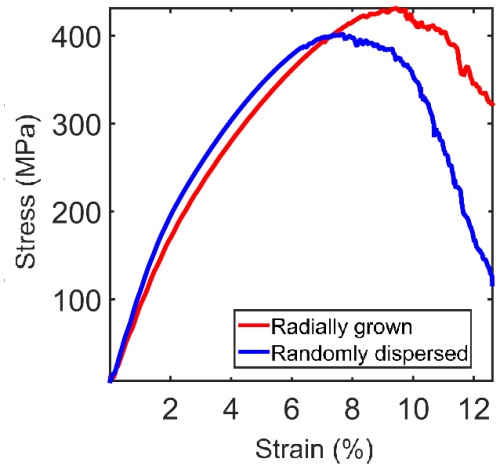

Figure 5.4. Comparison of stress-strain response

Figure 5.4 compares the stress-strain response of the CNT/CFRP models with radially grown and randomly dispersed CNT architectures respectively. It is seen that the randomly dispersed CNT architecture displays slightly higher stiffness compared to the radially grown architecture.

However, the radially grown architecture shows delayed damage initiation and slower propagation of damage compared to the randomly dispersed configuration. This observation is consistent with existing experimental literature (Wicks et al. 2014), where radially grown CNTs displayed better fracture properties than randomly dispersed CNT nanocomposites and traditional composites. An attempt to understand this phenomenon is undertaken by investigating the damage trends, local stress hot spots, and the sub-microscale stress state at the interacting region between the CNT and the matrix.

Figure 5.5 depicts the progression of damage in the polymer and the state of stress in the nanotubes in a nanocomposite model with randomly dispersed CNTs at various stages of loading. Figures 5.5b, 5.5d, and 5.5f illustrate the axial stress state of the CNTs, where the blue end of the spectrum shows zero stress conditions and red colors of the spectrum shows tension. All negative stresses are visualized in black color; hence all CNTs visualized as black are in compression. Since the maximum compression stresses are significantly lower than maximum tensile stresses, all negative stresses are chosen to be visualized as black for clarity. The stress state is measured along the axial direction of the tube in the corresponding CNT local coordinate system, which allows the visualization of the local stress state of each CNT under a global transverse load. Figure 5.5b shows that at strains below the elastic limit, local regions that are relatively matrix rich display higher local stresses corresponding to stress concentration zones. Furthermore, since they are randomly oriented, the CNTs that are most favorably oriented in the loading direction carry the highest load; yet, note that the majority of the CNTs are loaded and activated, leading to an almost uniform stress distribution among the CNTs with stress gradients occurring in matrix rich zones. Additionally, some CNTs are also noted to be in compression due to the Poisson's effect during extension.

The contours displayed in Figure 5.5a, 5.5c and 5.5e, depict the damage state in the matrix, with blue representing zero damage and red indicating completely damaged/failed elements. Fig-

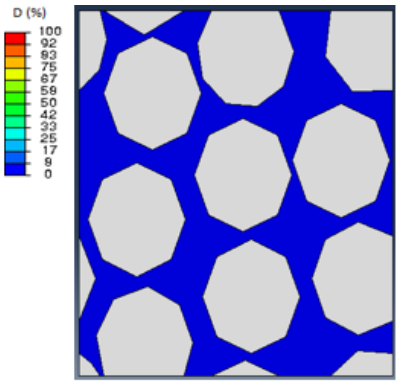

(a) Polymer damage state at 0.5% strain

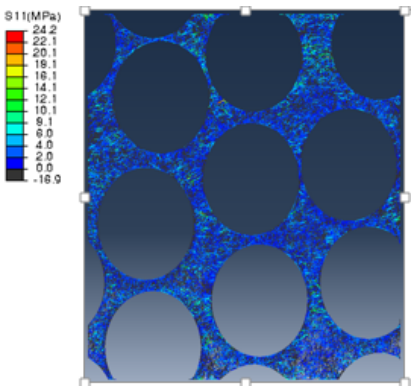

(b) CNT stress state at 0.5% strain

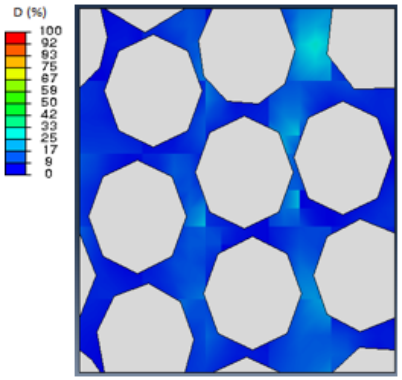

(c) Polymer damage state at 7% strain

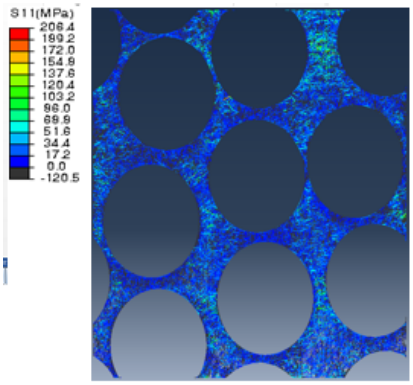

(d) CNT stress state at 7% strain

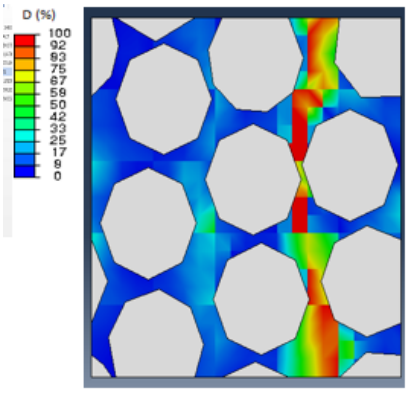

(e) Polymer damage state at 12% strain

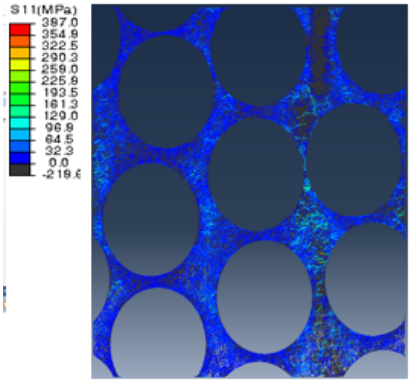

(f) CNT stress state at 12% strain

Figure 5.5. Randomly dispersed CNT architecture under loading

ure 5.5c describes the beginning of damage in the structure, initiating at the local stress concentration zones. The authors have previously demonstrated that local volume concentration difference

between the CNTs and surrounding matrix in nanopolymer can lead to local stress concentration zones, which accelerates damage progression due to the stiffness difference between the CNT and the polymer matrix (Rai et al. 2017). A similar phenomenon is observed in the current model of the nanocomposite, with stress concentration regions occurring at matrix rich zones that contain relatively large volume concentration gradients of CNTs. Figure 5.5e shows the final damage state of the nanocomposite wherein failure is caused due to matrix cracks. It can be inferred from Figure 5.5f that the matrix cracks lead to CNT pullout in the cracked region. Additionally, the stress state in the CNTs around the crack zone is reduced due to energy dissipation. The CNT pullout also leads to further increase in volume concentration gradients of CNTs, which subsequently leads to further acceleration of the rate of damage. Hence, the randomly dispersed CNT architecture does not take advantage of the unique mechanical properties of the CNTs, thereby leading to a rapid decay of the material after damage saturation.

Figure 5.6 illustrates the progression of damage in the polymer and the state of stress in the CNTs in a nanocomposite model with radially grown CNTs at various stages of loading. Figure 5.6b depicts the state of stress in the CNTs within the elastic limit. It is observed that fewer CNTs are activated due to the directionality effects; however, the activated CNTs are under higher stresses than in the randomly dispersed architecture. The CNTs transverse to the loading direction are under high compression stresses due to the Poisson's effect. The high stresses on the activated CNTs may lead to failure or buckling of the CNTs. In contrast, the CNTs in the randomly dispersed architecture are relatively less susceptible to failure, since more CNTs contribute to the load sharing process and thus, the average stress on each CNT is lower. Hence, the quality of CNTs play a significantly larger role in the radially grown architecture. It is also observed that regions that display the largest changes in volume concentration of CNTs lead to stress concentration zones. Regions with thin volumes of matrix between the microfibers, surrounded by CNTs, show significant stress concentrations. Figure 5.6c demonstrates that the damage initiates and

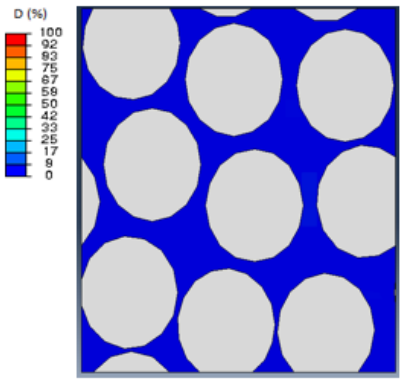

(a) Polymer damage state at 5% final strain

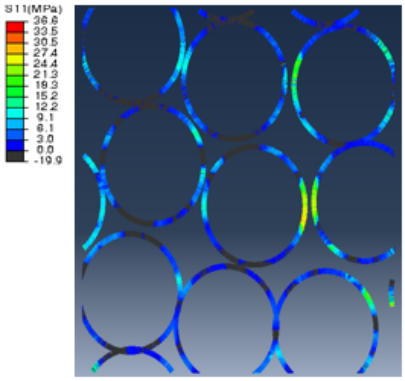

(b) CNT stress state at 5% strain

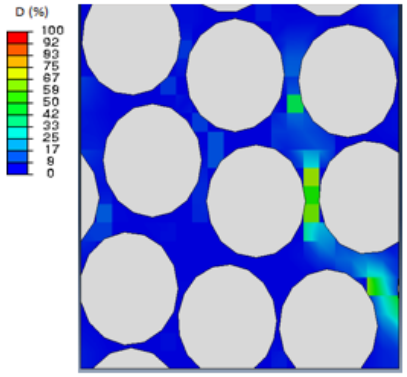

(c) Polymer damage state at 60% final strain

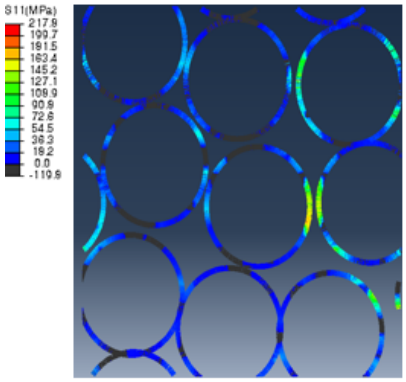

(d) CNT stress state at 60% final strain

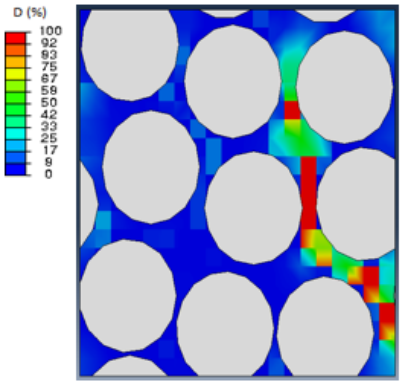

(e) Polymer damage state at 99% final strain

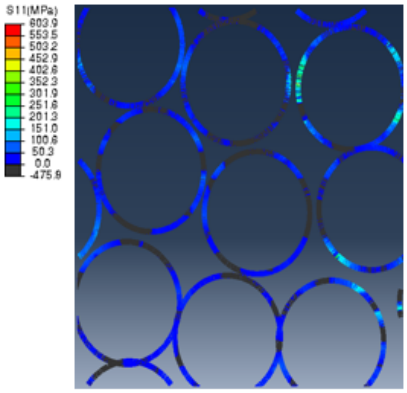

(f) CNT stress state at 99% final strain

Figure 5.6. Radially grown CNT architecture under loading

propagates around these stress concentration zones. However, Figure 5.6d shows that the CNTs surrounding the damage path continue to be loaded even after significant polymer damage. This is indicative of CNT bridging, which is possible due to the directionality of the CNTs in the radially grown architecture. CNT bridging slows the crack growth rate in the nanocomposite, thus changing the damage profile compared to the randomly dispersed architecture. Figure 5.6e shows the damage state of the nanocomposite near failure. Like the randomly dispersed architecture, the nanocomposite fails due to matrix cracks; however, it is observed that the damaged regions are strictly contained around the CNTs corresponding to the stress concentration zones. Unlike the radially grown architecture, the randomly dispersed architecture displayed significant volumetric damage. The radially grown architecture displayed a concentrated damage area around the circumference of the microfibers. This damage mechanism leads to the conclusion that the cracks originate around the CNT matrix interphase zones, which is supported by previous research (Subramanian et al. 2015; Rai et al. 2017; Rai, Subramanian, and Chattopadhyay 2017). Hence, the architecture of the CNTs can be used to control the directionality of originating damage and its progression. Figure 5.6f also shows that the CNTs around the crack path are deactivated and in a stress-free condition, indicating CNT pullout.

5.3 Orthotropic Surrogate Model

The high fidelity model of the CNT/CFRP material system described in the previous section provides a direct numerical simulation (DNS) of the nanocomposite and hence allows for a thorough study of local interactions between the three main constituents at the micro and submicroscale. Such studies are important to realize microstructure kinetics and kinematics which assists in material development studies and fundamental understanding of the mechanics of heterogeneous media. However, performing multiscale studies which involve macroscale elements,

concurrently with high fidelity models of the microscale at each FE integration point, can be computationally prohibitive. Since an efficient multiscale structural analysis would require only the RUC response at the microscale, without the local sub-microscale information, it is advantageous to reproduce the global microscale RUC behavior without running the high fidelity DNS. Hence, a low fidelity orthotropic damage model based on the Schapery potential theory is developed in this section, which can be calibrated with the DNS of the polymer or the CNT-polymer mixture applied in a conventional micromechanics techniques, to rapidly evaluate the microscale RUC response of the composite or nanocomposite material.

The progressive damage theory is based on the work potential model (Schapery 1990) which considers the total strain energy U to be the sum of the elastic strain energy density W_e and dissipated strain energy density W_d such that:

$$U = W_e + W_d \tag{5.1}$$

The dissipated strain energy, W_d describes the material or geometric irreversible processes occurring at the micro or nanoscale that causes nonlinearity in the material response. W_d can be described using a set of i internal state variables S_i, that can account for all the irreversible processes occurring within the system. The thermodynamic force F_i responsible for producing these structural changes due to ISV S_i can be obtained by measuring the gradient of W_d due to the change in ISV S_i.

$$F_i = \frac{\partial W_d}{\partial S_i} \tag{5.2}$$

Additionally, it should also be noted that the second law of thermodynamics does not permit healing of the material and by definition an irreversible process cannot be reversed. Using the second law of thermodynamics, the following inequality is established (Rice 1971):

$$F_i \dot{S}_i \geqslant 0 \tag{5.3}$$

For isotropic materials accounting for a single damage source, such as polymer matrix micro-damage, the dissipated strain energy can be represented using a single ISV, $S_{i=1} = S$ (Pineda et al. 2009). However, damage in orthotropic material systems can be directionally dependent and hence, will require a separate ISV for each strain element $\epsilon_{11}, \epsilon_{22}, \epsilon_{33}, \epsilon_{12}, \epsilon_{23}, \epsilon_{31}$. The dissipated strain energy can then be expressed as:

$$W_d = \sum_{i=1}^{i=6} S_i \tag{5.4}$$

$$S_i = \delta_i s_i \tag{5.5}$$

where s_i is a state variable that will be defined explicitly and δ_i is an activation function which is used to activate the appropriate ISV at the existence of strain in that direction. It can be expressed as:

$$\begin{aligned}
\delta_1 &= \begin{cases} 1 & \text{when } |\epsilon_{11}| > 0 \text{ and} \\ 0 & \text{when } |\epsilon_{11}| = 0 \end{cases} \\
&\vdots \\
\delta_5 &= \begin{cases} 1 & \text{when } |\epsilon_{13}| > 0 \text{ and} \\ 0 & \text{when } |\epsilon_{13}| = 0 \end{cases} \\
\delta_6 &= \begin{cases} 1 & \text{when } |\epsilon_{12}| > 0 \text{ and} \\ 0 & \text{when } |\epsilon_{12}| = 0 \end{cases}
\end{aligned} \tag{5.6}$$

It has been shown that the total strain energy density is stationary with respect to the changes in ISVs associated with damage and structural processes (Schapery 1990, 1989), such that:

$$\frac{\partial U}{\partial S_i} = 0 \tag{5.7}$$

Substituting equation 5.1 and 5.4, in equation 5.7, the following expression can be obtained:

$$\frac{\partial W_e}{\partial S_i} = -1 \tag{5.8}$$

Equation 5.8 can be used to apply bounds on the evolution of the ISVs by combining it with equation 5.3 and using the definition of F_i which leads to the following evolution law:

$$\dot{S}_i \geqslant 0 \tag{5.9}$$

Using the chain rule, equation 5.8 can be further written as:

$$\frac{\partial W_e}{\partial S_i} = \frac{\partial W_e}{\partial s_i} \cdot \frac{\partial s_i}{\partial S_i} \tag{5.10}$$

The second term in equation 5.10 can be obtained by differentiating equation 5.5 with respect to S_i, which is found to be:

$$\frac{\partial s_i}{\partial S_i} = \frac{1}{\delta_i} \tag{5.11}$$

which can be substituted in equation 5.10 and the result of which can be substituted in equation 5.8 to obtain:

$$\frac{\partial W_e}{\partial s_i} = -\delta_i \tag{5.12}$$

Equation 5.12 represents a system of equations that describe the evolution of the state variables on the application of any form of strain energy. The elastic strain energy as a function of strain for a general orthotropic system is:

$$\begin{aligned} W_e =& \frac{1}{2}\Big(C_{11}\epsilon_{11}^2 + C_{22}\epsilon_{22}^2 + C_{33}\epsilon_{33}^2 + C_{44}\epsilon_{23}^2 + C_{55}\epsilon_{13}^2 \\ &+ C_{66}\epsilon_{12}^2 + C_{12}\epsilon_{11}\epsilon_{22} + C_{13}\epsilon_{11}\epsilon_{33} + C_{21}\epsilon_{22}\epsilon_{11} \\ &+ C_{23}\epsilon_{22}\epsilon_{33} + C_{31}\epsilon_{33}\epsilon_{11} + C_{32}\epsilon_{33}\epsilon_{22}\Big) \end{aligned} \tag{5.13}$$

where $C_{i=1-6,j=1-6}$ are elements of the stiffness matrix of the material system. The system of equations represented in equation 5.12 can be reduced to a single equation for isotropic materials, where $S_1 = S_2 \cdots = S_6 = \frac{S}{6}$ such that $W_d = S$, and δ is always 1 to avoid triviality. Such a case leads to the original equations for isotropic materials as derived in previous works (Pineda et al. 2009; Johnston 2016). Since C_{ij} is dictated by the state variables s_i, it can be functionally

expressed as $C_{ij} = f(s_1, \cdots, s_6)$. These functions can be chosen appropriately to model the selected material system, for example, Pineda et al. used a polynomial function to describe the dependence of the elastic constants with the state variables (Pineda et al. 2009). In the current work, a second order polynomial function is used such that:

$$\begin{aligned} C_{ij} =& C_{ij}^{\dot{1}} + C_{ij}^{\dot{2}} s_1 + C_{ij}^{\dot{3}} s_2 + C_{ij}^{\dot{4}} s_3 + C_{ij}^{\dot{5}} s_4 + C_{ij}^{\dot{6}} s_5 + C_{ij}^{\dot{7}} s_6 + \\ & C_{ij}^{\dot{8}} s_1^2 + C_{ij}^{\dot{9}} s_2^2 + C_{ij}^{\dot{1}\dot{0}} s_3^2 + C_{ij}^{\dot{1}\dot{1}} s_4^2 + C_{ij}^{\dot{1}\dot{2}} s_5^2 + C_{ij}^{\dot{1}\dot{3}} s_6^2 \end{aligned} \tag{5.14}$$

where $C_{ij}^{\dot{k}}$ are constants. The independent constants can be selectively calibrated depending on the application of the model and can also be dramatically reduced using symmetry conditions if they exist. As can be seen from equation 5.14, any strain in a certain direction may produce changes in the material properties in the non-dominant directions, the amount of which is governed by equation 5.12. For example, application of any loading in the transverse (22) direction will activate the state variable s_2, which then produces a change in all the material constants. This methodology simulates the reduced ability of the material to resist loads in non-dominant directions as a consequence of damage in the dominant direction.

5.3.1 Subcell Micromechanics

The proposed low fidelity Schapery damage model can now be used to replicate the CNT-epoxy nanomatrix response calibrated with the high fidelity explicit model of the CNT-epoxy system. However, this can only be used to analyze the matrix properties of the composite or nanocomposite material. Since global loads are applied to the composite material system, a framework for decomposing the global loads to fiber and (nano)matrix properties must be utilized for the application of the (nano)matrix surrogate. Several micromechanics techniques have been discussed in Chapter 1 that perform this decomposition through the use of a concentration factor, relating global properties to the microscale constituent properties. One such micromechanics framework

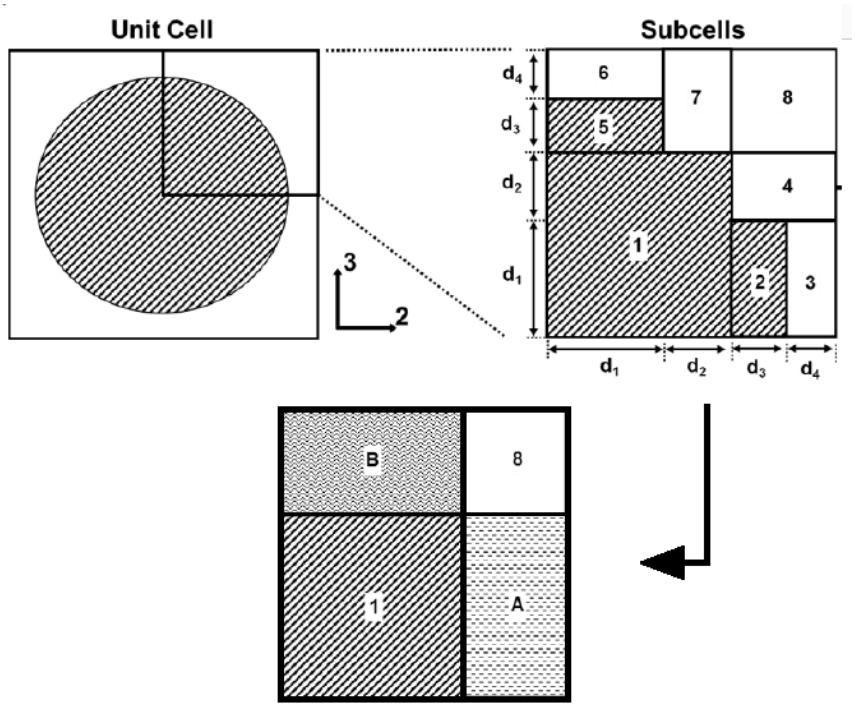

Figure 5.7. Unitcell discretization in the subcell method

Source: (Zhu 2006)

is the 3D subcell model (Zhu, Chattopadhyay, and Goldberg 2006; Zhu 2006) that discretizes a perfectly ordered square unit cell with a central circular fiber into 32 subcells. Perfect fiber-matrix interfacial bonding is assumed. These subcells are governed by 32 independent sets of constitutive properties which are all related along with the global loads through appropriate sets of continuity conditions that create a combination of Voight and Reuss approximations. The actual analysis considers symmetry conditions and explicitly develops these equations for 8 subcells that make up one quarter of the unit cell, as illustrated in Figure 5.7. In this framework, subcells 2, 3, 4 and 5, 6, 7 are connected through a system of equations and homogenized as intermediate subcells A and B respectively. Then the subcells 1, 8, A, and B are related through another system of equations to create a homogenized composite constitutive model that describes the global composite response. In this manner, the global initial and boundary conditions can be used to perform a global-local

analysis for each individual subcell. Since subcells 3, 4, 6, 7, and 8 describe matrix behavior, the material properties for these subcells can be defined using the Schapery model to incorporate the high-fidelity matrix response.

Since the individual subcell mechanics is a function of the subcell geometry, a relationship between subcell geometry and experimentally measurable parameters can make the analysis practically viable. The volume fraction V_f of composites, defined as the volume ratio of the fiber to that of the unit cell, can be measured using simple microscopy studies and can be easily related to the subcell geometry variables d_1, d_2, d_3, and d_4. Assuming the radius of the fiber is R_f and unit length of the unit cell cube ($1 \times 1 \times 1$), the cylindrical volume of the fiber equals the volume fraction.

$$\pi R_f^2 = V_f \Rightarrow R_f = \sqrt{\frac{V_f}{\pi}} \tag{5.15}$$

To relate the four subcell variables with V_f, four distinct equations are required which are obtained by considering the subcell geometries such as:

$$\begin{aligned} (d_1 + d_2)^2 + (d_1 + d_2)^2 &= R_f^2 \quad \text{Radius of the fiber} \\ d_1 + d_2 + d_3 &= R_f \quad \text{Radius of the fiber} \\ 2\left(d_1 + d_2 + d_3 + d_4\right) &= 1 \quad \text{Unit length of the unit cell} \\ 4(d_1 + d_2)^2 + 8(d_1 d_2) &= V_f \quad \text{Volume fraction of the fiber} \end{aligned} \tag{5.16}$$

The subcell miromechanics theory performs intermediate homogenization of the subcell 2, 3, 4 by assuming appropriate continuity conditions for relating the homogenized properties of subcell A, $\dot{\sigma}^{(A)}$ and $\dot{\epsilon}^{(A)}$, with properties of the individual subcells, $\dot{\sigma}^{(2,3,4)}$ and $\dot{\epsilon}^{(2,3,4)}$. These conditions are expanded as:

$$\begin{aligned} \dot{\epsilon}_{11}^{(2)} = \dot{\epsilon}_{11}^{(3)} = \dot{\epsilon}_{11}^{(4)} = \dot{\epsilon}_{11}^{(A)} \\ A_1\dot{\sigma}_{11}^{(2)} + A_2\dot{\sigma}_{11}^{(3)} + A_3\dot{\sigma}_{11}^{(4)} = \dot{\sigma}_{11}^{(A)} \end{aligned} \tag{5.17}$$

$$
\begin{gathered}
A_3\dot{\sigma}_{22}^{(4)} + A_4\dot{\sigma}_{22}^{(3)} = \dot{\sigma}_{22}^{(A)} \\
\dot{\sigma}_{22}^{(2)} = \dot{\sigma}_{22}^{(3)} \\
\dot{\epsilon}_{22}^{(4)} = \dot{\epsilon}_{22}^{(A)} \\
A_5\dot{\epsilon}_{22}^{(2)} + A_6\dot{\epsilon}_{22}^{(3)} = \dot{\epsilon}_{22}^{(A)}
\end{gathered} \tag{5.18}
$$

$$
\begin{gathered}
A_5\dot{\sigma}_{33}^{(2)} + A_6\dot{\sigma}_{33}^{(3)} = \dot{\sigma}_{33}^{(A)} \\
\dot{\sigma}_{33}^{(4)} = \dot{\sigma}_{33}^{(A)} \\
\dot{\epsilon}_{33}^{(2)} = \dot{\epsilon}_{33}^{(3)} \\
A_3\dot{\epsilon}_{33}^{(4)} + A_4\dot{\epsilon}_{33}^{(3)} = \dot{\epsilon}_{33}^{(A)}
\end{gathered} \tag{5.19}
$$

$$
\begin{gathered}
\dot{\sigma}_{12}^{(2)} = \dot{\sigma}_{12}^{(3)} = \dot{\sigma}_{12}^{(4)} = \dot{\sigma}_{12}^{(A)} \\
2A_1\dot{\epsilon}_{12}^{2} + 2A_2\dot{\epsilon}_{12}^{3} + 2A_3\dot{\epsilon}_{12}^{4} = 2\dot{\epsilon}_{12}^{A}
\end{gathered} \tag{5.20}
$$

$$
\begin{gathered}
\dot{\sigma}_{13}^{(2)} = \dot{\sigma}_{13}^{(3)} = \dot{\sigma}_{13}^{(4)} = \dot{\sigma}_{13}^{(A)} \\
2A_1\dot{\epsilon}_{13}^{2} + 2A_2\dot{\epsilon}_{13}^{3} + 2A_3\dot{\epsilon}_{13}^{4} = 2\dot{\epsilon}_{13}^{A}
\end{gathered} \tag{5.21}
$$

$$
\begin{gathered}
A_3\dot{\sigma}_{23}^{(4)} + A_4\dot{\sigma}_{23}^{(3)} = \dot{\sigma}_{23}^{(A)} \\
\dot{\sigma}_{23}^{(2)} = \dot{\sigma}_{23}^{(3)} \\
\dot{\epsilon}_{23}^{(4)} = \dot{\epsilon}_{23}^{(A)} \\
2A_5\dot{\epsilon}_{23}^{(2)} + 2A_6\dot{\epsilon}_{23}^{(3)} = 2\dot{\epsilon}_{23}^{(A)}
\end{gathered} \tag{5.22}
$$

$$
\begin{aligned}
A_1 &= \frac{d_1 d_3}{(d_1+d_2)(d_3+d_4)} \\
A_2 &= \frac{d_1 d_4}{(d_1+d_2)(d_3+d_4)} \\
A_3 &= \frac{d_2}{(d_1+d_2)} \\
A_4 &= \frac{d_1}{(d_1+d_2)} \\
A_5 &= \frac{d_3}{(d_1+d_2)} \\
A_6 &= \frac{d_4}{(d_1+d_2)}
\end{aligned}
\tag{5.23}
$$

Similar formulations can be used to relate subcell B properties, $\dot{\sigma}^{(B)}$ and $\dot{\epsilon}^{(B)}$, with properties of the individual subcells, $\dot{\sigma}^{(5,6,7)}$ and $\dot{\epsilon}^{(5,6,7)}$. Finally, the homogenized properties of the single unit cell material, $\dot{\sigma}^{(u)}$ and $\dot{\epsilon}^{(u)}$, can be related with properties of the individual subcells, $\dot{\sigma}^{(1,8,A,B)}$ and $\dot{\epsilon}^{(1,8,A,B)}$. However, the continuity conditions do not provide the complete set of equations to fully define local properties with the global properties. The constitutive relations can be used to obtain a fully analytical relation for the local-global analysis. The constitutive relations for the fiber subcells 1, 2, and 5 are:

$$
\epsilon_{ij}^{1,2,5} = S_{ijkl}^{f} \sigma_{kl}^{1,2,5} \tag{5.24}
$$

where S_{ijkl} is the transversely isotropic compliance tensor used to describe the carbon fiber material. The constitutive relations for the matrix subcells 3, 4, 6, 7, and 8 are determined from the Schapery theory. Finally the unit cell constitutive response can be written as:

$$
\epsilon_{ij}^{u} = S_{ijkl}^{u} \sigma_{kl}^{u} \tag{5.25}
$$

where the compliance tensor for the unit cell S_{ijkl}^{u} is a function of the geometric and material properties of the subcells, obtained using the continuity equations and the subcell constitutive relations. The homogenized unit cell tensorial relations, then, provide the bridging between the global and local properties in a framework consistent with the theory of elasticity.

Using such a methodology, incorporating the surrogate Schapery model with a computationally rapid micromechanics framework, allows the investigation of the effects of the matrix phase as well as the fiber phase as a function of applied global loads, and permits the application of classical macroscale failure theories to perform a coherent computationally efficient multiscale study that may involve the structural scale. It is to be noted that since the matrix phase response is calibrated with the high fidelity atomistically informed model, the nanoscale influences are implicitly accounted for in the surrogate low fidelity Schapery model of the CNT-epoxy system. However, the local sub-microscale information from the high fidelity model is lost and only the global RUC response of the CNT-epoxy system is bridged. The sectional micromechanics model then accounts for in-plane deformations, out of plane normal deformations, and transverse shear deformations, allowing for 3D characterization and analysis.

5.3.2 Low Fidelity Parametric Analysis

Table 5.1. Calibration parameters for the polymer Schapery model

$C_{11}^{\dot{1}}$	2.383E9	$C_{12}^{\dot{1}}$	1.021E9	$C_{66}^{\dot{1}}$	1.362E9
$C_{11}^{\dot{2}}$	10151	$C_{12}^{\dot{2}}$	101025	$C_{66}^{\dot{2}}$	634
$C_{11}^{\dot{3}}$	91632	$C_{12}^{\dot{3}}$	101025	$C_{66}^{\dot{3}}$	634
$C_{11}^{\dot{4}}$	91632	$C_{12}^{\dot{4}}$	245	$C_{66}^{\dot{4}}$	1249
$C_{11}^{\dot{5}}$	1.0	$C_{12}^{\dot{5}}$	1.0	$C_{66}^{\dot{5}}$	1.0
$C_{11}^{\dot{6}}$	1.0	$C_{12}^{\dot{6}}$	1.0	$C_{66}^{\dot{6}}$	1.0
$C_{11}^{\dot{7}}$	1.0	$C_{12}^{\dot{7}}$	1.0	$C_{66}^{\dot{7}}$	1.0
$C_{11}^{\dot{8}}$	1.05	$C_{12}^{\dot{8}}$	0.012	$C_{66}^{\dot{8}}$	0.0045
$C_{11}^{\dot{9}}$	1.95	$C_{12}^{\dot{9}}$	0.012	$C_{66}^{\dot{9}}$	0.0045
$C_{11}^{\dot{10}}$	1.95	$C_{12}^{\dot{10}}$	0.002	$C_{66}^{\dot{10}}$	0.0045
$C_{11}^{\dot{11}}$	0.001	$C_{12}^{\dot{11}}$	0.001	$C_{66}^{\dot{11}}$	0.001
$C_{11}^{\dot{12}}$	0.001	$C_{12}^{\dot{12}}$	0.001	$C_{66}^{\dot{12}}$	0.001
$C_{11}^{\dot{13}}$	0.001	$C_{12}^{\dot{13}}$	0.001	$C_{66}^{\dot{13}}$	0.001

To perform the low-fidelity equivalent of the DNS model, the matrix phase is represented

using the equations derived in Section 5.3. Both the polymer matrix as well as the nanopolymer matrix can be approximated. As mentioned in Section 5.3, this model can be calibrated with experimental or simulated response of standard characterization tests. Figure 5.8 shows the calibration of the Schapery model with the response of a uniaxial quasi-static tensile test of a flat dogbone specimen made from Epon E863 Resin and Epi-Cure 3290 hardener (100/27 weight ratio). Table 5.1 lists the constants for the calibrated Schapery model. The number of constants is reduced due to the isotropic nature of the polymer as well as the intended application of this model, which is uniaxial transverse loading of the CFRP composite. The calibrated model can be used to represent the matrix constitutive equations in the subcell micromechanics to simulate global fiber-matrix response. A comparison of the subcell CFRP unit cell response with the calibrated damage model, and quasi-static CFRP tests under transverse loading (Gilat, Goldberg, and Roberts 2002) can be seen in Figure 5.9. The Schapery model determines the damage state in the matrix phase and the overall unit cell failure is determined by the modified Hashin's criteria (Johnston 2016). Average total computational time for the transverse loading case was fount be 8.23 seconds and for the transverse shear case was found to be 22.51 seconds, computed on a regular desktop computer. It can be seen that with the combination of an independently calibrated Schapery model and the subcell micromechanics theory, the global response of the CFRP can be predicted.

The Schapery surrogate is further calibrated with the atomistically informed damage model, to capture polymer damage through a model-only methodology. In this case, experimental calibration of the Schapery model is completely avoided. Figure 5.10 shows the comparison of the predicted transverse stress-strain response of the CFRP composite modeled using the methodology developed in this chapter and various popular damage models. In this case the matrix is modeled using the developed Schapery surrogate calibrated with the atomistically informed damage model. 'Hashin-Macro' refers to linear elastic simulations of a CFRP specimen with macro level elastic properties calculated using rule of mixtures and the Hashin failure theory applied at the

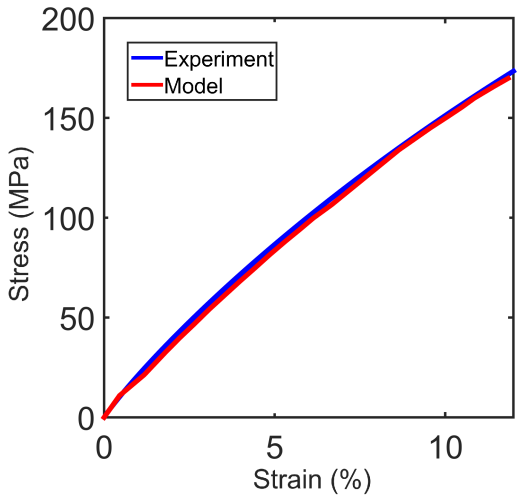

Figure 5.8. Calibration of Schapery model with experimental polymer response

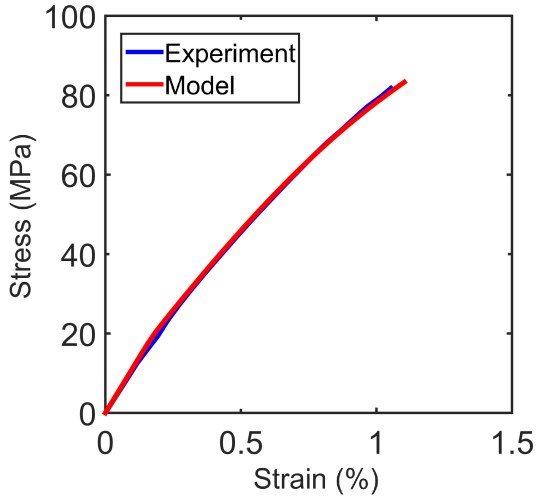

Figure 5.9. Comparison of experimental CFRP response under transverse loading and polymer subcell/Schapery model

structural scale (Hashin 1980). The 'Pineda-Macro' model refers to a macro level CFRP model with a combination of Hashin's failure theory and the work energy based matrix damage model developed by Pineda et al (Pineda et al. 2009). The 'Damage-Multiscale' model refers to a sectional micromechanics based analysis with a 3D progressive failure theory applied to the polymer at the micro scale along with the Hashin's failure theory at the macro scale (Johnston 2016). The

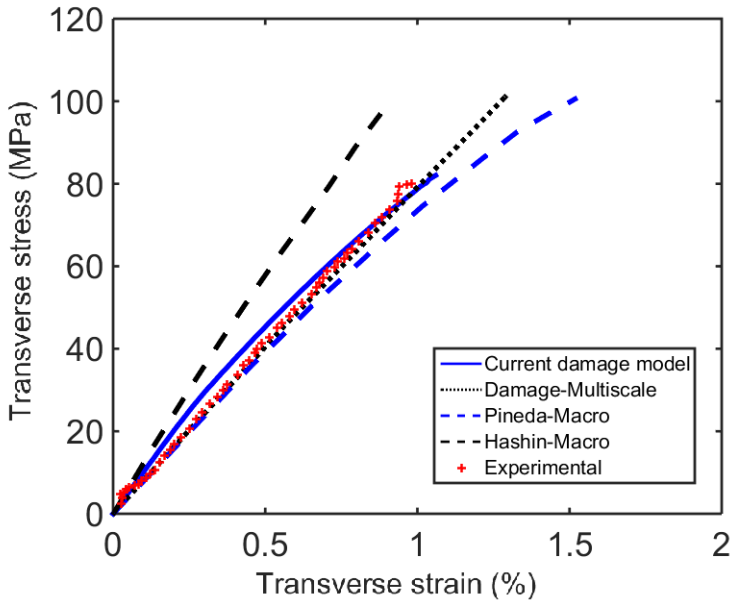

Figure 5.10. Comparison of experimental CFRP response under transverse loading and polymer subcell/Schapery model

'current damage model' refers to the framework developed in this chapter. It can be seen that the multiscale models perform better than the macroscale-only models and the current damage model further improves upon previous multiscale models. Global failure of the CFRP system was captured with higher accuracy which is attributed to the complementary application of microscale damage and macroscale failure models.

Further insight into the failure process and the performance of the damage model can be gained by studying the stresses in the matrix subcells. Figure 5.11 shows the transverse stresses in each matrix subcell versus the applied strain. It is observed that subcell 3 is the first to begin damaging and to fail. This is attributed to the fact that subcell 3 is in the loading plane and neighbors a fiber subcell. Hence, the large stress gradient causes damage accumulation faster in subcell 3 compared to the other subcells. Similarly, it is observed that subcell 4 fails next. However there is only a slight difference in failure stresses between subcell 4, 7 and 8. The stress gradients are slightly higher in subcell 4 due to the neighboring subcell being a fiber subcell, hence subcell 4

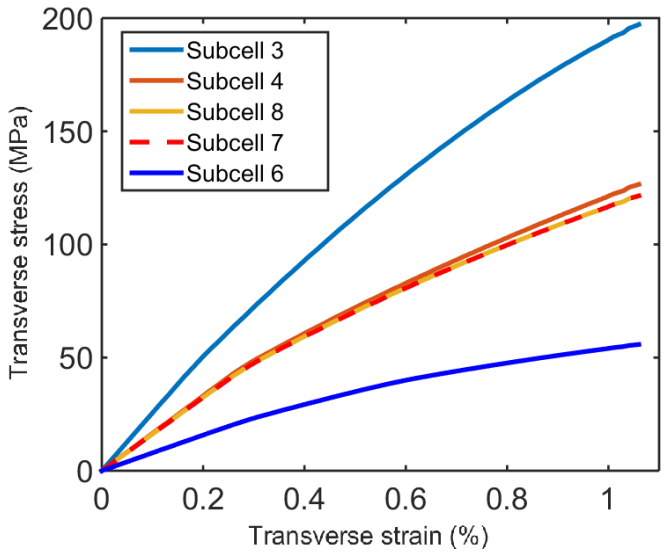

Figure 5.11. Comparison of stresses in the various subcells

fails before 7 and 8. Subcell 7 is oriented away from the loading plane compared to subcell 4 and hence subcell 4 fails before subcell 7. It is also observed that subcell 6 does not fail before global failure and this can be attributed to the geometry of the unit cell and the location of subcell 6 which is the farthest away from the loading plane.

Characterizing CFRP composites in the in-plane directions is relatively straightforward, however characterizing the shear stress response can be quite complex. In general, validated computational methods have been used to characterize CFRPs in the 1-3 and 2-3 directions. Two popular methods are finite elements (Barbero 2013) and multiscale analysis model using generalized method cells (MAC/GMC) (Arnold et al. 1999). Figure 5.13 shows the comparison of the current sectional model with the Schapery damage formulation compared to a finite element simulation of unit cell using ABAQUS and a MAC/GMC simulation of a fiber centered unit cell. Good comparison between all three models is observed, however the damage sectional model is seen to simulates the nonlinearity in the material at larger strains.

Stochastic simulations are also carried out that lead to a spectrum of behavior depending on

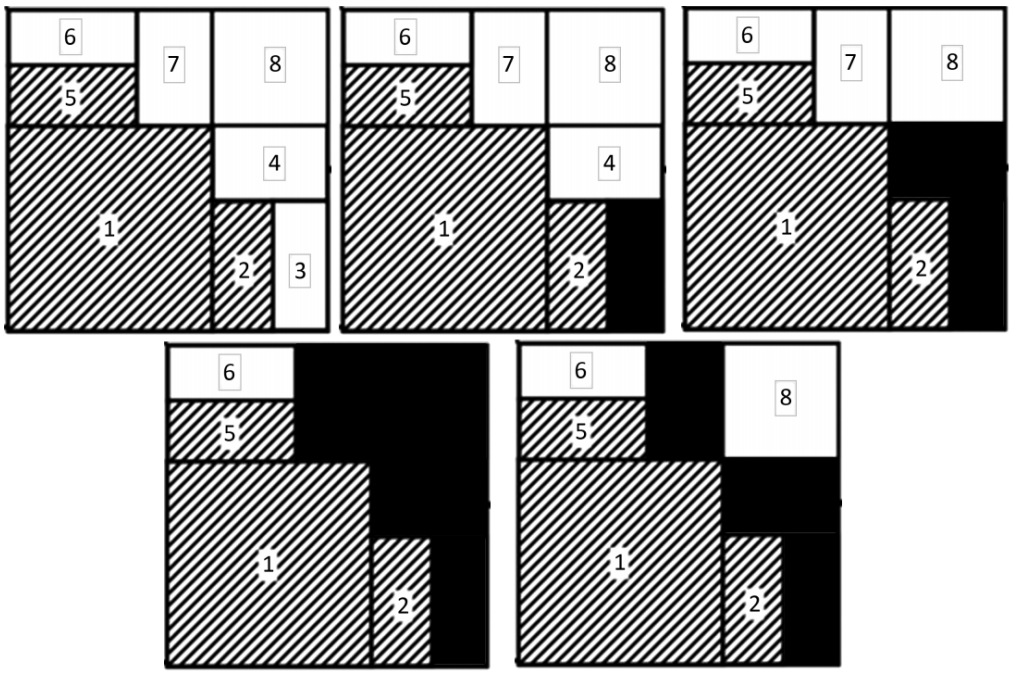

Figure 5.12. Progression of damage in the subcells in clockwise order

the uncertainty in the geometric or material variables. The probability distributions for the uncertain variables, which is assumed to be only the volume fraction, V_f, and the crosslinking degree of the polymer, η, are used to perform the analysis. For a composite system manufactured with IM7 fiber and Di-Glycidyl Ether of Bisphenol F (DGEBF)-based resin system using standard manufacturing processes, it is found that the fiber volume fraction shows a Gaussian distribution with an average of 63.9% and a standard deviation of 2.21% (Johnston 2016). Additionally, fundamental variation in crosslinking in the polymer can be calculated from MD simulations for the DGEBF resin system as discussed in Chapter 2. The average and standard deviation of the crosslinking variation is calculated to be 56.02% and 4.11%, respectively (Subramanian, Rai, and Chattopadhyay 2015). These two random variables, approximated using normal distributions, can be randomly sampled and applied as input to the subcell model to compute the distribution of nanocomposite CFRP response under uncertainty. The simulations are performed in a Monte Carlo approach,

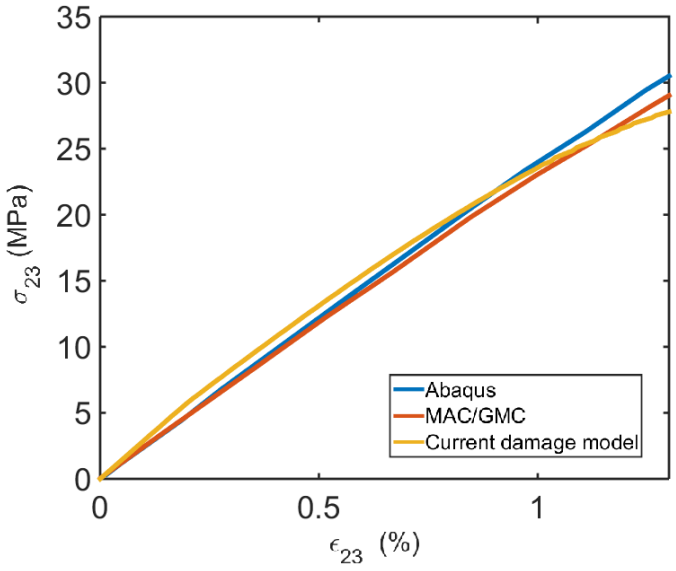

Figure 5.13. Comparison of transverse shear strain response between various models

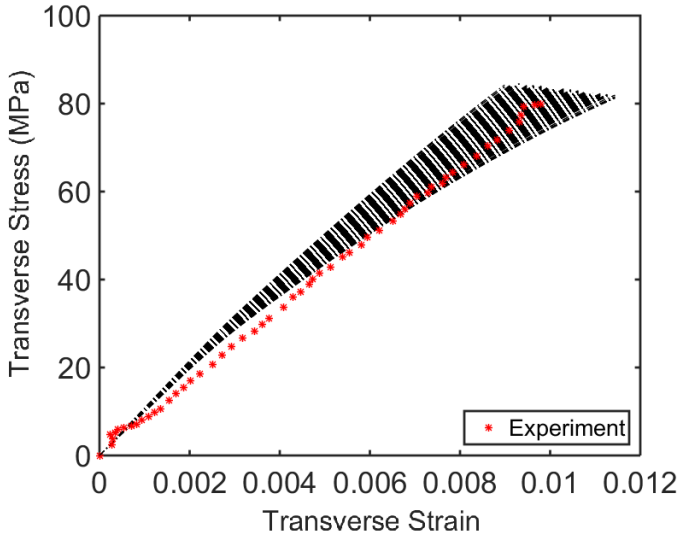

Figure 5.14. Distribution of transverse stress strain response under stochastic parameters

wherein 1000 simulations of the CFRP sectional model were run for two cases: transverse loading and transverse shear.

Figure 5.14 shows the stress-strain response space for the transverse loading condition. The modeling response is also compared with experiments from Gilat et al (Gilat, Goldberg, and

Roberts 2002). It is observed that lower elastic response corresponds to higher failure strains and vice versa. It is also observed that the response is fairly tight for the applied input variation in parameters until up to larger applied strains.

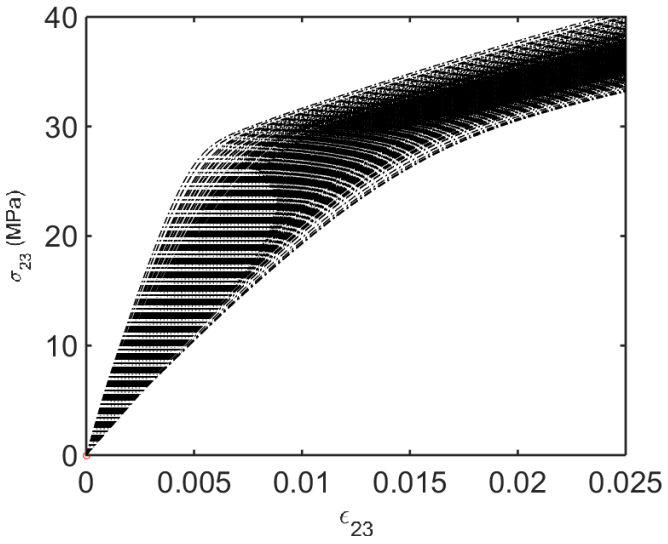

Figure 5.15. Distribution of response under shear loading and stochastic parameters

Figure 5.15 shows the stress-strain response space for the transverse shear case. It is observed that considerably higher nonlinearities are expected for elastically stiffer response. A large spread in response is also predicted which is contrary to the observation in the transverse loading response. The existence of considerable nonlinearities and the large spread in the prediction of their occurrence should discourage the use of deterministic simulations of shear behavior for design purposes.

For the analysis of the CNT/CFRP system, the Schapery model must be calibrated to the nanopolymer response. High fidelity nanopolymer models can be generated using the framework described in section 5.2.2, without the incorporation of the microfibers. The Schapery model can then be used to represent the CNT-epoxy system, and applied as the matrix phase in the subcell micromechanics. This provides a 'model-only' methodology for the analysis of nanocomposites, avoiding experimental calibration of the Schapery damage model. Figure 5.16 displays the comparison of the high fidelity dispersed CNT/CFRP model response and the Subcell/Schapery model

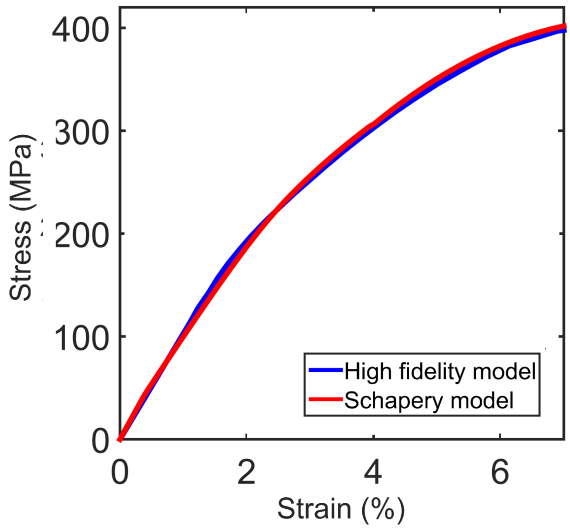

Figure 5.16. Comparison of nanocomposite CFRP response from direct numerical simulation and nanopolymer Schapery/Subcell model

response under uniaxial transverse loading. The Subcell/Schapery model captures all the essential characteristics of the RUC global response as obtained from the high fidelity model, while utilizing significantly decreased computational time. However, the local sub-microscale information, which can be computed using the high fidelity models, is lost using the low fidelity Subcell/Schapery methodology. However the significant computational efficiency allows parametric studies of the CNT/CFRP system while considering the various causes of uncertainties, such as variation in volume fraction and polymer curing.

Uncertain variables and characteristics used for the stochastic analysis of the CFRP system are also used for the stochastic analysis of the nanocomposites. Figure 5.17 exhibits the result of 1000 simulations of the subcell model with randomly sampled crosslinking and volume fraction information. The CNT-epoxy matrix is represented using the previously calibrated Schapery model and computes the degradation of the nanomatrix phase. The figure show a spectrum of response for the dispersed CNT/CFRP system and it can be observed that, although the elastic response

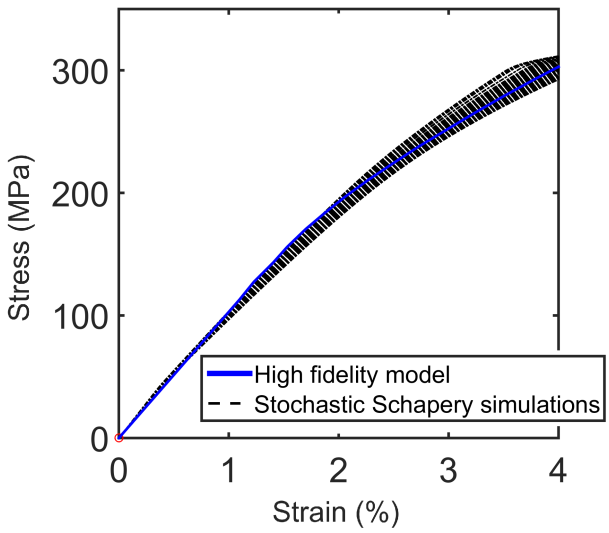

Figure 5.17. Stochastic nanocomposite CFRP response under transverse loading

of the material does not present large variabilities, the damage and failure response is associated with significant stochasticity.

5.4 Summary

In this chapter, a methodology for direct numerical simulations and low-fidelity, surrogate, nanocomposite modeling and analysis were detailed. These tools were used to generate nanocomposites with CNTs as nanofillers for deterministic and stochastic studies with various levels of detail. For microstructural analysis, the high-fidelity direct numerical simulation was used to understand the phenomenon of damage in dispersed and radially grown CNT/CFRP systems. Since the high-fidelity model is coupled with the previously developed multiscale damage formulation that utilizes atomistic information of the polymer chain motion and covalent bond dissociation, an accurate investigation at the sub microscale could be performed. Through the analysis of CNT/CFRPs it was demonstrated that the CNT architectures may be engineered to direct dam-

age for greater nanocomposite mechanical performance. Furthermore, the work potential theory was extended to account for orthotropy and damage history, and was applied as a low fidelity surrogate constitutive model for the polymer and CNT-epoxy matrix that was calibrated with the high-fidelity models. By using the Schapery model as a surrogate in combination with 3D subcell-based micromechanics techniques, the CNT/CFRP unit cell response under uniaxial transverse loading was reproduced with significantly increased computational efficiency. It was shown that such models can be easily adapted for probabilistic and parametric studies.

With the developed low fidelity modeling techniques, bridging the microscale with the macroscale for structural analysis becomes a possibility. Since the microscale derives its properties and damage mechanics from nanoscale events, a successful nano-micro-macro bridging framework may now be developed. However, all techniques presented so far assumes perfect interfaces between the fiber and the matrix. The next chapter presents a technique to incorporate imperfect interfaces in the multiscale analysis methodology where the physics of the imperfection of interfaces is incorporated from MD studies of the fiber-matrix interface. Introduction of the physics of imperfect interfaces to the atomistically informed damage model permits the development of a comprehensive analysis framework for advanced composite structures.

Chapter 6

ATOMISTICALLY INFORMED MODELING OF IMPERFECT FIBER-MATRIX BONDING

6.1 Introduction

The previous chapters 2-5 introduced several modeling strategies for predicting the linear and nonlinear properties of advanced composites under a primary assumption of perfect bonding between the fiber and the matrix. It is inherently assumed that perfect continuity of displacements and tractions occur through the interface of the fiber and the matrix such that:

$$\begin{aligned} u_f \Big|_{\partial V^-} &= u_m \Big|_{\partial V^+} \\ T_f \Big|_{\partial V^-} &= T_m \Big|_{\partial V^+} \end{aligned} \tag{6.1}$$

where u is the displacement, T is the traction, and $\partial V^{(+,-)}$ signifies a section next to the interface on the matrix side or fiber side respectively. However, two arguments persist against this assumption: (i) At the coupon level, experimental investigations find that the fiber-matrix interfacial properties can determine global composite response. Several experiments have been performed to characterize the fiber-matrix interfacial strength in composites through single fiber pushout and pullout tests, and have reported a traction separation type behavior at the interface (Wagner, Nairn, and Detassis 1995; Zhandarov and Mäder 2005; Sha et al. 2014). This type of behavior is characteristic of interfacial separation, and hence plays a role in the composite global elastic properties, as well as precursors to damage initiation and propagation. (ii) At the atomic length scale, several high resolution microscopy studies of the interface indicate irregular surface interlocking of the matrix chains with the carbon substructure of the microfibers (Cooper and Chyung 1987; Pietak et al. 2007). At this length scale, fiber-matrix bonding is a function of microfiber surface

irregularity and of the crosslinking dynamics of the resin and hardener polymer chains. For real systems, perfect bonding cannot be achieved without significant engineering of the carbon-resin-hardener system. As a result, imperfect bonding conditions must be included in any realistically advanced composite modeling framework.

Modeling of imperfect bonding in advanced composites is challenging due to the associated length scale, difficulty in experimentally characterizing interfacial properties for model calibration, and the complicated physical mechanisms that lead to interfacial degradation. Past studies have attempted composite analyses with imperfect bonding by assuming interfacial strength as a variable within standard micromechanics techniques, and by empirically determining the relationship with unidirectional composite strength (Reifsnider 1994). Such techniques can be further expanded by implicitly computing the interfacial strength through cohesive zone methods and elaborate material constitutive behavior (Souza, Allen, and Kim 2008). However, the cohesive zone method is intricately reliant on the assumed traction-separation law and many studies have concentrated on investigating the most appropriate traction-separation behavior for modeling advanced composites. Bi-linear, quadrilateral, and functionally varying traction-separation laws have been applied to various degrees of success (Wang et al. 2011; B. Zhang et al. 2010). Some studies have also considered the interface between the fiber matrix to contain non-zero thickness, thus essentially converting it into an interphase (Asp, Berglund, and Talreja 1996). In such studies, the thickness of the interphase is varied until the microscale properties can be calibrated with experimental observations. Though such techniques provide a viable methodology for introducing imperfect bonding concepts in composite analysis techniques, they are entirely dependent on calibration with large-scale coupon testing or assumptions of interfacial behavior. Hence, these techniques provide limited insight into the interfacial properties and their relationship with the macroscale composite response.

Since the width of the fiber-matrix interface is in the order of a few nanometers, the interfacial

behavior is controlled by the molecular interactions at this zone. A focus of significant research recently has been on the nanoscale characterization of the interfacial properties through analytical and computational modeling techniques in lieu of expensive experimental methods. Fundamental first-principle approaches such as *ab-initio* quantum chemistry and density functional theory have been used to calculate particulate interfacial properties and mixing properties through phase-diagrams in nanocomposites (Ginzburg and Balazs 1999). However, these approaches continue to provide limited use due to their high computational requirements. Fully continuum approaches for interfacial analysis provide some interesting insights (Jiang et al. 2006; Wagner 2002); however, these techniques are critically limited by the breakdown of the continuum assumption at this length scale. MD approaches have been far more successful in calculating bulk properties that can be easily scaled to higher length scales for comprehensive composite analyses. Course-grained MD models have been used to calculate carbon nanotube (CNT) matrix interfacial properties for functionalized nanocomposites (Odegard, Frankland, and Gates 2005). MD simulations have also been used to characterize the elastic properties of the non-zero thickness interphase between the fiber and matrix, which is then upscaled using micromechanics techniques (Johnston et al. 2017). To offset the presumed nature of traction-separation laws in the previous studies, and to take advantage of the atomistically dominated nature of this mechanism, MD simulations have additionally been used to deduce the fundamental traction-separation between CNT and matrix interfaces (Namilae and Chandra 2006).

The aforementioned background motivates the inclusion of imperfect interface effects in the analysis of advanced composites, with nanoscale parameters characterized through MD simulations. Atomic models provide the appropriate resolution for investigating the nanoscale dominated interface effects and the continuum scale analysis permits up-scaling of these mechanisms. This chapter briefly describes the MD model for analyzing the traction-separation behavior of fiber-matrix interfaces, which is then integrated into a continuum GMC imperfect interface

framework. The deterministic and stochastic effects of imperfect interfaces on composite microstructures are then analyzed.

6.2 Atomistic Simulation of the Interphase

The atomistic model is generated under the same conditions as described in section 2.2. The fiber/matrix interface is modeled as a separate phase to simulate molecular interactions between the carbon atoms of the microfiber and the resin and hardener molecules. The surface roughness of the carbon fiber is attributed to the semi-crystalline nature of the material; hence the carbon fiber is modeled by stacking several hydrogenated graphene layers with voids. This effectively simulates the defects in the microfiber through irregular stacking, which also models the mechanical/chemical entanglement and interlocking of the polymer molecules at the fiber surface.[3]

The epoxy resin and hardener molecules are introduced into the system such that roughly half the volume of the RUC is occupied by the graphene layers and the other half is occupied by the polymer molecules. As described in section 2.2 the curing of the epoxy and hardener molecules is simulated numerically, which allows the polymer molecules to populate the voids on the carbon fiber surfaces. This entanglement roughly simulates the bonding process of the polymer molecules to the microfiber surface. To decrease the computational requirements, periodic boundary conditions (PBCs) are applied in the fiber direction (z axis) and transverse to the fiber direction (y axis), effectively simulating an infinite plate with a thin film of polymer molecules (see Figure 6.1 for reference axis). The RUC dimension after application of the PBCs is $13 \times 10 \times 5\, nm^3$ totaling 58,000 atoms.

Three loading cases are investigated: (i) matrix pullout where load is applied to the matrix in

[3] It is to be noted that the atomistic model presented in this section was developed by Ms. Nithya Subramanian. All MD simulations are credited to her.

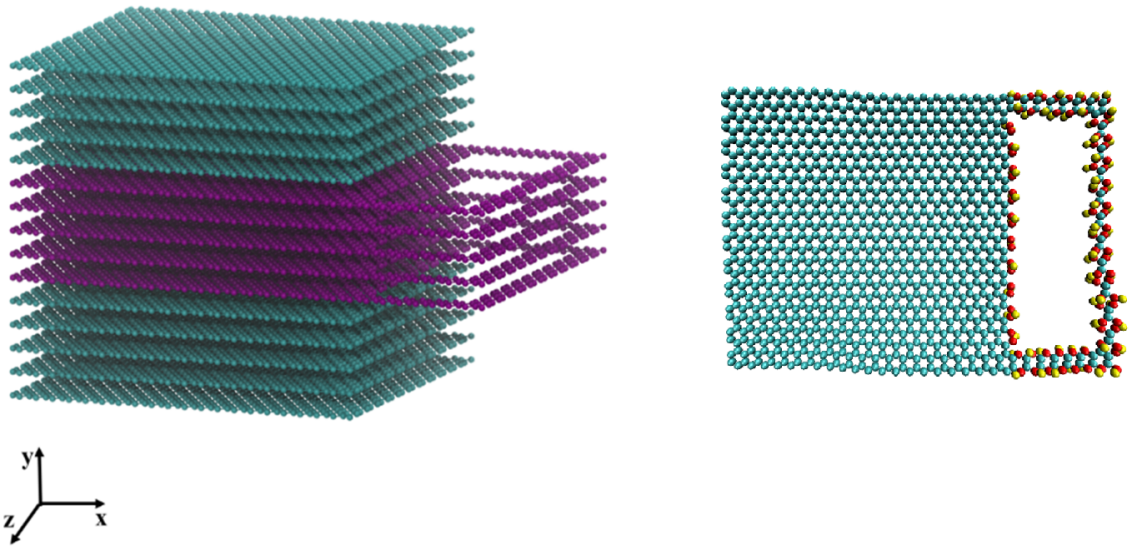

Figure 6.1. Carbon fiber surface and a hydrogenated graphene layer

Source: (Subramanian, Rai, and Chattopadhyay 2017)

the x direction which simulates fiber/matrix disbond under tensile loads; (ii) matrix shear where load is applied in the y direction, which simulates interface failure under fiber rotation; (iii) fiber pullout where load is applied on the fiber in the z direction. The objective of this model is to characterize the interface behavior especially in the non-linear regions; hence the traction forces required to separate the interfaces is studied. Reactive force fields are used to model the fundamental covalent bond dissociation during the interface separation. Five random atomic configurations are tested for each case and the averaged response of these configurations are collected for analysis.

Figure 6.2 shows the traction-separation behavior observed under matrix pullout loading. A linear traction-separation relationship is observed under an initial elastic regime, followed by the dissociation of the weakest covalent bonds. Load redistribution among the remaining bonded pairs leads to hardening until the global maxima is reached signifying failure of the interface. Frictional sliding after failure leads to secondary resistance and renewal of the hardening response until complete failure of the system occurs. It can be observed that the traction-separation behavior can

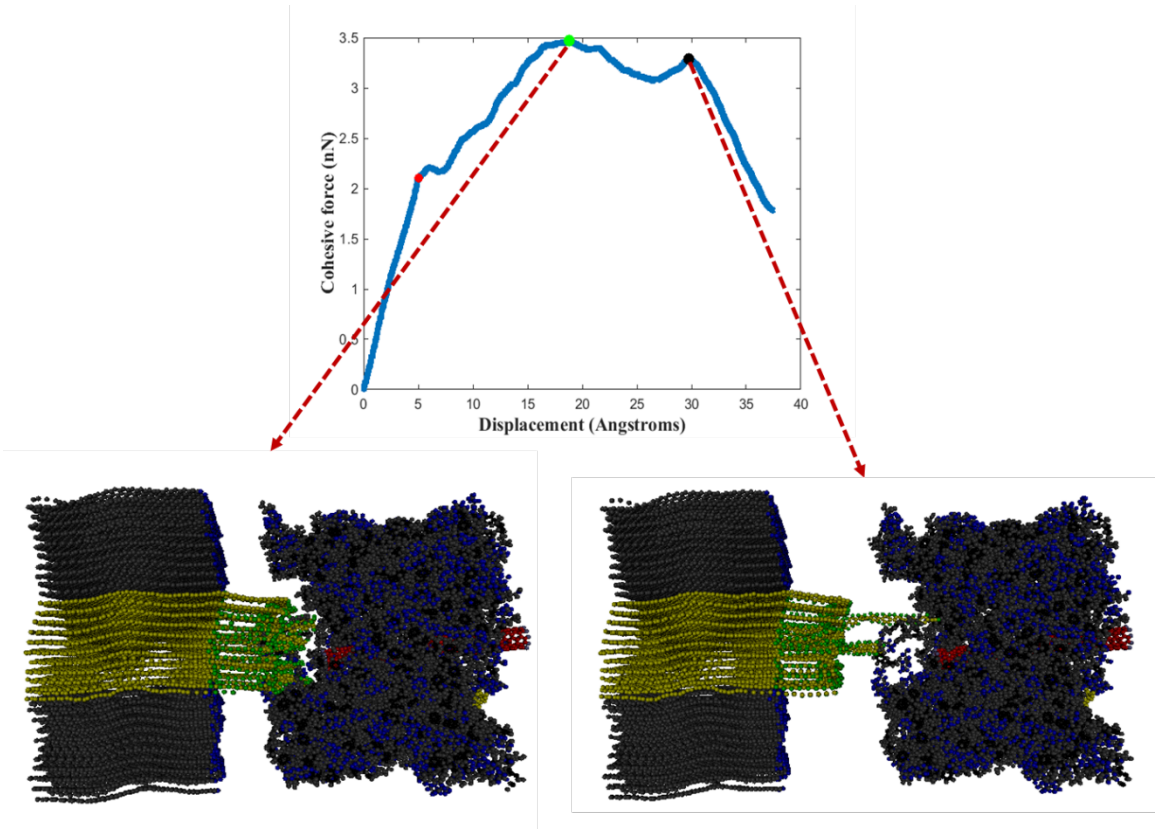

Figure 6.2. MD simulation of interface failure under matrix pullout

Source: (Subramanian, Rai, and Chattopadhyay 2017)

be approximately modeled using a bimodal Gaussian function. The traction-separation response of the matrix shear loading case can be seen in Figure 6.3, which also exhibits an initial elastic response. The failure of physical entanglement between the carbon fiber voids and the polymer molecules leads to the nonlinear response, which slowly softens with continuous covalent bond dissociations. A trapezoidal relationship may be used to analytically approximate this behavior. Figure 6.4 illustrates the traction-separation response for the fiber pullout case. The linear response is disturbed due to the failure of the mechanical entanglement between the carbon fiber defects and the polymer molecules. The nonlinear response is then characterized by smooth sliding of the polymer system along the carbon fiber similar to the dynamic frictional sliding mechanism. The

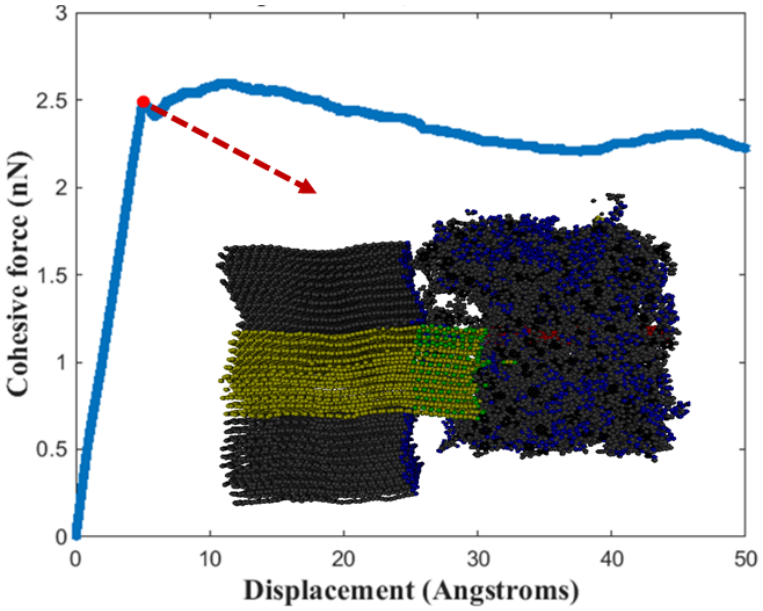

Figure 6.3. MD simulation of interface failure under matrix shear

Source: (Subramanian, Rai, and Chattopadhyay 2017)

resistance against this sliding motion slowly deteriorates due to continual bond dissociation. As in the case of matrix shear, a trapezoidal relationship can be used to approximate the fiber pullout interfacial behavior.

Using MD simulations, the nanoscale characterization of the interfacial behavior can be performed; however, for the analysis of practical composite structures these properties need to be effectively used at the next length scale. The following section introduces the generalized method of cells (GMCs) micromechanics framework and develops a methodology for incorporating the MD characterized interfacial properties between the fiber and matrix to simulate atomistically consistent imperfect bonding.

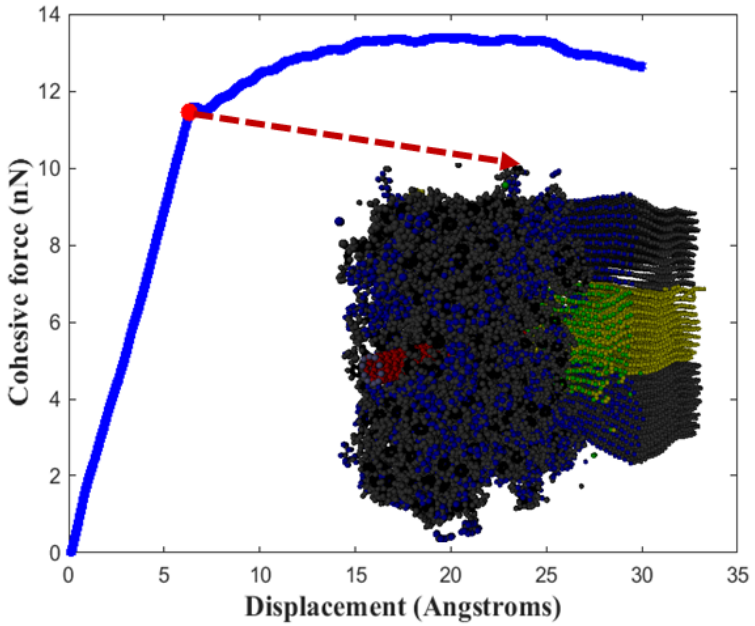

Figure 6.4. MD simulation of interface failure under fiber pullout

Source: (Subramanian, Rai, and Chattopadhyay 2017)

6.3 Generalized Method of Cells with Imperfect Interface

The Method of Cells (MOC) is a semi-analytical approach for estimating the volume-averaged phase concentration tensors through the analysis of a periodic repeating unit cell (RUC) for two-phased materials. The RUC comprises of four subcells, which is assumed to completely form the macroscale structure under a periodic assumption (Aboudi 1989). The analytical formulation is arrived at by the appropriate use of displacement and traction continuity through neighboring subcells and equilibrium equations. The primary disadvantage of the MOC approach is the limited amount of subcells which only permit the analysis of idealized microstructures with two phases. However, the MOC approach can be generalized for a completely arbitrary representative unit cell (RUC) called the Generalized Method of Cells (GMC) (Aboudi 1996; Aboudi, Arnold, and Bednarcyk 2012). The generalized approach is suitable for the analysis of completely ran-

dom composite microstructures with multiple phases. Additionally, the approach can be easily applied as a supplemental analysis for structural finite element techniques to perform concurrent multiscale studies. This section illustrates the general concepts, the governing equations, and the semi-analytical formulations of the concentration tensors derived from the GMC approach.

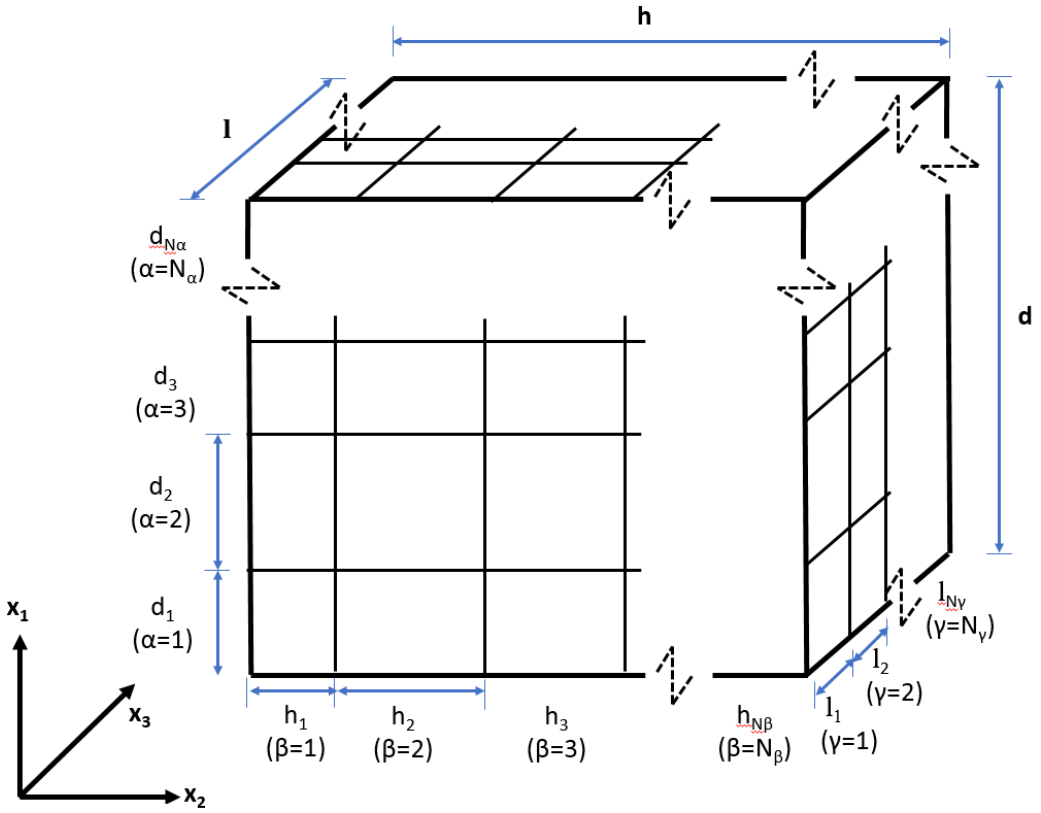

Figure 6.5. GMC element orientations and geometry

Assuming a periodic microstructure can fully define the macroscale composite material on infinite repetition, the microstructure can be approximated as a parallelepiped RUC of dimension $d \times h \times l$ itself comprising of $N_\alpha \times N_\beta \times N_\gamma$ parallelepiped subcells of dimensions $d_\alpha \times h_\beta \times l_\gamma$. Each subcell may be defined by independent material properties, however, it is assumed that continuity of tractions and displacements between neighboring subcells is always maintained. It is further assumed that the subcells are in static equilibrium. Under these conditions, the RUC

behavior is approximately defined by the volume averaged behavior of its subcells. To find this exact relationship, the subcell behavior is analyzed. Before performing such an analysis a local subcell orientation needs to be constructed, as shown in Figure 6.6. The local coordinate system $(\bar{x}_1^{(\alpha)}, \bar{x}_2^{(\beta)}, \bar{x}_3^{(\gamma)})$ is so introduced such that its origin always remains at the center of the subcell $(\alpha\beta\gamma)$. To maintain periodicity, neighboring subcells are defined using the following nomenclature:

$$\hat{\alpha} = \begin{cases} \alpha + 1 & \alpha < N_\alpha \\ 1 & \alpha = N_\alpha \end{cases} \tag{6.2}$$

$$\hat{\beta} = \begin{cases} \beta + 1 & \beta < N_\beta \\ 1 & \beta = N_\beta \end{cases} \tag{6.3}$$

$$\hat{\gamma} = \begin{cases} \gamma + 1 & \gamma < N_\gamma \\ 1 & \gamma = N_\gamma \end{cases} \tag{6.4}$$

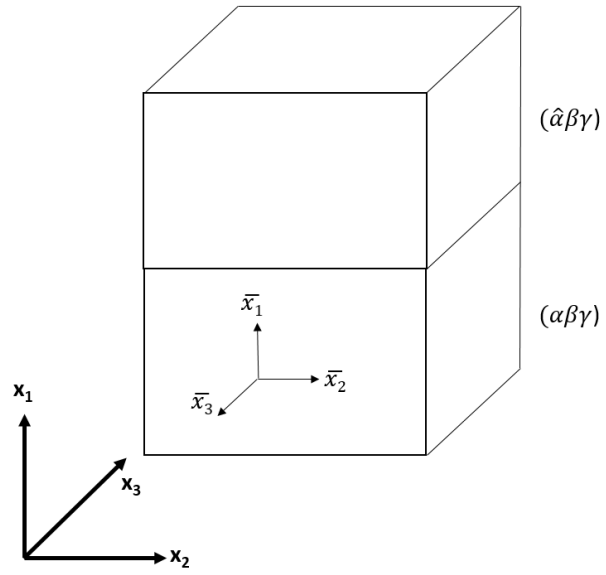

Figure 6.6. Local subcell orientations and neighboring subcell nomenclature

The general subcell displacements $u_i^{(\alpha\beta\gamma)}$ are assumed to be first order linear expansions of the subcell center displacement i terms of $(\bar{x}_1^{(\alpha)}, \bar{x}_2^{(\beta)}, \bar{x}_3^{(\gamma)})$.[4]

$$u_i^{(\alpha\beta\gamma)} = w_i^{(\alpha\beta\gamma)}(\boldsymbol{x}) + \bar{x}_1^{(\alpha)}\chi_i^{(\alpha\beta\gamma)} + \bar{x}_2^{(\beta)}\phi_i^{(\alpha\beta\gamma)} + \bar{x}_3^{(\gamma)}\psi_i^{(\alpha\beta\gamma)} \tag{6.5}$$

where $w_i^{(\alpha\beta\gamma)}(\boldsymbol{x})$ quantifies the subcell center displacement components, χ,ϕ, and ψ are mapping variables that map the dependences of $u_i^{(\alpha\beta\gamma)}$ on the local subcell coordinates, and the bold dimensional variables $\boldsymbol{x}$ is a vector of the global coordinate system (x_1, x_2, x_3).

In the GMC approach, the displacements between subells are assumed to be continuous, however this continuity is applied in an averaged sense. Perfectly continuous displacements between subcells can be denoted by:

$$u_i^{(\alpha\beta\gamma)}\Big|_{\bar{x}_1^{(\alpha)}=\frac{d_\alpha}{2}} = u_i^{(\hat{\alpha}\beta\gamma)}\Big|_{\bar{x}_1^{(\hat{\alpha})}=-\frac{d_{\hat{\alpha}}}{2}} \tag{6.6}$$

However, this continuity may also be applied in an averaged sense for the surface $\partial V = d\bar{x}_2^{(\beta)} d\bar{x}_3^{(\gamma)}$. Such application does not fulfill continuity at every point, however, any violations average out to zero over the surface ∂V.

$$\int_{-\frac{h_\beta}{2}}^{\frac{h_\beta}{2}}\int_{-\frac{l_\gamma}{2}}^{\frac{l_\gamma}{2}} \left(u_i^{(\alpha\beta\gamma)}\Big|_{\bar{x}_1^{(\alpha)}=\frac{d_\alpha}{2}} \right) d\bar{x}_2^{(\beta)} d\bar{x}_3^{(\gamma)} = \int_{-\frac{h_\beta}{2}}^{\frac{h_\beta}{2}}\int_{-\frac{l_\gamma}{2}}^{\frac{l_\gamma}{2}} \left(u_i^{(\hat{\alpha}\beta\gamma)}\Big|_{\bar{x}_1^{(\hat{\alpha})}=-\frac{d_{\hat{\alpha}}}{2}} \right) d\bar{x}_2^{(\beta)} d\bar{x}_3^{(\gamma)} \tag{6.7}$$

Applying the averaged continuity concept to the subcell displacements in equation 6.5 the following relationship for displacements between subcells can be obtained:

$$w_i^{(\alpha\beta\gamma)} + \frac{1}{2} d_\alpha \chi_i^{(\alpha\beta\gamma)} = w_i^{(\hat{\alpha}\beta\gamma)} - \frac{1}{2} d_{\hat{\alpha}} \chi_i^{(\hat{\alpha}\beta\gamma)} \tag{6.8}$$

Equation 6.8 is a first order relationship between the center displacements of adjacent subcells. These relations can be further reduced to an equation with variables from only the original subcell $(\alpha\beta\gamma)$ by expanding the neighboring subcell displacements $w_i^{(\hat{\alpha}\beta\gamma)}$ using the Taylor's expansion.

[4] Indicial notations are used in this section

Summing all these relations in the operating dimension $1, 2 \cdots, N_\alpha$, the following equation can be obtained:

$$\sum_{\alpha=1}^{N_\alpha} d_\alpha \chi_i^{(\alpha\beta\gamma)} = d \frac{\partial}{\partial x_1} w_i^{(1\beta\gamma)} \tag{6.9}$$

Similar expansions and summing in the other operating dimensions leads to:

$$\sum_{\alpha=1}^{N_\beta} h_\beta \phi_i^{(\alpha\beta\gamma)} = h \frac{\partial}{\partial x_2} w_i^{(\alpha 1\gamma)} \tag{6.10}$$

$$\sum_{\alpha=1}^{N_\gamma} l_\gamma \psi_i^{(\alpha\beta\gamma)} = l \frac{\partial}{\partial x_3} w_i^{(\alpha\beta 1)} \tag{6.11}$$

The Taylor's expansion can also be used for the next step of relations in equation 6.8 which on subtraction with the original equation 6.8 leads to:

$$\begin{aligned} \frac{\partial}{\partial x_1} w_i^{(\alpha\beta\gamma)} &= \frac{\partial}{\partial x_1} w_i^{(\hat{\alpha}\beta\gamma)} \\ \frac{\partial}{\partial x_2} w_i^{(\alpha\beta\gamma)} &= \frac{\partial}{\partial x_2} w_i^{(\alpha\hat{\beta}\gamma)} \\ \frac{\partial}{\partial x_3} w_i^{(\alpha\beta\gamma)} &= \frac{\partial}{\partial x_3} w_i^{(\alpha\beta\hat{\gamma})} \end{aligned} \tag{6.12}$$

However, the set of relations described by equation 6.12 can only be true if the subcell displacements are all related by a common displacement variable w_i:

$$\frac{\partial}{\partial x_j} w_i^{(\alpha\beta\gamma)} = \frac{\partial}{\partial x_j} w_i \tag{6.13}$$

This relationship proves that the total stress and strain components for a subcell are independent of the subcell orientations and are constant for each subcell. No spatial gradients of the stress and strain exist within a subcell and the volume averaged stress and strain quantities are equal to the point field measures:

$$\begin{aligned} \bar{\epsilon}_{ij}^{(\alpha\beta\gamma)} &= \epsilon_{ij}^{(\alpha\beta\gamma)} \\ \bar{\sigma}_{ij}^{(\alpha\beta\gamma)} &= \sigma_{ij}^{(\alpha\beta\gamma)} \end{aligned} \tag{6.14}$$

It should be noted that the infinitesimal strain definition in the subcell orientations is used in this analysis:

$$\epsilon_{ij}^{(\alpha\beta\gamma)} = \frac{1}{2}\left(\partial_i u_j^{(\alpha\beta\gamma)} + \partial_j u_i^{(\alpha\beta\gamma)}\right) \tag{6.15}$$

The volume averaged strain in the composite material can now be obtained through the discretized form of the ensemble averaging technique such that:

$$\bar{\epsilon}_{ij} = \frac{1}{dhl}\sum_{\alpha=1}^{N_\alpha}\sum_{\beta=1}^{N_\beta}\sum_{\gamma=1}^{N_\gamma} d_\alpha h_\beta l_\gamma \epsilon_{ij}^{(\alpha\beta\gamma)} \tag{6.16}$$

6.3.1 Imperfect Subcell Interfaces

In cases of imperfect interfaces between subcells, the displacement continuity equation 6.6 should be modified to account for the interfacial displacement jumps due to imperfect bonding. Assuming a jump in displacement at the interfaces to be proportional to the interfacial stresses and using the relations in equation 6.14, the continuity equation for subcells with imperfect interfaces can be expressed as:

$$u_i^{(\alpha\beta\gamma)}\Big|_{\bar{x}_1^{(\alpha)}=\frac{d_\alpha}{2}} + R_{1i}^{(\alpha\beta\gamma)}\sigma_{1i}^{(\alpha\beta\gamma)} = u_i^{(\hat{\alpha}\beta\gamma)}\Big|_{\bar{x}_1^{(\hat{\alpha})}=-\frac{d_{\hat{\alpha}}}{2}} \tag{6.17}$$

where the loss factor is represented using R_{ij}. A similar procedure as represented in equations 6.8-6.12 can be followed with the imperfect interfacial continuity equation to prove equation 6.13 for the imperfect bonding case. However the ensemble averaged composite strains will need to be adjusted for the displacement jump losses.

$$\bar{\epsilon}_{ij} = \frac{1}{dhl}\sum_{\alpha=1}^{N_\alpha}\sum_{\beta=1}^{N_\beta}\sum_{\gamma=1}^{N_\gamma} d_\alpha h_\beta l_\gamma \epsilon_{ij}^{(\alpha\beta\gamma)} - \frac{1}{2dhl}\int\int_l \{[u_i]n_j + [u_j]n_i\}\, dI \tag{6.18}$$

where $[u_i]$ are the interfacial displacement jumps at interface I, and n_i are the unit normal vectors to the interfaces. Since the displacement jump at the interfaces are proportional to the interfacial

stresses, the second part of equation 6.18 can be formulated as:

$$\begin{aligned}\int\int_I [u_I] n_I \, dI &= -\sum_{\alpha=1}^{N_\alpha}\sum_{\beta=1}^{N_\beta}\sum_{\gamma=1}^{N_\gamma}\int_{-\frac{h_\beta}{2}}^{\frac{h_\beta}{2}}\int_{-\frac{l_\gamma}{2}}^{\frac{l_\gamma}{2}} R_{11}^{(\alpha\beta\gamma)}\sigma_{11}^{(\alpha\beta\gamma)}\, d\bar{x}_2^{(\beta)} d\bar{x}_3^{(\gamma)} \\ &= -\sum_{\alpha=1}^{N_\alpha}\sum_{\beta=1}^{N_\beta}\sum_{\gamma=1}^{N_\gamma} h_\beta l_\gamma R_{11}^{(\alpha\beta\gamma)}\sigma_{11}^{(\alpha\beta\gamma)}\end{aligned} \tag{6.19}$$

Using these derived properties, equations 6.8, 6.13, 6.18, and 6.19 can be combined to form a tractable relation between the composite global strain $\bar{\epsilon}_{ij}$ and the subcell local strains $\epsilon_{ij}^{(\alpha\beta\gamma)}$ as:

$$\sum_{\alpha=1}^{N_\alpha}\left(d_\alpha \epsilon_{11}^{(\alpha\beta\gamma)} + R_{11}^{(\alpha\beta\gamma)}\sigma_{11}^{(\alpha\beta\gamma)}\right) = d\bar{\epsilon}_{11}, \quad \beta = 1, \cdots, N_\beta \quad \gamma = 1, \cdots, N_\gamma \tag{6.20}$$

$$\sum_{\beta=1}^{N_\beta}\left(h_\beta \epsilon_{22}^{(\alpha\beta\gamma)} + R_{22}^{(\alpha\beta\gamma)}\sigma_{22}^{(\alpha\beta\gamma)}\right) = d\bar{\epsilon}_{22}, \quad \alpha = 1, \cdots, N_\alpha \quad \gamma = 1, \cdots, N_\gamma \tag{6.21}$$

$$\sum_{\gamma=1}^{N_\gamma}\left(l_\gamma \epsilon_{33}^{(\alpha\beta\gamma)} + R_{33}^{(\alpha\beta\gamma)}\sigma_{33}^{(\alpha\beta\gamma)}\right) = d\bar{\epsilon}_{33}, \quad \alpha = 1, \cdots, N_\alpha \quad \beta = 1, \cdots, N_\beta \tag{6.22}$$

$$\sum_{\alpha=1}^{N_\alpha}\sum_{\beta=1}^{N_\beta}\left(d_\alpha h_\beta \epsilon_{12}^{(\alpha\beta\gamma)} + h_\beta R_{12}^{(\alpha\beta\gamma)}\sigma_{12}^{(\alpha\beta\gamma)} + d_\alpha R_{21}^{(\alpha\beta\gamma)}\sigma_{21}^{(\alpha\beta\gamma)}\right) = dh\bar{\epsilon}_{12} \quad \gamma = 1, \cdots, N_\gamma \tag{6.23}$$

$$\sum_{\beta=1}^{N_\beta}\sum_{\gamma=1}^{N_\gamma}\left(h_\beta l_\gamma \epsilon_{23}^{(\alpha\beta\gamma)} + l_\gamma R_{23}^{(\alpha\beta\gamma)}\sigma_{23}^{(\alpha\beta\gamma)} + h_\beta R_{32}^{(\alpha\beta\gamma)}\sigma_{32}^{(\alpha\beta\gamma)}\right) = hl\bar{\epsilon}_{23} \quad \alpha = 1, \cdots, N_\alpha \tag{6.24}$$

$$\sum_{\alpha=1}^{N_\alpha}\sum_{\gamma=1}^{N_\gamma}\left(d_\alpha l_\gamma \epsilon_{13}^{(\alpha\beta\gamma)} + l_\gamma R_{13}^{(\alpha\beta\gamma)}\sigma_{13}^{(\alpha\beta\gamma)} + d_\alpha R_{31}^{(\alpha\beta\gamma)}\sigma_{31}^{(\alpha\beta\gamma)}\right) = dl\bar{\epsilon}_{31} \quad \beta = 1, \cdots, N_\beta \tag{6.25}$$

To maintain generality, each subcell may be associated with an independent anisotropic compliance tensor $S_{ijkl}^{(\alpha\beta\gamma)}$. This leads to the subcell constitutive equation:

$$\epsilon_{ij}^{(\alpha\beta\gamma)} = S_{ijkl}^{(\alpha\beta\gamma)} \sigma_{kl}^{(\alpha\beta\gamma)} \tag{6.26}$$

The subcell constitutive equation 6.26 allows to form a general relation between the local and global strains which can be represented in the matrix form for convenience as:

$$\boldsymbol{\epsilon}^{(\alpha\beta\gamma)} = \boldsymbol{A}^{(\alpha\beta\gamma)} \bar{\boldsymbol{\epsilon}} \tag{6.27}$$

where $\boldsymbol{A}^{(\alpha\beta\gamma)}$ is a bridging tensor that allows the computation of strains in every subcell if the global composite strains are known, and vice-versa. The bridging tensor is a function of the subcell material properties, subcell geometry, the loss factors, and RUC geometry. On the computation of subcell strains, the inverse of equation 6.26 can be used to find subcell stresses which on ensemble averaging leads to the global composites stresses. Hence, the general global composite material constitutive equation can be written as:

$$\bar{\boldsymbol{\sigma}} = \boldsymbol{C}^* \bar{\boldsymbol{\epsilon}} \tag{6.28}$$

where $\boldsymbol{C}^*$ is the phase averaged concentration tensor that is used to represent the general composite material as a phase averaged quantity of individual subcell materials and geometry. The general relation for the phase averaged stiffness concentration is:

$$\boldsymbol{C}^* = \frac{1}{dhl} \sum_{\alpha=1}^{N_\alpha} \sum_{\beta=1}^{N_\beta} \sum_{\gamma=1}^{N_\gamma} d_\alpha h_\beta l_\gamma \boldsymbol{C}^{(\alpha\beta\gamma)} A^{(\alpha\beta\gamma)} \tag{6.29}$$

where $\boldsymbol{C}^{(\alpha\beta\gamma)}$ is the subcell stiffness tensor.

$\boldsymbol{C}^*$ is an analytical relation between the subcell properties and the global composite material which allows rapid computation of the local response given the global response (and vice-versa) as well as analytical homogenization of the composite material properties. Additionally, the GMC formulations are not limited to any number of subcells and are triply periodic. This permits the

analysis of 2D and 3D materials with complicated microstructures. Calculation of local subcell response can then be used for local damage and failure analysis and evaluation of microstructure-property relations at the higher lengths scale. The analytical formulations of the concentration tensor also lead to exact solutions for equation 6.29 that prevents the need for any form of convergence studies, as in the case of numerical homogenization techniques. This leads to significant gains in computational time required for implementation of the GMC method.

The introduction of imperfect interfaces also allows the customization of microstructures with imperfect bonding between phases. However, in the current framework the loss factors are evaluated by calibration of subcell properties to attain the experimentally observed global composite response. This empirical relationship is difficult to justify since global properties may be affected by factors other than the interfacial weaknesses. In section 6.2 the interface properties were explicitly studied at the atomic scale disregarding any possible higher length scale mechanisms that may interfere with the interfacial response. The loss factors can now be evaluated through the atomic studies of the interface, which ensures that the physics of imperfect bonding between subcells and the evaluated parameters are consistent.

The continuity between imperfectly bonded subcells maybe written as:

$$u_i^{(\alpha\beta\gamma)}\Big|_{\bar{x}_1^{(\alpha)}=\frac{d_\alpha}{2}} + u_i^{\boldsymbol{j},(\alpha\beta\gamma)}\Big|_{\bar{x}_1^{(\alpha)}=\frac{d_\alpha}{2}} = u_i^{(\hat{\alpha}\beta\gamma)}\Big|_{\bar{x}_1^{(\hat{\alpha})}=-\frac{d_{\hat{\alpha}}}{2}} \tag{6.30}$$

where $u_i^{\boldsymbol{j}}$ is the jump discontinuity between subcells due to the imperfect bonding. This quantity produces interfacial stresses which is calculated through the loss factors R_{ij} as presented in equation 6.17. In the case of fiber/matrix interfaces, a common assumption is that the interface is very thin compared to the fiber and matrix phases. Under a thin interface assumption, the loss factors causing fiber pullout, matrix pullout, and matrix shear are the only parameters of significance. If the fiber is oriented in the (11) direction, then only the loss factors $R_{11}^{(\alpha\beta\gamma)}$, $R_{12}^{(\alpha\beta\gamma)}$, and $R_{13}^{(\alpha\beta\gamma)}$

need to be evaluated. According to the definition of the loss factors, they can be represented as:

$$\left\{ R_{11}^{(\alpha\beta\gamma)} \; R_{12}^{(\alpha\beta\gamma)} \; R_{13}^{(\alpha\beta\gamma)} \right\} = \left\{ \frac{u_1^{\boldsymbol{j},(\alpha\beta\gamma)}}{\sigma_{11}^{(\alpha\beta\gamma)}} \; \frac{u_2^{\boldsymbol{j},(\alpha\beta\gamma)}}{\sigma_{12}^{(\alpha\beta\gamma)}} \; \frac{u_3^{\boldsymbol{j},(\alpha\beta\gamma)}}{\sigma_{13}^{(\alpha\beta\gamma)}} \right\} \tag{6.31}$$

The traction-separation relation for interfacial debonding can be generally written as:

$$T_i = \frac{u_i^{\boldsymbol{j}}}{u_i^{\boldsymbol{j},\boldsymbol{C}}} \, T_i^{\max} F(\Psi, \Phi, \Theta) \tag{6.32}$$

where $u^{\boldsymbol{j},\boldsymbol{C}}$ is the critical separation where failure occurs, $T_i^{\max}$ is the maximum traction that can be applied at the interface and is the global maxima of the traction-separation curve, and $F(\Psi, \Phi, \Theta)$ is a function with dependencies Ψ in the fiber pullout direction, Φ in the matrix pullout direction, and Θ in the matrix shear direction which can be used to describe the nature of the interface response. For a very thin interface of thickness h^I and unit length, the general traction-separation relation can be instead written as an approximate constitutive equation for the interface:

$$\sigma_{ij} = \frac{\epsilon_{ij}}{\epsilon_{ij}^{\boldsymbol{C}}} \, \sigma_{ij}^{\max} F(\Psi, \Phi, \Theta) \tag{6.33}$$

Substitution of equation 6.33 into equation 6.31, the loss factors for each subcell $(\alpha\beta\gamma)$ can be evaluated.

$$\left\{ R_{11}^{(\alpha\beta\gamma)} \; R_{12}^{(\alpha\beta\gamma)} \; R_{13}^{(\alpha\beta\gamma)} \right\} = h^I \left\{ \frac{\epsilon_{11}^{\boldsymbol{C},(\alpha\beta\gamma)}}{\sigma_{11}^{\max,(\alpha\beta\gamma)} F(\Psi)} \; \frac{\epsilon_{12}^{\boldsymbol{C},(\alpha\beta\gamma)}}{\sigma_{12}^{\max,(\alpha\beta\gamma)} F(\Phi)} \; \frac{\epsilon_{13}^{\boldsymbol{C},(\alpha\beta\gamma)}}{\sigma_{13}^{\max,(\alpha\beta\gamma)} F(\Theta)} \right\} \tag{6.34}$$

The values for $\epsilon^{\boldsymbol{C}}$, $\sigma^{\max}$, and $F(\Psi, \Phi, \Theta)$ can be obtained from the MD studies of the fiber pullout, matrix pullout, and matrix shear, illustrated in Figures 6.2, 6.3, and 6.4 respectively. Using this methodology, continuum mechanics is used to approximate the effects of imperfect bonding at the microscale and the consequent effects at the higher length scale, however MD simulations are used to estimate the interfacial response at the nanoscale which is applied as parameters in the continuum definition. Through this hierarchical-concurrent hybrid approach, interfacial physics is ensured to be consistent at each length scale while maintaining high computational efficiency.

6.3.2 Generating the Microstructure RUC

The homogenization approach in GMC is primarily dependent on the RUC subcell characteristics as evident in equations 6.20-6.25. The accuracy of the composite properties is directly related to the subcell geometric variables, d_α, h_β, l_γ, the subcell material properties $C_{ijkl}^{(\alpha\beta\gamma)}$, and the subcell interface loss factors $R_{ij}^{(\alpha\beta\gamma)}$. Due to the significance associated with the RUC, it is important to design the RUC representation of the microstructure with accuracy. Although it is possible to design the RUC manually, this task becomes very cumbersome if realistic microstructures, such as the one illustrated in Figure 5.2a, need to be discretized into subcells. Simple microstructures may be meshed into a GMC ready RUC through simple shape discretization algorithms (Johnston 2016), however such approaches are limited to certain geometries. These approaches also tend to produce an ineffective number of subcells for non-standard geometries which may significantly increase computational time without proportionally increasing the accuracy of the solution. Hence, an automated approach for designing the RUC for any general microstructure geometry should be developed for an accurate GMC analysis.

The general GMC homogenization methodology is developed for rectangular subcells with independent subcell geometries $d_\alpha, h_\beta, l_\gamma$. On the assumption that a two-phase RUC is constructed with subcells of equal sizes in the in-plane directions such that:

$$\begin{aligned} d_1, d_2, \cdots, d_\alpha, \cdots, d_{N_\alpha} &= \boldsymbol{d}, \quad \sum_1^{N_\alpha} d_\alpha = N_\alpha \, \boldsymbol{d} = d \\ h_1, h_2, \cdots, h_\beta, \cdots, h_{N_\beta} &= \boldsymbol{d}, \quad \sum_1^{N_\beta} h_\beta = N_\beta \, \boldsymbol{d} = h \\ l_1, l_2, \cdots, l_\gamma, \cdots, l_{N_\gamma} &= \boldsymbol{l}, \quad \sum_1^{N_\gamma} l_\gamma = N_\gamma \, \boldsymbol{l} = l \end{aligned} \tag{6.35}$$

which can lead to a visual and algorithmic similarity between the organization of digital images and the microstructural RUC for doubly periodic materials. Furthermore, if we assume cubic sub-

cells with $\boldsymbol{d} = \boldsymbol{l}$ then there exists a visual and algorithmic similarity between the organization of digital voxels and the microstructural RUC for triply periodic materials. Since random microstructures of continuous fiber composites are considered to be doubly periodic, the similarity with digital images is further explored.

Figure 6.7. Digital image array representation of fiber-centered RUC

Digital machines convert images into an array of integer data (Gonzalez, Woods, et al. 1992). These arrays may be a simple 2D matrix in the case of gray-scale two tone images, or can be complex higher dimensional arrays that contain information on pixel location, color tone, shade, brightness etc. Considering the simple case of two tone gray-scale images, the digital image comprises of a 2D integer matrix corresponding to pixel color tone. White tone may be represented by 0 and the black tone by 1. A larger matrix of 1's and 0's corresponds to a smoother picture which also consumes higher memory and a smaller matrix corresponds to 'pixelated' course images that consume minimal memory. Figure 6.7 illustrates the digital image integer array representation of a single fiber RUC system. The integer array provides a ready-made solution for generating the RUCs with each pixel converted into a subcell with dimensions $\boldsymbol{d} \times \boldsymbol{d} \times \boldsymbol{l}$, and the material properties chosen according to the pixel tone. In the case of the fiber-centered digital representation shown

in Figure 6.7, the integer value 1 corresponds to fiber and 0 corresponds to the matrix.

$$\boldsymbol{P}^{(\alpha\beta\gamma)} = \begin{cases} 1, & \text{Fiber material properties} \\ 0, & \text{Matrix material properties} \end{cases} \tag{6.36}$$

where $\boldsymbol{P}$ is the value of the pixel tone which represents the material (fiber or matrix), and the fiber is assumed to be oriented along the 11 direction. This system can be easily generalized to any two-phase microstructure saved in a gray-scale 2 tone digital image format. Furthermore, the fineness of the RUC mesh can be controlled by increasing or decreasing the image matrix size. However, it should be noted that the matrix size cannot be larger than the available pixels in the original image. The 75×75 subcell RUC generated using this image processing technique for a simulated random microstructure can be seen in Figure 6.8.

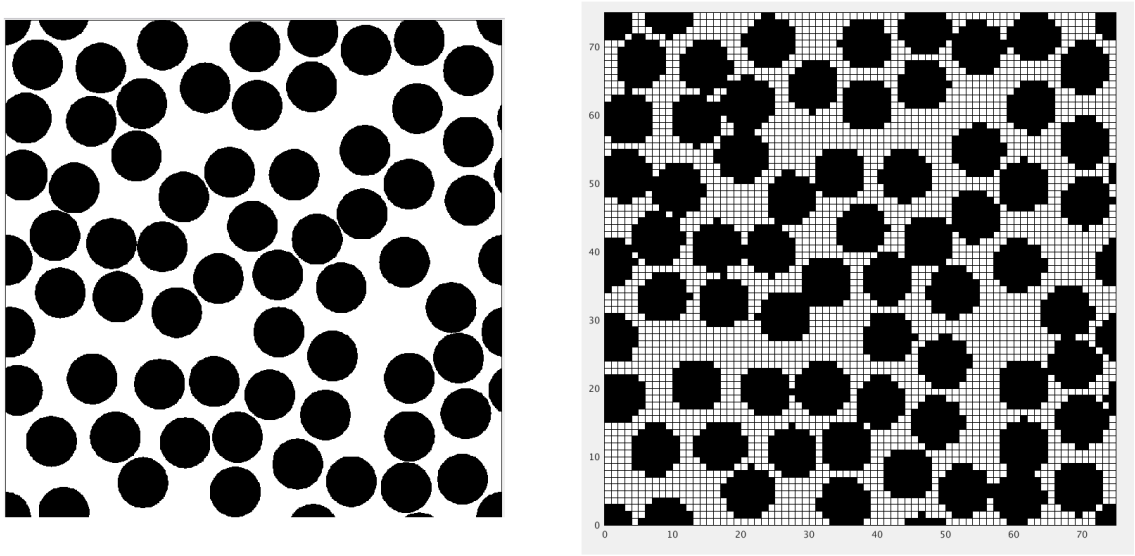

Figure 6.8. GMC RUC of a random microstructure

The image processing based meshing algorithm hence provides a convenient solution for generating microstructural RUCs for random configurations of two-phase doubly periodic material systems. Furthermore, the 2D digital image array also permits easy detection of interfaces by scanning for variations in pixel tone. Changes in pixel tones signify a change in material, which can

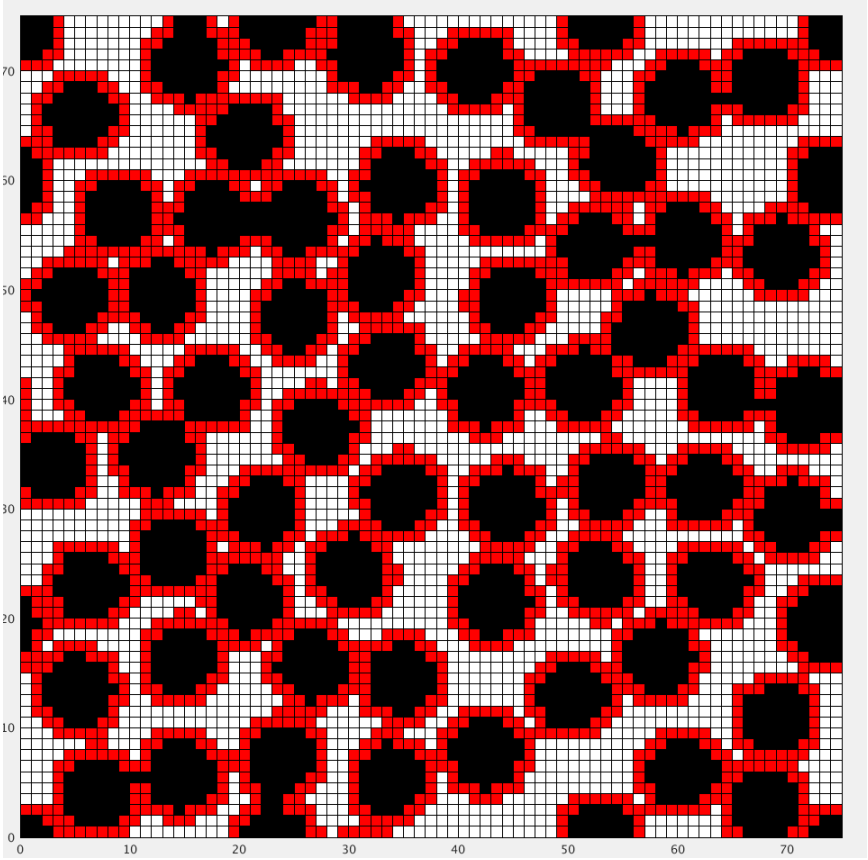

Figure 6.9. Detection of interface subcells

then be marked as a material interfacing subcell.

$$\boldsymbol{P}^{(\alpha\hat{\beta}\gamma)} - \boldsymbol{P}^{(\alpha\beta\gamma)} = \begin{cases} 1, & \text{Fiber/matrix interface subcell} \\ 0, & \text{No interfaces} \\ -1, & \text{Matrix/fiber interface subcell} \end{cases} \tag{6.37}$$

$$\boldsymbol{P}^{(\alpha\beta\hat{\gamma})} - \boldsymbol{P}^{(\alpha\beta\gamma)} = \begin{cases} 1, & \text{Fiber/matrix interface subcell} \\ 0, & \text{No interfaces} \\ -1, & \text{Matrix/fiber interface subcell} \end{cases} \tag{6.38}$$

Interfacing subcells will be assigned non-zero values of R_{11}, R_{12}, and R_{13}, while all non-interfacing subcells will be assigned null values for R_{ij}. This process is illustrated in Figure 6.9,

which shows the detected interface subcells of a random microstructure in red. The RUC can now be analyzed under static loading conditions for material response with explicit consideration for weak interfaces.

6.4 Effect of Interface at the Microstructure

The approach detailed in the previous section is implemented in FORTRAN using a MATLAB preprocessor that generates the random microstructure RUC. The analysis is performed using average values for fiber volume fraction and matrix properties to compute the deterministic response, as well as with distributions for these variables to determine the stochastic response. The RUC size is controlled at 75×75 subcells and the applied constant strain rate is 0.001 strains per second to ensure quasi-static conditions. Fiber properties are assumed to be linear-elastic orthotropic and are based on standard tests and data presented in manufacturer data sheets (Hexcel 2016) and detailed in Table 2.2. The matrix properties and damage parameters are presented in Table 3.2.

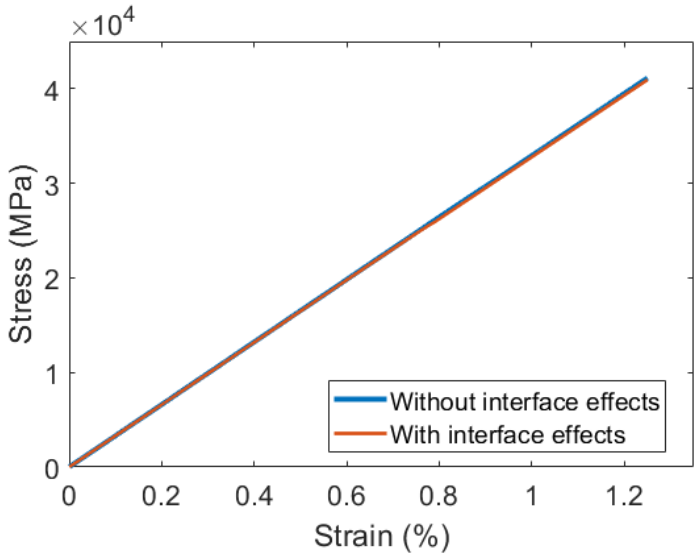

Figure 6.10. Uniaxial stress-strain response in the fiber direction

The effect of the weak interface on elastic response of the composite material is investigated first. For the analysis of uniaxial elastic response in the fiber direction, a uniaxial strain is applied in the fiber (11) direction with stress-free boundary conditions in the non-loading directions. The global stress in the 11 direction is then compared against applied strain ($\bar{\boldsymbol{\sigma}}$ vs. $\bar{\boldsymbol{\epsilon}}$), where the slope of this curve is considered to be the uniaxial elastic modulus in the fiber direction. The 11 stress-strain response can be seen in Figure 6.10 and it is apparent that the weak interface does not play a significant role in determining elastic properties in the fiber direction of the composite material. The reason for this effect can be deduced by reviewing the fiber-pullout mechanism as computed by the nanoscale study shown in Figure 6.4. The general elastic effect of the interface can be idealized as a spring like structure connecting the fiber and the matrix substructure as visualized in Figure 6.11. Under perfectly bonded conditions, the interface behaves as a spring with an infinite spring constant ($= \infty$) where perfect continuity in displacements and tractions are observed between the fiber and the matrix. However, under weak interface conditions the idealization will consist of a spring with a real non-imaginary spring constant ($> \infty$) causing loss in displacement and traction continuity between the fiber and the matrix. Failed interfaces could be visualized as a spring with 0 spring constant. It can then be concluded that as the spring constant increases (stiffer springs) the response of the interface approaches perfect bonding behavior. The atomic simulations of the fiber-pullout shows the stiffest linear response leading to an almost perfect bonding-like behavior. Hence, the weak interface does not affect the elastic properties of the composite in the fiber direction.

Table 6.1. Comparison of 11 elastic modulus from GMC, linear FE, and literature

Method	E_1 (GPa)	Error relative to literature (%)
Literature	164 (σ_{dev}=11.85)	-
GMC with perfect interface	165.343	0.8123
GMC with imperfect interface	164.89	0.5398

The elastic properties obtained using the GMC perfect/imperfect interface model is com-

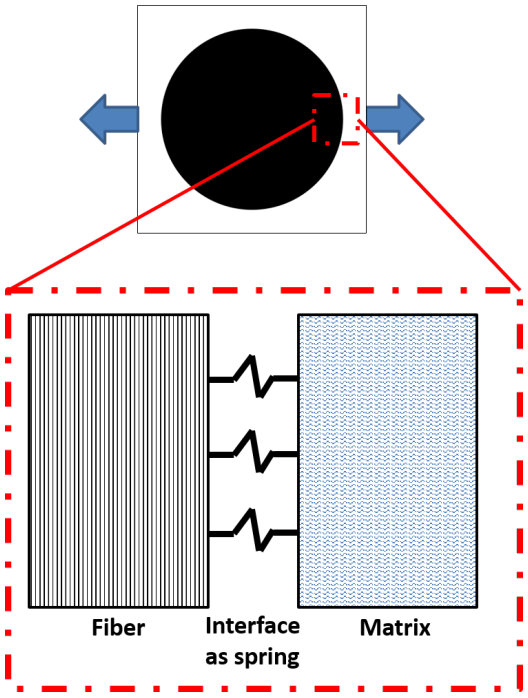

Figure 6.11. Idealization of the interface

pared with literature values and is reported in Table 6.1. It is interesting to note that the imperfect interface leads to a .27% decrease in elastic modulus compared to the perfect interface model, which brings it closer to the experimentally observed value by .2725%.

The response under transverse normal loading is also measured with and without the interface effects. The interface effects lower the elastic response of the composite system by 7.93% as can be seen in Figure 6.12. Using the spring analogy, and referring to the nanoscale matrix pullout studies in Figure 6.2, the mechanism for the lowered elastic response can be understood. The nanoscale simulation of the matrix pullout produces a ductile-like response with reduced stiffness as compared to matrix shear and fiber pullout. This leads to a compliant behavior that reduces the stiffness of an ideal and perfectly bonded composite system in the transverse direction. Figure 6.13 exhibits the comparison of the predicted transverse response by the GMC model with interface effects, the subcell model with damage but perfect bonding utilized in section 5.3.1, and experimental data from Gilat et al (Gilat, Goldberg, and Roberts 2002). There appears to be excellent

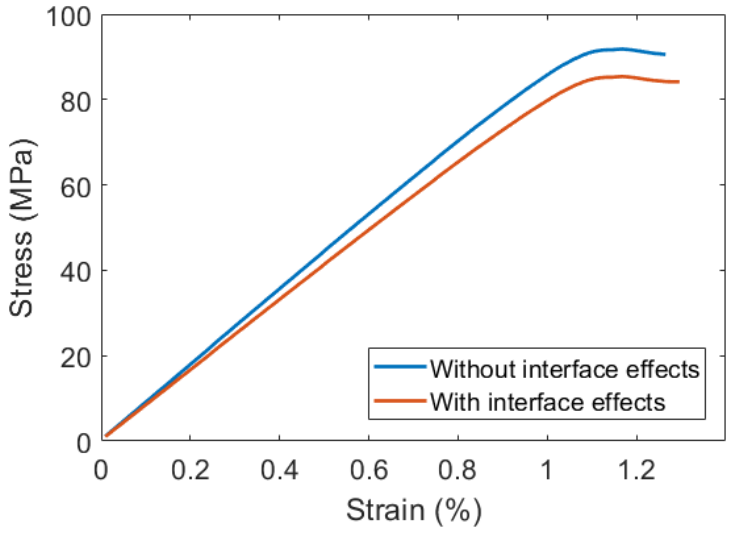

Figure 6.12. Uniaxial stress-strain response under normal loading transverse to the fiber direction

convergence of the elastic response between the experimental data and the predicted values from the GMC model with imperfect interface. Although, the subcell model performed reasonably, an 8.3% error remained in the elastic property predictions. This result proves that the imperfect interface physics plays a significant role in material behavior and this condition should be employed whenever possible for accurate analysis of material properties. Furthermore, it also shows the viability of using nanoscale models to accurately characterize the interfacial properties.

The effects on the nonlinear regime can also be investigated to reveal insights into damage and failure mechanisms. The progression of damage in the microstructure under transverse normal loading can be seen Figure 6.14, which is simulated by applying the atomistically informed damage model, developed in Chapter 3, for evaluating the local response $\sigma_{ij}^{(\alpha\beta\gamma)}$ and $\epsilon_{ij}^{(\alpha\beta\gamma)}$. The application flow is similar to the one used in the subcell model in section 5.3.1. The global properties are converted to subcell response using the GMC concentration tensor C^*. The subcell response is scrutinized for damage using the dissipation inequality, and if the subcell enters into the damage phase, the state variables are updated appropriately. Homogenization of the modified subcell response then provide the updated global response. Figure 6.14 shows progression of dam-

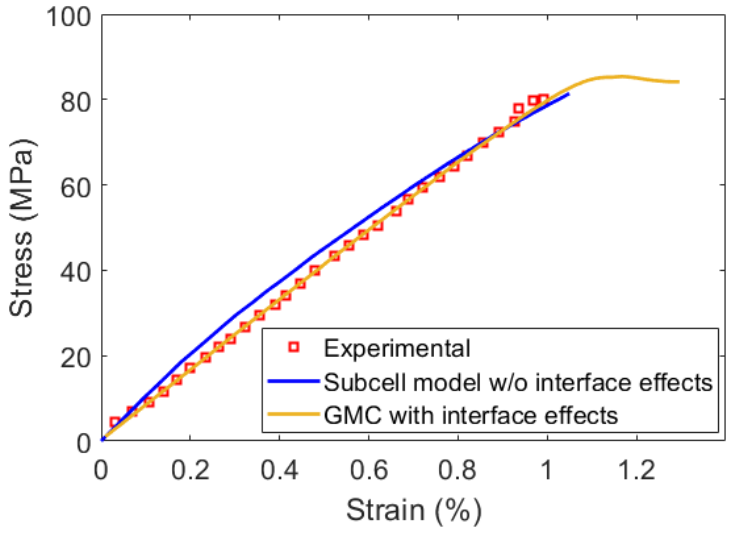

Figure 6.13. Comparison of predictions and experimental transverse response

age in the subcells under global transverse normal loading in the 22 direction. Damaged subcells are shown in red, healthy subcells in blue. The predictions show the classic propagation of transverse splitting cracks that travel from fiber to fiber under mechanical loading (Kashtalyan and Soutis 2000). It can be noted that similar damage progression and transverse splitting was also predicted through a purely numerical finite element approach (see Figure 5.5) and through the purely analytical micromechanics subcell approach (see Figure 5.12). The analytical technique did not deliver significant local resolution at the fiber/matrix length scale and could not simulate random microstructures explicitly. However, the analytical technique showed high computational efficiency. The numerical finite element (FE) approach does not exhibit any limitations towards local resolution or explicit microstructure integration. However, the penalty for higher resolution is an exponential increase in required computational power, which remains high even for simplistic models. The GMC approach combines the advantages of the numerical and analytical techniques, with a package that allows explicit generation of random microstructures, provides reasonable local field resolutions, and that consumes moderate computational resources even for nonlinear analysis of large microstructures. Hence, the approach developed in this chapter fulfills

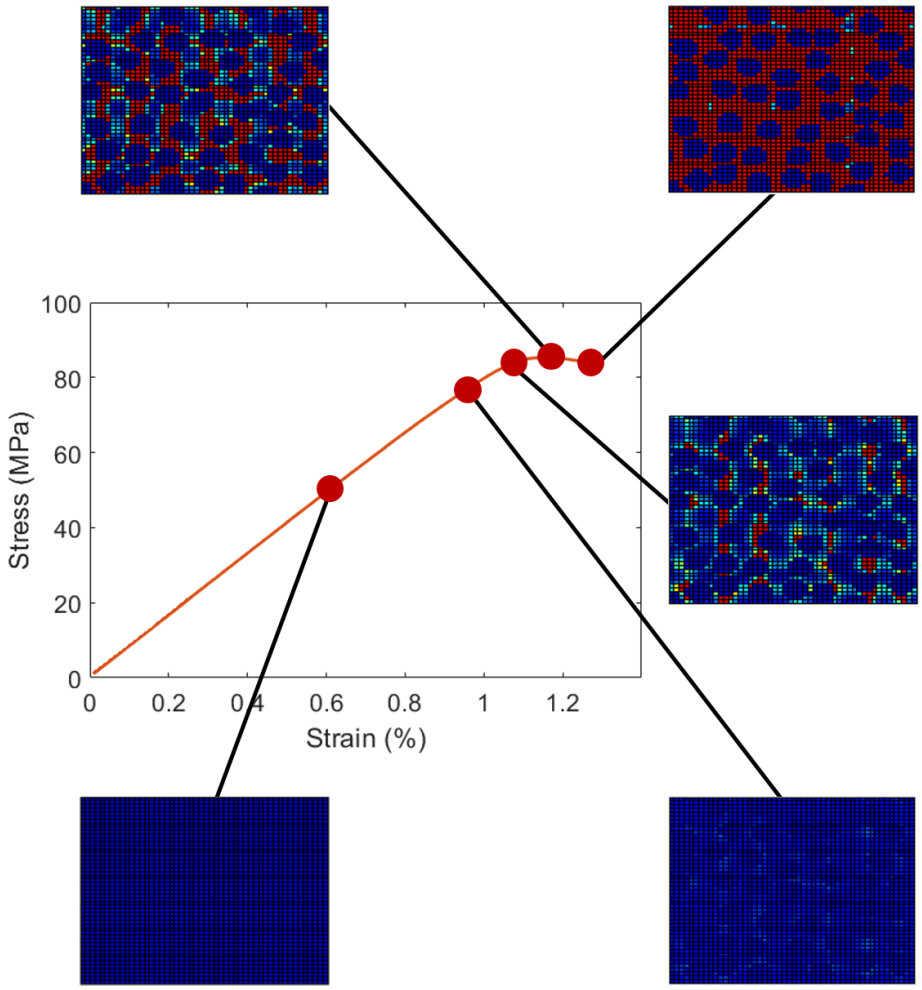

Figure 6.14. Progression of damage in matrix under transverse normal loading

the requirement for practical multiscale models and provides deep insight into advanced composite material performance in the linear and non-linear regime, while also being deployable for macroscale modeling.

In addition to the advantages described above, the GMC approach also includes the possibility of performing stochastic analysis by introducing random variables with characterized uncertainty. Section 5.3.2 described a methodology for incorporating the volume fraction and the polymer crosslinking degree as random variables, with the randomness in volume fraction characterized through microscopy studies, and randomness in crosslinking degree characterized from stochas-

tic MD simulations. A similar approach is used in this section, where the volume fraction, which is used to control the microstructure, is randomly sampled from the normal distribution of experimentally observed values, and the crosslinking degree for each matrix subcell is randomly sampled from the normal distributions presented in Chapter 2. The material response for at least 500 mutually independent microstructures with interface effects are then analyzed using GMC. The maximum and minimum bounds for the response in the transverse normal direction is illustrated in Figure 6.15b with an equivalent comparison obtained from the subcell model from section 5.3.2 and the experimental response from Gilat et al (Gilat, Goldberg, and Roberts 2002).

The comparisons in Figure 6.15 clearly show the effect of the weak interface, where even a minimum response from the subcell model was unable to capture the experimentally observed elastic properties. The predictions from the GMC approach bounds the experimental observation, further exhibiting the appropriateness of this approach and the importance of utilizing the imperfect bonding hypothesis. At the nonlinear regime, the GMC model shows increased plastic flow before failure for low elasticity samples while high elasticity samples show limited plastic flow representing a brittle response. The plastic flow for low elasticity samples is affected by the

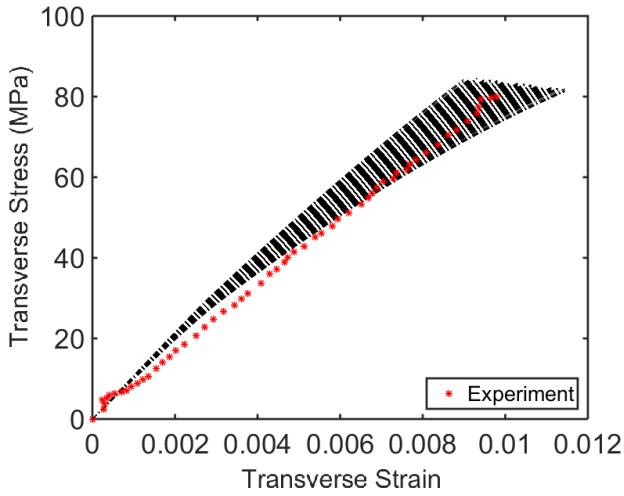

(a) Stochastic response using the subcell method

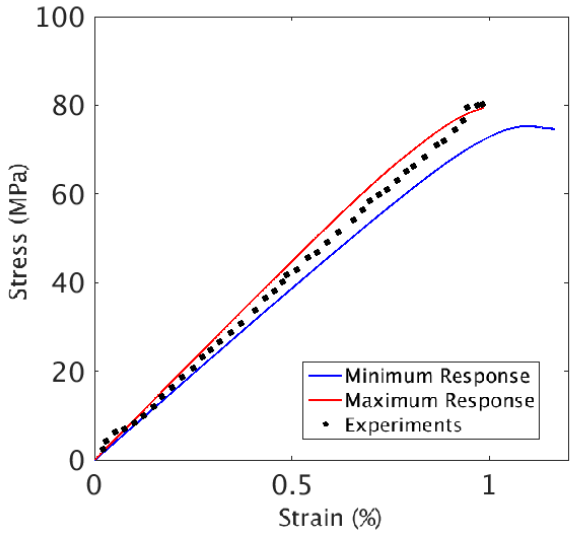

(b) Stochastic response using GMC with interface effects

Figure 6.15. Stochastic analyses under transverse normal loading with the atomistically informed damage model

imperfect bonding due to increased ductility presented by the weakening of the fiber matrix interface. However, after comparisons with the subcell approach it can be inferred that weak interfaces do not contribute critically towards the nonlinear response; the significance is limited to a slight increase in plastic flow under low elasticity conditions. Additionally, the bounds for elastic and inelastic response are found to be relatively tight.

The stochastic response investigation is also performed for transverse shear loading. Figure 6.16 shows the comparison of the stochastic analysis of material response under transverse shear loading using the subcell model with perfect interface and the GMC approach with imperfect bonding. Both approaches make use of the atomistically informed damage model to predict damage in the matrix. Although there is a slight decrease in the elastic response due to the weak interface, the main significance of imperfect bonding can be seen in the nonlinear regime. The subcell model in Figure 6.16a exhibits an unrealistic material response at high strains. This occurs due to the perfect bonding between the fiber and matrix that allows load distribution between these

two constituents until damage in the matrix. Due to the lower shear modulus of the matrix as compared to the elastic modulus, failure of the matrix constituent, under transverse shear strain, can only occur with the introduction of considerable energy. Hence, under a perfect interface assumption the composite system cannot fail until high strains are reached. This mechanism is not consistent with experimental observations since the primary mechanism of damage initiation under such conditions is through fiber/matrix interface failure, which in turn revokes the fiber contribution to the load distribution, thus leading to rapid failure of the matrix. Since the GMC approach utilizes an imperfect interface characterized for matrix shear, the fiber/matrix interface damage is simulated, leading to rapid system failure. The prediction of this response is seen in Figure 6.16b, where failure of the composite system occurs at practical levels of strain (as compared to Figure 6.16a). Minimal plastic flow is observed for stiffer samples, while a moderate amount of plastic flow is seen for compliant samples, even though the plasticity displayed is much lower than under transverse normal loading. After the fiber/matrix interface failure, the load redistribution onto the surface of the matrix quickly depletes its load carrying capabilities, resulting in minimal plastic flow after interface failure.

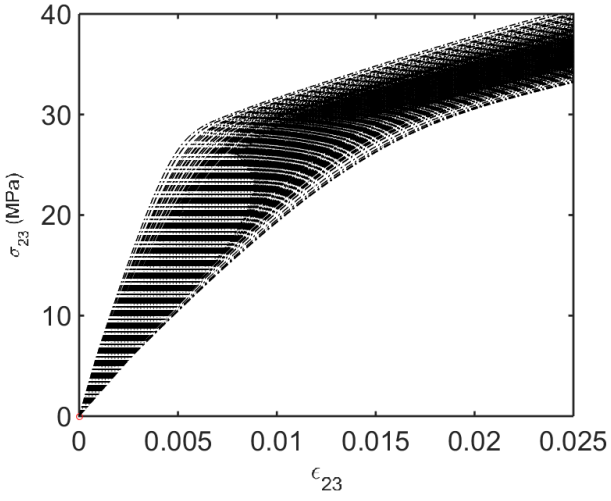

(a) Stochastic response using the subcell method

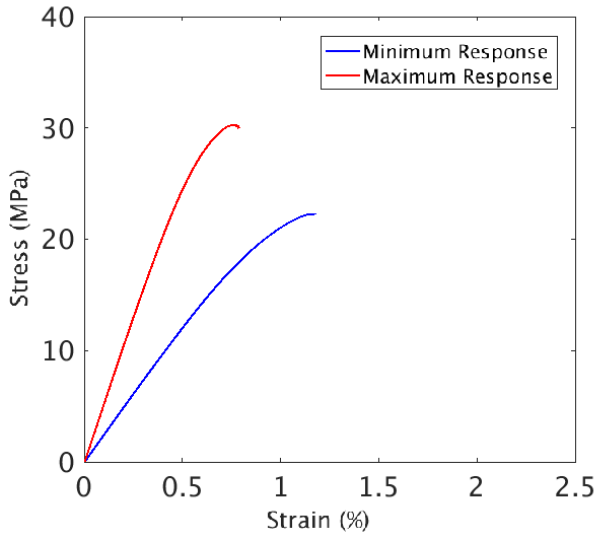

(b) Stochastic response using GMC with interface effects

Figure 6.16. Stochastic analyses under transverse shear loading with the atomistically informed damage model

6.5 Summary

This chapter introduced the concept of weak bonding between the fiber matrix interfaces, which motivates the need to incorporate this effect in the mathematical analysis of advanced composites. Due to the nanoscale nature of these interfaces, the characterization of these interfacial effects through atomic modeling was reviewed. This chapter also introduced the semi-analytical GMC approach for homogenizing complex triply periodic microstructures. This methodology was modified to include imperfect interface effects characterized by the MD simulations for a consistent modeling approach of the weak interface between the fiber and matrix. Finally, advanced composite microstructures were analyzed using this GMC approach under stochastic conditions to investigate the effect of the weak interface on the elastic and inelastic material response. The analysis revealed the importance of including weak interfaces for accurate predictions of the elastic response of composites. Furthermore, it also displayed the need for introducing weak interface

effects for the inelastic analysis of these material systems, especially under shearing conditions, which may lead to fiber/matrix interface failure. Simulating such mechanisms can have considerable effects in predicting the composite system response. It was observed that composite system failure may be inadequately modeled without the weak interface effects. This is especially important for shear loading due to the complexities involved in experimentally characterizing the material response. Hence models that can predict this response can be of great use to design engineers. To demonstrate the usability of such models, the next chapter will utilize the developed multiscale framework with imperfect interfaces for the analysis of practical composite structures.

Chapter 7

MULTISCALE MODELING FRAMEWORK FOR ANALYSIS OF BONDED COMPOSITE STRUCTURES

7.1 Introduction

A primary objective of the research presented in this dissertation is the integration of elastic and inelastic nanoscale information in multiscale nano-to-macro analysis of advanced composites, such as carbon fiber reinforced polymer (CFRP) composites and carbon nanotube (CNT) enhanced CFRPs. The previous chapters 2-6 discussed development of a novel methodology for bridging the nano-, submicro-, and microscale as well as elastic and inelastic information for the analysis of advanced composite microstructures. These methods include high and low fidelity damage models that factor in the effects of a weak fiber/matrix interface. which were validated against experiments and numerical benchmarks. In this chapter, a multiscale framework for the structural analysis of practical composite components is detailed, integrating the previously developed nano- to microscale bridging techniques for a comprehensive multiscale study of damage initiation and failure. Specifically, the adhesively bonded composite joint will be used as a case study in this investigation.

Adhesive bonding of composite components offers numerous benefits, over traditional joining methods like riveting and fastening. Advantages of adhesive bonding include improved stress distribution in bonded joints, increased joint stiffness, increased vibration damping, and fewer mechanical fasteners and fillers, resulting in reduced weight and the ability to join dissimilar materials (Brotherhood, Drinkwater, and Dixon 2003; Allin 2002). These benefits have made adhesively bonded composite joints increasingly popular for aerospace industry applications. However, due

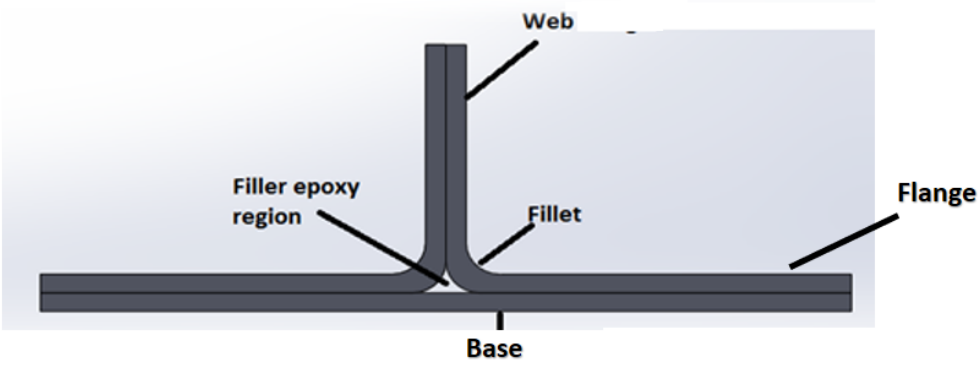

Figure 7.1. Components of the T-joint

to a lack of appropriate material models as well as comprehensive damage initiation, progression and failure criteria, mechanical fasteners (bolts) are often introduced when adhesively bonded structures are used in primary load-bearing applications. This current conservative design practice leads to the 'overdesign' of composite structures.

Primary service- and environment-induced damages in composite bonded joints include crack initiation and propagation along the interface, cracking within the adhesive layer (cohesive failure), adherent failure, adhesive failure, or a combination of these issues (Yarrington et al. 2005). In most of the reported failure models, cohesive and adhesive failures are seen as indistinguishable (Brotherhood, Drinkwater, and Guild 2002) due to the difficulties associated with the modeling of the bondline, interfacial stresses, and stress singularities. Investigation of the response of the structure at the bondline is important since containing failures within the adhesive layer is preferred in adhesive joint design. The bonding layer is susceptible to defects including gross defects (e.g. debonding and cracking), poor cohesion, and poor adhesion. Based on these risks associated with predicting the strength and residual life of bonded joints, adhesive bonding is not extensively used even though it is highly desirable for major structural components in military and commercial aircrafts.

Numerous methodologies have been reported for the mechanical and failure analysis of ad-

hesively bonded joints including closed-form analytical equations, numerical methods, and phenomenological models based on experiments. The elementary shear lag analysis and resulting closed-form analytical equations for lap joints with simple geometries have led to the development of scarfing (local thickening of the adhesive layer) to alleviate peel stresses in bonded joints (Volkersen 1938; Cornell 1953; Hart-Smith 1973). However modern joints cannot be analyzed with simplistic assumptions and require the introduction of complex joint geometries, damage and plasticity, and complex stress states for an exhaustive analysis. Numerical methods, such as variational techniques and finite element (FE) analysis have been used for performing damage and failure analysis of various bonded joints including a benchmark investigation of CFRP single lap joints conducted by Diaz et al (Harris and Adams 1984; Diaz et al. 2010). Through these techniques it was systematically proved that the elastic properties of the adhesive material have considerable impact on the response of single lap joints (You et al. 2008). Since then, several damage modeling techniques have been demonstrated for integration with FE analysis such as analytical fracture mechanics (J-integral method), numerical fracture mechanics (virtual crack closure technique and extended FE method), continuum mechanics and plasticity approach, and cohesive zone modeling. The continuum and plasticity damage mechanics approaches homogenize the properties of the adherends, adhesives, and the adherend/adhesive interface while capturing composite damage using macro level failure criteria (Fish and Yu 2001; Ghosh, Bai, and Raghavan 2007). Such treatments do not account for the multiscale nature of damage evolution and lead to a phenomenological understanding of damage and failure.

Numerical fracture mechanics techniques such as the extended FE method has been used to model crack propagation and predict the fracture behavior of thin structural epoxy adhesive bonds under tension; however, due to the assumed nature of energy dissipation, unphysical crack propagation was reported (Campilho et al. 2011). The virtual crack closure technique was also used to simulate damage propagation in a CNT-enhanced adhesive layer of a composite T-joint, and

although this technique showed some success in predicting crack propagation, it was limited by difficulties in convergence and the requirement of *a-priori* knowledge of the crack path. Hence, it could not be used for general investigations and was limited to certain configurations of the bonded joint with known damages (Hasan, Chattopadhyay, and Liu 2014). Additionally, linear elastic fracture mechanics formulations cannot be easily integrated with plastic flow and plasticity calculations by definition, which can considerably complicate failure analyses.

The above discussion presents a clear rationale for a multiscale approach that offers accurate damage and failure analyses of bonded composite joints and that can accommodate complex joint geometries while integrating the elastic/plastic characteristics of the thin adhesive bondline. In this chapter, a multiscale modeling approach is developed to assess the mechanical property degradation, damage, and failure in adhesive bonded composite joints under mechanical loading. This is accomplished by introducing a concurrent framework that integrates the previously developed atomistically informed multiscale damage model and the imperfect interface generalized method of cells (GMC) micromechanics technique. GMC permits a comprehensive nano- to structural level analysis while accounting for the material constituents and interfaces. Additionally, this multiscale framework is validated using experimental observations at the global scale and mesoscale whereby global load-displacement response and mesoscale strains are compared at the 'hot-spot' regions. This study effectively addresses existing technology gaps that impede the widespread use of adhesively bonded joints in structural applications.

7.2 Experimental Investigation of T-joints Under Pull-off Loading

This section describes the manufacturing, testing, and characterization process used in the experimental investigation of damage and failure mechanisms in adhesively bonded composite T-joints under pull-off loading. In the experimental set up, the T-joints were machined from com-

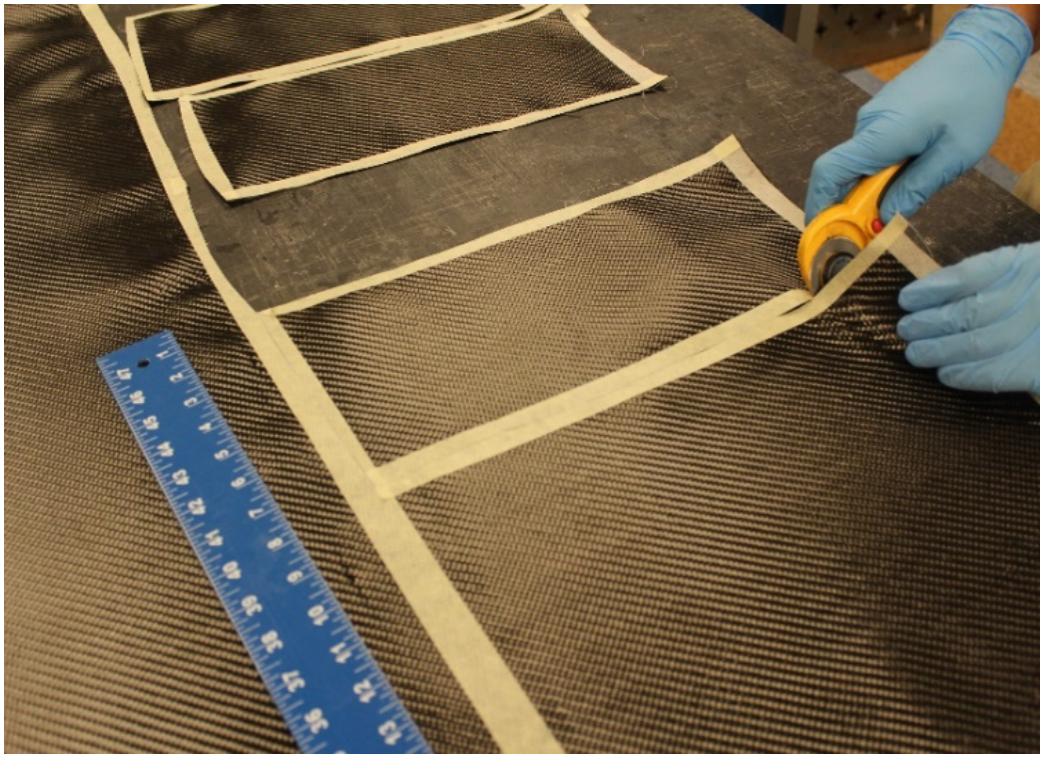

Figure 7.2. Plain weave fabric plies

posite stiffened panels manufactured using the wet layup process. To construct the stiffened panels, plies were cut from IM7 carbon fiber plain weave fabrics to which the resin-hardener mixture (Epon E862 Resin and Epi-Cure 3290 hardener at a 100/27 weight ratio) was applied for uniform wetting of the ply. This process was used to generate the laminate stack. The composite laminates were placed between U-shaped aluminum molds and a surface plate, and subsequently clamped as shown in Figure 7.3. The base skin laminate was manufactured using three plies. Each section of the web was also manufactured using three plies, such that the web totals six plies, and the web + skin section totals six plies. The wet, clamped, pre-cure composite structure was then placed in a vertical heated press to cure under a standard cure-cycle for IM7/Epoxy composite laminates. Vertical pressure was applied by a hydraulic press and horizontal pressure, applied on the web section, was maintained through the mechanical clamps during the curing process. Following the curing stage the stiffened panel was sectioned using a diamond tipped cutting saw to generate the

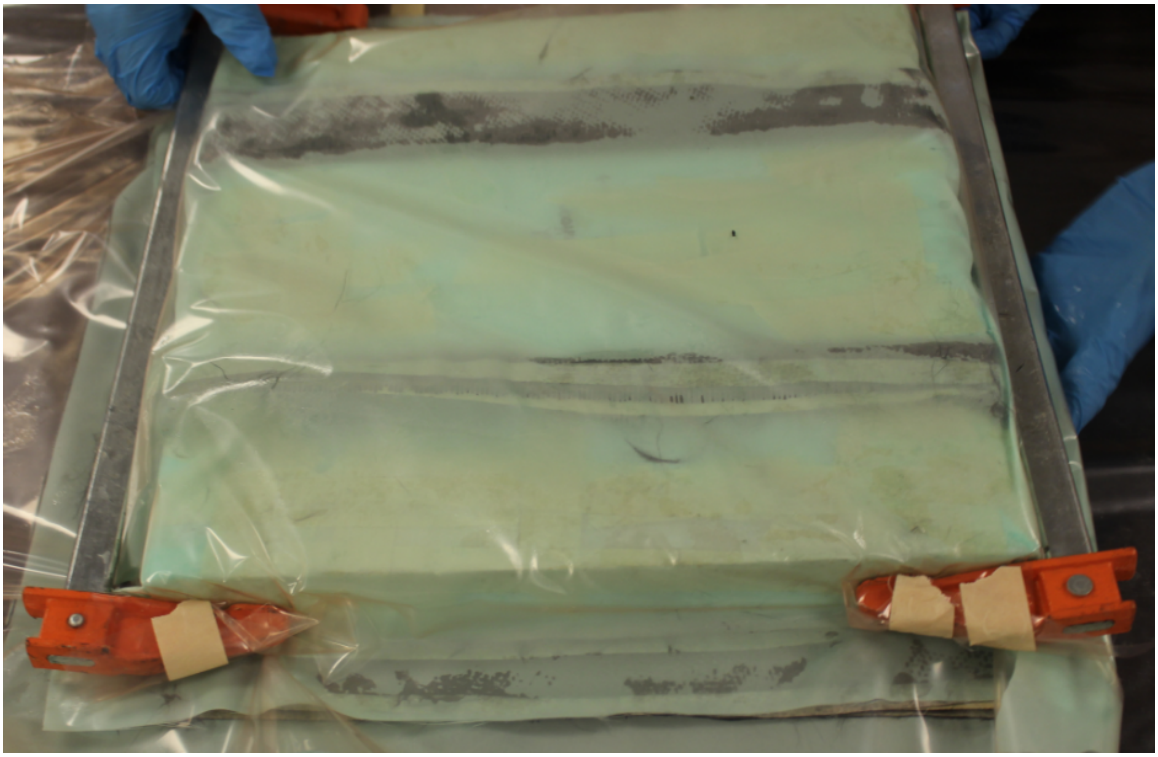

Figure 7.3. Clamped pre-cure stiffened panel within mold

T-joint geometries, which were also drilled using diamond tipped drill bits to generate the end-holes. The dimensions of the T-joint geometry are detailed in Figure 7.4. The filler region, which encompasses the interface of the web plies, fillets, and the skin plies, were further sectioned for microscopy investigations.

In order to conduct microscopy studies, a microscopy-ready specimen preparation stage is necessary. The sectioned filler region, which plays a significant role in the mechanical response of the T-joint, was placed in an epoxy-cured holding puck and polished using a multistage polishing process. The polishing stages include grinding the face of the specimen using an abrasive sheet under constant pressure and gradually increasing grit sizes. The final stage of the polishing process requires grinding the face using a diamond suspended solution for ultra-fine polishing. This process is performed for microscopic clarity, ease of handling, and generating an even surface topology at

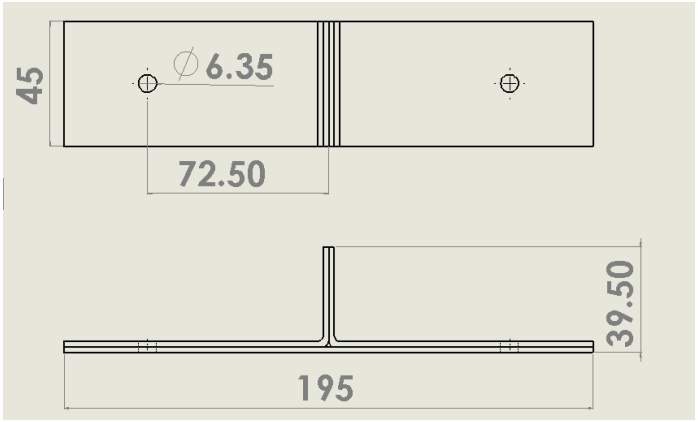

Figure 7.4. T-joint dimensions

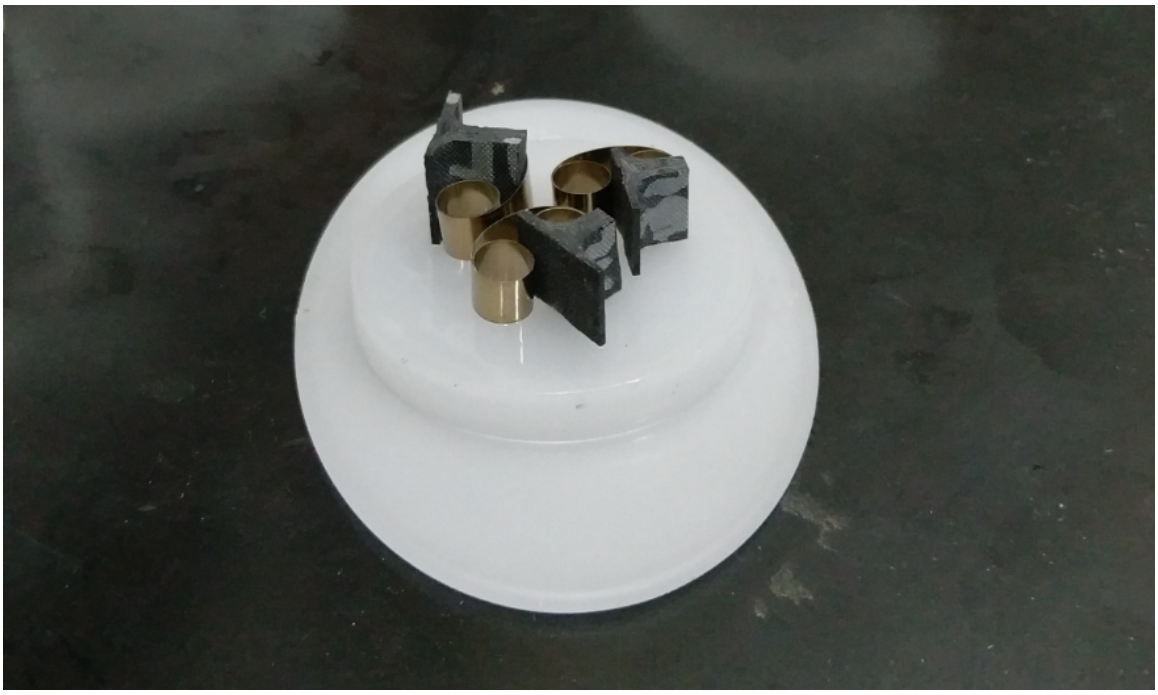

Figure 7.5. Preparation for the polishing stage

the microscale. The Zeiss LSM 780, confocal microscope was then used to study the mesostructure of the samples under fluorescent light and the DAPI filter. The natural fluorescence of the epoxy matrix was used to enable a high contrast characterization of the mesostructure of the filler region.

Figure 7.7 shows the filler region of the epoxy-matrix T-joint under fluorescence microscopy.

Figure 7.6. Zeiss LSM 780 confocal microscope used for microscopy of the T-joint specimens

It was observed from the microscopy images that the skin plies crimped during the curing process, possibly due to hydrodynamic pressures in the matrix of the filler region from vertical forces applied by the hydraulic press. Large matrix gaps, along with a differential in winding rates between the web plies at the fillet regions, were also observed. It is necessary to include such deviations from the ideal filler geometry in simulated T-joint models to accurately recreate the structural response, particularly since these deviations may cause a shift from ideal failure mechanisms.

The composite bonded T-joints were tested in the tension pull-off configuration. The tests were performed on a Test-resources universal testing machine, with a 5000N load cell. The

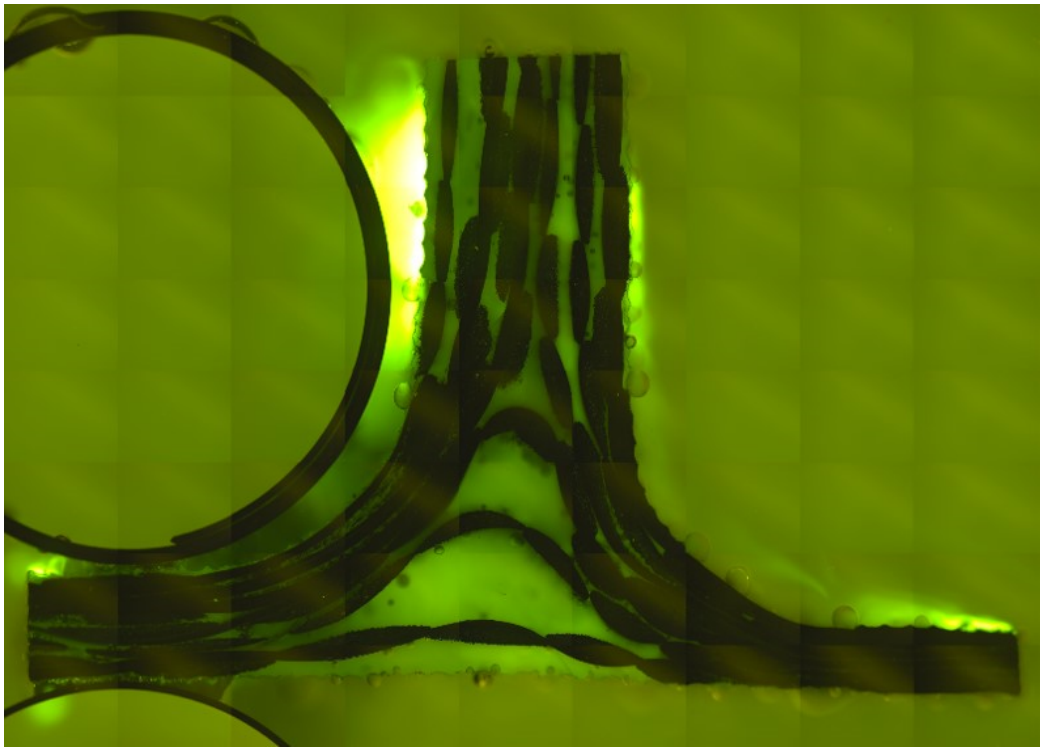

Figure 7.7. Filler region of the T-joint under confocal microscopy

crosshead displacement and the load cell force response was recorded and analyzed. The web of the T-joint was gripped in the Test-resources mechanical grips, with marks noting the grip ends in order to measure any slipping of the grip. To ensure pure tension conditions with fixed flange edges, the fixture was designed with screwed in platforms. The T-joint flanges were fixed in position during the duration of the test such that there was no rigid motion at the flange ends. The loading and boundary constraints are schematically illustrated in Figure 7.9. Three dimensional digital image correlation (DIC) was used to measure the displacement and strain field contours on the face of the T-joint specimens. The DIC system tracks a random speckle pattern painted on the face of the specimen, as shown in Figure 7.10, and uses this random grid of speckles to calculate relative and rigid body displacements. The displacement field is then post-processed to obtain corresponding strain fields. The stereo-vision capabilities of the GOM ARAMIS 5M DIC system, used in these tests, allow accurate in-plane and out-of-plane displacement measurement as

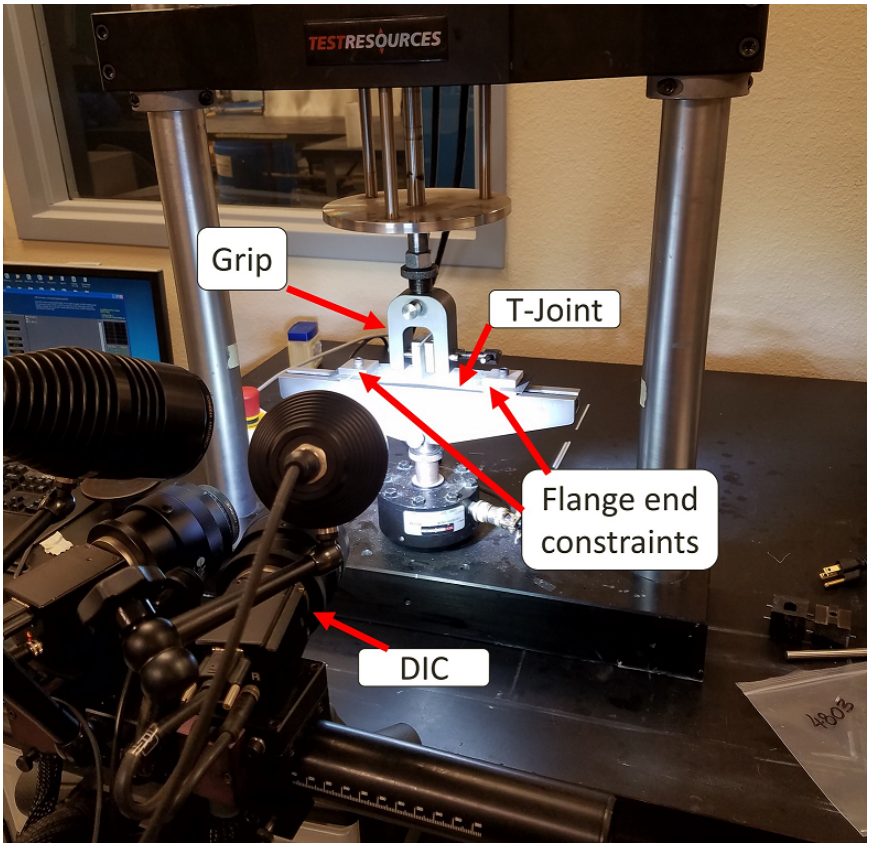

Figure 7.8. T-joint pull-off test setup

well as strain on the face of the T-joints. The pull-off tests were performed at a displacement rate of 1 mm per minute, to ensure quasi-static testing conditions. A total of seven specimens were tested, out of which two were discarded due to measurement errors. Figure 7.8 displays the test setup with the DIC system and the T-joint in focus.

Figure 7.11 exhibits the load-displacement response for the tested T-joint specimens. The end of the load-displacement curves displayed in Figure 7.11 corresponds to the presence of macroscale cracks in the T-joint. Although the joint can bear mechanical loads until complete separation of the web and the skin occurs, structural failure of the joint is largely considered to transpire during first ply separation. Figure 7.12 shows the strain contours in the loading direction from the DIC system at damage initiation. It can be observed from the strain contours that the initial

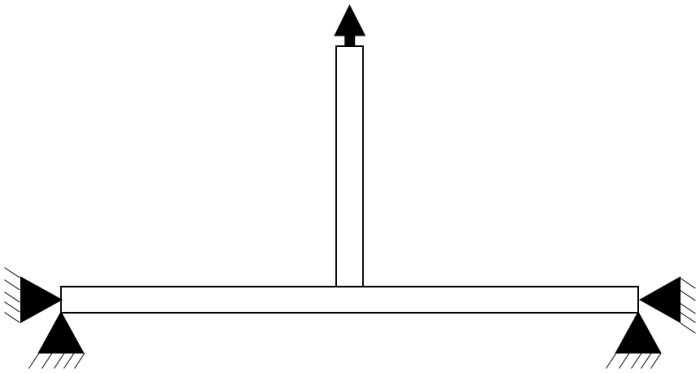

Figure 7.9. Loading and boundary conditions

Figure 7.10. Speckle pattern on the face of the T-joint

cracks begin at the fillet rather than the middle of the filler region, as may be predicted based on the idealized geometries of the T-joint filler. This can be due to a combination of the skin ply crimp and the large epoxy region between the fillet plies. The crimped ply reinforces the epoxy filler and leads to the creation of the fillet as the region of lowest resistance to damage. The fillet region damage then causes cracks to propagate along the fillet, leading to eventual debonding of the bonded joint.

The experimental data obtained in this section provides a benchmark for T-joint models, which need to reproduce the mechanisms observed during pull-off testing of the adhesively

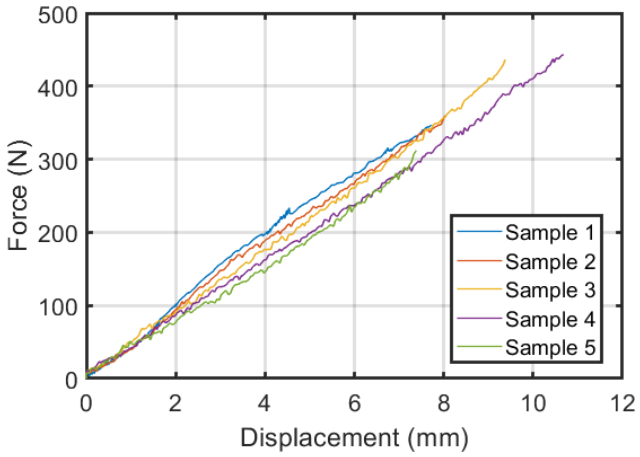

Figure 7.11. T-joint load-displacement response under pull-off loading

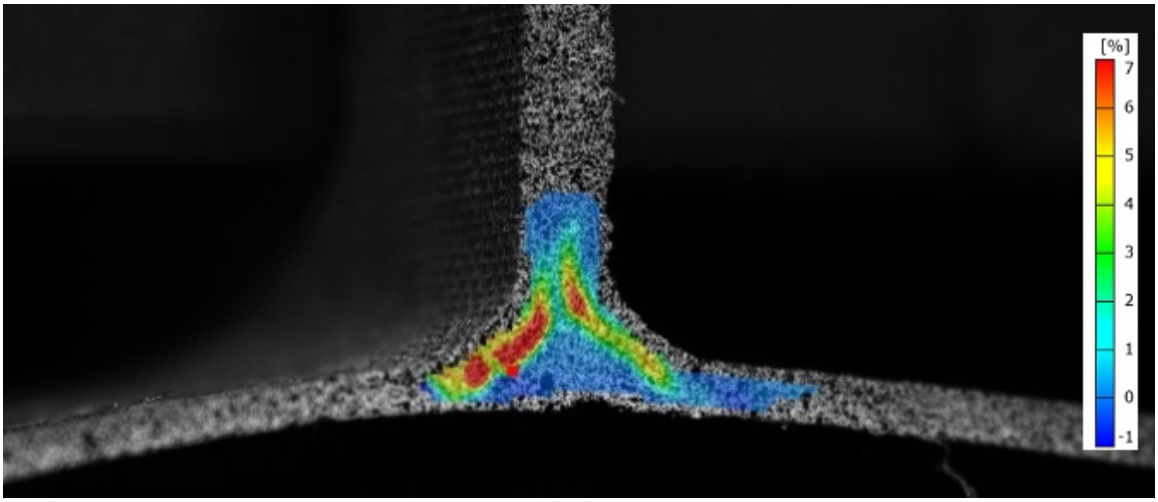

Figure 7.12. DIC strain contours in the direction of loading

bonded composite T-joints. At the macroscale, an accurate T-joint model must display the same load-displacement curve seen in Figure 7.11 with minimum calibration, and at the mesoscale, the fillet region damage characteristics must be captured. Further investigations at the microscale can then be conducted to understand the damage mechanisms occurring at the fiber/matrix length scale, which may provide insights for manufacturing superior composite T-joints.

7.3 Multiscale Structural Analysis Framework

The multiscale model for the analysis of bonded T-joints developed in this section consolidates information from the previous chapters to create a nano-to-macroscale analysis framework, schematically shown in Figure 7.13. The atomistic information generated in chapters 2, 3, and 4 informs the matrix behavior, and the microscale model developed in chapters 5 and 6 models the microstructure. The T-joint macro- and mesoscale details are affected by the mesoscale and structural information, as presented in section 7.2.

The 3D full-scale T-joint geometry is generated in ABAQUS using the actual measured dimensions of sample 1. The geometry is created in four parts: (1) the web, (2) the left base and flange, (3) the right base and flange, and (4) the filler region, which is assembled to create the complete geometry. The four individual parts are exhibited in Figure 7.14. Assembly of the parts automatically ties adjacent nodes such that the assembled model is numerically equivalent to a single part model. The three planar parts 1, 2, and 3, resemble a composite laminate with six plies. These parts are idealized as a set of perfectly rectangular composite plies with constant thickness and linear elastic orthotropic properties. Additionally, the plies are also assumed to be perfectly bonded with negligible interfaces such that no matrix-rich regions exist in these parts. The idealization of the fringe parts allow for higher computational efficiency of the T-joint model and is justified since the experiments did not indicate any substantial damaging mechanisms in these areas. However, a multiscale approach is utilized to obtain the elastic properties of these composite plies.

The elastic properties of the composite plain weave fabric ply can be fully defined by its stiffness or compliance matrix. Typically, these properties are obtained through a series of mechanical coupon tests that measure uniaxial response in various normal and shear directions, and that can be analyzed to estimate the elastic constants (Carlsson, Adams, and Pipes 2014). Although such

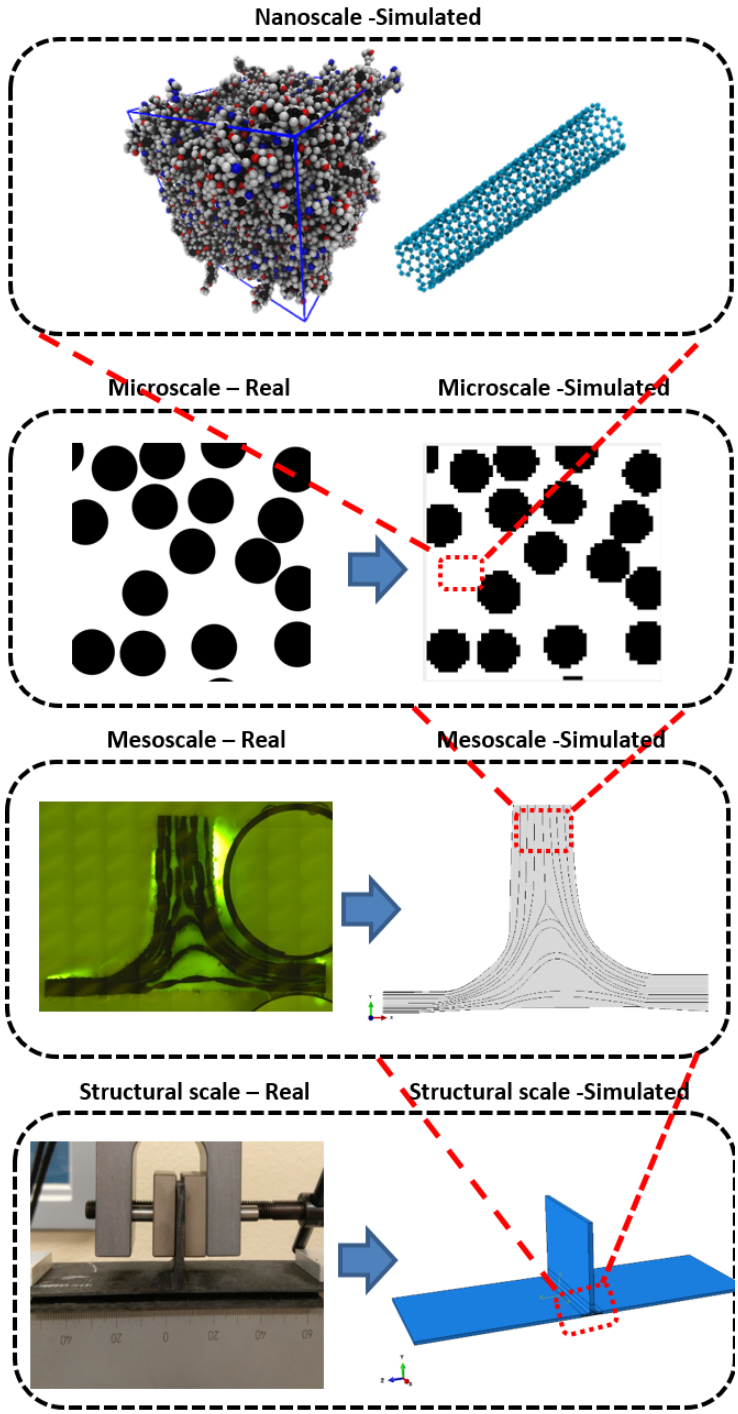

Figure 7.13. Atomistic to structural multiscale modeling scheme

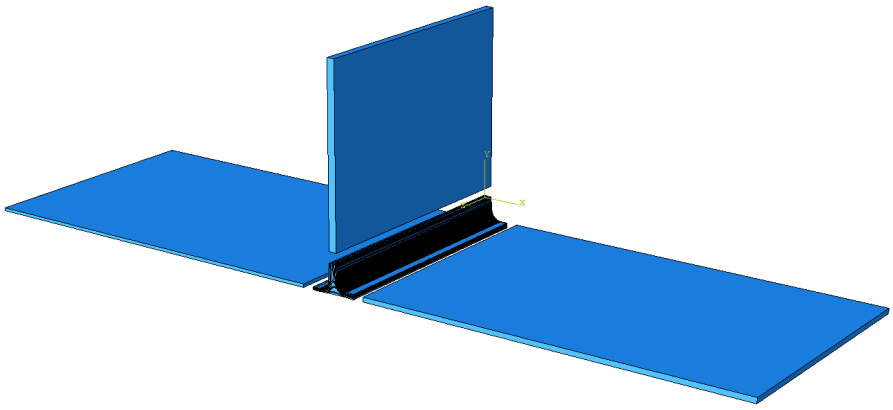

Figure 7.14. T-joint parts before assembly

experimental efforts can be avoided for unidirectional and standard composite plies using traditional micromechanics, the mesostructure of the fabric weave complicates application of these mathematical techniques. In this case, a two-step homogenization process is required where the first step homogenizes the fiber/matrix system and the second stage homogenizes the plain weave geometry into a ply with orthotropic properties. This multistep homogenization can be performed with the GMC framework developed in chapter 6.

To estimate the elastic properties of the plain weave ply, a fiber/matrix GMC mesh, similar to Figure 6.9, is generated with transversely isotropic IM7 fiber properties (Hexcel 2016) and isotropic matrix properties relating to a crosslinking degree of $\eta = 0.19$. The fiber volume fraction, measured by image processing of ply section microscopy images, is controlled at 63.4%. A linear elastic GMC analysis is then performed on the fiber/matrix mesh to obtain the stiffness matrix of the homogenized fiber/matrix representative unit cell (RUC). A second GMC mesh, representing the checkerboard geometry of a plain weave ply, is then generated with the subcell material properties derived from the fiber/matrix GMC analysis. Two forms of subcells are repeated to form the plain weave RUC, one subcell representing fibers running in the primary direction, and the

second subcell representing fibers running in the transverse direction. The homogenized stiffness matrix of the fiber/matrix system is then rotated 90 degrees to obtain the stiffness matrix for the subcell with transverse fibers. A schematic of this multiscale estimation process is shown in Figure 7.15 where $x-y-z$ is the microscale coordinate system and $1-2-3$ is the ply level coordinate system, and direction z corresponds to 2 while direction x corresponds to 3. To avoid overly compliant elastic properties of the homogenized lamina due to homogenization errors (Bednarcyk and Arnold 2000), multiple such RUCs are repeated in the thickness direction with the location of the subcells shifted in each layer. This leads to a primary homogenization process in the 11 direction followed by the homogenization process in the 22 direction with subcells that have comparable elastic properties. A linear elastic GMC analysis, performed on the plain weave RUC, reveals the composite ply elastic properties. Table 7.1 details the stiffness matrices obtained at each step. The ply elastic properties are then applied to the FE part models.

Table 7.1. Stiffness matrices after GMC homogenization

Stage-1 microscale stiffness matrix (10^{10} Pa)					
2.5601	0.4466	0.4466	0	0	0
0.4466	2.5601	0.4053	0	0	0
0.4466	0.4053	5.0245	0	0	0
0	0	0	1.8355	0	0
0	0	0	0	1.8355	0
0	0	0	0	0	1.0887
Stage-2 ply stiffness matrix (10^{10} Pa)					
1.2390	0.1032	0.1032	0	0	0
0.1032	1.6543	0.0793	0	0	0
0.1032	0.0793	1.6543	0	0	0
0	0	0	0.9178	0	0
0	0	0	0	0.6834	0
0	0	0	0	0	0.6834

The FE filler region part (part 4) is developed using greater detail since experimental investigations suggest this region to be a critical section; namely, where damage initiates and accumulates before structural failure. The face of the model is constructed by tracing the mesostructure

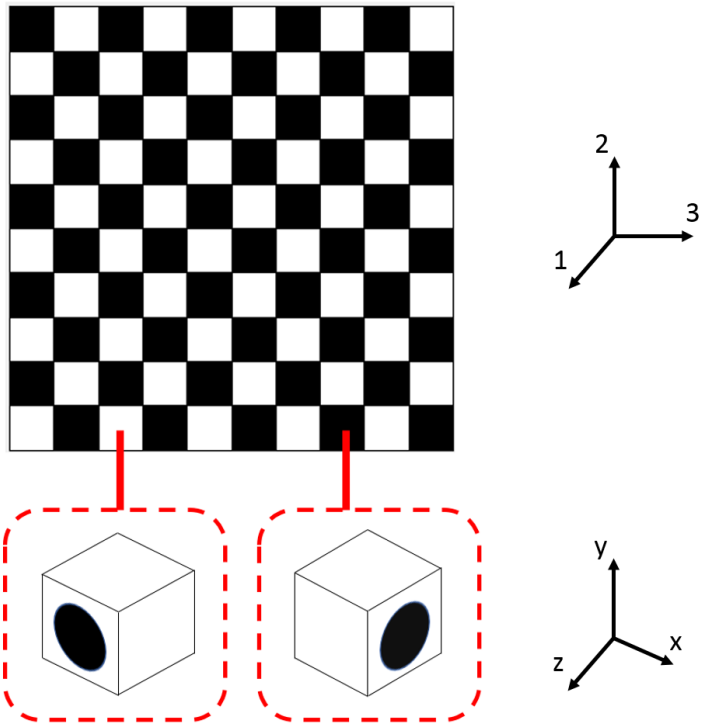

Figure 7.15. Two step homogenization to estimate fabric properties

obtained from confocal microscopy (see Figure 7.7) using multiple spline functions. Special consideration is applied to recreate the matrix-rich regions and the weave geometry, including the fabric crimping. This geometry re-creation allows a thorough analysis of the regions and permits investigation of damage mechanics caused by commonly occurring manufacturing irregularities. Since the geometry consists of separate matrix and composite regions, two material property definitions are used to describe the material relations. The matrix-rich regions utilize the atomistically informed damage model described in chapter 3 with $\eta = 0.19$, and the composite region is associated with the multiscale GMC model developed in chapter 6. The matrix-rich regions behave as pure polymer materials with the CDM equations detailing the initiation and accumulation of damage. Perfect bonding between the matrix rich regions and the composite plies are assumed.

The GMC method is applied to the composite plies using a FORTRAN subroutine to define a custom material property definition. The subroutine is activated by ABAQUS at each integration point and at each solver iteration of the composite ply mesh. The process of generating a random fiber GMC mesh is similar to the steps described above for the elastic property investigations. However, based on the need to study damage in the filler region, the polymer subcells of the GMC mesh use the atomistically informed damage model. Hence, GMC in the composite plies of the filler region run concurrently with the macroscale model, connecting the nonlinear microscale fiber/matrix properties to the mesoscale filler region kinematics. This linking process creates a two-way coupling of properties, schematically shown in Figure 7.16. As the microscale properties degrade, this causes macroscale degradation, which ultimately coalesces along the path of least resistance to create a fracture path. The newly generated fracture path may lead to debonding, delamination, or structural failure. It should be noted that the coordinate system for the GMC equations is ordered along the subcell edges; hence, the integration point strains that are passed into the VUMAT subroutine by the FE solver is rotated from the element coordinate system to the GMC coordinate system to maintain consistency.

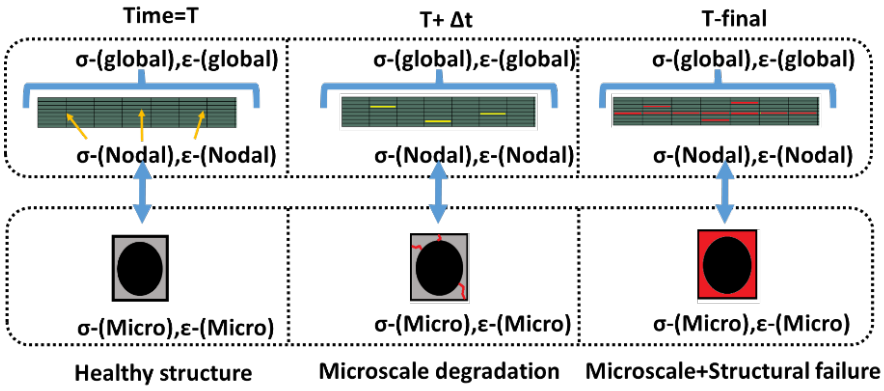

Figure 7.16. Damage and failure interaction

The loading and boundary conditions applied to the assembled FE model mimic the experiment and is equivalent to Figure 7.9. The right and left flange edge displacements are constrained,

and loading is applied as a displacement condition to the top of the web edge at a rate of 0.01 mm per second up to a total of 1000 seconds. This ensures a total displacement of 10 mm at quasi-static loading rates, which is determined by monitoring the inertial energies. The loading is applied through a reference point that is kinematically tied using TIE constraints to the nodes of the web top edge. This makes it convenient to measure system reaction forces by recording the reference point history variables. Parts 1, 2, and 3, which represent the planar composite laminates, are meshed using $1,080$ C3D8 linear hexahedral brick elements with linear elastic orthotropic material property definitions. Each ply is modeled individually by sectioning the laminate geometry. The filler region is meshed using $10,040$ C3D10 quadratic tetrahedral elements due to the complicated nature of the geometry. The geometry is meshed using an iterative algorithm to avoid any regions with poor mesh qualities. The user subroutine VUMAT with GMC integration is used to define the material property definitions for the C3D10 elements belonging to the composite plies, and the user subroutine VUMAT with just the atomistically informed damage model is used to define the material property definitions for the C3D10 elements belonging to the matrix. The resulting input file is solved in double precision using the ABAQUS explicit solver and the IFORT environment.

7.4 Model Validation

The results of the macroscale FE model is post-processed in the ABAQUS visualizer. However, the results of the microscale GMC mesh is obtained separately in a CSV file written by the VUMAT user subroutine and post-processed in MATLAB. To validate the FE macroscale model, the load-displacement curve obtained from the T-joint pull-off simulation is compared to experimental results exhibited in Figure 7.11. This comparison is used to confirm if the homogenized physics of the T-joint has been reproduced in the models. To calculate the load-displacement

curve of the T-joint model, the reaction forces and applied load at each time step is extracted from the history variable associated with the reference point tied to the web edge. Since the reference point simulates the function of the loading arm, the displacement of the reference point replicates the crosshead data obtained from experiments under the assumption that no grip slip occurs during the test. The reaction forces at the reference point then is a physical average of the reactions observed at this point, resulting from the applied load and the constraints at the flange end. Based on this, the reaction forces at the reference point are able to model the readings of the load cell from the experiments. Figure 7.17 exhibits a comparison of the reaction forces versus applied displacement obtained from the T-joint model of sample-1 and the load cell reading versus crosshead displacement obtained from the pull-off testing of sample-1. It should be noted that the only parameter calibrated for better comparison is the fiber elastic properties, which is set at 289 GPa. This is found to be 4.7% higher than the mean elastic properties for IM7 fiber and is well within the observed standard deviation of IM7 fiber properties (Hexcel 2016). The calibrated model hence captures the general homogenized macroscale physics of the T-joint which permits the comparison of the response at specific localized regions to ensure simultaneous local validation.

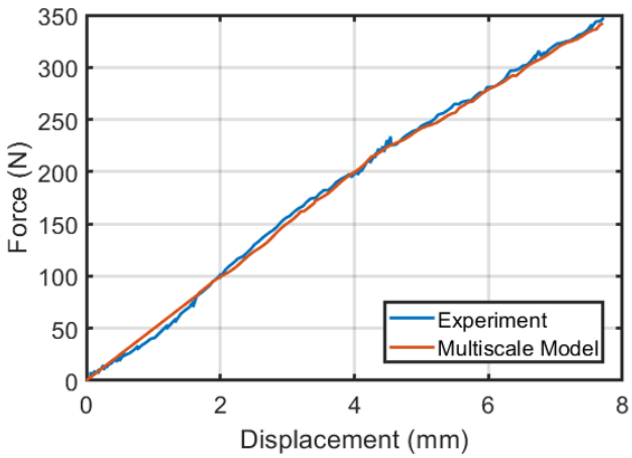

Figure 7.17. Comparison of load-displacement curves for sample-1 obtained from model and experiment

Since the experiments indicated the filler region to be the 'hot-spot' region, the response in this area is compared with the T-joint model. By using DIC, the local strains at the filler region was obtained during the pull-off experiment as a full-field strain contour in the loading direction, which is compared to the strain contours obtained from the filler region part of the T-joint FE model. Figure 7.20 illustrates this comparison. The limits of the contour spectrum are maintained to be the same for the model and the DIC results in order to arrive at a valid comparison. A reasonable similarity between the experimental strain contour results and the model is observed, with the high strain 'hot-spot' regions replicated in the model. During the pull-off experiments, the T-joints were observed to fail along the interface of the filler region (see Figure 7.18) and composite plies, with damage initiating at the fillet ends. This corresponds to the 'hot-spot' regions observed in the DIC strain contours. Such a mechanism is not predicted when idealized T-joint geometries are considered with flat base plies, perfectly radial fillets, and a triangular matrix filled filler region. In such cases, the bending of the base plies and the fillet plies leads to predictions of a large compressive stress in the middle of the filler region (Gleich, Van Tooren, and Buekers 2002). Application of structural failure theories then anticipate damage initiation at the center of the filler region, which results in incorrect damage and failure predictions. An example of such a stress contour is shown in Figure 7.19 where an idealized T-joint geometry is subjected to pull-off loading. Accumulation of compressive stresses at the filler region can also be observed in these geometries. Such discrepancies between experimental observations and theory have led to the use of cohesive zone models, where the cohesive elements are applied at the interface of the fillet plies to study fracture behavior (Xu et al. 2016). However, studies that use cohesive zones require *a-priori* knowledge of the fracture path, which in turn limits the use of these techniques. In comparison, the analysis framework developed in this chapter can predict the fracture path, which can then be used in combination with fracture mechanics techniques to analyze separation of surfaces.

The FE model is also able to predict interface differentials in strain at the borders of composite

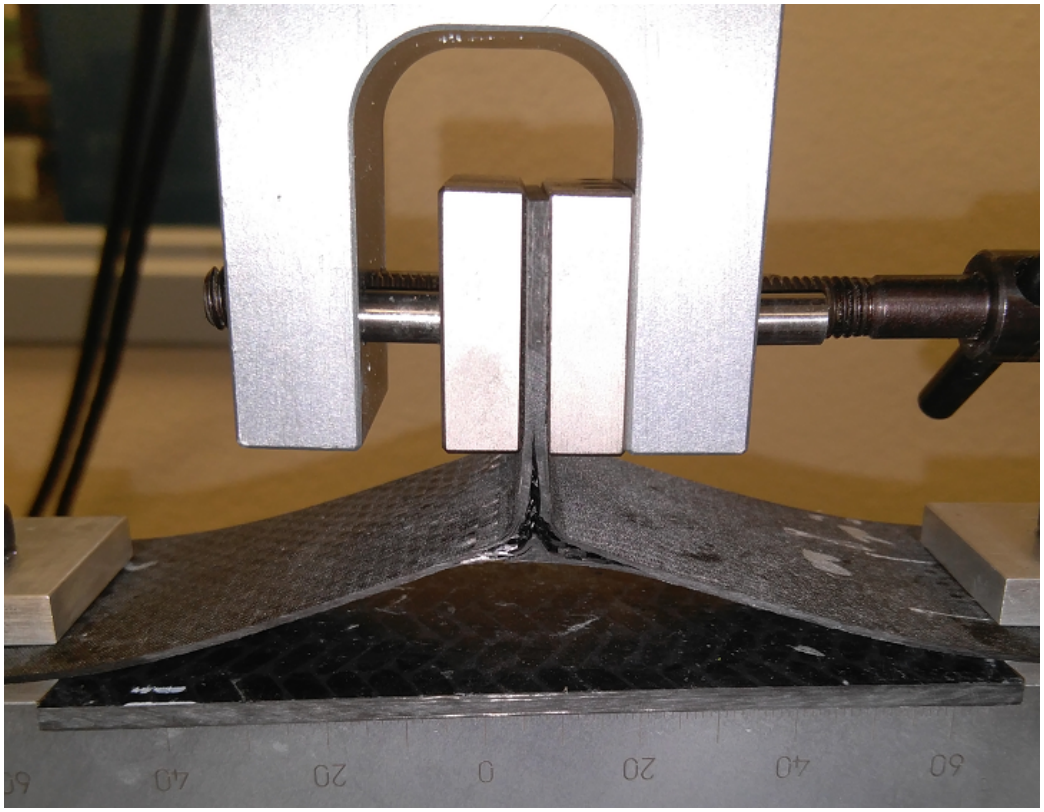

Figure 7.18. T-joint after failure and separation of base ply

ply/matrix regions. Due to the large material property gradients between the composite plies and the matrix, strain differential exists between these regions, which is largely homogenized by the DIC algorithm. Due to the limited region of interest, resolution, and available focus, the DIC algorithm homogenizes the calculated strain over the region of interest leading to a larger spread of strain contours. Such errors have been demonstrated through multiscale DIC studies, which have shown that the mesoscale DIC contours can significantly differ from higher length scale DIC contours due to resolution homogenization for structures with a multiscale geometry (Koohbor, Ravindran, and Kidane 2015). Additional errors, known as edge errors, are also introduced at the edges of the DIC window. Such a disadvantage does not exist in the FE model since each component is modeled separately with appropriately applied material properties that allow the measurement of stress and strain gradients between specific regions and the resulting interfacial

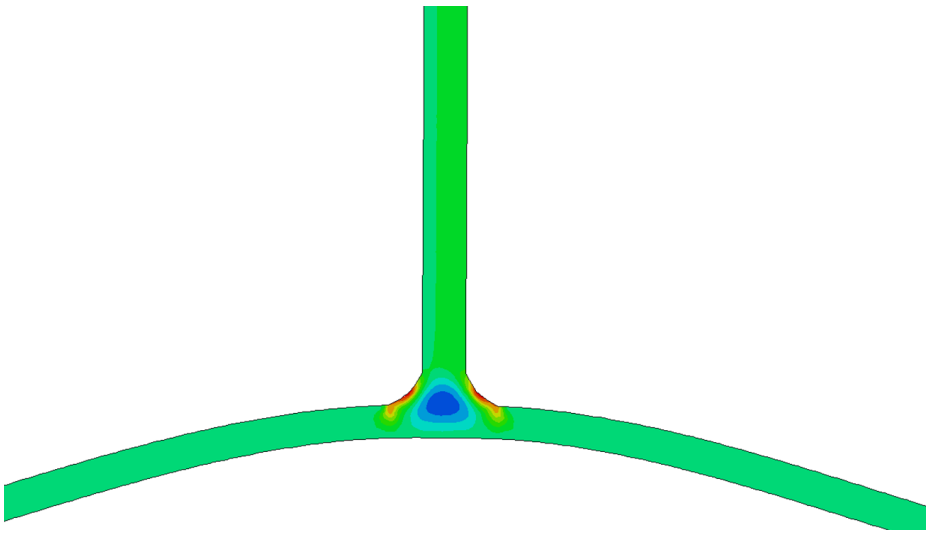

Figure 7.19. Loading direction strain contours in the filler region of an idealized T-joint geometry

damage. Further investigations at the microscale can now be initiated to study the microscale damage mechanisms at various locations by extracting the GMC stress-strain-damage results at specific integration points of the FE model.

7.5 Microscale Investigation of Damage in T-joints

Since each integration point in the FE model is represented as a random microstructure, which is modeled using GMC, the fiber/matrix response at the 'hot-spot' regions can be explicitly studied. Three regions of interest (see Figure 7.20) along the fillets and the base are chosen to be studied in detail: (i) region 'A' on the left fillet ply where the structural damage initiates; (ii) region 'B' on the right fillet ply; (iii) region 'C' on the bottom ply. The GMC data at these integration points are extracted from the FE material subroutine outputs and post-processed in MATLAB. The stress and strain data exhibited in this section are oriented along the GMC coordinate system, where in the 11 direction is along the fiber, and the 22 and 33 directions are perpendicular.

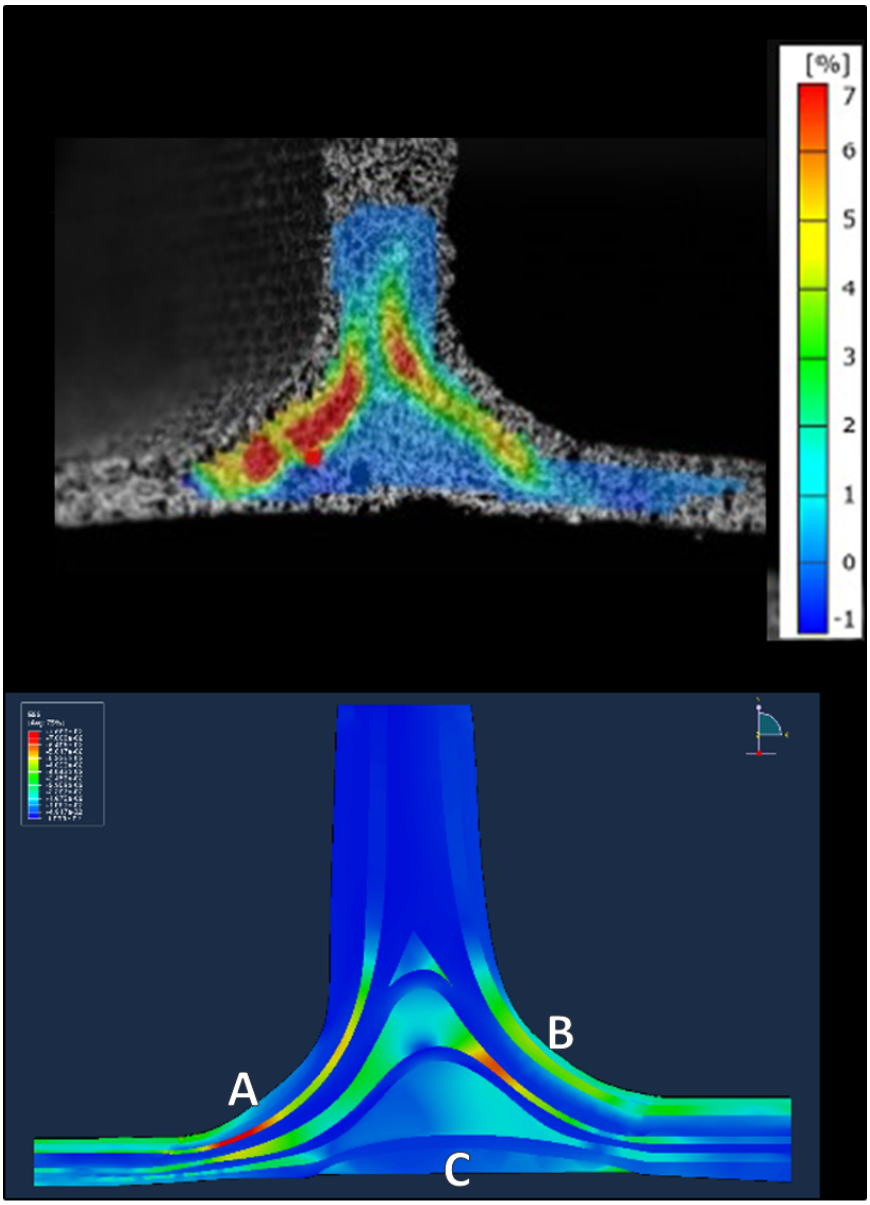

Figure 7.20. DIC and FE comparison of loading direction strain contours in the filler region of sample-1

The RUC damage can be arrived at by ensemble averaging the damage value of each subcell due to its scalar nature. Figure 7.21 shows a comparison of the mean damage in the RUCs belonging to left fillet ply, the right fillet ply, and the bottom ply. The left fillet ply displays considerable damage in the micro RUC, the right fillet ply experiences mild damage, while the bottom ply remains

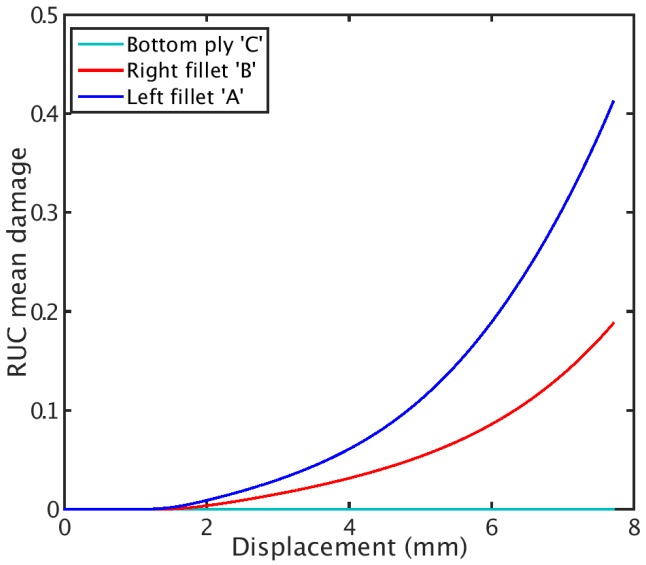

Figure 7.21. Comparison of microscale RUC damage along filler regions

relatively pristine. This is directly related to the strain state of these regions, as can be seen in Figure 7.20, where the left fillet ply experiences substantially larger strains due to the geometry of the filler regions and associated field concentrations. The nature of the damage can also be visualized by observing the damage contours in the RUCs, displayed in Figure 7.22. The contours of damage in the left fillet ply RUC suggests subcell degradation due to local strain concentrations as well as volumetric matrix damage, while the right ply damage contours exhibit minimal volumetric damage. The bottom ply does not show any local damage suggesting that this region remains within the elastic limit when macroscale damage initiates in the T-joint.

Although, the RUC damage contours provide an interesting visualization of property degradation at the microscale, the RUC stress-strain response needs to be studied to infer causal mechanisms of damage. Due to the degree of damage in the left fillet ply, the associated RUC is studied further. A comparison of the RUC stress state can be seen in Figure 7.23, which shows that the in-plane shear stress and the in-plane normal stress in the fiber direction is dominant in this region. Hence, the stress-strain response in these directions are chosen for further investigation. To understand the progression and consequence of damage in the RUC, the subcell stress and strain con-

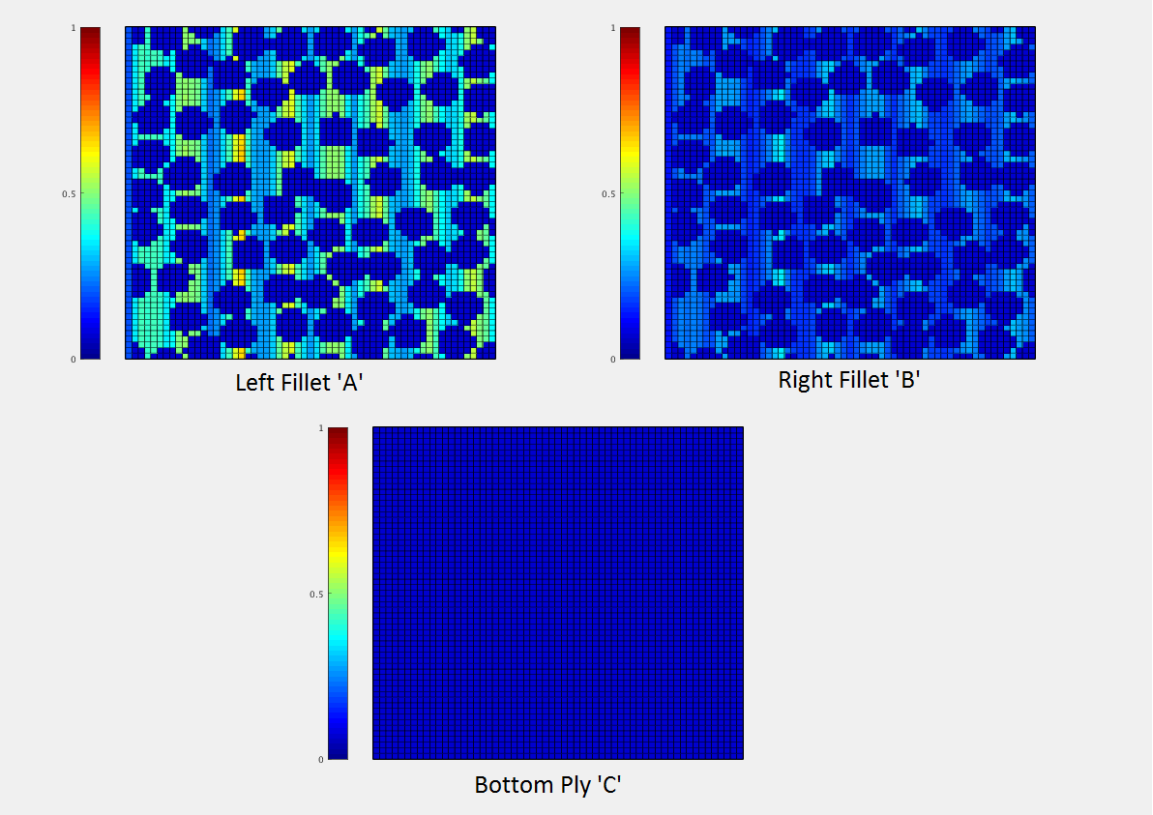

Figure 7.22. Comparison of subcell damage contours along filler regions

tours are compared at the elastic limit and just before structural failure, as in Figure 7.24. Stresses and strains in the two dominant directions, namely, the normal direction along the fiber and the in-plane shear along the fiber and matrix, are compared. In the elastic regime, a homogeneous strain contour can be observed in the normal and shear directions. Due to the substantial elastic property variation between the fiber and the matrix in the 11 direction, the stress contours clearly show the stress gradients between the fiber subcells and the matrix subcells. Alternatively, it can be seen that a much lower variation between the shear properties of the fiber and the matrix leads to relatively mild homogenized stress gradients in the shear stress contours. However, in the non-linear regime, it is observed that the matrix damage leads to large strain gradients in the RUC due to property degradation, which in turn leads to existence of stress risers along the fiber/matrix interfaces, signifying fiber shear pullout.

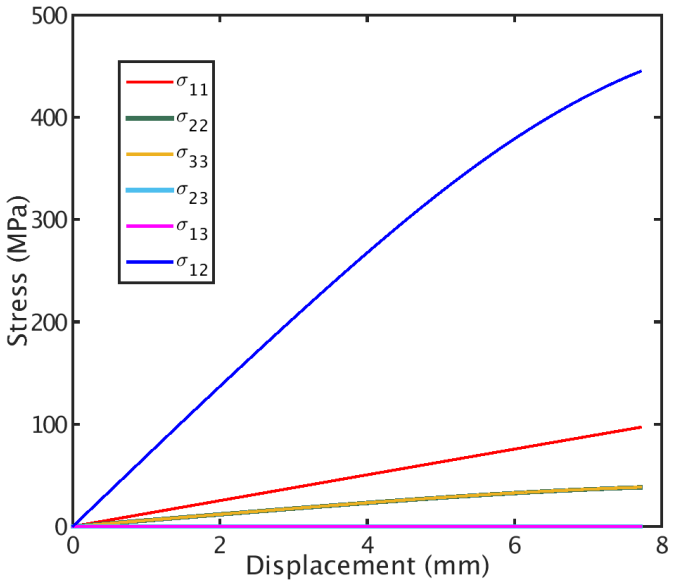

Figure 7.23. Comparison of microscale RUC damage along filler regions

The effect of damage can also be seen in the difference between the shear stress contours at the elastic and in-elastic regimes, where the damage causes stress-risers not initially present, thereby leading to further damage accumulation, and providing an explanation for the exponential trend of the mean RUC damage curves, as illustrated in Figure 7.22. A similar comparison in the 11 direction shows gradients in the strain contours at the in-elastic regime, but the large elastic property variations between the fibers and the matrix lead to the fiber system handling most of the mechanical load, and not contributing further to the mean RUC damage. It can construed that the microscale region at the fillet undergoes fiber pullout as a result of the local shearing of the fiber and the matrix when the T-joint is subjected to pull-off loading. Experimental studies on mechanical loading of T-joints have also revealed similar fiber pullout mechanisms under local shear, resulting in failure of ply and ply interfaces, as well as delaminations that progress to final structural failure (Cui 2014). Processing techniques such as fiber-coatings that reinforce the interface and resist in-plane fiber shearing, can then be used to engineer T-joints with capabilities for higher energy absorption by resisting shear damage at the microscale.

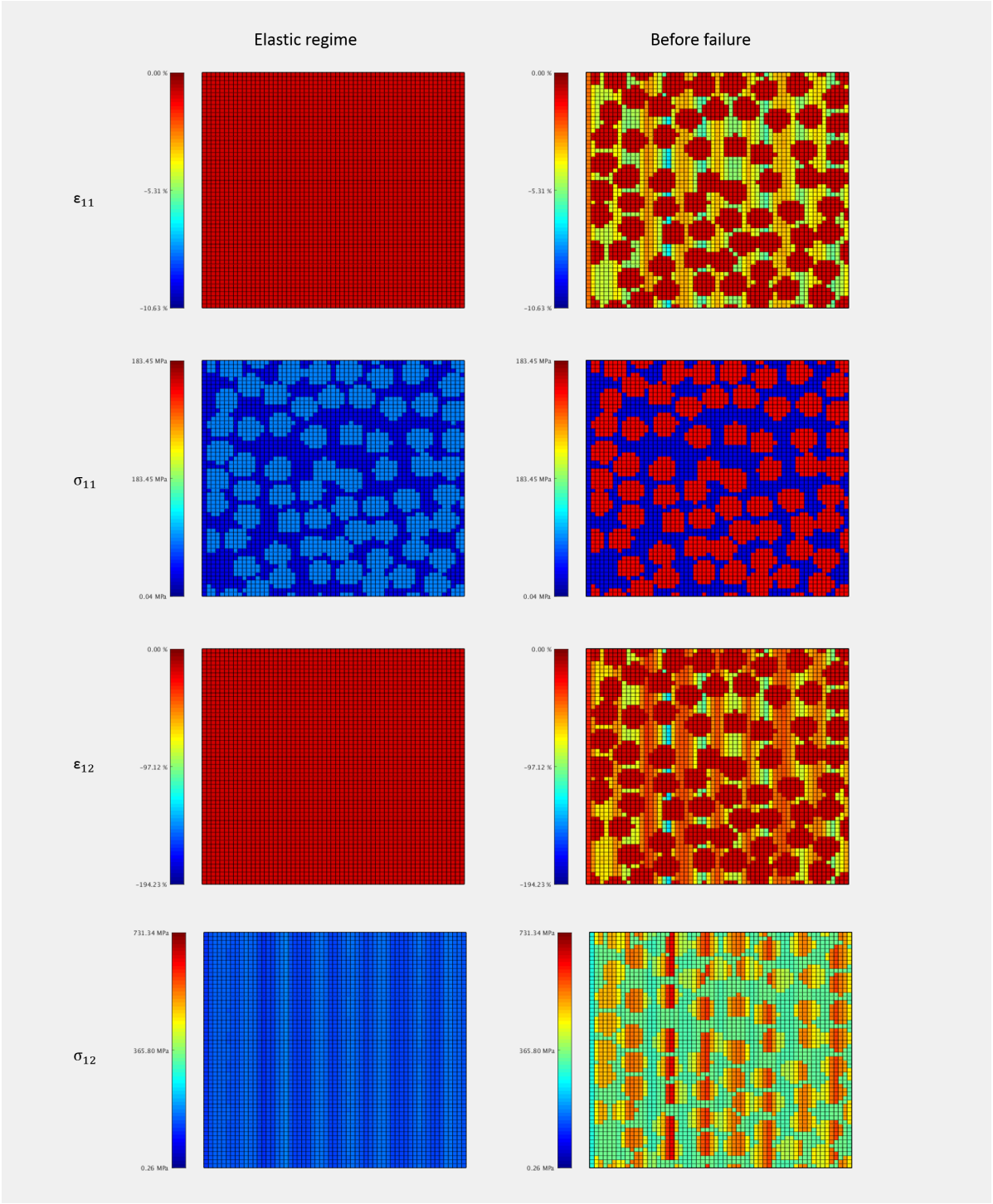

Figure 7.24. Comparison of stress and strain subcell contours in the elastic regime and before structural failure

7.6 Summary

Motivated by the need for a modeling approach for the length-scale dependent damage and failure analysis of bonded composite joints, this chapter presented a multiscale composite structural analysis framework that also integrated several of the concepts presented in earlier chapters. Due to the requirement of accommodating complex joint geometries while integrating the elastoplastic characteristics of the thin adhesive bondline, this framework utilized a concurrent approach wherein the macroscale geometry is modeled using FE and the microscale constituents are modeled using the previously developed microscale random fiber GMC model with imperfect interfaces. Furthermore, the atomistically informed damage model is used to simulate damage initiation and propagation in the matrix, and the GMC model is also used to calculate the elastic properties of the laminates.

To validate the model, T-joint pull-off tests were performed with DIC to measure the global load-displacement response and the local full field strain response at critical areas of the T-joint. The manufactured T-joints were also subjected to a confocal microscopy study for characterizing microscale parameters and for recreating the mesoscale filler region explicitly in the FE model. Close agreement of the load-displacement response, obtained from the FE model and experiments, was observed confirming that the global elastic and geometric properties of the T-joint was successfully captured. Furthermore, agreement in the local strain fields at the filler region, between the FE model and the experimental DIC results, were also achieved. The multiscale model successfully predicted 'hot-spot' damage initiation areas along the filler region, a phenomenon that cannot be captured using idealized single-scale finite element T-joint models. The microscale analysis of the composite regions in the damage initiation zone showed that damage and failure largely occur due to fiber shear and consequent fiber pull-out, leading to macroscale composite failure. Hence, it was demonstrated that through such multiscale modeling efforts, constituent behavior

at 'hot-spot' regions can be analyzed, providing critical insight into possible material processing requirements. Such efforts can then lead to the development of stronger, tougher, and damage-resistant composite structures.

Chapter 8

CONTRIBUTIONS AND FUTURE WORK

8.1 Contributions

The research presented in this dissertation was primarily motivated by a lack of practical techniques to couple molecular scale information with structurally focused multiscale models for the analysis of advanced composite materials and components. To address this gap in literature, several atomistically informed mutiscale analysis techniques were developed in this work for the linear and nonlinear analysis of advanced composite structures. Summarizing the major contributions of this work, the following achievements are noted:

1. A stochastic multiscale model for carbon fiber reinforced polymers (CFRPs) and carbon nanotube (CNT) CFRPs that utilizes nanoscale derived elastic information and variation in the curing degree to efficiently estimate the composite properties under fundamental uncertainty was developed and validated with experimental observations.
2. A thermodynamically admissible bridging technique to efficiently transfer inelastic information from discrete nanoscale MD simulations of the polymer matrix to higher length scales was developed using the framework of continuum damage mechanics (CDM) and validated with experiments.
3. The nonlinear effects of the presence of nanofillers such as CNTs in polymer matrix under mechanical loading, using the developed atomistically informed damage model was investigated which led to the understanding of fundamental damage processes at the submicroscale.
4. The variation of piezoresistive properties of the CNTs in the polymer matrix under damage

due to mechanical loading was studied which led to the explanation of various piezoresistive mechanisms.

5. An algorithm to generate integrated representative unit cells (RUCs) for the high fidelity analysis of CFRPs and CNT enhanced CFRP microstructures was developed and studied to explain damage processes under mechanical loading.
6. Low-fidelity physics based damage models with subcell based micromechanics was developed that capture global microscale response and integrate behavior of the constituent interfaces based on nanoscale information.
7. The low-fidelity models were integrated with macroscale finite element models to investigate mechanical behavior of practical composite structures, the adhesively bonded composite T-joints, using a comprehensive nano-to-macro multiscale framework.

With these achievements, the research presented in this dissertation advances the state of the art in multiscale modeling of advanced composite structures, which can be utilized to design optimal material systems leading to a material-by-design approach in composite applications.

8.2 Future Work

Although this research presents practical methods for nano-to-macro multiscale modeling of advance composites, several topics can be further expanded for an in-depth understanding of linear and nonlinear mechanisms in these material systems. Additionally, the developed models can be used for parametric studies or combined with mathematical optimization to generate optimal material systems for any given conditions. The following future work topics are suggested for advancing this research: (i) the atomistically informed damage model developed in Chapter 3 considers only a sigmoidal bond disassociation energy (BDE) density trend. This tendency was observed through molecular dynamics simulation of Di-Glycidyl Ether of Bisphenol F and Di-

Ethylene Tri-Amine system. A general formulation for rate of damage $\dot{D}$ can be developed applicable for any material system; (ii) the low-fidelity models, including the subcell model and the generalized method of cells (GMC) model, may be reformulated within an optimization framework to investigate the optimal parameter values, which will expedite the calibration process; (iii) the validated structural analysis framework for adhesively bonded composite joints introduced in Chapter 7 can be further utilized to create a parametric study of various T-joint geometries and their mechanical response. This methodology can be used to investigate other built-up structural systems; (iv) the GMC model, which currently considers neat polymer matrix with an imperfect fiber interface, can be extended to include CNTs and other nanofillers. With this extension, it will be possible to study the effects of nanofillers in structural components.

REFERENCES

ABAQUS. 2013. *ABAQUS/Standard Analysis User's Manual Version 6.13-2.* Providence, Rhode Island, USA: Dassault Systémes Simulia Corp.

Aboudi, Jacob. 1989. "Micromechanical analysis of composites by the method of cells." *Appl Mech Rev* 42 (7): 2.

———. 1996. "Micromechanical analysis of composites by the method of cells-update." *Applied Mechanics Reviews* 49:S83–S91.

Aboudi, Jacob, Steven M Arnold, and Brett A Bednarcyk. 2012. *Micromechanics of composite materials: a generalized multiscale analysis approach.* Butterworth-Heinemann.

Allin, Jonathan Mark. 2002. *Disbond detection in adhesive joints using low frequency ultrasound.* University of London.

Anand, Lallit, and Morton E Gurtin. 2003. "A theory of amorphous solids undergoing large deformations, with application to polymeric glasses." *International Journal of Solids and Structures* 40 (6): 1465–1487.

Arnold, SM, BA Bednarcyk, TE Wilt, and D Trowbridge. 1999. "Micromechanics analysis code with generalized method of cells (mac/gmc): User guide. version 3."

Ashton, JE, and James Martin Whitney. 1970. *Theory of laminated plates.* Vol. 4. CRC Press.

Asp, LE, Lars A Berglund, and Ramesh Talreja. 1996. "Effects of fiber and interphase on matrix-initiated transverse failure in polymer composites." *Composites Science and Technology* 56 (6): 657–665.

ASTM-D638-14. 2014. "Standard Test Method for Tensile Properties of Plastics." *West Conshohocken, PA: ASTM International.*

Atkins, Peter W, and Ronald S Friedman. 2011. *Molecular quantum mechanics.* Oxford university press.

Vu-Bac, N, R Rafiee, X Zhuang, Tom Lahmer, and Timon Rabczuk. 2015. "Uncertainty quantification for multiscale modeling of polymer nanocomposites with correlated parameters." *Composites Part B: Engineering* 68:446–464.

Badia, Santiago, Michael Parks, Pavel Bochev, Max Gunzburger, and Richard Lehoucq. 2008. "On atomistic-to-continuum coupling by blending." *Multiscale Modeling & Simulation* 7 (1): 381–406.

Balazs, Anna C, Todd Emrick, and Thomas P Russell. 2006. "Nanoparticle polymer composites: where two small worlds meet." *Science* 314 (5802): 1107–1110.

Barbero, Ever J. 2013. *Finite element analysis of composite materials using Abaqus.* CRC press.

Bednarcyk, Brett A, and Steven M Arnold. 2000. *Modeling woven polymer matrix composites with MAC/GMC.* Technical report.

Benveniste, Y1. 1987. "A new approach to the application of Mori-Tanaka's theory in composite materials." *Mechanics of materials* 6 (2): 147–157.

Besson, J, and C Guillemer-Neel. 2003. "An extension of the Green and Gurson models to kinematic hardening." *Mechanics of materials* 35 (1): 1–18.

Best, Robert B, Susan B Fowler, Jose L Toca Herrera, Annette Steward, Emanuele Paci, and Jane Clarke. 2003. "Mechanical unfolding of a titin Ig domain: structure of transition state revealed by combining atomic force microscopy, protein engineering and molecular dynamics simulations." *Journal of molecular biology* 330 (4): 867–877.

Best, Robert B, Bin Li, Annette Steward, Valerie Daggett, and Jane Clarke. 2001. "Can non-mechanical proteins withstand force? Stretching barnase by atomic force microscopy and molecular dynamics simulation." *Biophysical journal* 81 (4): 2344–2356.

Biercuk, MJ, Mark C Llaguno, M Radosavljevic, JK Hyun, Alan T Johnson, and John E Fischer. 2002. "Carbon nanotube composites for thermal management." *Applied physics letters* 80 (15): 2767–2769.

Bogdanor, Michael J, and Caglar Oskay. 2016. "Prediction of progressive damage and strength of IM7/977-3 composites using the Eigendeformation-based homogenization approach: Static loading." *Journal of Composite Materials:* 0021998316650982.

Borkowski, LB, KC Liu, and A Chattopadhyay. 2013. "From ordered to disordered: The effect of microstructure on composite mechanical performance." *CMC: Computers, Materials & Continua* 37 (3): 161–193.

Bose, Suryasarathi, Arup R Bhattacharyya, Ajit R Kulkarni, and Petra Pötschke. 2009. "Electrical, rheological and morphological studies in co-continuous blends of polyamide 6 and acrylonitrile–butadiene–styrene with multiwall carbon nanotubes prepared by melt blending." *Composites Science and Technology* 69 (3): 365–372.

Bouvard, JL, DK Ward, D Hossain, EB Marin, DJ Bammann, and MF Horstemeyer. 2010. "A general inelastic internal state variable model for amorphous glassy polymers." *Acta mechanica* 213 (1-2): 71–96.

Brenner, Donald W, Olga A Shenderova, Judith A Harrison, Steven J Stuart, Boris Ni, and Susan B Sinnott. 2002. "A second-generation reactive empirical bond order (REBO) potential energy expression for hydrocarbons." *Journal of Physics: Condensed Matter* 14 (4): 783.

Brotherhood, CJ, BW Drinkwater, and S Dixon. 2003. "The detectability of kissing bonds in adhesive joints using ultrasonic techniques." *Ultrasonics* 41 (7): 521–529.

Brotherhood, CJ, BW Drinkwater, and FJ Guild. 2002. "The effect of compressive loading on the ultrasonic detectability of kissing bonds in adhesive joints." *Journal of Nondestructive evaluation* 21 (3): 95–104.

Budiansky, Bernard. 1965. "On the elastic moduli of some heterogeneous materials." *Journal of the Mechanics and Physics of Solids* 13 (4): 223–227.

Buryachenko, Valeriy. 2001. "Multiparticle effective field and related methods in micromechanics of composite materials." *Applied Mechanics Reviews* 54 (1): 1–48.

———. 2007. *Micromechanics of heterogeneous materials.* Springer Science & Business Media.

Camanho, Pedro P, and Carlos G Dávila. 2002. "Mixed-mode decohesion finite elements for the simulation of delamination in composite materials."

Campilho, Raul DSG, Mariana D Banea, Arnaldo MG Pinto, Lucas FM da Silva, and AMP De Jesus. 2011. "Strength prediction of single-and double-lap joints by standard and extended finite element modelling." *International Journal of Adhesion and Adhesives* 31 (5): 363–372.

Cantoni, Stefania, Felice De Nicola, Umberto Mercurio, and Vincenzo Quaranta. 2014. "The role of polymer based composites materials in modern and future aerospace structures." In *AIP Conference Proceedings,* 1599:10–13. 1. AIP.

Car, Richard, and Mark Parrinello. 1985. "Unified approach for molecular dynamics and density-functional theory." *Physical review letters* 55 (22): 2471.

Carlsson, Leif A, Donald F Adams, and R Byron Pipes. 2014. *Experimental characterization of advanced composite materials.* CRC press.

Chaboche, JL, M Boudifa, and K Saanouni. 2006. "A CDM approach of ductile damage with plastic compressibility." *International Journal of Fracture* 137 (1): 51–75.

Charalambakis, Nicolas. 2010. "Homogenization techniques and micromechanics. A survey and perspectives." *Applied Mechanics Reviews* 63 (3): 030803.

Chen, Linfeng, Edward E Urquhart, and Marek-Jerzy Pindera. 2005. "Microstructural effects in multilayers with large moduli contrast loaded by flat punch." *AIAA journal* 43 (5): 962–973.

Chiachio, Manuel, Juan Chiachio, and Guillermo Rus. 2012. "Reliability in composites–A selective review and survey of current development." *Composites Part B: Engineering* 43 (3): 902–913.

Cho, J, IM Daniel, and DA Dikin. 2008. "Effects of block copolymer dispersant and nanotube length on reinforcement of carbon/epoxy composites." *Composites Part A: Applied Science and Manufacturing* 39 (12): 1844–1850.

Chou, Tsu-Wei, Limin Gao, Erik T Thostenson, Zuoguang Zhang, and Joon-Hyung Byun. 2010. "An assessment of the science and technology of carbon nanotube-based fibers and composites." *Composites Science and Technology* 70 (1): 1–19.

Christensen, Richard M. 2007. "A comprehensive theory of yielding and failure for isotropic materials." *Journal of Engineering materials and Technology* 129 (2): 173–181.

Chui, Clarence, and Mary C Boyce. 1999. "Monte Carlo modeling of amorphous polymer deformation: evolution of stress with strain." *Macromolecules* 32 (11): 3795–3808.

Coleman, Bernard D, and Morton E Gurtin. 1967. "Thermodynamics with internal state variables." *The Journal of Chemical Physics* 47 (2): 597–613.

Coleman, Jonathan N, Umar Khan, Werner J Blau, and Yurii K Gun'ko. 2006. "Small but strong: a review of the mechanical properties of carbon nanotube–polymer composites." *Carbon* 44 (9): 1624–1652.

Cooper, Reid F, and K Chyung. 1987. "Structure and chemistry of fibre-matrix interfaces in silicon carbide fibre-reinforced glass-ceramic composites: an electron microscopy study." *Journal of materials science* 22 (9): 3148–3160.

Cornell, Robert Witherspoon. 1953. "Determination of stresses in cemented lap joints." *Journal of Applied Mechanics-Transactions of the ASME* 20 (3): 355–364.

Cui, Hao. 2014. "Delamination and debonding failure of laminated composite T-joints." PhD diss., Technische Universiteit Delft.

Czél, Gergely, Meisam Jalalvand, and Michael R Wisnom. 2016. "Design and characterisation of advanced pseudo-ductile unidirectional thin-ply carbon/epoxy–glass/epoxy hybrid composites." *Composite Structures* 143:362–370.

Daniel, IM, JM Whitney, and RB Pipes. 1983. "Experimental mechanics of fiber reinforced composite materials." *Experimental Techniques* 7 (3): 25–25.

Daniel, Isaac M, Ori Ishai, Issac M Daniel, and Ishai Daniel. 1994. *Engineering mechanics of composite materials.* Vol. 3. Oxford university press New York.

Datta, S, MY Fard, JP Johnston, E Quigley, and A Chattopadhyay. 2015. "In-situ Strain and Damage Sensing in Glass Fiber Laminates Using Embedded CNT." *Structural Health Monitoring 2015.*

Day, Dwayne A. 2008. "Composites and Advanced Materials." *US Centennial of Flight Commission* 24.

Dean, Derrick, Apollo M Obore, Sylvester Richmond, and Elijah Nyairo. 2006. "Multiscale fiber-reinforced nanocomposites: synthesis, processing and properties." *Composites Science and Technology* 66 (13): 2135–2142.

Dharap, Prasad, Zhiling Li, Satish Nagarajaiah, and EV Barrera. 2004. "Nanotube film based on single-wall carbon nanotubes for strain sensing." *Nanotechnology* 15 (3): 379.

Diaz, J, L Romera, S Hernandez, and A Baldomir. 2010. "Benchmarking of three-dimensional finite element models of CFRP single-lap bonded joints." *International Journal of Adhesion and Adhesives* 30 (3): 178–189.

Dolbow, John, and Isaac Harari. 2009. "An efficient finite element method for embedded interface problems." *International journal for numerical methods in engineering* 78 (2): 229–252.

Drzal, Lawrence T, Michael J Rich, and Pamela F Lloyd. 1983. "Adhesion of graphite fibers to epoxy matrices: I. The role of fiber surface treatment." *The Journal of Adhesion* 16 (1): 1–30.

Eshelby, John D. 1957. "The determination of the elastic field of an ellipsoidal inclusion, and related problems." In *Proceedings of the Royal Society of London A: Mathematical, Physical and Engineering Sciences,* 241:376–396. 1226. The Royal Society.

Evans, AG, FW Zok, and J Davis. 1991. "The role of interfaces in fiber-reinforced brittle matrix composites." *Composites Science and Technology* 42 (1-3): 3–24.

Fan, Hai Bo, and Matthew MF Yuen. 2007. "Material properties of the cross-linked epoxy resin compound predicted by molecular dynamics simulation." *Polymer* 48 (7): 2174–2178.

Fard, Masoud Yekani, Yingtao Liu, and Aditi Chattopadhyay. 2011. "Characterization of epoxy resin including strain rate effects using digital image correlation system." *Journal of Aerospace Engineering* 25 (2): 308–319.

Fish, Jacob, Mohan A Nuggehally, Mark S Shephard, Catalin R Picu, Santiago Badia, Michael L Parks, and Max Gunzburger. 2007. "Concurrent AtC coupling based on a blend of the continuum stress and the atomistic force." *Computer Methods in Applied Mechanics and Engineering* 196 (45): 4548–4560.

Fish, Jacob, and Qing Yu. 2001. "Multiscale damage modelling for composite materials: theory and computational framework." *International Journal for Numerical Methods in Engineering* 52 (1-2): 161–191.

Fish, Jacob, Qing Yu, and KamLun Shek. 1999. "Computational damage mechanics for composite materials based on mathematical homogenization." *International journal for numerical methods in engineering* 45 (11): 1657–1679.

Fisher, FT, RD Bradshaw, and LC Brinson. 2002. "Effects of nanotube waviness on the modulus of nanotube-reinforced polymers." *Applied Physics Letters* 80 (24): 4647–4649.

Forest, Samuel. 1998. "Mechanics of generalized continua: construction by homogenizaton." *Le Journal de Physique IV* 8 (PR4): Pr4–39.

Forest, Samuel, and Karam Sab. 1998. "Cosserat overall modeling of heterogeneous materials." *Mechanics Research Communications* 25 (4): 449–454.

Frankland, SJV, VM Harik, GM Odegard, DW Brenner, and TS Gates. 2003. "The stress–strain behavior of polymer–nanotube composites from molecular dynamics simulation." *Composites Science and Technology* 63 (11): 1655–1661.

Fu, SY, B Lauke, E Mäder, X Hu, and CY Yue. 1999. "Fracture resistance of short-glass-fiber-reinforced and short-carbon-fiber-reinforced polypropylene under Charpy impact load and its dependence on processing." *Journal of Materials Processing Technology* 89:501–507.

Gallo, Gerard J, and Erik T Thostenson. 2015. "Electrical characterization and modeling of carbon nanotube and carbon fiber self-sensing composites for enhanced sensing of microcracks." *Materials Today Communications* 3:17–26.

Garcia, Enrique J, A John Hart, and Brian L Wardle. 2008. "Long carbon nanotubes grown on the surface of fibers for hybrid composites." *AIAA journal* 46 (6): 1405–1412.

Gau, Chie, Cheng-Yung Kuo, and HS Ko. 2009. "Electron tunneling in carbon nanotube composites." *Nanotechnology* 20 (39): 395705.

Gay, Daniel. 2014. *Composite materials: design and applications.* CRC press.

Ghosh, S, J Bai, and P Raghavan. 2007. "Concurrent multi-level model for damage evolution in microstructurally debonding composites." *Mechanics of Materials* 39 (3): 241–266.

Gilat, Amos, Robert K Goldberg, and Gary D Roberts. 2002. "Experimental study of strain-rate-dependent behavior of carbon/epoxy composite." *Composites Science and Technology* 62 (10): 1469–1476.

Ginzburg, Valeriy V, and Anna C Balazs. 1999. "Calculating Phase Diagrams of Polymer- Platelet Mixtures Using Density Functional Theory: Implications for Polymer/Clay Composites." *Macromolecules* 32 (17): 5681–5688.

Gleich, DM, MJL Van Tooren, and A Buekers. 2002. "Structural bonded joint analysis: An overview." *Adhesive Joints: Formation, Characteristics and Testing* 2:159–199.

Gojny, FH, MHG Wichmann, U Köpke, B Fiedler, and K Schulte. 2004. "Carbon nanotube-reinforced epoxy-composites: enhanced stiffness and fracture toughness at low nanotube content." *Composites science and technology* 64 (15): 2363–2371.

Goldberg, Robert K, Gary D Roberts, and Amos Gilat. 2005. "Implementation of an associative flow rule including hydrostatic stress effects into the high strain rate deformation analysis of polymer matrix composites." *Journal of Aerospace Engineering* 18 (1): 18–27.

Gonzalez, Rafael C, Richard E Woods, et al. 1992. *Digital image processing*. Vol. 3. Addison-wesley Reading.

Green, Keith J, Derrick R Dean, Uday K Vaidya, and Elijah Nyairo. 2009. "Multiscale fiber reinforced composites based on a carbon nanofiber/epoxy nanophased polymer matrix: synthesis, mechanical, and thermomechanical behavior." *Composites Part A: applied science and manufacturing* 40 (9): 1470–1475.

Green, RJ. 1972. "A plasticity theory for porous solids." *International Journal of Mechanical Sciences* 14 (4): 215–224.

Gurtin, Morton E, and William O Williams. 1966. "On the clausius-duhem inequality." *Zeitschrift für Angewandte Mathematik und Physik (ZAMP)* 17 (5): 626–633.

Ha, Sung Kyu, Kyo Kook Jin, and Yuanchen Huang. 2008. "Micro-mechanics of failure (MMF) for continuous fiber reinforced composites." *Journal of Composite Materials* 42 (18): 1873–1895.

Hackett, E, E Manias, and EP Giannelis. 1998. "Molecular dynamics simulations of organically modified layered silicates." *The Journal of chemical physics* 108 (17): 7410–7415.

Hague, Jacob R. 2016. "Carbon Fiber Reinforced Polymer Roofing at AC2 Auditorium: A Case Study."

Halgren, Thomas A. 1996. "Merck molecular force field. I. Basis, form, scope, parameterization, and performance of MMFF94." *Journal of computational chemistry* 17 (5-6): 490–519.

Harris, JA, and RA Adams. 1984. "Strength prediction of bonded single lap joints by non-linear finite element methods." *International Journal of Adhesion and Adhesives* 4 (2): 65–78.

Hart-Smith, Leonard John. 1973. *Adhesive-bonded single-lap joints.* National Aeronautics / Space Administration.

Hasan, Zeaid, Aditi Chattopadhyay, and Yingtao Liu. 2014. "Multiscale approach to analysis of composite joints incorporating nanocomposites." *Journal of Aircraft* 52 (1): 204–215.

Hashin, Zvi. 1980. "Failure criteria for unidirectional fiber composites." *Journal of applied mechanics* 47 (2): 329–334.

Hashin, Zvi, and B Walter Rosen. 1964. "The elastic moduli of fiber-reinforced materials." *Journal of applied mechanics* 31 (2): 223–232.

Heinbockel, John Henry. 2001. *Introduction to tensor calculus and continuum mechanics.* Vol. 52. Trafford.

Herakovich, CT. 1998. *Mechanics of fibrous composites.*

Hexcel. 2016. "HexTow IM7 Carbon Fiber Product Datasheet." http://www.hexcel.com/user_area/content_media/raw/IM7_HexTow_DataSheet.pdf.

Hill, Rodney. 1963. "Elastic properties of reinforced solids: some theoretical principles." *Journal of the Mechanics and Physics of Solids* 11 (5): 357–372.

———. 1965. "A self-consistent mechanics of composite materials." *Journal of the Mechanics and Physics of Solids* 13 (4): 213–222.

Hoover, Wm G. 1986. "Molecular dynamics." In *Molecular Dynamics,* vol. 258.

Horstemeyer, Mark F. 2009. "Multiscale modeling: a review." In *Practical aspects of computational chemistry,* 87–135. Springer.

Horstemeyer, Mark F, and Vera Revelli. 1997. "Stress history dependent localization and failure using continuum damage mechanics concepts." In *Applications of continuum damage mechanics to fatigue and fracture.* ASTM International.

Hu, Ning, Hisao Fukunaga, Satoshi Atobe, Yaolu Liu, Jinhua Li, et al. 2011. "Piezoresistive strain sensors made from carbon nanotubes based polymer nanocomposites." *Sensors* 11 (11): 10691–10723.

Hu, Ning, Yoshifumi Karube, Masahiro Arai, Tomonori Watanabe, Cheng Yan, Yuan Li, Yaolu Liu, and Hisao Fukunaga. 2010. "Investigation on sensitivity of a polymer/carbon nanotube composite strain sensor." *Carbon* 48 (3): 680–687.

Hu, Ning, Yoshifumi Karube, Cheng Yan, Zen Masuda, and Hisao Fukunaga. 2008. "Tunneling effect in a polymer/carbon nanotube nanocomposite strain sensor." *Acta Materialia* 56 (13): 2929–2936.

Hu, Ning, Zen Masuda, Cheng Yan, Go Yamamoto, Hisao Fukunaga, and Toshiyuki Hashida. 2008. "The electrical properties of polymer nanocomposites with carbon nanotube fillers." *Nanotechnology* 19 (21): 215701.

Huang, Y, KX Hu, X Wei, and A Chandra. 1994. "A generalized self-consistent mechanics method for composite materials with multiphase inclusions." *Journal of the Mechanics and Physics of Solids* 42 (3): 491–504.

Humphrey, William, Andrew Dalke, and Klaus Schulten. 1996. "VMD: visual molecular dynamics." *Journal of molecular graphics* 14 (1): 33–38.

Inam, Fawad, Doris WY Wong, Manabu Kuwata, and Ton Peijs. 2010. "Multiscale hybrid micro-nanocomposites based on carbon nanotubes and carbon fibers." *Journal of Nanomaterials* 2010:9.

Jeridi, M, Lucien Laiarinandrasana, and Kacem Sai. 2015. "Comparative study of continuum damage mechanics and mechanics of porous media based on multi-mechanism model on polyamide 6 semi-crystalline polymer." *International Journal of Solids and Structures* 53:12–27.

Jiang, L, Y Huang, H Jiang, G Ravichandran, H Gao, KC Hwang, and B Liu. 2006. "A cohesive law for carbon nanotube/polymer interfaces based on the van der Waals force." *Journal of the Mechanics and Physics of Solids* 54 (11): 2436–2452.

Jin, Kyo-Kook, Yuanchen Huang, Young-Hwan Lee, and Sung Kyu Ha. 2008. "Distribution of micro stresses and interfacial tractions in unidirectional composites." *Journal of Composite Materials* 42 (18): 1825–1849.

Johnston, Joel P, Bonsung Koo, Nithya Subramanian, and Aditi Chattopadhyay. 2017. "Modeling the molecular structure of the carbon fiber/polymer interphase for multiscale analysis of composites." *Composites Part B: Engineering* 111:27–36.

Johnston, Joel Philip. 2016. "Stochastic multiscale modeling and statistical characterization of complex polymer matrix composites." PhD diss., Arizona State University.

Johnston, Joel, and Aditi Chattopadhyay. 2013. "Stochastic multiscale modeling and damage progression for composite materials." In *ASME 2013 International Mechanical Engineering Congress and Exposition,* V009T10A011–V009T10A011. American Society of Mechanical Engineers.

Jones, Robert M. 1998. *Mechanics of composite materials.* CRC press.

Jorgensen, William L, David S Maxwell, and Julian Tirado-Rives. 1996. "Development and testing of the OPLS all-atom force field on conformational energetics and properties of organic liquids." *J. Am. Chem. Soc* 118 (45): 11225–11236.

Ju, JW. 1990. "Isotropic and anisotropic damage variables in continuum damage mechanics." *Journal of Engineering Mechanics* 116 (12): 2764–2770.

Kadla, JF, S Kubo, RA Venditti, RD Gilbert, AL Compere, and W Griffith. 2002. "Lignin-based carbon fibers for composite fiber applications." *Carbon* 40 (15): 2913–2920.

Kalamkarov, Alexander L, Igor V Andrianov, Vladyslav V Danishevsâ, et al. 2009. "Asymptotic homogenization of composite materials and structures." *Applied Mechanics Reviews* 62 (3): 030802.

Kang, Inpil, Mark J Schulz, Jay H Kim, Vesselin Shanov, and Donglu Shi. 2006. "A carbon nanotube strain sensor for structural health monitoring." *Smart materials and structures* 15 (3): 737.

Kanit, T, S Forest, Ia Galliet, Va Mounoury, and D Jeulin. 2003. "Determination of the size of the representative volume element for random composites: statistical and numerical approach." *International Journal of solids and structures* 40 (13): 3647–3679.

Kanouté, P, DP Boso, JL Chaboche, and BA Schrefler. 2009. "Multiscale methods for composites: a review." *Archives of Computational Methods in Engineering* 16 (1): 31–75.

Kashtalyan, M, and C Soutis. 2000. "Stiffness degradation in cross-ply laminates damaged by transverse cracking and splitting." *Composites Part A: Applied Science and Manufacturing* 31 (4): 335–351.

Kaw, Autar K. 2005. *Mechanics of composite materials.* CRC press.

Koo, B, Y Liu, J Zou, A Chattopadhyay, and LL Dai. 2014. "Study of glass transition temperature (Tg) of novel stress-sensitive composites using molecular dynamic simulation." *Modelling and Simulation in Materials Science and Engineering* 22 (6): 065018.

Koohbor, Behrad, Suraj Ravindran, and Addis Kidane. 2015. "Meso-scale strain localization and failure response of an orthotropic woven glass–fiber reinforced composite." *Composites Part B: Engineering* 78:308–318.

Kundalwal, SI, and S Kumar. 2015a. "Multiscale modeling of microscale fiber reinforced composites with nano-engineered interphases." *arXiv preprint arXiv:1509.05140.*

Kundalwal, SI, and S Kumar. 2015b. "Multiscale modeling of microscale fiber reinforced composites with nano-engineered interphases." *arXiv preprint arXiv:1509.05140.*

Kwon, Young W, David H Allen, and Ramesh Talreja. 2008. *Multiscale modeling and simulation of composite materials and structures.* Vol. 47. Springer.

Lacroix, Th, B Tilmans, Roland Keunings, M Desaeger, and Ignace Verpoest. 1992. "Modelling of critical fibre length and interfacial debonding in the fragmentation testing of polymer composites." *Composites science and technology* 43 (4): 379–387.

Larsen, Troy, Katerina Moloni, Frank Flack, Mark A Eriksson, Max G Lagally, and Charles T Black. 2002. "Comparison of wear characteristics of etched-silicon and carbon nanotube atomic-force microscopy probes." *Applied physics letters* 80 (11): 1996–1998.

Lemaitre, Jean. 1985. "A continuous damage mechanics model for ductile fracture." *Transactions of the ASME. Journal of Engineering Materials and Technology* 107 (1): 83–89.

———. 2012. *A course on damage mechanics.* Springer Science & Business Media.

Li, Chunyu, and Alejandro Strachan. 2011. "Molecular dynamics predictions of thermal and mechanical properties of thermoset polymer EPON862/DETDA." *Polymer* 52 (13): 2920–2928.

Li, Jing, Peng Cheng Ma, Wing Sze Chow, Chi Kai To, Ben Zhong Tang, and J-K Kim. 2007. "Correlations between percolation threshold, dispersion state, and aspect ratio of carbon nanotubes." *Advanced Functional Materials* 17 (16): 3207–3215.

Li, Richard, Noa Lachman, Peter Florin, H Daniel Wagner, and Brian L Wardle. 2015. "Hierarchical carbon nanotube carbon fiber unidirectional composites with preserved tensile and interfacial properties." *Composites Science and Technology* 117:139–145.

Loos, Alfred C, and George S Springer. 1983. "Curing of epoxy matrix composites." *Journal of composite materials* 17 (2): 135–169.

Lovatt, Andrew, Hugh Shercliff, and Philip Withers. 2000. "Material selection and processing; data courtesy of Granta Design Ltd, Cambridge, UK." www - materials . eng . cam . ac . uk / mpsite.

Luan, BQ, S Hyun, JF Molinari, N Bernstein, and Mark O Robbins. 2006. "Multiscale modeling of two-dimensional contacts." *Physical Review E* 74 (4): 046710.

Lutsko, JF. 1988. "Stress and elastic constants in anisotropic solids: molecular dynamics techniques." *Journal of Applied Physics* 64 (3): 1152–1154.

Meincke, Olaf, Dirk Kaempfer, Hans Weickmann, Christian Friedrich, Marc Vathauer, and Holger Warth. 2004. "Mechanical properties and electrical conductivity of carbon-nanotube filled polyamide-6 and its blends with acrylonitrile/butadiene/styrene." *Polymer* 45 (3): 739–748.

Menzer, Katharina, Beate Krause, Regine Boldt, Bernd Kretzschmar, Roland Weidisch, and Petra Pötschke. 2011. "Percolation behaviour of multiwalled carbon nanotubes of altered length and primary agglomerate morphology in melt mixed isotactic polypropylene-based composites." *Composites Science and Technology* 71 (16): 1936–1943.

Mesogitis, TS, AA Skordos, and AC Long. 2014. "Uncertainty in the manufacturing of fibrous thermosetting composites: A review." *Composites Part A: Applied Science and Manufacturing* 57:67–75.

Miller, Ronald E, and Ellad B Tadmor. 2009. "A unified framework and performance benchmark of fourteen multiscale atomistic/continuum coupling methods." *Modelling and Simulation in Materials Science and Engineering* 17 (5): 053001.

Misra, Abha, Pawan K Tyagi, MANOJ K Singh, and DS Misra. 2006. "FTIR studies of nitrogen doped carbon nanotubes." *Diamond and related materials* 15 (2): 385–388.

Mori, Tanaka, and K Tanaka. 1973. "Average stress in matrix and average elastic energy of materials with misfitting inclusions." *Acta metallurgica* 21 (5): 571–574.

Murari, V, and CS Upadhyay. 2012. "Micromechanics based ply level material degradation model for unidirectional composites." *Composite Structures* 94 (2): 671–680.

Namilae, S, and Namas Chandra. 2006. "Role of atomic scale interfaces in the compressive behavior of carbon nanotubes in composites." *Composites Science and Technology* 66 (13): 2030–2038.

National-Research-Council. 2008. *Integrated computational materials engineering: a transformational discipline for improved competitiveness and national security*. National Academies Press.

Neerukatti, Rajesh Kumar, Kuang C Liu, Narayan Kovvali, and Aditi Chattopadhyay. 2014. "Fatigue life prediction using hybrid prognosis for structural health monitoring." *Journal of Aerospace Information Systems*.

Nemat-Nasser, Sia, and Muneo Hori. 2013. *Micromechanics: overall properties of heterogeneous materials*. Vol. 37. Elsevier.

Odegard, Gregory M, Sarah-Jane V Frankland, and Thomas S Gates. 2005. "Effect of nanotube functionalization on the elastic properties of polyethylene nanotube composites." *Aiaa Journal* 43 (8): 1828.

Olson, Gregory B. 2000. "Designing a new material world." *Science* 288 (5468): 993–998.

Oskay, Caglar, and Jacob Fish. 2004. "Fatigue life prediction using 2-scale temporal asymptotic homogenization." *International Journal for Numerical Methods in Engineering* 61 (3): 329–359.

———. 2007. "Eigendeformation-based reduced order homogenization for failure analysis of heterogeneous materials." *Computer Methods in Applied Mechanics and Engineering* 196 (7): 1216–1243.

Park, Myounggu, Hyonny Kim, and Jeffrey P Youngblood. 2008. "Strain-dependent electrical resistance of multi-walled carbon nanotube/polymer composite films." *Nanotechnology* 19 (5): 055705.

Pasternak, Elena, and H-B Mühlhaus. 2005. "Generalised homogenisation procedures for granular materials." *Journal of Engineering Mathematics* 52 (1-3): 199.

Patel, N, V Rohatgi, and L James Lee. 1993. "Influence of processing and material variables on resin-fiber interface in liquid composite molding." *Polymer Composites* 14 (2): 161–172.

Peerlings, RHJ, and NA Fleck. 2004. "Computational evaluation of strain gradient elasticity constants." *International Journal for Multiscale Computational Engineering* 2 (4).

Pellegrino, C, U Galvanetto, and BA Schrefler. 1999. "Numerical homogenization of periodic composite materials with non-linear material components." *International Journal for Numerical Methods in Engineering* 46 (10): 1609–1637.

Peng, Bo, and Wenbin Yu. 2015. "A New Micromechanics Theory for Homogenization and Dehomogenization of Heterogeneous Materials." In *American Society of Composites-30th Technical Conference*.

Peric, Djordje. 1993. "On a class of constitutive equations in viscoplasticity: formulation and computational issues." *International Journal for Numerical Methods in Engineering* 36 (8): 1365–1393.

Pietak, Alexis, Sandra Korte, Emelyn Tan, Alison Downard, and Mark P Staiger. 2007. "Atomic force microscopy characterization of the surface wettability of natural fibres." *Applied surface science* 253 (7): 3627–3635.

Pindera, Marek-Jerzy, Hamed Khatam, Anthony S Drago, and Yogesh Bansal. 2009. "Micromechanics of spatially uniform heterogeneous media: a critical review and emerging approaches." *Composites Part B: Engineering* 40 (5): 349–378.

Pineda, Evan J, Anthony M Waas, Brett A Bednarcyk, Craig S Collier, and Phillip W Yarrington. 2009. "Progressive damage and failure modeling in notched laminated fiber reinforced composites." *International journal of fracture* 158 (2): 125–143.

Plimpton, Steve, Paul Crozier, and Aidan Thompson. 2007. "LAMMPS-large-scale atomic/molecular massively parallel simulator." *Sandia National Laboratories* 18.

Qian, Dong, Gregory J Wagner, and Wing Kam Liu. 2004. "A multiscale projection method for the analysis of carbon nanotubes." *Computer Methods in Applied Mechanics and Engineering* 193 (17): 1603–1632.

Qiu, Jingjing, Chuck Zhang, Ben Wang, and Richard Liang. 2007. "Carbon nanotube integrated multifunctional multiscale composites." *Nanotechnology* 18 (27): 275708.

Qu, Jianmin, and Mohammed Cherkaoui. 2006. *Fundamentals of micromechanics of solids.* Wiley Online Library.

Rai, Ashwin, Nithya Subramanian, and Aditi Chattopadhyay. 2017. "Investigation of damage mechanisms in CNT nanocomposites using multiscale analysis." *International Journal of Solids and Structures.*

Rai, Ashwin, Nithya Subramanian, Bonsung Koo, and Aditi Chattopadhyay. 2017. "Multiscale damage analysis of carbon nanotube nanocomposite using a continuum damage mechanics approach." *Journal of Composite Materials* 51 (6): 847–858.

Ramsden, Mike. 1968. "Stand Points." *Flight International* 93.

Rapaport, Dennis C, Robin L Blumberg, Susan R McKay, Wolfgang Christian, et al. 1996. "The art of molecular dynamics simulation." *Computers in Physics* 10 (5): 456–456.

Reddy, Junuthula N. 1984. "A simple higher-order theory for laminated composite plates." *Journal of applied mechanics* 51 (4): 745–752.

Reifsnider, KL. 1994. "Modelling of the interphase in polymer-matrix composite material systems." *Composites* 25 (7): 461–469.

Ren, Xiang, Josh Burton, Gary D Seidel, and Khalid Lafdi. 2015. "Computational multiscale modeling and characterization of piezoresistivity in fuzzy fiber reinforced polymer composites." *International Journal of Solids and Structures* 54:121–134.

Ren, Xiang, and Gary D Seidel. 2013. "Computational micromechanics modeling of inherent piezoresistivity in carbon nanotube–polymer nanocomposites." *Journal of Intelligent Material Systems and Structures* 24 (12): 1459–1483.

Ren, Y, Yong Qing Fu, K Liao, F Li, and Hui-Ming Cheng. 2004. "Fatigue failure mechanisms of single-walled carbon nanotube ropes embedded in epoxy." *Applied Physics Letters* 84 (15): 2811–2813.

Reuss, A. 1929. "Berechnung der fließgrenze von mischkristallen auf grund der plastizitätsbedingung für einkristalle." *ZAMM-Journal of Applied Mathematics and Mechanics/Zeitschrift für Angewandte Mathematik und Mechanik* 9 (1): 49–58.

Rice, James R. 1971. "Inelastic constitutive relations for solids: an internal-variable theory and its application to metal plasticity." *Journal of the Mechanics and Physics of Solids* 19 (6): 433–455.

Rigatos, Gerasimos. 2011. *Modelling and control for intelligent industrial systems: adaptive algorithms in robotics and industrial engineering.* Vol. 7. Springer Science & Business Media.

Robach, JS, IM Robertson, BD Wirth, and A Arsenlis. 2003. "In-situ transmission electron microscopy observations and molecular dynamics simulations of dislocation-defect interactions in ion-irradiated copper." *Philosophical Magazine* 83 (8): 955–967.

Robertson, BF, and DF Radcliffe. 2009. "Impact of CAD tools on creative problem solving in engineering design." *Computer-Aided Design* 41 (3): 136–146.

Roeseler, William G, Branko Sarh, Max U Kismarton, J Quinlivan, J Sutter, and D Roberts. 2007. "Composite structures: the first 100 years." In *16th International Conference on Composite Materials,* 1–41.

Romanov, Valentin S, Stepan V Lomov, Ignaas Verpoest, and Larissa Gorbatikh. 2015. "Modelling evidence of stress concentration mitigation at the micro-scale in polymer composites by the addition of carbon nanotubes." *Carbon* 82:184–194.

Romanov, Valentin, SV Lomov, L Gorbatikh, and Ignace Verpoest. 2013. "A novel approach to modelling of fiber-reinforced composites with carbon nanotubes." In *20th international conference on composite materials.*

Sandler, J, MSP Shaffer, T Prasse, W Bauhofer, K Schulte, and AH Windle. 1999. "Development of a dispersion process for carbon nanotubes in an epoxy matrix and the resulting electrical properties." *Polymer* 40 (21): 5967–5971.

Schapery, RA. 1989. "Mechanical characterization and analysis of inelastic composite laminates with growing damage." *Mechanics of composite materials and structures:* 1–9.

Schapery, RA. 1990. "A theory of mechanical behavior of elastic media with growing damage and other changes in structure." *Journal of the Mechanics and Physics of Solids* 38 (2): 215–253.

Segurado, J, and J Llorca. 2002. "A numerical approximation to the elastic properties of sphere-reinforced composites." *Journal of the Mechanics and Physics of Solids* 50 (10): 2107–2121.

Sha, JJ, JX Dai, J Li, ZQ Wei, JM Hausherr, and W Krenkel. 2014. "Measurement and analysis of fiber-matrix interface strength of carbon fiber-reinforced phenolic resin matrix composites." *Journal of Composite Materials* 48 (11): 1303–1311.

Shaw, Andrew, Srinivas Sriramula, Peter D Gosling, and Marios K Chryssanthopoulos. 2010. "A critical reliability evaluation of fibre reinforced composite materials based on probabilistic micro and macro-mechanical analysis." *Composites Part B: Engineering* 41 (6): 446–453.

Shenoy, VB, R Miller, EB Tadmor, R Phillips, and M Ortiz. 1998. "Quasicontinuum models of interfacial structure and deformation." *Physical Review Letters* 80 (4): 742.

Shimamura, Yoshinobu, Tetsuo Yasuoka, and Akira Todoroki. 2007. "Strain sensing by using piezoresistivity of carbon nanotube/flexible-epoxy composite." In *Proceedings of the 16th International Conference on Composite Materials,* vol. 224503.

Shinoda, Wataru, Motoyuki Shiga, and Masuhiro Mikami. 2004. "Rapid estimation of elastic constants by molecular dynamics simulation under constant stress." *Physical Review B* 69 (13): 134103.

Shojaei, Amir, Guoqiang Li, Jacob Fish, and PJ Tan. 2014. "Multi-scale constitutive modeling of ceramic matrix composites by continuum damage mechanics." *International Journal of Solids and Structures* 51 (23): 4068–4081.

Simmons, John G. 1963. "Electric tunnel effect between dissimilar electrodes separated by a thin insulating film." *Journal of applied physics* 34 (9): 2581–2590.

Singh, Sandeep Kumar, S Goverapet Srinivasan, M Neek-Amal, S Costamagna, Adri CT van Duin, and FM Peeters. 2013. "Thermal properties of fluorinated graphene." *Physical Review B* 87 (10): 104114.

Smyshlyaev, Valery P. 2009. "Propagation and localization of elastic waves in highly anisotropic periodic composites via two-scale homogenization." *Mechanics of Materials* 41 (4): 434–447.

Sochi, Emilie J. 2012. "Challenges for Insertion of Structural Nanomaterials in Aerospace Applications."

Souza, FV, DH Allen, and Y-R Kim. 2008. "Multiscale model for predicting damage evolution in composites due to impact loading." *Composites science and technology* 68 (13): 2624–2634.

Sriramula, Srinivas, and Marios K Chryssanthopoulos. 2009. "Quantification of uncertainty modelling in stochastic analysis of FRP composites." *Composites Part A: Applied Science and Manufacturing* 40 (11): 1673–1684.

Stamm, Henry. 1993. *On the Potential Structure of Viscoplastic Constitutive Equations.* Commission of the European Communities, ASIN: B001ABIM3K.

Subramanian, Nithya, Ashwin Rai, and Aditi Chattopadhyay. 2015. "Atomistically informed stochastic multiscale model to predict the behavior of carbon nanotube-enhanced nanocomposites." *Carbon* 94:661–672.

———. 2017. "Atomistically derived cohesive behavior of interphases in carbon fiber reinforced CNT nanocomposites." *Carbon* 117:55–64.

Subramanian, Nithya, Ashwin Rai, Siddhant Datta, Bonsung Koo, and Aditi Chattopadhyay. 2015. "A multiscale model coupling molecular dynamics simulations and micromechanics to study the behavior of CNT-enhanced nanocomposites." In *56th AIAA/ASCE/AHS/ASC Structures, Structural Dynamics, and Materials Conference 2015.* American Institute of Aeronautics and Astronautics Inc.

Subramaniyan, Arun K, and CT Sun. 2008. "Continuum interpretation of virial stress in molecular simulations." *International Journal of Solids and Structures* 45 (14): 4340–4346.

Sun, CT, and RS Vaidya. 1996. "Prediction of composite properties from a representative volume element." *Composites Science and Technology* 56 (2): 171–179.

Tack, Jeremy L, and David M Ford. 2008. "Thermodynamic and mechanical properties of epoxy resin DGEBF crosslinked with DETDA by molecular dynamics." *Journal of Molecular Graphics and Modelling* 26 (8): 1269–1275.

Tadmor, Ellad B, Michael Ortiz, and Rob Phillips. 1996. "Quasicontinuum analysis of defects in solids." *Philosophical magazine A* 73 (6): 1529–1563.

Talebi, Hossein, Mohammad Silani, Stéphane PA Bordas, Pierre Kerfriden, and Timon Rabczuk. 2014. "A computational library for multiscale modeling of material failure." *Computational Mechanics* 53 (5): 1047–1071.

Taranath, Bungale S. 2016. *Structural analysis and design of tall buildings: Steel and composite construction.* CRC press.

Thostenson, Erik T, and Tsu-Wei Chou. 2008. "Real-time in situ sensing of damage evolution in advanced fiber composites using carbon nanotube networks." *Nanotechnology* 19 (21): 215713.

Thostenson, Erik T, Zhifeng Ren, and Tsu-Wei Chou. 2001. "Advances in the science and technology of carbon nanotubes and their composites: a review." *Composites science and technology* 61 (13): 1899–1912.

Tillet, Guillaume, Bernard Boutevin, and Bruno Ameduri. 2011. "Chemical reactions of polymer crosslinking and post-crosslinking at room and medium temperature." *Progress in Polymer Science* 36 (2): 191–217.

Tsai, Stephen W, and Edward M Wu. 1971. "A general theory of strength for anisotropic materials." *Journal of composite materials* 5 (1): 58–80.

Tvergaard, Viggo, and Alan Needleman. 1984. "Analysis of the cup-cone fracture in a round tensile bar." *Acta metallurgica* 32 (1): 157–169.

Van Duin, Adri CT, Siddharth Dasgupta, Francois Lorant, and William A Goddard. 2001. "ReaxFF: a reactive force field for hydrocarbons." *The Journal of Physical Chemistry A* 105 (41): 9396–9409.

Verlet, Loup. 1967. "Computer" experiments" on classical fluids. I. Thermodynamical properties of Lennard-Jones molecules." *Physical review* 159 (1): 98.

Voigt, Woldemar. 1889. "Ueber die Beziehung zwischen den beiden Elasticitätsconstanten isotroper Körper." *Annalen der physik* 274 (12): 573–587.

Volkersen, Olaf. 1938. "Die Nietkraftverteilung in zugbeanspruchten Nietverbindungen mit konstanten Laschenquerschnitten." *Luftfahrtforschung* 15 (1/2): 41–47.

Voyiadjis, George Z, and Peter I Kattan. 2006. "Damage mechanics with fabric tensors." *Mechanics of Advanced Materials and Structures* 13 (4): 285–301.

Wagner, Gregory J, and Wing Kam Liu. 2003. "Coupling of atomistic and continuum simulations using a bridging scale decomposition." *Journal of Computational Physics* 190 (1): 249–274.

Wagner, H Daniel. 2002. "Nanotube–polymer adhesion: a mechanics approach." *Chemical Physics Letters* 361 (1): 57–61.

Wagner, HD, JA Nairn, and M Detassis. 1995. "Toughness of interfaces from initial fiber-matrix debonding in a single fiber composite fragmentation test." *Applied Composite Materials* 2 (2): 107–117.

Wang, Xiaoqiang, Jifeng Zhang, Zhenqing Wang, Song Zhou, and Xinyang Sun. 2011. "Effects of interphase properties in unidirectional fiber reinforced composite materials." *Materials & Design* 32 (6): 3486–3492.

Wang, ZL, P Poncharal, and WA De Heer. 2000. "Measuring physical and mechanical properties of individual carbon nanotubes by in situ TEM." *Journal of Physics and Chemistry of Solids* 61 (7): 1025–1030.

Wichmann, Malte HG, Samuel T Buschhorn, Jan Gehrmann, and Karl Schulte. 2009. "Piezoresistive response of epoxy composites with carbon nanoparticles under tensile load." *Physical Review B* 80 (24): 245437.

Wicks, Sunny S, Roberto Guzman de Villoria, and Brian L Wardle. 2010. "Interlaminar and intralaminar reinforcement of composite laminates with aligned carbon nanotubes." *Composites Science and Technology* 70 (1): 20–28.

Wicks, Sunny S, Wennie Wang, Marcel R Williams, and Brian L Wardle. 2014. "Multi-scale interlaminar fracture mechanisms in woven composite laminates reinforced with aligned carbon nanotubes." *Composites Science and Technology* 100:128–135.

Wikimedia. 2012. "Jet-liner's cabin pressure B-787." https://commons.wikimedia.org/wiki/File:Jet-liner%27s_cabin_pressure_(B-787).PNG.

Wu, HA. 2006. "Molecular dynamics study on mechanics of metal nanowire." *Mechanics Research Communications* 33 (1): 9–16.

Xiao, SP, and Ted Belytschko. 2004. "A bridging domain method for coupling continua with molecular dynamics." *Computer methods in applied mechanics and engineering* 193 (17): 1645–1669.

Xie, Xiao-Lin, Yiu-Wing Mai, and Xing-Ping Zhou. 2005. "Dispersion and alignment of carbon nanotubes in polymer matrix: a review." *Materials Science and Engineering: R: Reports* 49 (4): 89–112.

Xu, Xiaodong, Michael R Wisnom, Stephen R Hallett, Gary Holden, and Barbara Gordon. 2016. "Predicting debonding and delamination in adhesively bonded T-joints." In *17th European Conference on Composite Materials.*

Yamakov, V, D Wolf, SR Phillpot, AK Mukherjee, and H Gleiter. 2004. "Deformation-mechanism map for nanocrystalline metals by molecular-dynamics simulation." *Nature materials* 3 (1): 43–47.

Yarrington, Phil, James Zhang, Craig Collier, and Brett Bednarcyk. 2005. "Failure analysis of adhesively bonded composite joints." In *46th AIAA/ASME/ASCE/AHS/ASC Structures, Structural Dynamics and Materials Conference,* 2376.

Yasuoka, Tetsuo, Yoshinobu Shimamura, and Akira Todoroki. 2010. "Electrical resistance change under strain of CNF/flexible-epoxy composite." *Advanced Composite Materials* 19 (2): 123–138.

You, Min, Zhan-Mou Yan, Xiao-Ling Zheng, Hai-Zhou Yu, and Zhi Li. 2008. "A numerical and experimental study of adhesively bonded aluminium single lap joints with an inner chamfer on the adherends." *International Journal of Adhesion and Adhesives* 28 (1): 71–76.

Yu, Wenbin, and Tian Tang. 2007. "A variational asymptotic micromechanics model for predicting thermoelastic properties of heterogeneous materials." *International Journal of Solids and Structures* 44 (22): 7510–7525.

Yu, Xun, and Eil Kwon. 2009. "A carbon nanotube/cement composite with piezoresistive properties." *Smart Materials and Structures* 18 (5): 055010.

Zang, Jin-Liang, Quanzi Yuan, Feng-Chao Wang, and Ya-Pu Zhao. 2009. "A comparative study of Young's modulus of single-walled carbon nanotube by CPMD, MD and first principle simulations." *Computational Materials Science* 46 (3): 621–625.

Zhandarov, Serge, and Edith Mäder. 2005. "Characterization of fiber/matrix interface strength: applicability of different tests, approaches and parameters." *Composites Science and Technology* 65 (1): 149–160.

Zhang, Boming, Zhong Yang, Xinyang Sun, and Zhanwen Tang. 2010. "A virtual experimental approach to estimate composite mechanical properties: Modeling with an explicit finite element method." *Computational Materials Science* 49 (3): 645–651.

Zhang, Jinjun, Bonsung Koo, Nithya Subramanian, Yingtao Liu, and Aditi Chattopadhyay. 2016. "An optimized cross-linked network model to simulate the linear elastic material response of a smart polymer." *Journal of Intelligent Material Systems and Structures* 27 (11): 1461–1475.

Zhang, W, J Suhr, and N Koratkar. 2006. "Carbon nanotube/polycarbonate composites as multifunctional strain sensors." *Journal of nanoscience and nanotechnology* 6 (4): 960–964.

Zhang, YB, SP Lau, L Huang, and BK Tay. 2006. "Carbon nanotubes grown on cobalt-containing amorphous carbon composite films." *Diamond and related materials* 15 (1): 171–175.

Zhou, Yuanxin, Farhana Pervin, Lance Lewis, and Shaik Jeelani. 2008. "Fabrication and characterization of carbon/epoxy composites mixed with multi-walled carbon nanotubes." *Materials Science and Engineering: A* 475 (1): 157–165.

Zhu, Linfa. 2006. "Multiscale high strain rate models for polymer matrix composites." *Doctor Thesis, Arizona State University*.

Zhu, Linfa, Aditi Chattopadhyay, and Robert Goldberg. 2006. "A 3D micromechanics model for strain rate dependent inelastic polymer matrix composites." In *47th AIAA/ASME/ASCE/AHS/ASC Structures, Structural Dynamics, and Materials Conference 14th AIAA/ASME/AHS Adaptive Structures Conference 7th,* 1689.